UNIVERSIDAD AUTÓNOMA DE MADRID

Facultad de Ciencias

Departamento de Química Inorgánica

Processing of Imine-based Covalent Organic Frameworks

Tesis presentada por

David Rodríguez San Miguel

para optar al grado de Doctor en Química Aplicada

Director de tesis

Prof. Félix Zamora Abanades

Madrid, junio de 2018

Contents

Abstract

Covalent organic frameworks (COFs) are a fairly novel type of porous materials characterised by being made of light elements joined by covalent bonds forming ordered and periodic networks. They have shown potential in a range of applications comprising from water purification to solar energy collection. However, its processability is underdeveloped and hinders its incorporation in functional devices. Thus, in this thesis, several approaches to process imine-linked COFs that have been developed during the last four years are described.

The first introductory chapter is intended to provide a general overview of COFs, explaining its design, the requisites they must adhere to, their chemistry and their properties and applications, in addition to a more comprehensive list of the processing methodologies that have been reported to date.

In Chapter 2, the first reported procedure for the room temperature synthesis of imine-based COFs is described. Moreover, taking advantage of this new possibility, patterns of COF are created on different substrates using inkjet printing and soft lithography.

Chapter 3 describes the synthesis of COFs in microfluidic systems, which results in the formation of crystalline materials with an unprecedented fibrous morphology in a few seconds.

In Chapter 4, the procedures developed in the two previous chapters are employed to prepare COFs loaded with different molecules enhancing their ionic conductivity. It is found that the addition of a small amount of acetic acid when pressing the powder to shape it allows the formation of

continuous COF films and that this processing methodology has a critical effect on the performance of the material as a membrane in fuel cells.

Finally, the last chapter describes the formation of monodisperse COF spheres in a two-step amorphous sphere formation/recrystallisation process that also enables the encapsulation of functional metal and metal oxide nanoparticles which are demonstrated to preserve their properties and be accessible due to the porous nature of the surrounding COF.

Resumen

Los "Covalent Organic Frameworks" (COFs por sus siglas en inglés), son una nueva clase de materiales porosos caracterizados por estar compuestos por elementos ligeros unidos mediante enlaces covalentes, de forma que generen redes periódicas y ordenadas. Han demostrado potencial aplicación en un amplio espectro de situaciones, abarcando desde la purificación de agua al aprovechamiento de energía solar. Sin embargo, su procesabilidad está poco desarrollada, lo que supone una barrera para su incorporación en dispositivos funcionales. Por tanto, en esta tesis se describen varias aproximaciones para procesar COFs basados en enlace imina que se han desarrollado en los últimos cuatro años.

El primer capítulo introductorio pretende proporcionar una visión general de los COFs, explicando su diseño, los requisitos que deben cumplir, su química y sus propiedades y aplicaciones, además de una lista detallada de las metodologías que se han usado hasta la fecha para procesar estos materiales.

En el capítulo 2 se describe el primer procedimiento que permitió la síntesis a temperatura ambiente de COFs basados en enlace imina. Además, aprovechando esta nueva posibilidad, se depositó COF en varios sustratos creando diseños de forma controlada usando impresoras de inyección de tinta y "soft lithography".

El capítulo 3 describe la síntesis de COFs en sistemas de microfluídica, lo que en unos pocos segundos da lugar a la formación de materiales cristalinos con morfología fibrilar desconocida hasta el momento.

En el capítulo 4, los procedimientos desarrollados en los dos capítulos anteriores se emplean para preparar COFs impregnados con distintas

moléculas que mejoran su conductividad iónica. Se descubre que la adición de pequeñas cantidades de ácido acético cuando los materiales son prensados permite la formación de películas continuas de COF y que el método de procesado usado tiene un efecto crucial en el comportamiento del material como membrana en pilas de combustible.

Por último, el capítulo 5 describe la formación de esferas de COF monodispersas en un mecanismo en dos pasos consistente en la formación de esferas amorfas y su posterior recristalización. Este proceso también permite la encapsulación de nanopartículas metálicas y de óxidos metálicos, que conservan sus propiedades y son accesibles gracias a la naturaleza porosa del COF que las envuelve.

Chapter 1. Introduction

1.1. Porous Materials

Porous materials are characterised by the presence of cavities in their structure, which confer some unique properties to these solids. As a result, and given that some of them are naturally occurring and others easily prepared, they have been employed by human beings for millennia. A few examples of these long-employed materials that deserve mentioning are wood, charcoal and ceramics, which were used because of their lightness, insulating properties or adsorptive capacities among others[1]. However, it was not until the 18th century that they became the subject of scientific experiments, when Scheele in 1773, Priestley in 1775 and Fontana in 1777 investigated the adsorptive capacity of charcoal[2]. Another remarkable milestone in the development of porous materials also happened during that century, it was the first description of a zeolite by Cronsted in 1756[3]. Since then, the theoretical basis of adsorption was developed, the preparation of activated carbons was refined and synthetic methods for the obtention of zeolites appeared. The low cost, high thermal and chemical stability and simple processing of these two classes of materials allowed them to perform effectively in most applications, therefore becoming widespread. More recently, some new molecularly designed porous materials such as metal organic frameworks (MOFs)[4], porous organic polymers[5], covalent organic frameworks (COFs)[6] and porous organic cages[7] have been developed. The range of applications of all these materials is huge, comprising from some of their classical functions such as catalysis, separation and purification to novel ones like gas storage, ionic conductors, energy storage and production, sensing and electronics.

Some major concerns for society nowadays are related to energy production and storage and with the availability of drinking water, as evidenced by the importance given to them in Horizon 2020 programs[8,9]. As the effects of global warming become evident, so does the need to find energy sources which do not generate large amounts of greenhouse gases. Not only does this pose the challenge of switching from fossil fuel based electricity generation plants to solar and wind power, but it also requires us to find new alternatives for the storage of the produced energy given the fluctuating nature of these cleaner energy sources. Several examples of the potential contribution of porous materials in the solution of these problems can already be found in the literature. An application solely for energy storage lies in the field of supercapacitors, where higher surface area is a synonym of higher energy density[10]. In fact, activated carbons are currently the dominant materials for electrodes owing to the high specific power that can be achieved at a moderate cost, although much improvement must still be made in terms of energy density and cyclability for their successful implementation in electric vehicles or other devices requiring a high amount of energy for a short time. Another example whose actual future impact is still to be assessed is the ability of MOFs[11] to serve as supports for the photocatalytic generation of hydrogen from water. As shown in the work of Wang *et al*.[12], the possibility of positioning metal nanoparticles close to immobilised photosensitisers while keeping all of them accessible to the solution improves the performance of the system when compared to its molecular analogue due to the proximity of photo- and catalytically active moieties and the retardation of the degradation of the photosensitiser. The successful development of this strategy of solar energy collection would solve both the problems of generation and storage, since the hydrogen produced could be kept until it would be necessary to meet a peak in electricity consumption.

Returning to the topic of water scarcity, droughts and water shortages are already common in many regions, Mediterranean countries for instance, and are predicted to become more frequent, harsher and affect larger areas[13,14]. The effects are not limited to drinking and hygiene, they also cause significant drops in food production and increase energy consumption since the only current alternatives consist of transporting water from other places or desalinating seawater by reverse osmosis, an extremely energy intensive process. As an example of what porous materials can offer in this area, a recent work published in *Science* that points towards the use of MOFs to lessen this issue has already generated a great deal of expectation[15]. The article describes a device that allows a layer of MOF to capture water from air even at low humidity levels during the night. The water adsorbed can be collected during the day and the MOF reactivated by simple exposure to sunlight. This process, which consumes little to no energy, is estimated to allow the harvesting of nearly 1 litre of water per square metre per day.

Concerning what each class of porous materials can add towards the solution of these and other problems, it is not likely that the emerging families will displace zeolites and porous carbons in their traditional applications, since after being optimised for many years they have reached excellent levels of performance. The little room left for improvement together with the higher cost and lower durability of MOFs and COFs precludes them from competing in many catalytic and adsorption processes. Nonetheless, there are still many niches occupied by zeolites or even completely different technological approaches due to the lack of a more suitable material, not to speak of the myriad of yet unsolved challenges that are holding back the development of many new promising technologies. These are the areas where MOFs, COFs and related materials could arguably be superior to currently existing options

owing to some features that are not present in classical materials, standing above all the possibility of a virtually à la carte chemical design[16].

1.1.1. Covalent Organic Frameworks

One of the most promising new porous materials are Covalent Organic Frameworks, usually shortened to the acronym COFs. They were reported for the first time in 2005 and are purely organic materials displaying porosity and crystallinity and formed by the linkage of organic building blocks through covalent bonds that extend periodically in 2 or 3 dimensions[6]. The concept of the structural design may be best explained using Figure 1.1, in which the chemical structures have been simplified so the building blocks are depicted as geometric shapes which can be linked

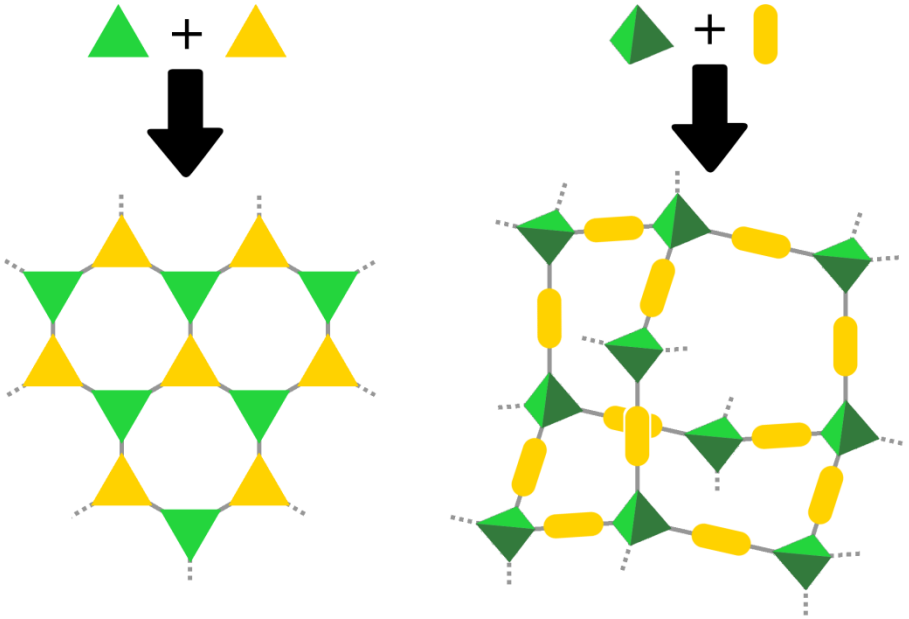

Figure 1.1. Schematic representation of COF networks generated by the bonding of two triangular building blocks (left) and a tetrahedral with a linear building block (right).

through the vertices. As illustrated in the image, the idea is to use molecules with several reactive groups oriented in a suitable manner so upon bonding they will create an infinite, periodic and ordered network of covalently bound atoms. The requirement for crystallinity arises from the fact that if the material is to possess such ordered structure, it necessarily has crystalline domains; a lack of them therefore indicates a highly defective material which does not comply either with the expected long-range order nor with the intended local chemical environment. Porosity, on the other hand, is not so critical, although it is true that the majority of the proposed structures are inherently porous and as a consequence it can be used as an additional proof that the correct structure has been obtained, some COFs are not porous due to interpenetration, staggered stacking or the presence of bulky functional groups that completely fill the pores.

1.2. Design of COFs

When designing a new COF or choosing between the already reported ones with a specific goal in mind, there are some aspects that need to be decided, like the type of bond between the building blocks, the symmetry of the network, pore size or the presence and position of functional moieties. Although it is not always the case when it comes to choosing the structure of a COF since some bonds and molecules are restricted to certain symmetries, it seems more appropriate to rationalise this discussion beginning with general features such as connectivity and geometry of the building blocks, that is, the topology of the network, and close it with apparently minor issues like the functionalisation of pore walls.

1.2.1. Topology

Conceptually, determining the topology of the network is the first step in the design of a new COF since it describes the connectivity the molecular building blocks must exhibit. Once the information about the number of linking points of each building block and their spatial orientation is known, it is possible to leave abstraction behind and start thinking about specific molecules. This is also important if the design process starts from another point; for example, if it is essential to include a certain molecule, knowing which networks are compatible with the geometry of the molecule allows the choice of a complementary building block that permits the formation of an ordered framework.

Of the numerous nets that can be thought of, only eight (shown in Figures 1.2 and 1.3 accompanied by an example) have been employed in the synthesis of COFs[17]. They can be classified into two big categories

attending to their dimensionality: they can extend either in 2 or in 3 dimensions.

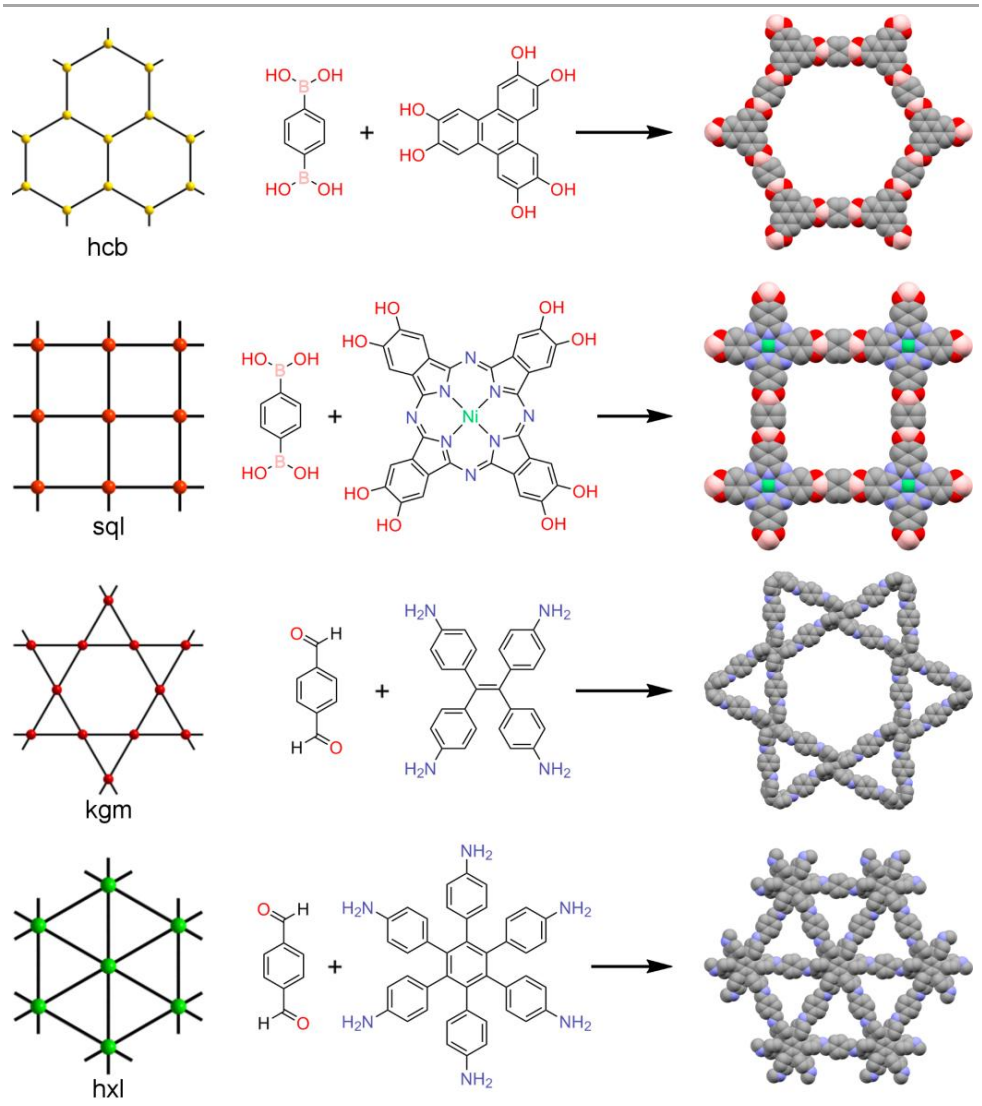

Figure 1.2. Representation of all the 2D topologies (left) found in reported COFs and examples of synthesised structures corresponding to each topology (space filling model, C: grey, B: pink, O: red, N: blue, Ni: green, H omitted for clarity). Adapted from Reference 17.

Networks that propagate only in 2 dimensions consequently restrict covalent bonds to be in a plane, resulting in the formation of layers. As expected, these layers do not remain isolated and have a strong tendency to aggregate and form a layered material in which the integrity of the layers is maintained by strong covalent bonds while weaker intermolecular interactions, frequently π-π stacking, hold the different layers together. The vast majority of the COFs reported to date display one of the four two-dimensional (2D) topologies, possibly because of the high synthetic availability of planar molecules with aromatic cores.

Three-dimensional (3D) topologies allow the formation of covalent bonds in all directions, as a result, the growth of the material is more isotropic as it depends on the same type of interaction in every direction. All four networks of this type rely on tetrahedral nodes to generate 3D structures, very likely for the reason that other types of vertices such as octahedra are difficult to obtain using organic molecules whose basic components are planar or tetrahedral carbon atoms.

Once the network and the geometric characteristics of the building blocks have been identified, it is necessary to select the core of the molecules that are going to form the COF. Although there are no strict requirements besides fulfilling the orientation conditions of the reactive groups, rigid cores are usually preferred. Even though it is possible to postulate the formation of a network using flexible building blocks, the high number of degrees of freedom adds an extra difficulty since many conformations will not provide a suitable orientation for the linkages, thus leading to a disordered structure. Another factor to consider when selecting building blocks is their size, it is especially attractive if there are linear linkers, since their length will determine the diameter of the pores and allows to obtain families of isoreticular COFs that differ only in the size of the cavities[18].

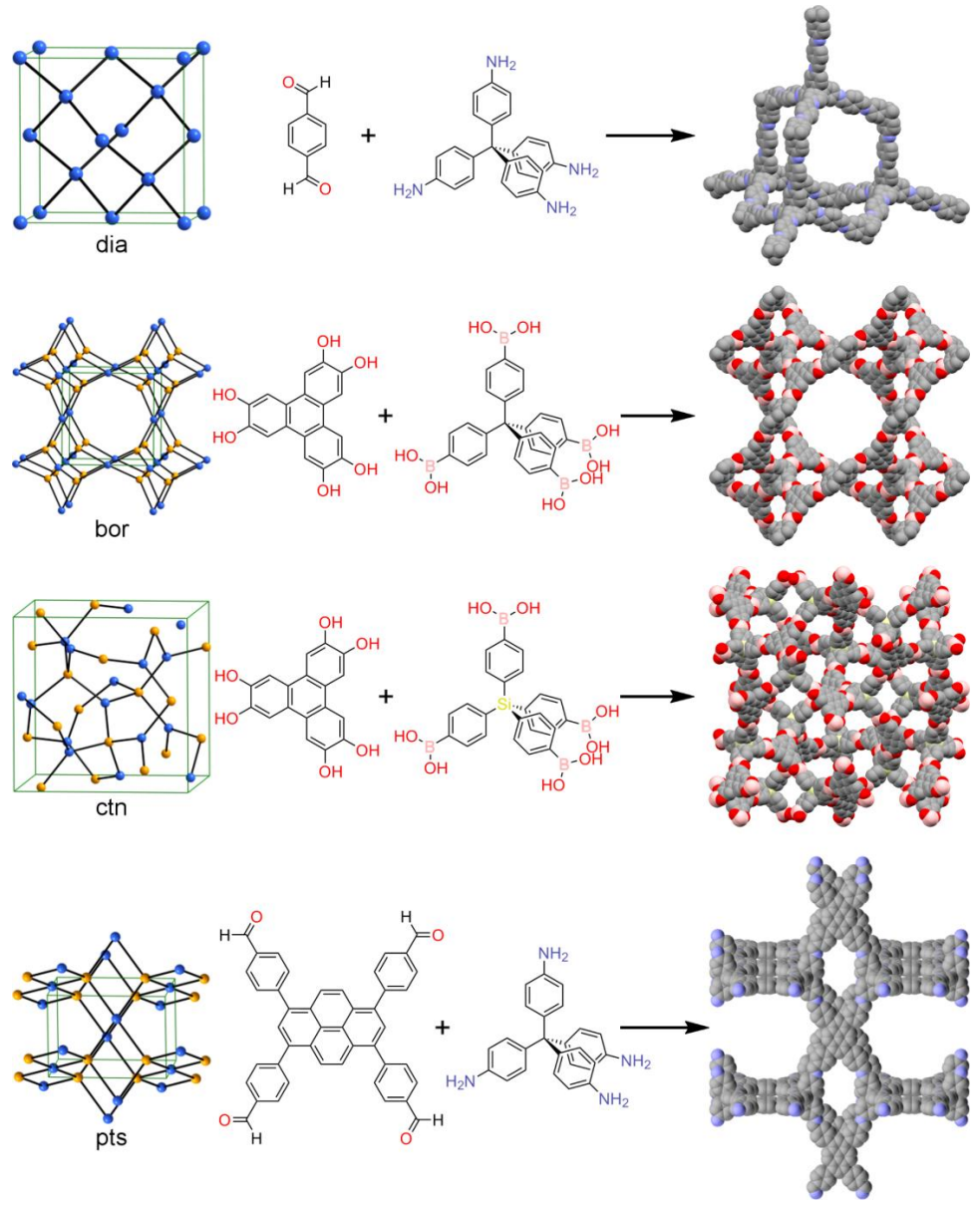

Figure 1.3. Representation of all the 3D topologies (left) found in reported COFs and examples of synthesised structures corresponding to each topology (space filling model, C: grey, B: pink, O: red, N: blue, Si: yellow, H omitted for clarity). Adapted from Reference 17.

1.2.2. Linkages

After deciding the shape of the building blocks, it is necessary to choose which reaction is going to be used to join them. This is probably one of the most important aspects in COFs since the correct formation of bonds is crucial to avoid defects and the nature of the bond is related to essential properties like stability. Such is the importance of the linkage, that from the nearly infinite possibilities offered by organic chemistry to create bonds, only reversible reactions yield crystalline networks.

The reason behind the importance of reversibility is that the intended ordered and periodic framework is not the only possible way in which the building blocks can assemble. Even if rigid molecules are used, they always tolerate a certain degree of strain, which allows small variations in bond angles giving rise to the formation of rings with shapes and sizes different from the expected ones, this type of defects that has been imaged by STM[19] (Figure 1.4a) is not exclusive of COFs and is also well documented in graphene[20]. Even more problematic is in laminar networks the formation of bonds out of plane, which leads to interlayer crosslinking and greatly disturbs the structure. In any case, regardless of the nature of the defects, the presence of too many of them results in a structure that is closer to an amorphous hypercrosslinked polymer than to an ordered COF. It is therefore vital to make sure that all the bonds created during the synthesis are in the proper conformation. This is achieved by conducting the reaction in conditions under which it is reversible. As illustrated in Figure 1.4b, this allows incorrectly formed bonds to be broken and formed again in an appropriate manner until a periodic and more thermodynamically stable structure is obtained, in a process akin to traditional crystallisation[21].

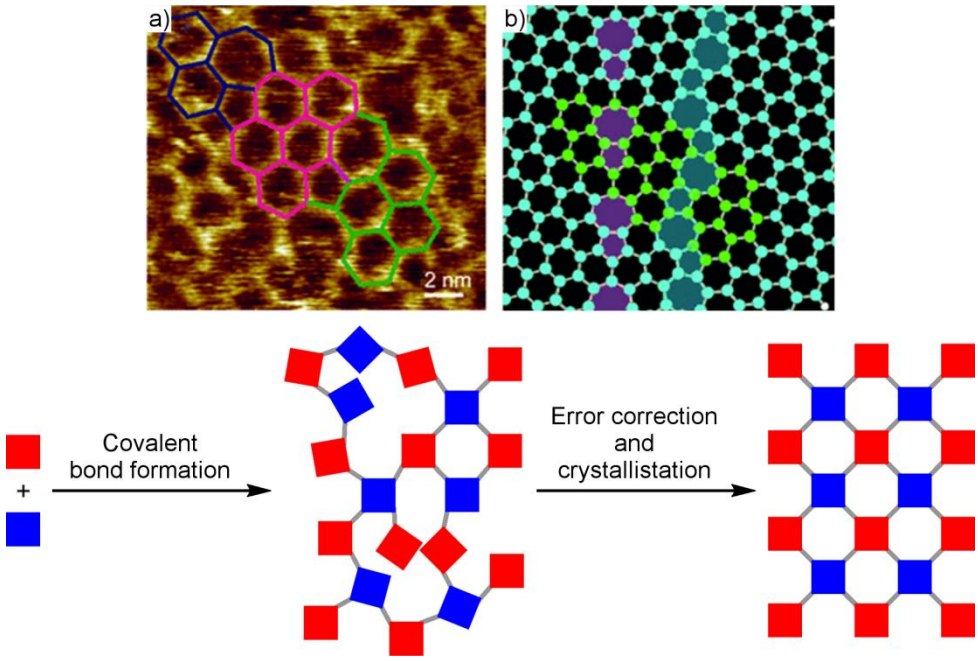

Figure 1.4. a) STM image showing a defective 2D COF network, the outine of the polygons formed by the COF is highlighted. b) Model of grain boundaries showing Stone-Wales defects highlighted in violet and blue. The region corresponding to the image in a) is highlighted in green. c) Schematic illustration of the formation of an ordered network through error correction enabled by reversible covalent bonds. Adapted from references 19 and 21.

Figure 1.5 provides a summary of the various reversible covalent linkages that have been reported to date and that will be discussed through the next paragraphs.

The self-condensation of boronic acids to form boroxine rings and the formation of boronic esters from boronic acids and catechols were the reactions first used in the synthesis of COFs[6]. Since then, numerous structures based on these types of bonds have been reported and COFs based on boronic esters have become one of the most common types. There are other networks featuring B-O single bonds and also B-N bonds,

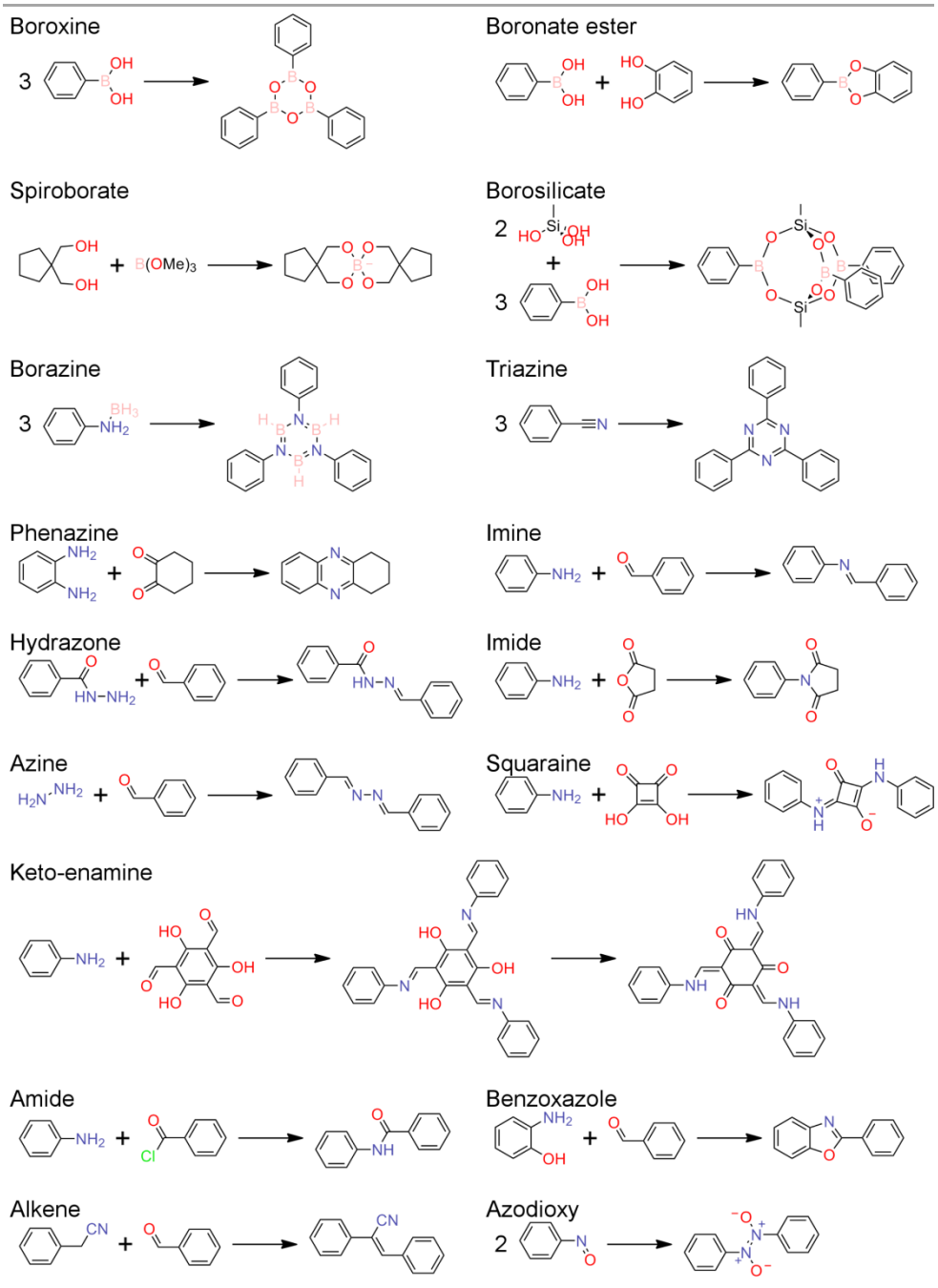

Figure 1.5. COF linkages and reactions used to generate them.

even though so far they have remained a synthetic curiosity, the possibility of preparing negatively charged spiroborate based COFs[22], borosilicate-linked networks[23] and borazine containing frameworks[24] has also been demonstrated. In general, these bonds provide the material with an acceptable thermal stability, however, the empty orbital of the boron atoms makes them prone to hydrolysis greatly impeding their use in applications involving exposure to ambient conditions[25].

Chronologically, the first alternative to boron containing COFs appeared in 2008 with the report on the use of the formation of triazines by cyclotrimerisation of nitriles to create an ordered network[26]. This structure is much more robust than that of boronic esters and does not suffer from stability problems. However, due to the harsh synthetic conditions involving an ionothermal process in molten zinc chloride, triazine-based COFs have enjoyed limited popularity, even after a new procedure using milder conditions was developed[27]. An almost identical problem affects phenazine-linked frameworks[28], despite the attractive properties displayed by structures without additional functionalisation, the difficulty in obtaining crystalline materials seems to be hampering their development[29].

In 2009 the first COF with imine bonds was prepared[30]. This reaction consisting in the condensation between an aldehyde and an amine has proved very useful for the synthesis of this type of materials and has probably become the most favoured strategy for the obtention of COFs[29,31]. The advantages of this reaction are the relatively high thermal and chemical stability of the final product while being very tolerant with different reaction conditions that range from room temperature reactions to solvothermal syntheses similar to those of boronic esters. A few related reactions that produce carbon-nitrogen bonds have been employed too, there are examples of hydrazone[32], imide[33], azine[34] and squaraine-linked[35] COFs. There is also an interesting variation of imine-bonding that is

achieved using 2,4,6-trihydroxy-1,3,5-benzenetricarbaldehyde as a building block, its structure greatly favours the displacement of the equilibrium of the tautomerism between the enol-imine and keto-enamine forms towards the latter[36], thus, the final structure of the COF will contain the less reactive enamine groups and its chemical stability will improve[37].

A further step in the quest for highly stable COFs with carbon-nitrogen bonds has been the synthesis of amide-linked networks. Frameworks featuring this type of bond were first prepared in 2016, although it is possible to consider it a case of post-synthetic modification as it was done by preparing and activating an imine-based COF and then oxidising it[38]. More recently, the direct synthesis of this type of framework from acyl chlorides and amines under hydrothermal conditions was reported[39]. Despite the different strategies, in both examples, the resulting materials showed outstanding chemical stability.

Recently, two novel strategies that combine reversible and irreversible steps have given fruitful results. One of them relies in the formation of an imine as a first reversible reaction followed by the nucleophilic attack of an adjacent phenol to form an benzoxazoline ring, finally, the benzoxazoline is oxidated to benzoxazole in the last irreversible step[40]. The other maybe more interesting approach due to the formation of carbon-carbon covalent bonds counts on a Knoevenagel condensation to join the building blocks[41]. In this case, the nucleophilic addition is a reversible reaction and once the adduct undergoes dehydration to form the alkene, the link is fixed. One of the main benefits of these irreversible reactions is that, as expected for networks containing such inert bonds, the stability of these COFs is exceptional[42].

Finally, a peculiar linkage that deserves to be discussed separately is the azodioxy moiety. This extremely weak covalent bond is formed by the dimerisation of nitroso groups. It is so labile and its formation so reversible

that it allowed to obtain for the first time single crystals of a COF, more specifically of a 3D network with diamond-like topology[43].

1.2.3. Synthetic procedures

Once the components of the framework are chosen, the only thing left is to synthesise it. Surprisingly, despite the variety of chemical reactions that can be used to build the network, the experimental approach to conduct most of them is fairly similar. In short, the great majority of the reported procedures are carried out in sealed Pyrex tubes and consist in mixing the building blocks in a suitable mixture of solvents, which curiously is not capable of dissolving the monomers in many cases[44], and adding any necessary catalyst before evacuating and sealing the tube. Then, the mixture is heated under solvothermal conditions for several days, after which the solid is recovered, washed and dried.

In terms of number of different synthetic strategies, the chemistry of imine-based COFs has been the most prolific. The reaction is most commonly carried out in a 1,4-dioxane:mesitylene mixture using aqueous acetic acid as catalyst at temperatures close to 120 ºC over several days in a sealed tube. Some minor variations include the use of different solvents, being quite frequent the mixtures of *o*-dichlorobenzene with *n*-butanol; performing the reaction in an open vessel, that is, under reflux without solvothermal conditions; or the more interesting room-temperature synthesis, though it has the drawback of affording less crystalline materials[31].

Moreover, deeper changes in the condensation between aldehydes and amines can be made with positive outcomes. For example, switching from a Brønsted acid catalyst to Lewis acid metals has appealing consequences. Scandium(III) catalysed reactions readily proceed at room

temperature in very few minutes and with low catalyst loadings below 2 % mol to yield highly crystalline and porous COFs. Unfortunately, this is not the universal remedy for COF synthesis since it struggles to crystallise highly functionalised building blocks[45].

A major difference is also produced by another, apparently innocent, change of catalyst. *p*-toluenesulfonic acid does not simply behave as an acid, upon mixing with the amines used as building blocks, they form salts with a lamellar structure in which amines are regularly spaced. Importantly, the distance between amines matches the dimensions of some commonly used aldehydes, so once the aldehyde is added to the mixture, it simply has to displace the *p*-toluenesulfonic molecules to form the network. The result is also a fast process for obtaining COFs with excellent crystallinity and outstanding porosity[46].

Other strategies to improve the quality of the networks consist in modifying the reactivity of the starting materials. Two options to modulate the reactivity by using protected amines that are slowly deprotected in situ have been reported nearly simultaneously. The first one introduces *tert*-butyloxycarbonyl (Boc) protecting groups in only one of the two amine moieties of a linear diamine (Figure 1.6a), the reaction thus evolves through the formation of small soluble oligomers capped by Boc groups that grow gradually as the deprotection of the amines proceeds. This approach has yielded exceptional results such as the synthesis of networks not feasible with other procedures and the preparation of monodisperse COF nanocrystals[47]. The other strategy involves the use of benzophenone-imine protected amines (Figure 1.6b) and has been demonstrated to be effective in the synthesis of networks from amines that oxidise easily, reaching surface area values close to the theoretically predicted ones[48]. The success of these two approaches is due to the fact that the slow removal of the protecting groups provides a low and steady

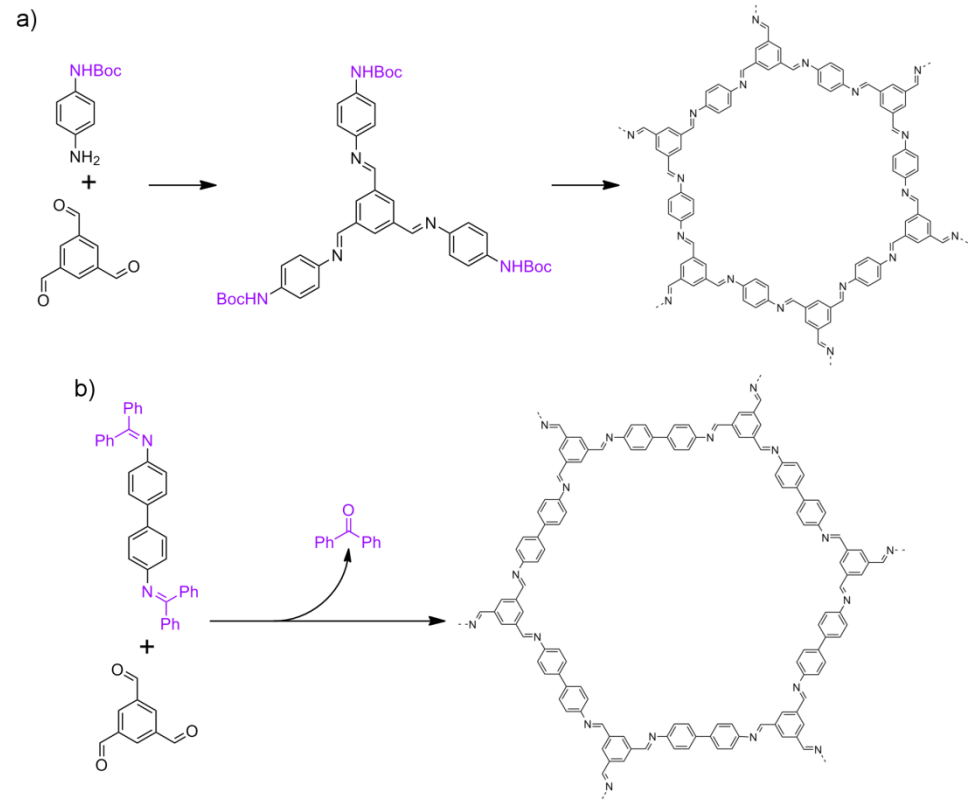

Figure 1.6. Scheme of the synthesis of imine-linked COFs starting from a) Boc-protected amines and b) benzophenone-imine protected amines. Protecting groups are highlighted in violet.

concentration of reactive amine that results in gradual COF growth and enough time for error correction before insoluble aggregates are formed.

Very recently, ionic liquids have been used as solvents for the synthesis of imine-linked COFs[49]. As expected because of the unusual properties of ionic liquids, this change of solvent greatly impacts the reaction, mostly in a positive way, although there are some drawbacks. First of all, the ionic liquid acts both as solvent and catalyst, allows the reaction to be performed at extremely high concentrations and yields highly crystalline materials within minutes. Moreover, it can be reused several times without

diminishing its effectiveness. The main weakness arises from the difficulty in completely removing the ionic liquid from the pores of the COF, and even though its presence is exploited in the work by Guan and co-workers to enhance selectivity towards CO_2 separation, it can be detrimental in other applications.

A completely different procedure from the ones described above was reported in 2013[18]. It is a solvent-free method in which the building blocks react in the solid state thanks to being finely divided and the mechanical energy provided by grinding. The properties of the obtained material are worse in general than those obtained by solvothermal synthesis, but the grinding process has applicable side-effects, for instance it causes the exfoliation the produced COF.

1.2.4. Functionalisation

Despite the great structural variability provided merely by the combinations of the different types of linkages and network topologies and sizes, it is desirable to be able to impart additional functionalities to the framework because it grants the possibility of tailoring the design of COFs to the meet the requirements of the targeted application. Additionally, using the backbone of the framework as the active moiety can be risky sometimes since it usually accelerates degradation, bringing as a consequence in this case the complete destruction of the material, which generally is more damaging than a simple loss of activity.

The approaches to functionalize COFs can be divided in two main groups depending on whether the additional groups are introduced in the building blocks prior to the formation of the COF or post-synthetic modifications are carried out. Both alternatives have benefits and disadvantages and are somewhat complementary. Modifications of the building blocks before

COF synthesis are usually easier to perform as the substrate of the reaction is a small molecule which can be purified by various methods, however, it is not always possible to resort to them because the additional functional group must not interfere with the COF forming reaction and has to be stable under the conditions used for the growth of the framework. Post-synthetic functionalisation is not hindered by this restrictions, but in exchange is more likely to generate defects in the network since it is possible for the reaction to not be complete and leave randomly distributed unreacted sites, while using a building block already containing the groups ensures that all repetition units will have the same composition[50].

An example of functionalisation carried to the framework from the monomers can be found in the series of COFs prepared by Lavigne *et al.*[51] (Figure 1.7). All the COFs in the work present the same scaffold but bear different alkyl side chains that fill the pores and therefore modulate

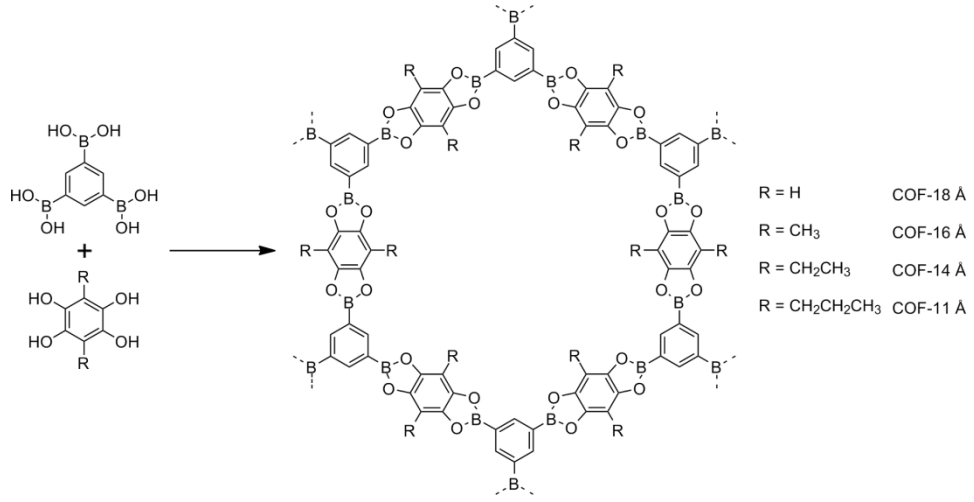

Figure 1.7. Modulation of the porosity of boronic ester-based COFs by modification of the catechol building block. The pore size obtained with each substituent is listed at the rightmost column. Adapted from reference 51.

the porosity. Since the aliphatic substituents are compatible with the boronic ester formation reaction they can be present in the catechol building block during COF growth thus guaranteeing that all cavities have the same size.

Post-synthetic modifications do not necessarily require the formation of covalent bonds, since the framework is already formed, it is possible to accommodate functional molecules in the pores. This is a very simple strategy that gives reasonable results in many cases. For example, COFs have been impregnated with phosphoric acid to provide them with ionic conductivity[52]. Even though at first glance it may seem as just filling the pores, the presence of groups in the scaffold that direct the organisation of the guest molecules can be crucial. As illustrated in Figure 1.8a, in the previous example two frameworks were impregnated with phosphoric acid, while the azo group in Tp-Azo COF interacts with it, the alkene in Tp-Stb COF does not contribute to orient the acid molecules. As a result, phosphoric acid loaded Tp-Stb COF presents a negligible ionic conductivity compared to the functionalized Tp-Azo COF.

Metal ions can also be used to add functionality to COFs. If porphyrins or phthalocyanines are used as part of square networks, then it is possible to use the metalated species as starting materials and obtain metal-functionalized COFs[53,54]. In COFs that do not contain any of these motifs the only option is to introduce the metal after the framework has been formed. Nitrogen-containing structures are very attractive for this purpose due to the coordinating ability of amines and imines, as exposed by the functionalisation of the imine-based COF LZU-1 (Figure 1.8b) with palladium(II) to give it catalytic properties[55].

Finally, there are situations in which it is necessary to perform the functionalisation in two steps because of the incompatibility of the desired

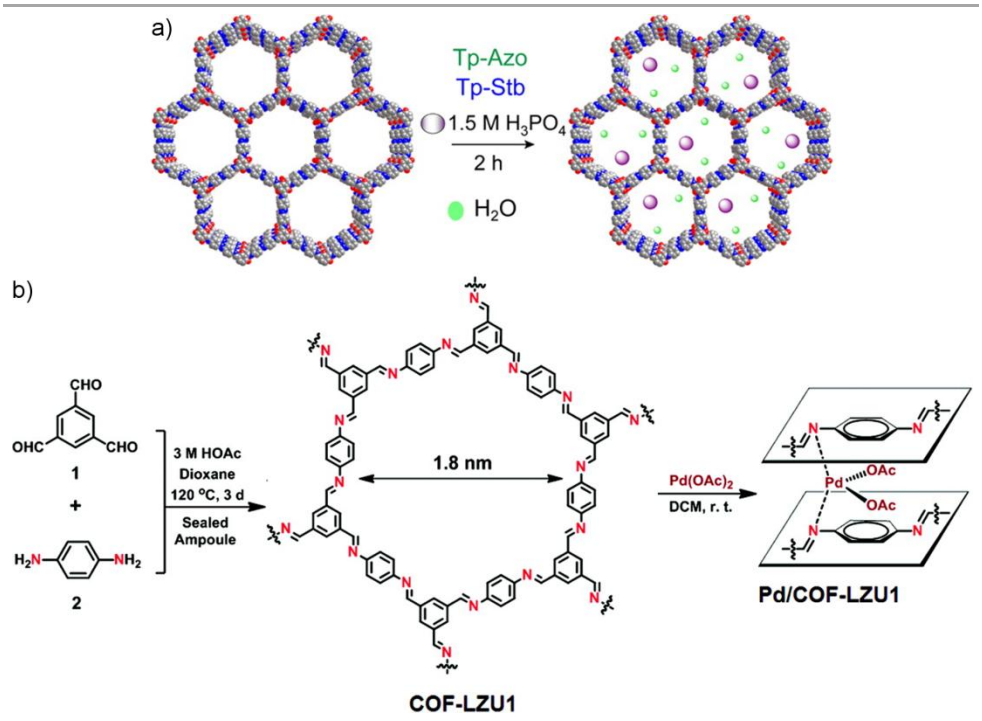

Figure 1.8. a) Scheme of post-synthetic modification by pore filling of an enamine-linked COF with phosphoric acid. b) Post-synthetic modification of an imine-based COF with palladium(II) by metal coordination. Adapted from references 52 and 55.

group with COF forming conditions and the complexity of carrying out the whole synthetic pathway over the framework. The usual solution in these circumstances is to functionalise the building blocks with groups that do not interfere with COF formation and also allow to access to the target moiety in the lowest possible number of synthetic steps. A representative case reported in the literature is summarised in Figure 1.9[56]. Since some of the terminal groups of the side chain are likely to affect imine formation, namely carboxylic acids and amines, it is decided to introduce innocent alkyne moieties in one of the monomers and then proceed with the formation of the COF. The resulting material can be functionalised via a click reaction between the alkyne and an azide not only with acids and

amines, but also with a long list of functional groups or even larger motifs[57], which makes this alkyne-functionalised framework an extremely versatile platform for post-synthetic modifications.

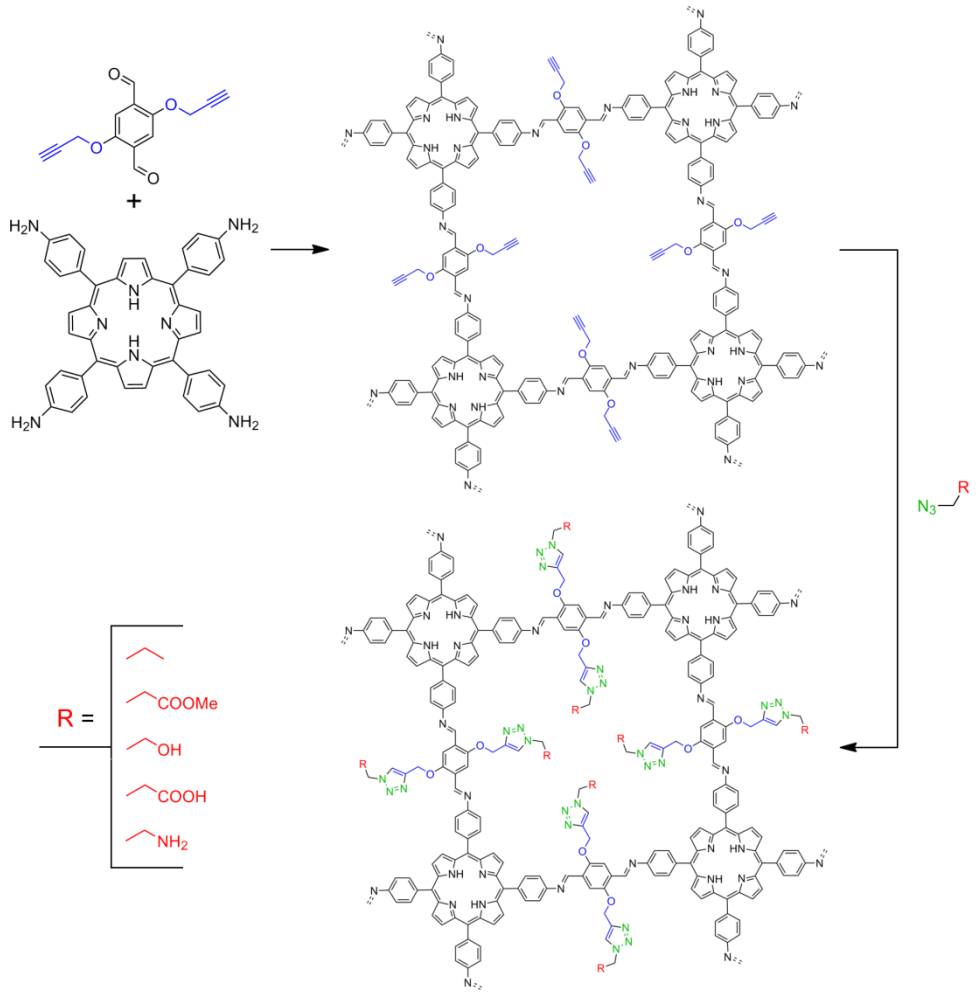

Figure 1.9. Functionalisation of an imine-linked COF through the installation of functional groups before and after polymerisation. Adapted from reference 56.

1.3. Properties of COFs

Besides the beauty some may find in the structures and the allure of being able to whimsically design a material and control its composition with atomic precision, the most important aspect of COFs, as of most compounds being researched, are their properties. As stated a few pages ago, COFs and their metal-organic counterparts, MOFs, are in direct competition with well-established and highly optimised materials as zeolites and activated carbons when it comes to straightforward application of their most basic properties such as porosity or catalytic activity. Their strength relies in their versatility and the ability of predesigning their structure, which allows an outstanding control for accurately position and distribute different functional moieties, tuning the distances and interactions among them and providing an environment that will contribute their performance. This opens the door to COFs and MOFs that combine properties in ways that are not possible for other materials that cannot be tailor-made, and may be instrumental in the solution some of today challenges.

COFs and MOFs share many characteristics and given that MOFs began developing several years before the first work on COFs appeared, many studies of COF properties and advances in processing had already been done in MOFs, which additionally present the advantage of being generally easier to crystallise. However, there are a few differences that play in favour of COFs. One of them derives from the fact that COFs can be made exclusively out of light elements such as boron, carbon, nitrogen and hydrogen while MOFs contain heavier metal atoms, because of this, COFs have the potential of achieving much lower densities[58]. The other, more determining, difference has the nature of the bonds in its origin; the more reversible nature of coordination bonds relative to covalent bonds makes synthesis of highly crystalline MOFs much easier, but in exchange,

the higher strength and stability of covalent bonds provides COFs with a much higher thermal and chemical stability. Now, some of the most remarkable properties of COFs will be discussed.

1.3.1. Crystallinity

Crystallinity is the signature of COFs, the property that sets them apart from any other organic polymer, because from a strictly chemical point of view COFs are just polymers, not formed by the classical polymer chains since the building blocks present more than two reactive points, but they are nevertheless formed by the repeated bonding of small molecules. Without order, the periodic and symmetric structures that are drawn on paper do not exist in the real material and it consists of randomly bonded monomers, much more like a linear polymer with a high degree of cross-linking. Moreover, many of the expected properties of a COF stem from the proper placement of its building units.

As explained above, bond reversibility is one of the key factors affecting crystallinity due to the possibility of removing incorrectly bonded molecules. In 3D COFs, in which the growth of the network proceeds exclusively by formation of covalent bonds, if nucleation is controlled and reversibility is high enough, it should be enough to obtain highly ordered materials. Actually, the use of the extremely weak and reversible azodioxy linkage allowed to obtain single crystals of the three COFs with diamond-like structure shown in Figure 1.10[43].

The case of 2D COFs presents additional challenges. Since covalent bonds only propagate in two dimensions, the growth in the other direction depends on non-covalent interactions, most commonly π-π stacking. Therefore, it is not only necessary to control the conditions to allow reversibility of covalent bond formation, but also to ensure that the

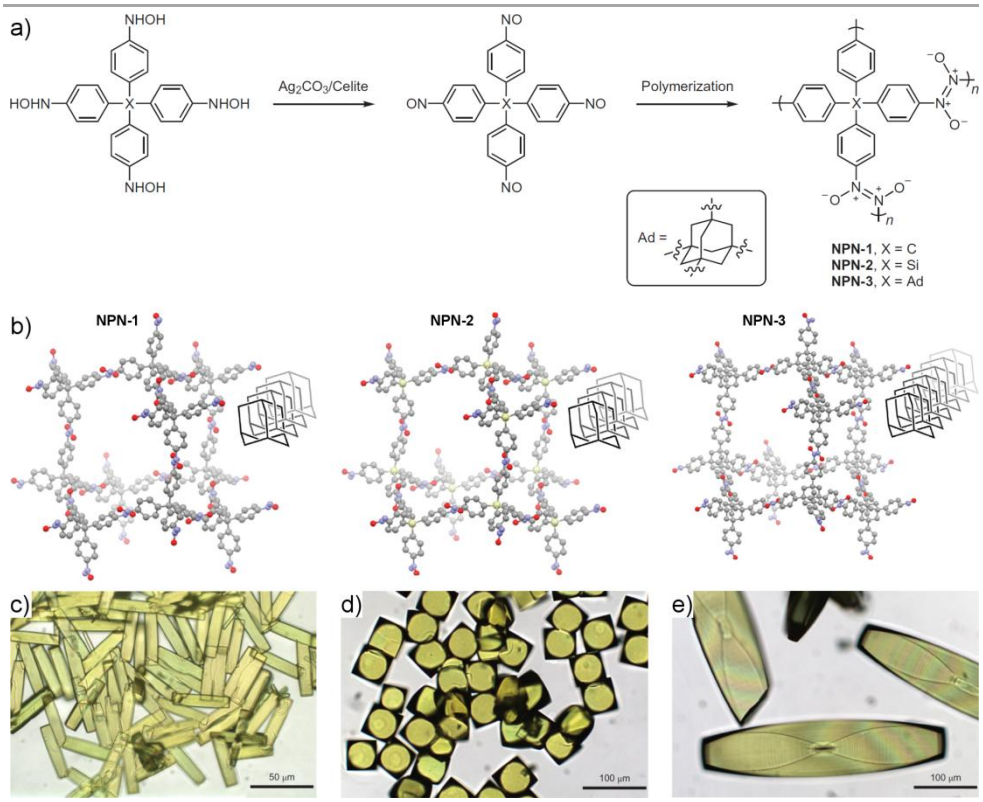

Figure 1.10. a) Construction ofazodioxy linked COFs by oxidation of hydroxylamines and polymerisation of the so-formed tetranitroso monomers. b) Ball-and-stick representations of the structures of crystals of COFs NPN-1, NPN-2 and NPN-3 and their corresponding degree of interpenetration. c-e) Photographs of single crystals of c) NPN-1, d) NPN-2 and e) NPN-3. (ball-and-stick model, C: grey, O: red, N: blue, Si: yellow, H and guests omitted for clarity). Adapted from reference 43.

stacking of layers proceeds in an ordered manner. This proves to be a difficult challenge, even though π-π stacking interactions are usually weak, when large sheets are formed, the huge number of aromatic rings interacting implies that a lot of energy is needed to separate the layers. Additionally, the potential well is fairly shallow (Figure 1.11a), so there is not a strong driving force to fix the layers in a specific position, resulting in

an imperfect stacking sequence that seems to be close to an eclipsed AA stacking situation[59,60].

Therefore, several strategies have been devised in order to tune layer stacking. Some of them consisted in using fluorinated building blocks to increase π-π interactions either by facing complementary electron-rich (non-fluorinated) with electron-poor (fluorinated) aromatic rings[61] or by taking advantage of the higher tendency of electron-deficient rings to arrange cofacially[62]. It has also been postulated that, in imine-linked COFs, the polarisation of the imine bond destabilises layer arrangement because of electrostatic repulsion, consequently, the introduction of electron-donating groups such as the methoxy substituent in Figure 1.11c in the positively charged phenyl rings could reduce this repulsion and improve the crystallinity[57]. Finally, the role played by the planarity of the monomers in modulating the stacking has also been studied. Triphenylarene cores are very commonly used as triangular building blocks, however, the steric repulsion between hydrogen atoms induces the rotation of the external phenyl rings, the substitution of the C-H moieties of the central ring by nitrogen atoms (Figure 1.11d) planarizes the building block facilitating the stacking, this translates in a higher porosity (Figure 1.11e), although it can be seen that the asymmetrisation generated by partial substitution of carbon atoms in the central ring has some negative effects[63].

Despite all the strategies described above to improve the order of the frameworks, crystallinity of COFs is still not impressive and they feature small domain sizes, typically under 100 nm. This nagging problem is still hindering their characterisation, since the lack of single crystals and the broad peaks of the powder diffraction patterns do not allow structure resolution, in fact the only example of a precisely determined COF

structure besides the already mentioned azodioxy-linked framework required the use electron diffraction to be obtained.[64]

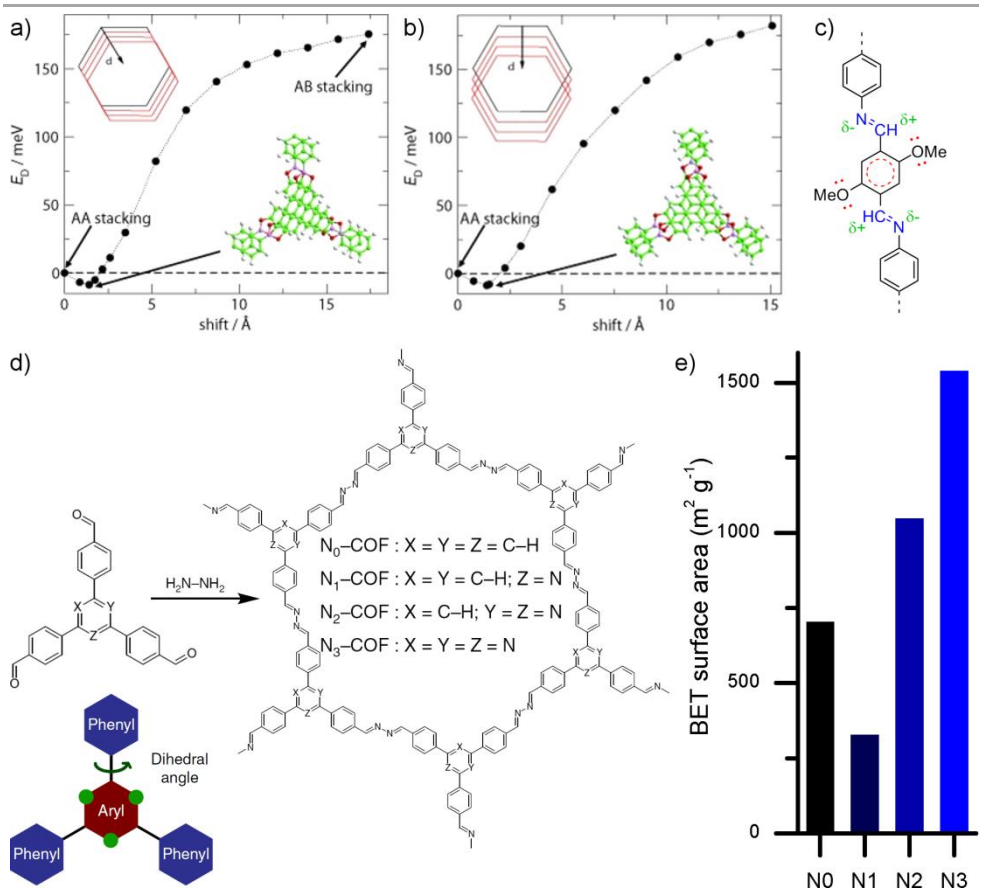

Figure 1.11. a-b) Change of the total energy (per created bond) when shifting boronate-based COF-5 layers in a) zigzag and b) armchair directions. The vector d shows the shift direction and the equilibrium structures are shown as well. Adapted from ref [59]. c) The resonance effect of oxygen lone pair softens the interlayer charge repulsion in imine linked COFs. d) Synthesis of planarised triphenylarene-containing COFs by substitution of C-H by N. This replacement at the green dots changes the angle between the central aryl and peripheral phenyl rings. d) BET surface areas of the COFs in c). Adapted from references 57, 59 and 63.

1.3.2. Stability

Perhaps the most important property of any material, including COFs, is its stability. A material with excellent properties for a certain application but lacking the sturdiness to withstand the operating conditions becomes useless in that application no matter how good its performance could be. COFs show good thermal stabilities up to 500 ºC and usually not below 300 ºC[33], as determined by thermogravimetric analysis (TGA), but they are not so proficient in terms of chemical stability, which is usually studied by immersing the solids in different solvents under a variety of conditions, quantifying the fraction of material that is recovered and checking its crystallinity and porosity afterwards.

Most aspects of the chemical stability of COFs have already been discussed in the section dedicated to types of linkages, so only a brief summary will be done here. The need for reversibility in COF linkages is the bane of their chemical stability because even though they consist of strong covalent bonds, boronate esters, imines, azines or hydrazones can all be hydrolysed, although it is true that nitrogen-based frameworks are rather stable even in acidic and basic conditions[57]. For this reason, reactions that are only reversible under highly energetic conditions, such as triazine formation, or those that involve a last step of irreversible nature, that is Knoevenagel condensation or benzoxale formation, are preferable for the synthesis of highly stable COFs. However, it is not always desirable to use these linkages, in those cases, modifications in the structure of the monomers can make the bonds less labile. One case is the condensation of 2,4,6-trihydroxy-1,3,5-benzenetricarbaldehyde with amines, it seems a normal imine forming reaction, but the structure of the aldehyde makes possible a tautomerism in which the major form is the highly stable keto-enamine. There is another way to stabilise imine bonds, it consists in the use of intralayer hydrogen bonding (Figure 1.12). By

introducing a hydroxyl group in the *ortho* position to the carbonyls in the aldehyde building blocks, upon formation of the imine bond, a six-membered ring is created in which the proton of the hydroxyl interacts via a hydrogen bond with the imine nitrogen. This blocks the conformation of all the bonds in the linkage in a coplanar conformation and increases the stability of the framework[65].

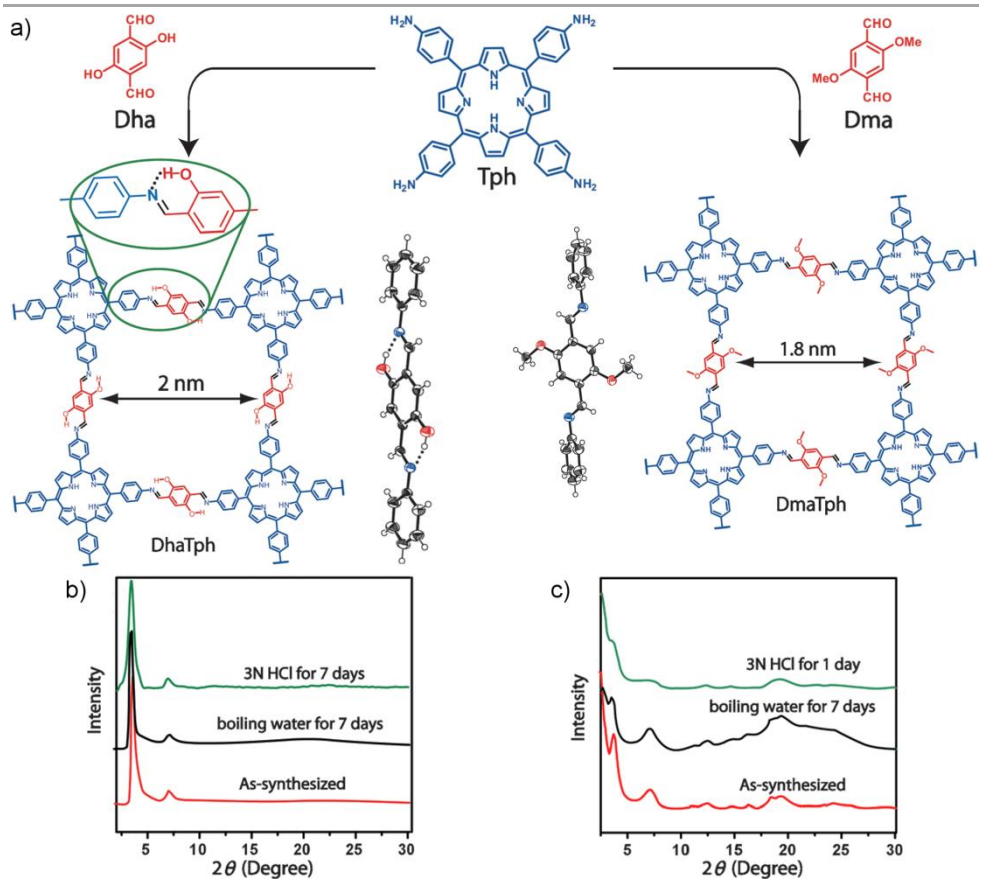

Figure 1.12. a) Synthesis of COFs with (left) and without (right) intramolecular hydrogen bonds. The ORTEP diagrams show the planar and non-planar conformation of hydrogen bonded (left) and normal (right) imines, respectively. b-c) PXRD patterns showing the stability of COFs b) with and c) without hydrogen bonds in different media. In c) there is a clear loss of crystallinity. Adapted from reference 65.

1.3.3. Porosity

Owing to the rigidity of the framework, almost all COFs are porous, with pore sizes ranging from 0.9 nm[66] to 4.7 nm[60]. Extremely high surface areas up to 4210 m^2 g^{-1} can be achieved[58] with a proper design and activation procedure. In fact, activation of the pores is a step that should not be overlooked, since the final performance of the material is highly dependent on it, the reported strategies range from solvent exchange and evacuation at high temperature under reduced pressure to drying with supercritical carbon dioxide. A final remark with regard to applications is that even though the porosity of COFs is commonly probed by nitrogen adsorption at 77 K, the cavities can be tuned both in size and composition to favour the adsorption of other more interesting gases.

For example, hydrogen uptake at room temperature can be increased by using COFs with extremely small pores[67] or by the incorporation of palladium nanoparticles in the COF[68], which is found to increase the adsorption capacity at room temperature.

Another gas which capture is interesting is carbon dioxide. In this sense, a thorough study of the performance of COFs post-functionalised with alkyl chains, amines, alcohols, esters and carboxylic acids through a click reaction has been done[56]. As shown in Figure 1.13, a higher degree of functionalisation with alkyne and alkane chain reduces the CO_2 uptake ability of the material due to the weak interaction of these groups with the gas and the reduction in surface area and pore volume derived from the space occupied by these chains. However, when other groups are introduced, the capacity of the material increases as a consequence of dipole interactions or even the formation of stronger acid-base pairs with amines, which was corroborated by the trend in the values of the isosteric heat of adsorption. Therefore, to maximise gas adsorption capacities, it is

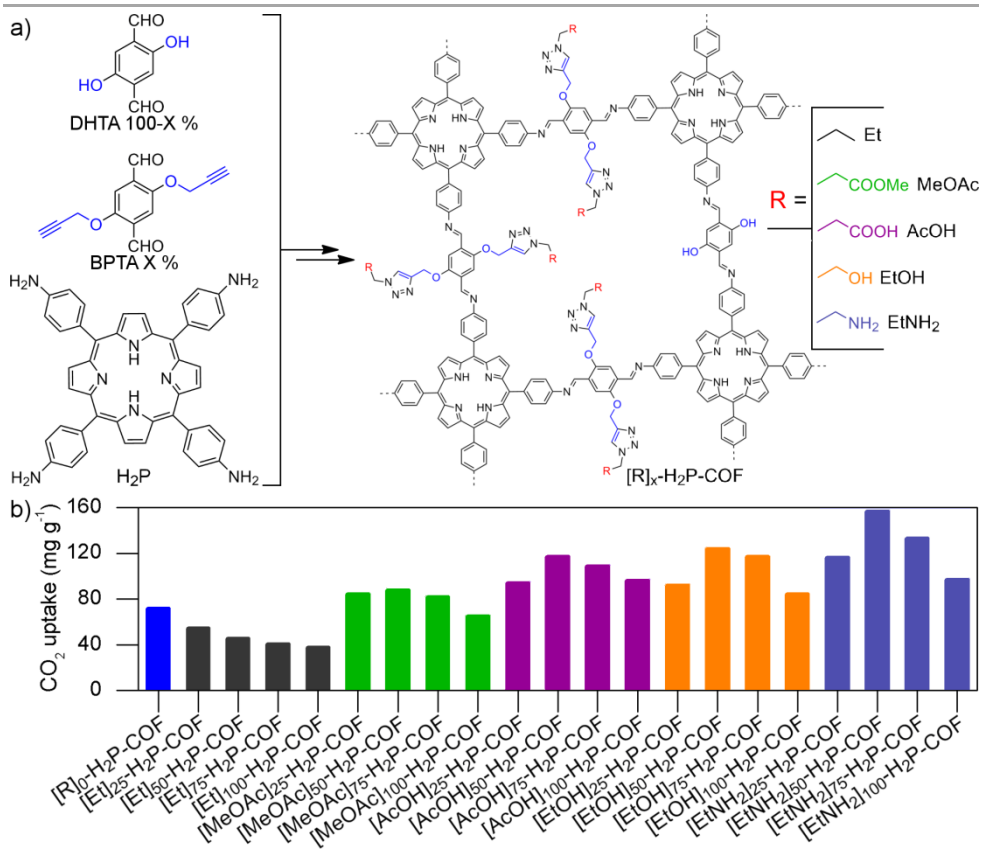

Figure 1.13 a) Post-functionalised COFs studied for CO_2 uptake. The X in the formula indicates the percentage of hydroxyl groups that are substituted by the corresponding functional group. b) CO_2 uptakes measured at 273 K of the COFs in a). Adapted from reference 56.

necessary to find the correct balance between pore-wall functionalisation and available volume in the cavities.

The use of the porosity of COFs is not restricted to gas phase adsorption, dissolved molecules and ions can also be selectively captured, which can be useful in water purification. A few COFs showing good affinity for mercury(II) ions have been prepared, usually bearing thiol groups in the channel walls, as the one shown in Figure 1.14. This material also showed

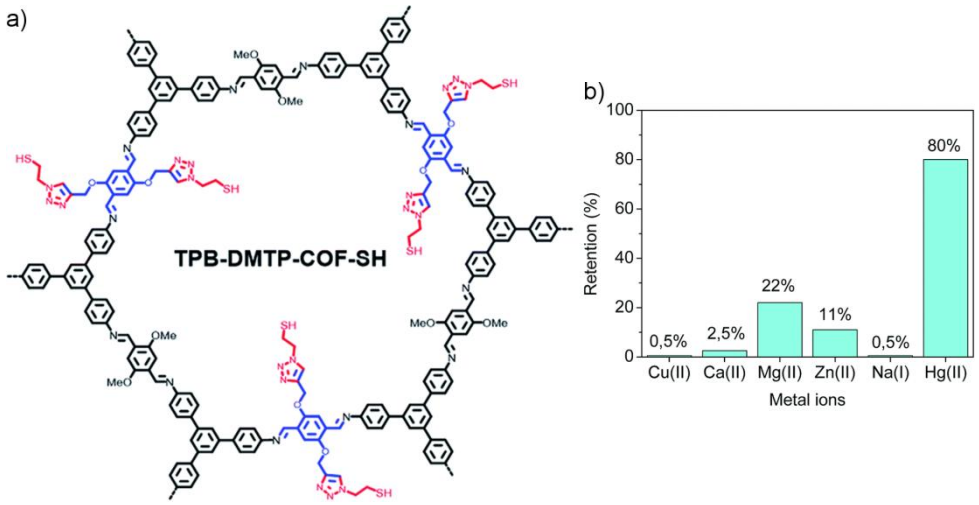

Figure 1.14. a) Structure of thiol-functionalised PB-DMTP-COF-SH used for mercury removal. b) Selectivity of TPB-DMTP-COF-SH in the presence of several metal ions in aqueous solution. Adapted from reference 69.

good selectivity towards mercury, which is suggested would allow its use even in seawater, and it was demonstrated that it can be reused several times[69].

1.3.4. Electrical Conductivity

The structure of COFs endows them with the ability to display both ionic and electronic conductivity. The presence of large delocalised π systems makes them attractive for electronic conductivity, whereas the possibility of including charged species in the pores makes them potential ionic conductive materials.

For example, in the field of ionic conductivity, it has been reported that 2D imine-based COFs with hexagonal channels of more than 3 nm can be loaded with triazole and imidazole molecules to act as proton carriers[70]. Upon impregnation with those molecules, the porosity of the framework

became negligible as the pores were completely full of proton carriers. The impedance measurements revealed that while the non-functionalised COF is an insulator, triazole and imidazole containing COFs display good conductivity values up to 4.37 x 10^{-3} S cm^{-1}.

Regarding electronic conductivity, COFs with fully conjugated structures are more desirable since they allow a better charge delocalisation. Moreover, it has been shown that fully carbon-bonded COFs show a better behaviour than those with heteroatom containing linkages such as imine-based COFs[71]. In that work it is also demonstrated that, as in the case of linear polymers, it is necessary to dope the framework in order to

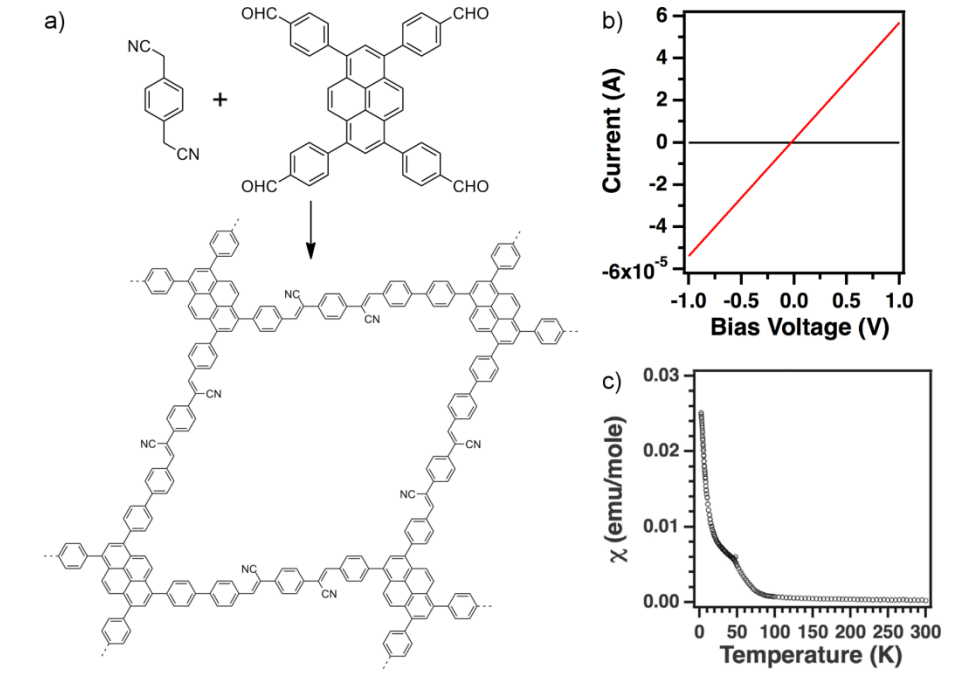

Figure 1.15. a) Synthesis of fully conjugated sp^2 carbon COF. b) Current-voltage curve of the pristine sp^2 COF (black) and the sp^2 COF after 26 h iodine doping (red). c) Temperature dependence of the spin susceptibility, χ, determined by a SQUID magnetometer for iodine doped sp^2 COF (emu: electromagnetic units). Adapted from reference 71.

make it conductive, showing a conductivity of 7.1 x 10^{-2} S m^{-1}. However, probably the most interesting fact of the structure is the spin-spin coherence it exhibits at low temperatures upon doping, therefore showing ferromagnetic properties (Figure 1.15).

Instead of relying on in-plane conjugation for electron delocalisation, it is also possible to exploit the formation of columnar arrays. For example, it well-known that tetrathiafulvalene (TTF) reacts with electron acceptors to form charge-transfer crystals with high conductivity[72]. Therefore, the adequate design of a COF allows to stack TTF moieties that can be partially oxidised by iodine or tetracyanoquinodimethane (TCNQ) (Figure 1.16). The doped material shows conductivities as high as 0.28 S m^{-1}, although after some time they revert to the original values of the pristine COF due to the loss of iodine[73].

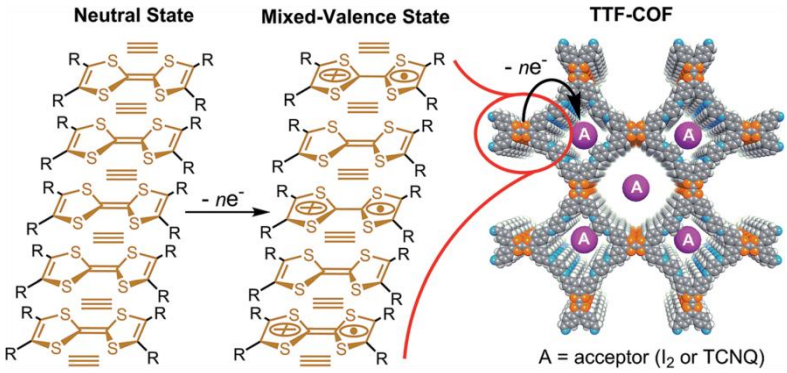

Figure 1.16. Illustration of the mixed-valence state in TTF-COF induced by acceptors such as I_2 or TCNQ. The "≡" indicates inter-TTF-layer interactions. (Space filling model, C: grey, H: white, N: blue, S: orange). Adapted from reference 73.

1.3.5. Catalytic activity

The high degree of functionalisation that can be performed on COFs and its porous nature render them very useful as catalytic scaffolds, since all

the volume of the material can be accessed by the reactants and they can be tailored to mediate in multiple chemical transformations.

For instance, imine-linked COFs are inherently basic due to the imine group, but if hydroxyl groups are introduced to enhance their stability, they can also act as acids. This was capitalised on by synthesising the COF shown in Figure 1.17, which has additional basic groups in the non-metalated porphyrin rings. It was used to catalyse a cascade reaction consisting in the acid-catalysed deprotection of an acetal and the subsequent addition of malonitrile to the resulting aldehyde in a base-mediated Knoevenagel reaction[74].

An interesting organocatalytic COF can be prepared by post-synthetically attaching chiral proline moieties by a click reaction (Figure 1.18a). It is employed in asymmetric Michael additions with good yields of 95 % and enantiomeric excess above 90 % while being also easily recyclable. It is noteworthy that the loading of proline turns out to be critical, since COFs

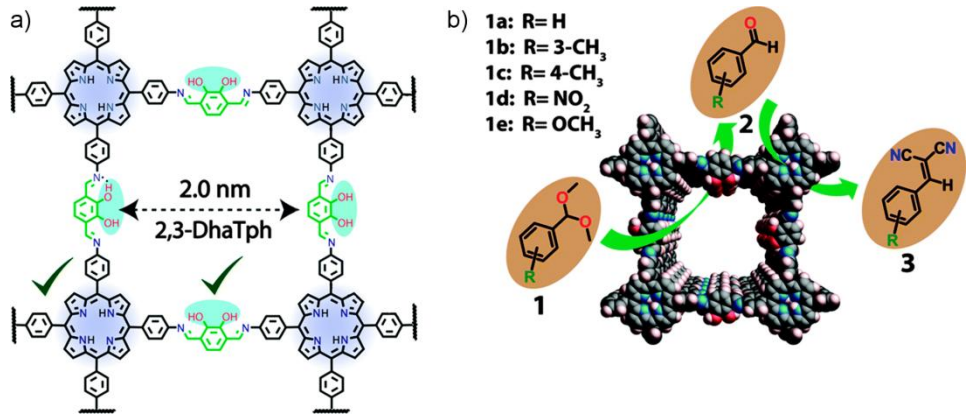

Figure 1.17. a) Structure of the bifunctional catalytic COF 2,3-DhaTph. The catalytically active porphyrin and catecholic -OH groups are showin in coral and cyan colours, respectively. b) Scheme of the catalytic activity of COF 2,3-DhaTPh in an acid-base catalysed cascade reaction with various reactants. Adapted from reference 74.

with high densities of proline moieties in their pores show lower catalytic effectiveness than those with a modest amount of organocatalytic sites. It is hypothesised that the presence of too many groups in the framework crams the channels and impedes the proper interaction of the substrate with the proline due to lack of space as illustrated in Figure 1.18b[57].

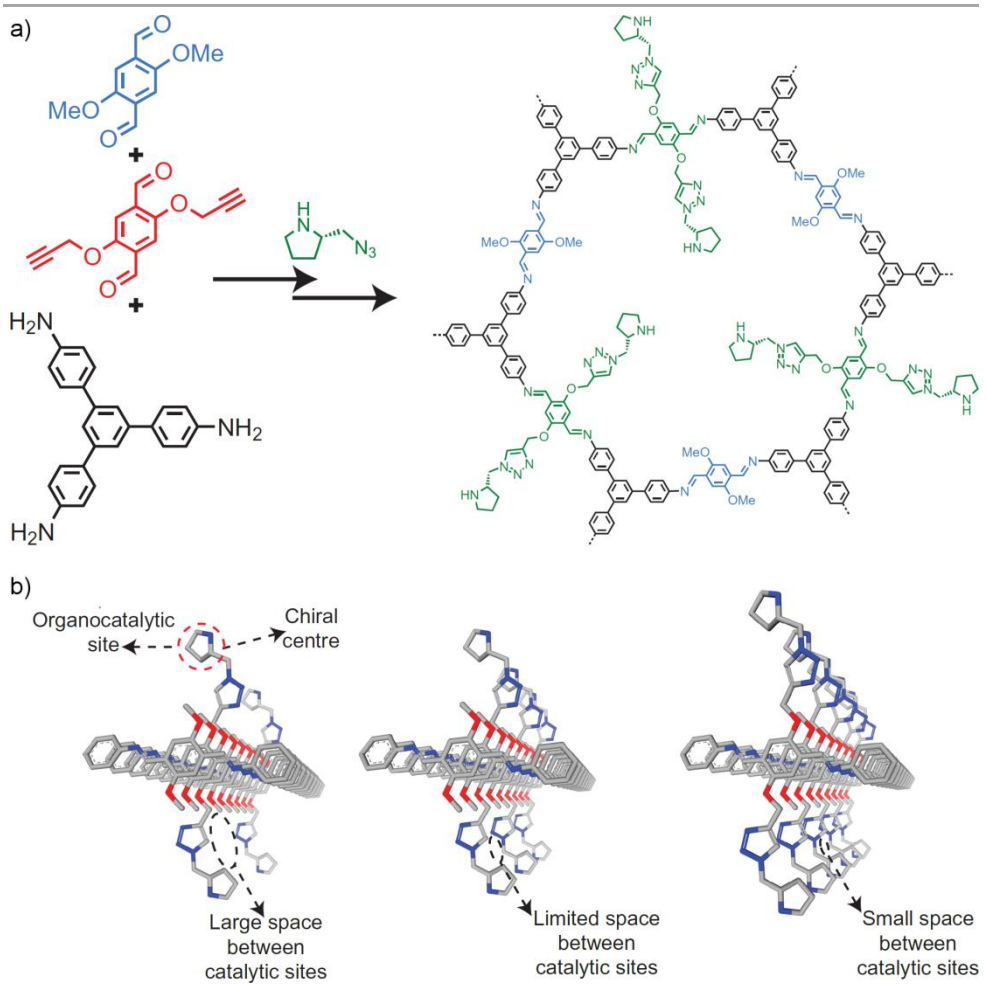

Figure 1.18. a) Synthesis of a COF with chiral proline moieties. b) Illustration of the effect of an increasing proline loading (left to right) on the available space in the pores. (C: grey, N: blue, O: red, H omitted for clarity). Adapted from reference 57.

Even though COFs are only made of light elements, it is also possible to carry out metallic catalysis. For example, palladium(II) ions can be coordinated to imine nitrogen atoms, this simple modification makes the material suitable for carbon-carbon coupling reactions[55]. Other alternative to take advantage of the outstanding catalytic capabilities of some metallic complexes is to introduce metalated porphyrins in the backbone of the COF. Some very interesting materials are the cobalt containing variation of COF-366 and it larger analogue COF-367 (Figure 1.19). They have been tested in the electrochemical reduction of carbon dioxide to carbon monoxide in water with promising results[53]. The cobalt porphyrins in the framework perform better than the molecular analogues, reaching turnover numbers up to 290 000 and turnover frequencies of 9 400 h^{-1} and showing great reusability, however, they still face some problems such as charge transfer in the framework, diffusion of CO_2 to the reactive centers and the higher overpotential needed.

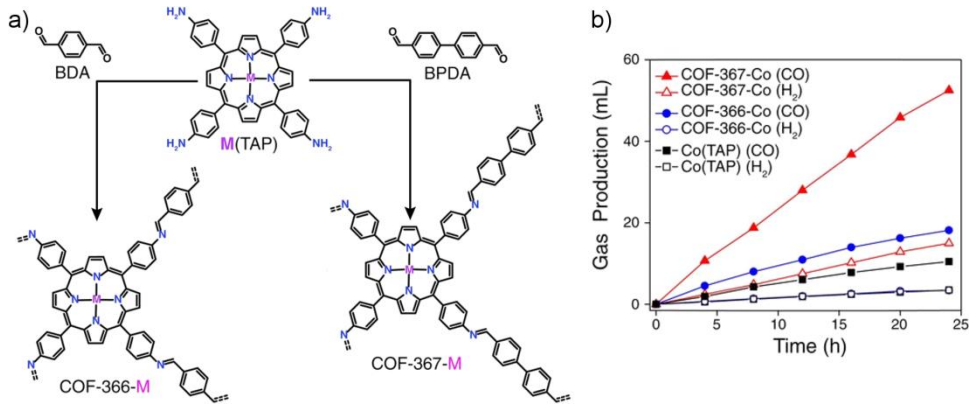

Figure 1.19. a) Synthesis of COF-366-M and COF-367-M from M(TAP), where M indicates the metal ion in the porphyrin. b) Long-term bulk electrolyses at -0.67 V (versus RHE) in a carbon dioxide-saturated aqueous bicarbonate buffer (pH = 7.3), showing the volume of carbon monoxide (solid symbols) and hydrogen (open symbols) produced by COF-367-Co (red), COF-366-Co (blue) and the molecular analogue Co(TAP) (black). Adapted from reference 53.

Finally, an interesting type of catalysis in which COFs have also demonstrated their potential is photocatalsys, which relies on the excitation of the catalyst by light to trigger the reaction. In this area, among a few examples[35,42,75,76], it can be mentioned a family of triazine containing COFs that has been reported to be able to produce hydrogen from water upon visible light irradiation in the presence of platinum nanoparticles as a co-catalyst and triethanolamine as a sacrificial electron donor. They show good stability and their performance rivals that of *state-of-the-art* carbon nitrides[63].

1.3.6. Luminiscence

Many of the properties of the molecular building blocks can be transferred to the framework. It is the case for example of fluorescent molecules, which in some situations can even act synergistically. Some of the subunits that have been used to prepare luminescent COFs are pyrenes[77], triphenylenes[78] and dehydrobenzoannulenes[79], moreover, they are usually combined in the same structure giving rise to interesting behaviours such as when both triphenylene and pyrene cores are present in the same framework, then, irradiation both at the excitation wavelength of triphenylene and pyrene results in emission by the pyrene.

1.3.7. Photovoltaics

Some of the most interesting properties are those that allow to harvest the power of sunlight and transform it in useful products using photocatalyic processes and in electrical energy, which is done in photovoltaic devices. COFs have also shown good light-induced charge separation properties. In fact, they may seem the dream material for this purpose since they provide a mean by which creating the long sought-after ordered

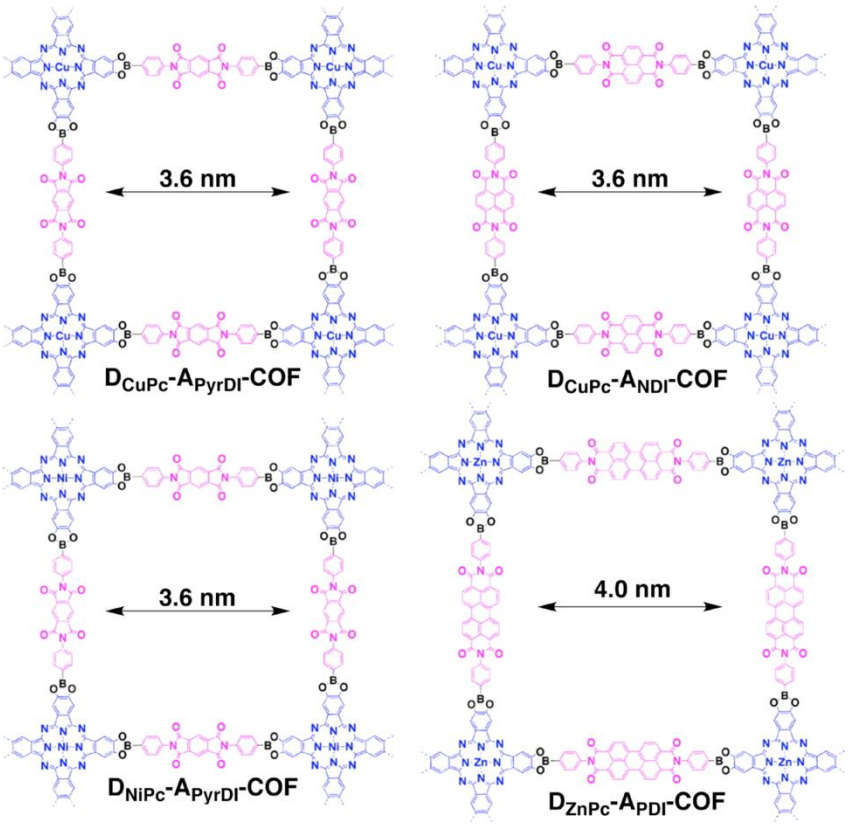

Figure 1.20. Structures of COFs containing alternating electron-donor (blue) and electron-acceptor (pink) moieties. Adapted from reference 81.

interpenetrated arrays of electron donor and acceptor groups and at the same time can be modified to present reasonable conductivity and light absorption[80]. An example of this approach are the structures depicted in Figure 1.20. These COFs contain phthalocyanines as electron-donors and imides as electron-acceptors, a judicious choice of these two units may allow to cover almost the whole visible and near-infrared spectrum, thus allowing to collect most of the sunlight. Moreover, the proximity of the donor and acceptor moieties favours a fast electron transfer and the ordered arrays their migration along the columns, resulting in charge separation states with lifetimes of several microseconds[81].

1.4. Processing of COFs

Besides featuring exceptional properties, materials need to be integrated in devices, this is done by processing them, that is, achieving a minimum degree of cohesion and shaping them as needed, placing and orienting them in their location, and interfacing them with the other components of the device. Of course, depending on the application, requirements related to some of the tasks will be more demanding while in others they will be virtually non-existent.

In the same way that stability is essential for any compound that aims to be applied to something, the possibility of a suitable processing also determines the usefulness of a material and is of the utmost importance in allowing it to perform at its best. In fact, one of the keys of the huge success of plastics is their extremely simple and powerful processing. In contrast, the poor and limited processability of COFs could be the main obstacle for them having a prominent role in the solution of present and future problems[82]. It has to be admitted that, despite their outstanding properties and potential, COFs face severe problems when it comes to integration in devices as a consequence of the fact that most synthetic methods yield completely insoluble powders formed by randomly aggregated crystallites and that solvothermal processes in the inside of sealed glass tubes do not leave much room for modifications. Given the central role played by the processing of COFs in this thesis, the reported advances in this area will be comprehensively reviewed.

1.4.1. Shaping of powdered materials

The simplest option to process COFs is to accept what is offered by most solvothermal syntheses and try to make the most out of it. All things considered, the situation would not be so different to that of popular

materials such as zeolites if not for the lower mechanical resistance of COFs. And this turns out to be a serious handicap, since the easiest way to deal with a powdered insoluble material is to press it into pellets, a process that is guaranteed to cause some damage to the structure. However, carefully controlling the applied pressure affords acceptable and interesting results, as shown by a detailed study of this method published in 2016[83]. In this work it was found that, as expected, high pressures amorphized COFs. Nonetheless, delicately finding the balance between the fragility of the porous framework and the compression needed to shape it, rewarded the authors with an appreciated alignment of the layers parallel to the flat surface of the pellet, as depicted in Figure 1.21.

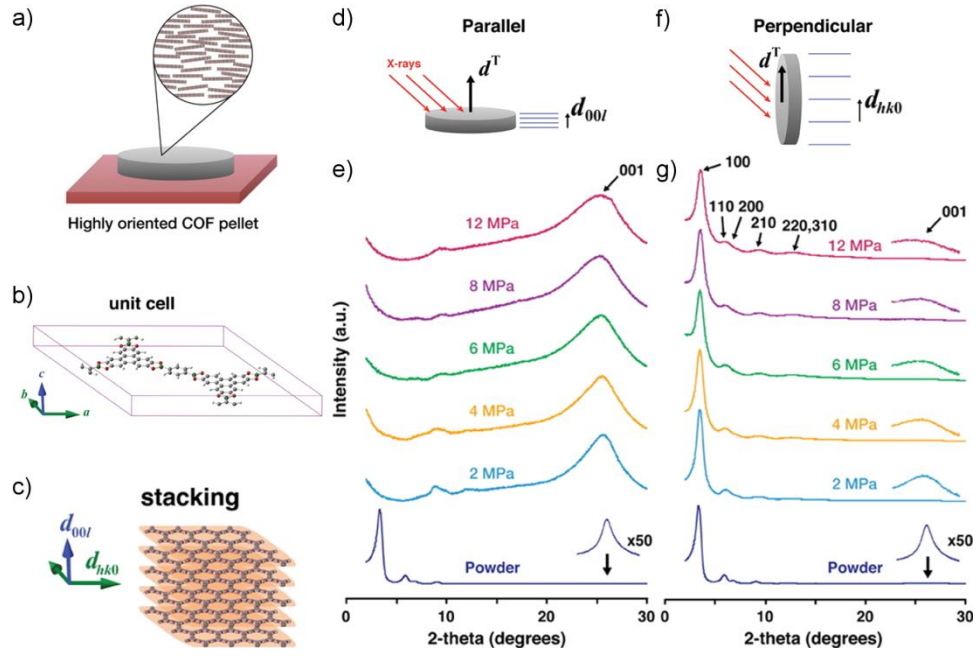

Figure 1.21. a) Scheme of the orientation of COF layers in the pellet. b) Unit cell of COF-5 illustrating c) the stacking and orthogonality between d_{hk0} and d_{00l} plane normal vectors. d,f) COF pellet oriented d) parallel and f) perpendicular to the optical axis allows diffraction from *00l* planes and *hk0* planes, respectively. e,g) PXRD of a COF-5 pellet in e) parallel and g) perpendicular mode at varying uniaxial pressure. Adapted from reference 83.

Other more elaborated strategies have been developed that allow to create macroscopic COF objects with enough cohesion to be used without additional support. For example, it has been demonstrated that keto-enamine COFs can be processed in a manner akin to that of terracotta[46]. For this, the amine is mixed with *p*-toluenesulfonic acid and the resulting mixture is ground with the aldehyde and a small amount of water to form a dough that after baking yields a highly porous and crystalline material (Figure 1.22a). The possibilities of this methodology are numerous, from using molds to shape centimetre-sized pieces of COF (Figure 1.22b), to large-scale continuous production by extrusion.

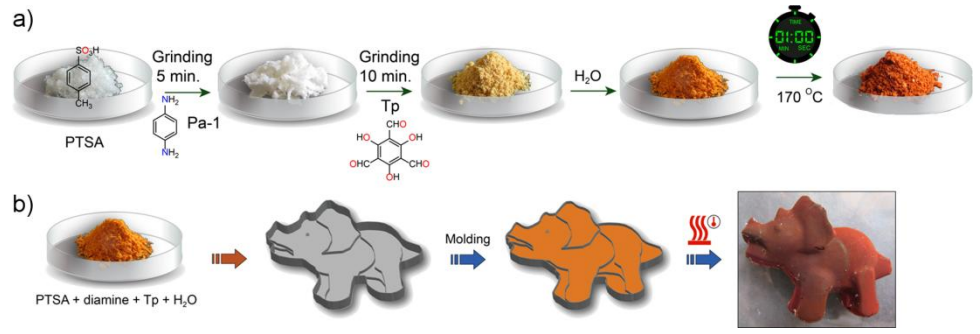

Figure 1.22. a) Scheme of COF preparation by a terracotta process. b) Sculpting of COFs using molds. Adapted from reference 46.

1.4.2. Thin Film Growth on Surface

For electronic applications, tight contacts and sharp and clean interfaces are generally preferred, which none of the methods described above is likely to provide. Therefore, methodologies that allow to integrate COFs on surfaces have been developed as well. A variety of strategies have been reported that serve this purpose.

The extreme of this reasoning is the synthesis of single and few-layer COFs in ultra-high vacuum, which is done by evaporating the building blocks over a metal surface on which they polymerise. As shown in Figure 1.23a, the product can be analysed by scanning tunnelling microscopy (STM) to confirm the correct formation of the framework and the number of layers created[84]. A variation of this procedure afforded large defect-free coverage of the substrate with an imine-linked COF, it is not carried under UHV conditions and includes the deposition of the less volatile monomer as a previous step before the evaporation of the other building block, which is done in a humid atmosphere to allow for bond formation reversibility (Figure 1.23b)[85].

A not so radical interpretation of the above statement leads to a solution that has been employed with certain success even for the preparation of functional devices, it consists in simply introducing the substrate in the reaction vessel. As rudimentary as this strategy may seem, continuous and crystalline films with a homogeneous tuneable thickness of not more than a few hundred nanometres like the one shown in Figure 1.24a can be

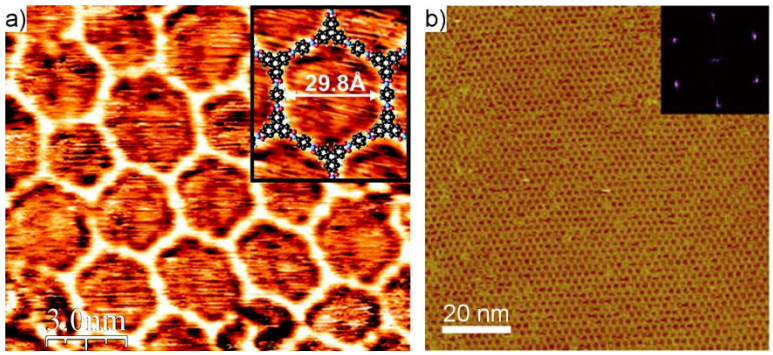

Figure 1.23. a) STM image of single-layer boronic ester-based COF prepared in UHV. The inset shows the COF-5 network with overlaid chemical structure obtained by DFT calculation. b) STM Image of a large defect-free area of an imine-linked COF. The inset depicts the corresponding FFT of the STM image. Adapted from references 84 and 85.

obtained. More importantly, the COF crystallites forming the film show a high preferential orientation towards lying with the stacking direction perpendicular to the substrate as illustrated by the drawing in Figure 1.24b. Another strength of this method is the wide range of materials that can be used as supports, being graphene[86] and indium-doped tin oxide (ITO)[87] just two examples. Adding even more flexibility, it has been proven that COF films are able to endure the evaporation of metal films on top of them, making it possible to obtain alternating COF and platinum multilayers[88].

In a further development of this technique, it was demonstrated that reaction conditions can be adjusted in order to restrict COF growth to graphene coated areas of a silicon oxide wafer. This allows to create patterns by selectively covering the substrate with graphene using lithographic methods and then proceeding to COF growth. As shown in

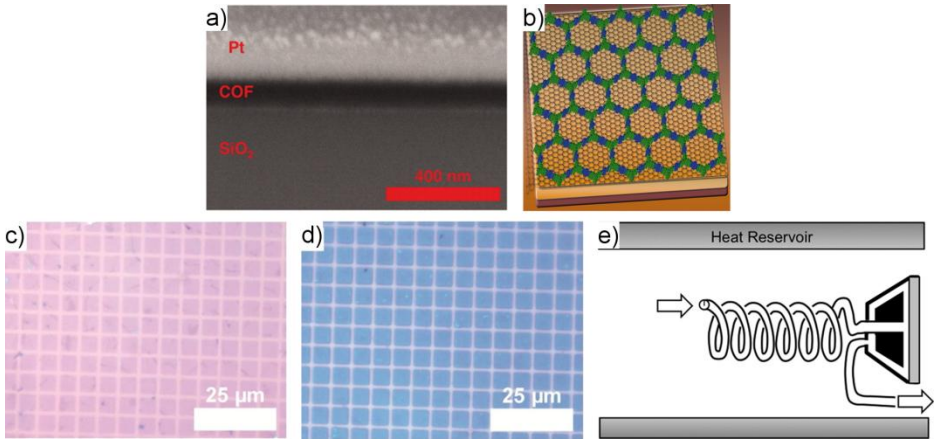

Figure 1.24. a) Cross-sectional SEM image of a COF film grown on single layer graphene on silicon oxide. b) Schematic illustration of the orientation of COF grown on graphene. c and d) Optical micrographs of patterned single layer graphene on silicon oxide c) before and d) after COF growth. The change of colour of the squares indicates an increase in their thickness. e) Scheme of the setup used for growth of COF films in flow. Adapted from references 86, 87 and 90.

Figure 1.24c-d, good resolutions can be achieved[89]. Moreover, if selective growth is not attained, a continuous COF film can be synthesised, a layer of photoresist casted on it and the pattern prepared using reactive ion etching, although in this case, the integrity of the COF film after the lithographic process was not confirmed[88].

If additional control over film growth is needed, it can be done in flow using a setup like one shown schematically in Figure 1.24e, which consists of a thermostatic chamber in which a solution of the building blocks flows through a tube of controlled length against the substrate and later abandons the system along its borders. This method is reported to provide more uniform films and to allow to independently modulate crystallinity and thickness through tuning of the residence time and the total time of the experiment[90].

1.4.3. Interfacial synthesis

Films are not only useful when attached to a substrate, free-standing materials that can form membranes can also find many applications, for example in filtration and separation processes. A method for obtaining large area, free-standing, thin films is interfacial synthesis, whether it is done at the air-liquid interface or at a liquid-liquid interface, the results can be fairly satisfactory.

Actually, synthesis at the air-water interface has proven successful in the obtention of monolayers of 2D polymers. The strategy relied on the use of anthracene-containing amphiphilic monomers, so, when a Langmuir-Blodgett film was formed, they would organise in such a way that the anthraceno moieties from different molecules would face each other. Upon irradiation, a cycloaddition reaction occurred and the covalent network was formed[91]. However, demonstrating an ordered structure in such thin

materials turned out to be extremely difficult and only STM images provided proof of it[92]. In the case of materials with linkages like those used in COFs, this approach was tested for the formation of imine-linked polymers, and, although spectroscopic analysis showed the formation of imine bonds, it was not possible to demonstrate crystallinity[93]. This issue has not been solved yet, although in the examples that will be presented next, thicker films were obtained that showed diffraction patterns matching the expected ones.

One of this cases was reported in 2015[94]. A thin film of an imine-linked COF was obtained at the air-liquid interface, although not using a Langmuir-Blodgett film approach. A solution in DMF of the building blocks with a concentration sufficiently low to prevent nucleation was left undisturbed in a water saturated atmosphere. This resulted in the formation of 50 nm thick films on the DMF surface that were found to be crystalline. Remarkably, depending on the incubation time, the thickness could be controlled, although thinner films were not checked for order.

Synthesis at the liquid-liquid interface has also been reported. An example is the formation of keto-enamine linked COFs at the interface between a dichloromethane solution containing the aldehyde and a water solution of the protonated amine with *p*-toluenesulfonic acid (Figure 1.25a). As the aldehyde is not soluble in water and the cationic protonated amine will stay on the aqueous phase, the reaction is confined at the interface. The result are crystalline, porous and transparent films with thickness that depends on the concentration of the monomers and can be as thin as 50 nm[95].

Instead of separating the monomers in different phases, it is also possible to confine the reaction at the interface by segregating the catalyst from the monomers. If scandium(III) triflate is used as a Lewis acid catalyst for

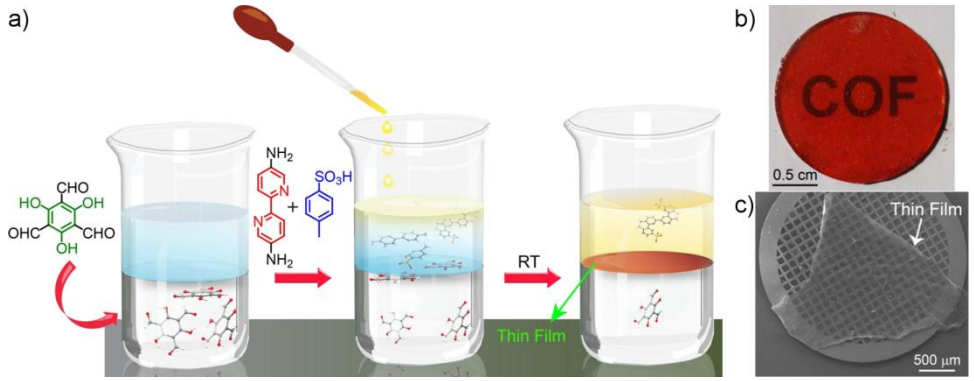

Figure 1.25. a) Scheme of the preparation of COF films at the liquid-liquid interface. The bottom colourless layer corresponds to aldehyde in dichloromethane solution, the blue layer contains only water as a spacer solution, and the top yellow layer is the amine-*p*-toluenesulfonic acid aqueous solution. b) Photograph showing a transparent COF film on a glass disk. c) SEM image of a free-standing COF thin-film on a TEM grid. Adapted from reference 95.

imine bond formation, this salt will be preferentially dissolved in water. Meanwhile, the monomers will stay in the organic phase but, if adequate concentration and solvent are chosen, they will not polymerise due to the lack of a catalyst. Therefore, the reaction can only take place at the interface, where the metal comes in contact with the building blocks. Similarly to the previous case, thicker films show good PXRD patterns and the thickness can be controlled through variation of monomer concentration[96].

It is remarkable about all these examples that the films showed enough mechanical stability to be handled and transferred to different supports as the glass disk in Figure 1.25b or the TEM grid in Figure 1.25c.

1.4.4. Exfoliation

Exfoliation of layered materials in a solvent is an alternative top-down approach to the bottom-up methodologies described above. It is to generate a suspension of few-layer-thick flakes that can be casted on a surface in order to cover it with COF. The basis of this process lies in the fact that in 2D COFs the forces that maintain the structure of the layers (covalent bonds) are much stronger than interlayer interactions (π-π stacking), therefore, when energy is applied in the form of ultrasounds, layers separate without decomposing. This has been found to be feasible with boronate[97] and hydrazone[98] COFs.

Liquid-phase exfoliation is widely used in other materials[99], graphene being the most famous, and apart from the possibility of residues of the solvent remaining trapped between the flakes and the substrate, the main drawback is the large amount of defects created by ultrasonication. For this reason, it is interesting to achieve exfoliation by less damaging means. This is usually done by mechanical exfoliation with adhesive tape when large and high quality crystals are available[100]. However, layered COF crystals suitable for this methodology have not been reported yet. Therefore, the closest procedure for exfoliation that has been reported involves grinding COF powder in the presence of a few drops of solvent. A suspension of nanosheets is thus generated. These nanosheets are found to retain some crystallinity and their thickness ranges between 3 and 10 nm while their length and width span for several micrometres[101].

Finally, a method based on the distortion of the stacking by post-synthetic modifications has been demonstrated[102]. It has the advantage of being even softer than mechanical exfoliation, but it necessarily implies the modification of the chemical structure, which may affect other properties. As shown in Figure 1.26a, the synthesised COF contains anthraceno

moieties on which a post-synthetic Diels-Alder reaction is performed. The loss of planarity of the layers disrupts the interlayer interactions making exfoliation easier. In fact, a dispersion is obtained directly from the reaction, with no need to apply additional external energy. Moreover, casting a few drops of the nanosheets dispersion in dichloromethane onto a water surface generates a continuous thin film upon solvent evaporation,

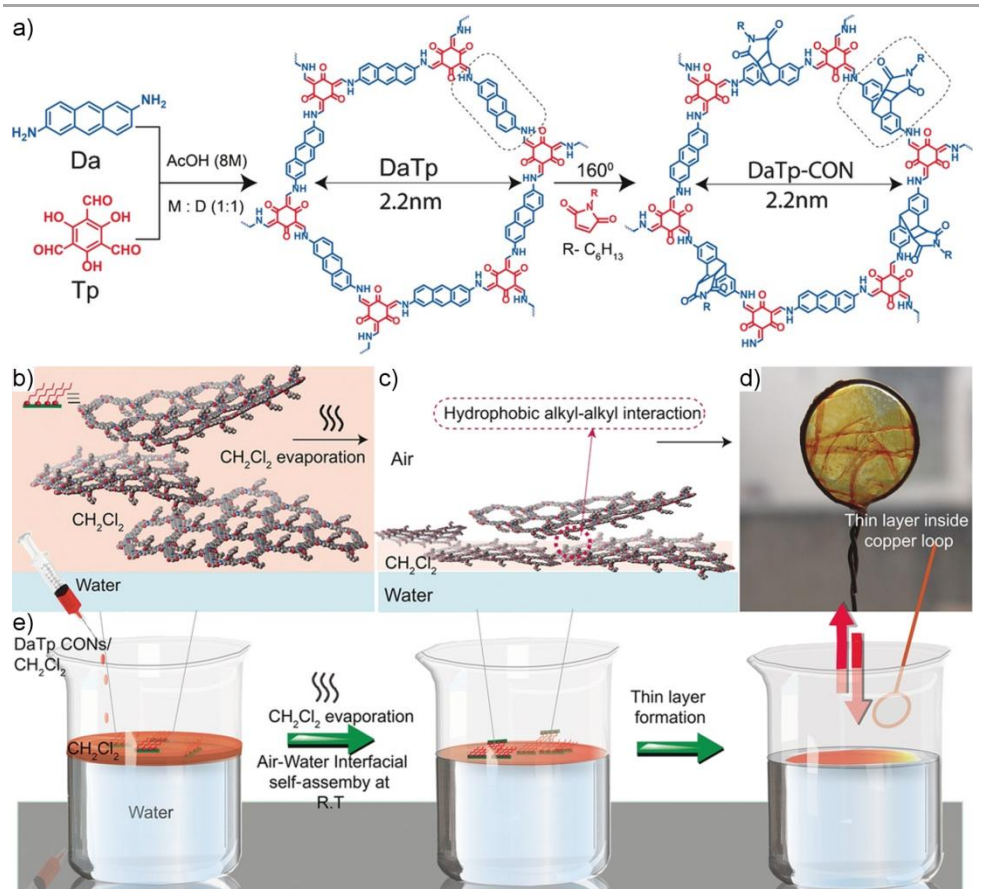

Figure 1.26. Synthesis of DaTP-COF and its chemical delamination through formation of a Diels-Alder adduct. b) DaTp nanolayers in dichloromethane. c) Layer-by-layer assembly upon dichloromethane evaporation. d) A thin layer inside a copper loop. e) Schematic representation of the thin film formation at an air-water interface. Adapted from reference 102.

in a process of interfacial self-assembly between the nanosheets (Figure 1.26b-e).

1.4.5. Particle Morphology

Nevertheless, extended thin films are not the only processing option, it can be very useful for some applications such as catalysis to have access to nanosized materials that can be dispersed in liquid media. The

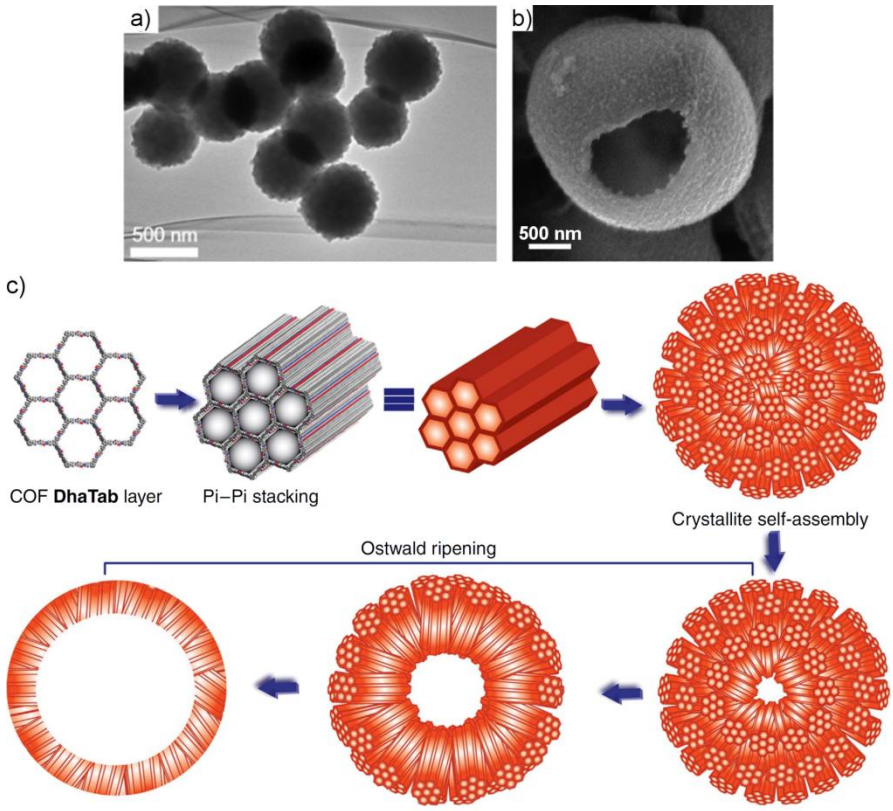

Figure 1.27. a) TEM image of imine-based COF spheres prepared at room temperature. b) SEM image of a hollow imine-linked COF sphere. c) Scheme of the mechanism of hollow sphere formation through crystallite aggregation followed by Ostwald ripening. Adapted from references 103 and 104.

requirements are usually not as simple as preparing small particles, they are also expected to be monodisperse and tunable in size and shape.

Given that spheres are one of the simplest shapes, there are many reports that describe their formation, although not always controlling their diameter. One of the first examples is noteworthy because of the simplicity of the procedure, which consists in mixing ethanolic building block solutions at room temperature to yield the spheres shown in Figure 1.27a, which have a diameter of 500 nm, decent crystallinity and good porosity[103]. An attractive modification of the spherical morphology is the generation of capsules, which was demonstrated to be possible under solvothermal conditions thanks to Ostwald ripening of initially formed spherical aggregates of COF crystallites (Figure 1.27b)[104].

More anisotropic morphologies can also be prepared, as shown by the remarkable case of the construction of hollow tubular COFs[105]. This interesting feat was achieved by adding zinc nanorods to the reaction mixture used for COF formation so the nanorods templated the growth of the organic framework. Once the composite material was obtained, etching with aqueous acid afforded the removal of the zinc template, yielding the hollow COF nanostructures (Figure 1.28a). Of course, this process can only be extended to acid stable COFs. An alternative to this templated approach was reported recently. It was found that an imine-linked diketopyrrolopyrrole containing COF formed small plate-like aggregates during the first stages of the solvothermal synthesis. Interestingly, if allowed to evolve, these plates became smoother and began rolling themselves, finally yielding hollow microtubes with an inner diameter close to 90 nm and outer diameter around 300 nm (Figure 1.28b)[106].

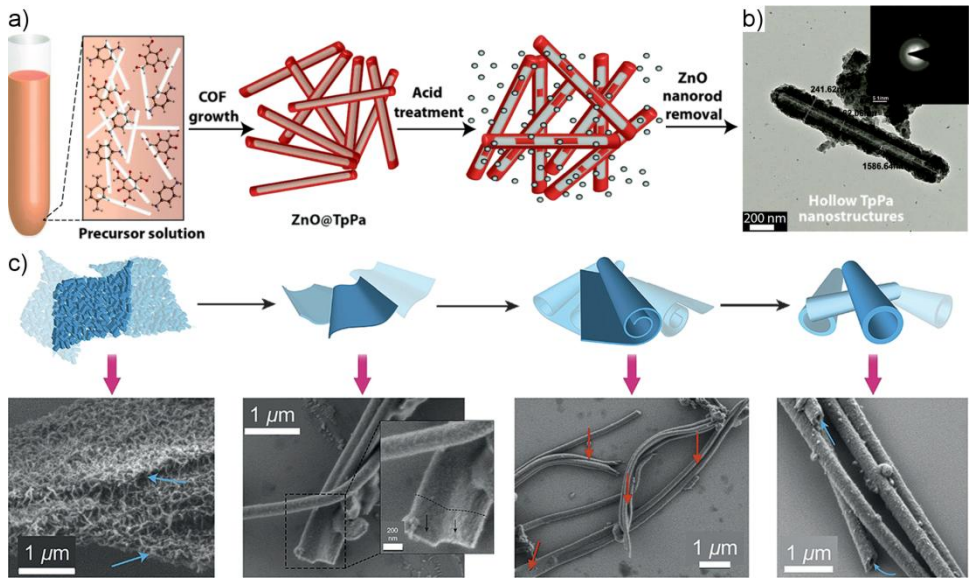

Figure 1.28. a) Scheme of the preparation of hollow tubular COFs *via* a templating strategy. b) TEM image of a hollow COF rod after template removal. The SAED in the inset shows the absence of diffraction from the template. c) Mechanism for microtube formation, beginning with the agglomeration of small crystallites into sheet-like aggregation, then the smoothing and densification of the sheets, their rolling and finally tube formation and recombination by imine condensation. Each step is accompanied by its corresponding SEM image. Adapted from references 105 and 106.

Finally, some works have appeared that try push the limit of COF miniaturisation as far as possible. In one of them, imine-based COF nanocrystals are obtained by adding poly(vinylpyrrolidinone) (PVP) to the reaction mixture[47]. It is suggested that the protonated imine increases the polarity of the COF and favours the binding of PVP, which acts as a capping agent and controls the growth and aggregation of the particles. The size of the nanocrystals can be tuned by varying the concentration of PVP and particles with dimensions close to 100 nm that form stable dispersions in ethanol have been obtained (Figure 1.29a). The other approach has been optimised for COFs linked by boronic ester moieties. It was found that using acetonitrile or other nitrile compounds as cosolvents

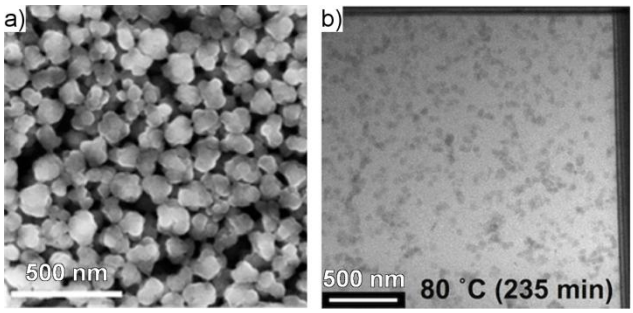

Figure 1.29. a) SEM image of imine-linked COF nanocrystals with an average size of 112 nm synthesised in ethanol and stabilised with PVP. b) Liquid-cell transmission electron microscopy (LCTEM) image of acetonitrile stabilised COF colloids. Adapted from references 47 and 107.

with classical dioxane:mesitylene mixtures for the formation of the framework generates an extremely stable suspension of COF particles that are characterised to have sizes between 45 and 60 nm (Figure 1.29b)[107].

1.4.6. Hybrid materials

Besides controlling size and shape, a good processability also endows a material with the possibility of becoming part of hybrid materials, which enables to combine the functionalities of the different components and, if carefully designed, may result in synergistic effects.

Some of the materials COFs can be mixed with are other COFs. It has been found that reacting a previously synthesised COF with a different amine compatible in size and shape with the one already incorporated in the structure enables to prepare particles containing both networks[108]. Curiously, depending on the order in which the two amines are incorporated into the material, the two structures can be homogeneously mixed or segregated in a core-shell morphology. The effects derived from

these different distributions are exposed by the different hydrophilicity of the two hybrid materials.

COFs have been combined with other types of materials, too. For example, the interaction with the extended π system of carbon nanotubes is expected to be rather strong and favourable. Thus, when the synthesis of COFs is conducted in the presence of carbon nanotubes, it grows around them, creating a material that combines the redox properties of the framework with the electrical conductivity of the nanotubes[109]. Similarly, PVP functionalised gold nanoparticles have been encapsulated inside COF spheres[110]. Of course, this latter strategy required an additional control over the morphology of the COF. In cases where there is no such dominion over the growth of the framework, the other material can be used as a template. For instance, this was the approach used for coating 200 nm in diameter Fe_3O_4 spheres with a 100 nm thick COF layer[111]. In order to do so, an amorphous polyimine network was polymerised in the presence of the metal oxide spheres, and growth around them. Then, it was subjected to conditions allowing bond reversibility to happen, which promoted the crystallisation of the COF shell of the spheres without modifying its morphology.

The preparation of all these hybrids is driven by non-covalent interactions, however, some applications may require a stronger anchoring of the COF to the other material. A common strategy to achieve this has consisted on the functionalisation of the surface of the other material with amino groups (Figure 1.30). Then, a layer of the aldehyde building block is grafted by formation of imine bonds with these amino groups. Finally, both monomers are added and COF nucleation begins at the anchored aldehydes. Using this method it has been possible to obtain structures strikingly resembling those in the previous paragraph, for instance, 200 nm iron oxide spheres have been coated with the same COF and TEM

images showed the success and similar result of both methodologies (Figure 1.30b-c)[112]. Additionally, silica microspheres[113] and MOF[114] particles have been prepared using this approach. Boronate ester-based COFs can also benefit from this strategy, although it has to be adapted to their different chemistry. For example, diboronic acids can anchored by condensed with the hydroxy groups of graphene oxide and serve as the nucleation point for the subsequent growth of the network. Interestingly, this method generates COF crystallites oriented perpendicular to the surface of the graphene oxide sheets (Figure 1.30d), in contrast with the parallel orientation usually obtained by direct synthesis[115].

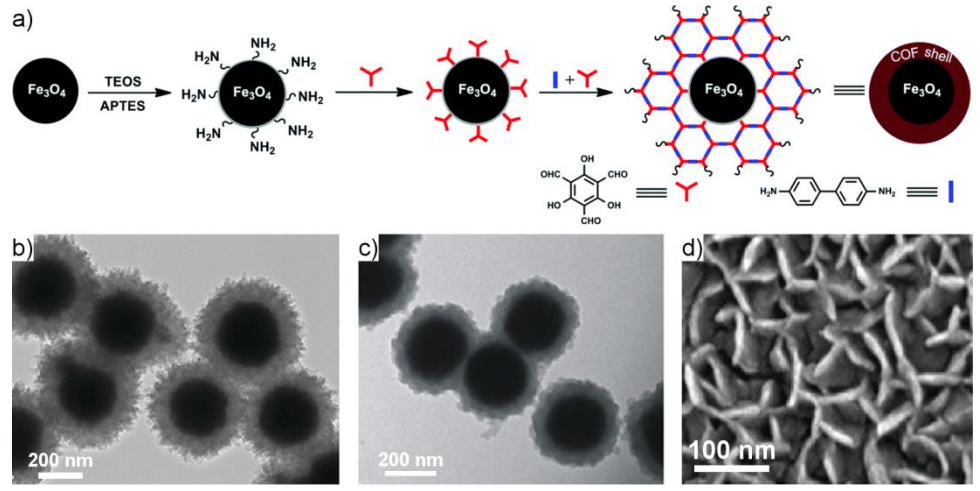

Figure 1.30. a) Scheme of the synthesis of grafted core-shell Fe_3O_4@COF spheres. b,c) TEM images of Fe_3O_4@COF spheres prepared by b) polymerising in the presence of the Fe_3O_4 spheres and c) previously anchoring a monomer to the metal oxide sphere. d) SEM image of COF-graphene oxide composite in which COF layers have grown vertically on the graphene oxide surface. Adapted from references 111, 112 and 115.

1.4.7. Membranes

An extremely versatile and useful form of processing is the creation of membranes, which can be used for separations both in gas or liquid phase.

The preparation can be as simple as dispersing COF powder in the polybenzimidazole solution typically used for casting polymer membranes[116]. However, even though the organic nature of COFs appears to favour a better mixing with the polymer matrix, it has been reported that MOF containing membranes perform better if an improved distribution of the filler particles is obtained[117]. Preparing membranes with these characteristics usually involves an elaborate process and can benefit from the methodologies discussed above. For example, an easy improvement on the modification of polymeric membranes comes from the previous delamination of COFs by mechanical grinding. This generates a suspension of nanosheets that can be homogeneously distributed in the polymer matrix. Moreover, the casting process of poly(ether sulfone) involves a step that allows the densification of the upper part of the membrane, and this step was employed to generate COF gradients inside

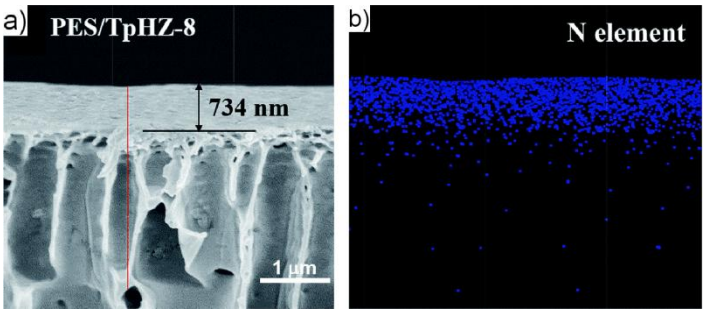

Figure 1.31. a) Cross sectional SEM image of a poly(ether sulfone) membrane with a gradient of an imine-based COF as filler. b) EDX N-mapping of the membrane in a) showing the gradient in the amount of COF across the membrane. Adapted from reference 118.

the polysulfone membrane (Figure 1.31), which was possible thanks to the good diffusion of the nanosheets allowing them to migrate to the denser region in which they were trapped[118].

Instead of embedding COF particles in a matrix, membranes can be prepared by covering a porous support with a layer of COF. Exfoliation has also been used for this purpose. In this case, the suspension of COF nanosheets was mixed with graphene oxide and filtered through an cellulose acetate support. During the filtering process, the COF and graphene oxide layers restacked due to the higher cohesion of graphene oxide and completely covered the support[119]. Likewise, thin films prepared at the liquid-liquid interface have been used to cover poly(ether sulfone) porous supports[120].

An alternative to cover supports with already formed COF sheets is directly growing them in the support. As a good mechanical stability of the final product is needed because under operation conditions it has to withstand the drag forces of the liquid flow, strategies that bond the COF crystallites to the support have been preferred. As explained before, surface functionalisation with amines is quite common, and it has been done on alumina supports to first graft a dialdehyde and then proceed to the growth of the framework. This whole process allowed the obtention of a continuous, homogenous and compact coverage (Figure 1.32a-b)[121]. In an example of the degree of complexity that is possible to reach with this strategy, a silicon oxide porous support was coated with polyaniline; then, an imine based COF was grown, with the polyaniline serving as a bridge between the support and the aldehyde groups of the COF. Next, a MOF was synthesised on this multilayer membrane, with the interacion between the carboxylic acids of the MOF and the unreacted amine groups of the COF connecting the two phases (Figure 1.32c). Thus, a composite of four different materials (silica, polyaniline, COF and MOF) was created[122].

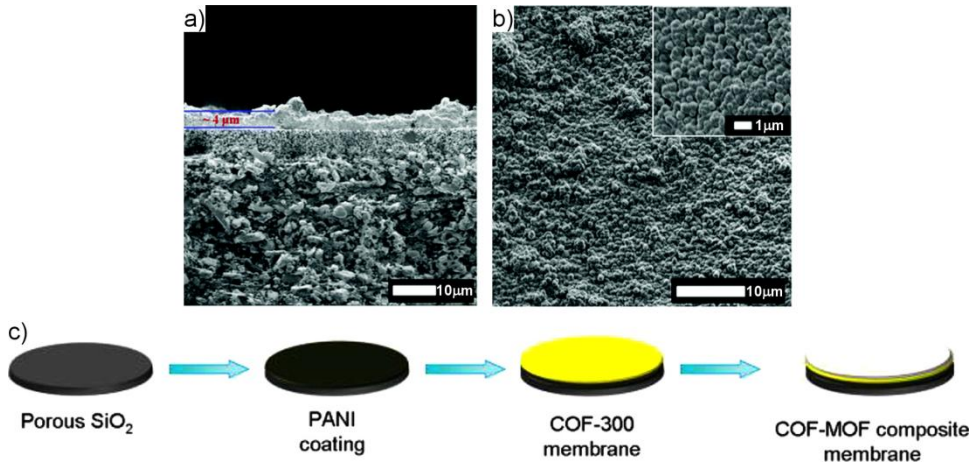

Figure 1.32. a) Cross sectional SEM image of a α-Al_2O_3 porous support with a 4 μm thick COF layer grown on top. b) SEM image of the surface of the alumina support covered with COF. The inset is an amplified image. Both show a homogeneous coverage. c) Scheme of the fabrication of COF-MOF composite membranes. Adapted from references 121 and 122.

Finally, if COFs can be processed with enough chemical resistance, it would not be necessary to blend them with other materials and pure COF membranes could be prepared. The terracotta-like processing (see Section 1.4.1) has been employed to prepare COF membranes by spreading the dough in a very thin sheet using knife-casting before baking. The resulting membranes are a few hundreds of micrometres thick, self-standing and flexible[123].

1.5. Potential applications of COFs

As it has been shown before, COFs can display excellent and diverse properties and a few methods to process them have been developed. However, examples of applications are still scarce and those reported generally do not show competitive performances and durability. The reason behind this is that, beside surface supported films, all these processing strategies are very recent, in fact, the earliest works described in the previous section date from 2015. This implies that there has not been enough time to fully combine into devices the existing knowledge of how to design functional COFs and how to process them, since the new question of to what extent processing affects some properties also needs to be addressed.

Some of the first applications were those using COF thin-films. For example, a COF with a structure featuring electron-donor and acceptor groups was prepared in the form of 50 nm thick oriented films on an ITO electrode with a 10 nm molibdenum oxide layer that acts as a hole extractor. Over the COF film, an aluminium electrode with a 20 nm hole-blocking layer of zinc oxide was deposited. This device contains all the components of a solar cell, being the COF the active layer. Upon irradiation, the device shows efficient charge separation, however, the performance is hindered by the high rate of recombination[124].

Another example of COF thin-film adapted to application is found in the field of electrical energy storage. An anthraquinone containing COF thin film was prepared on gold because its redox behaviour shows potential for charge storage. However, the poor conductivity of the network precluded most of the redox active moieties from participating. For this reason, the conductive polymer PEDOT was polymerised inside the channels of the COF (Figure 1.33a). The beneficial effect of PEDOT in distributing the

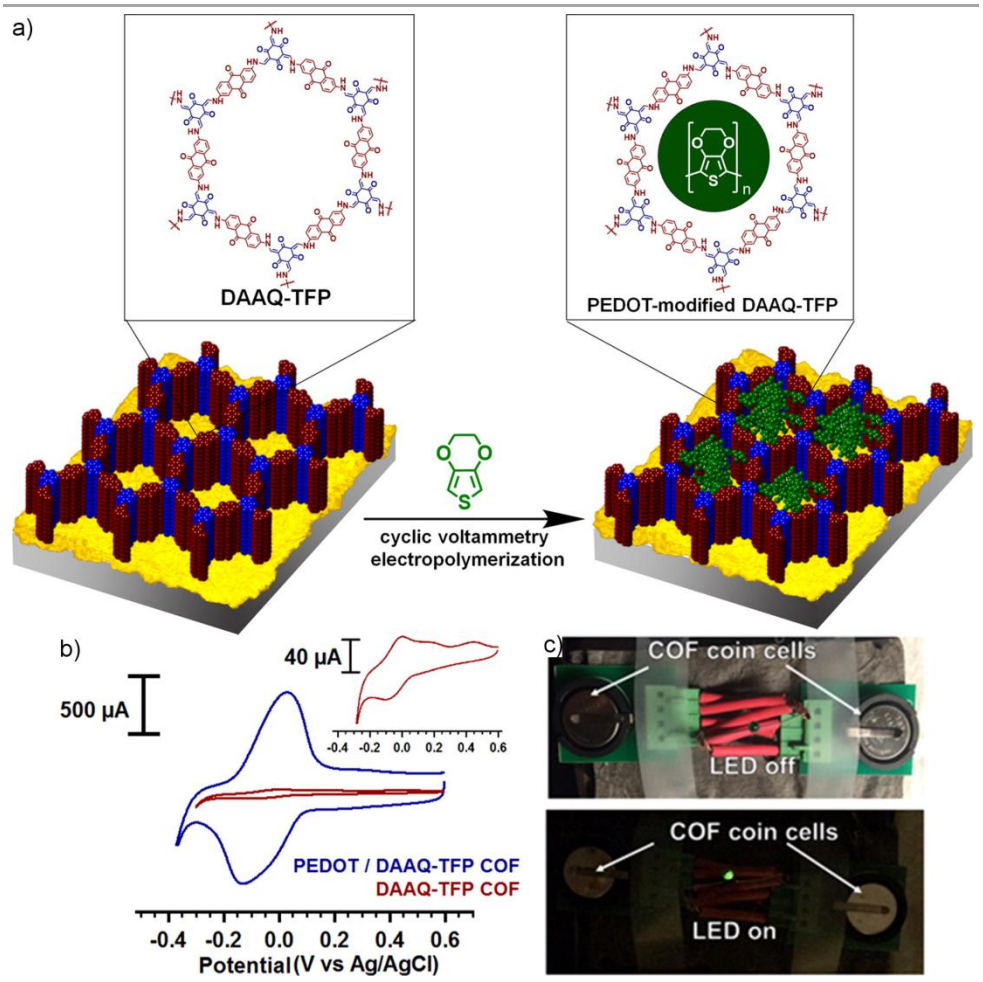

Figure 1.33. a) Depiction of the incorporation of PEDOT in the pores of a DAAQ-TFP COF film by electropolymerisation. b) Cyclic voltammetry response in 0.5 M H_2SO_4 of a DAAQ-TFP COF film before (red) and after (blue) PEDOT modification. The inset presents the cyclic voltammetric response for the unmodified film using an expanded current scale. c) Photographs of a PEDOT-modified DAAQ-TFP COF working device powering a green LED. Adapted from reference 125.

charge throughout the whole COF and allowing all the anthraquinones to be reduced was clearly seen by the huge current enhancement in cyclic voltammetries (Figure 1.33b). The full electrochemical studies showed

good performance over a range of charge-discharge rates and decent stability. As a proof-of-concept, two coin cells with COF electrodes were fabricated and succeeded in lighting a LED (Figure 1.33c-d)[125].

Moving onto another area, the preparation of monodisperse spheres and the anchoring of COFs to other materials has also been used to facilitate COF application in chromatographic separations. In the simplest case, a spherical COF was charged in a gas chromatography column and used as the stationary phase. The results obtained for alkane, alcohol and pinene isomers separation showed good resolution and selectivity[103]. However, the full potential of COFs in chromatography was shown in another example in which a chiral COF was synthesised *in situ* in a fused-silica capillary column. In order to retain the COF and steer its growth to the column walls, the silica was previously functionalised with amino groups. As a result, a chiral capillary column was obtained that even performed better than some commercially available ones in the separation of certain enantiomeric mixtures[126].

A last example of application made possible by the availability of a suitable processing technique is the use of COFs for nanofiltration. On the one hand, COF films were formed at the dichloromethane-water interface (see Section 1.4.3) with a thickness of a few micrometres to ensure its mechanical stability. The films were placed between two macroporous supports in order to study their performance when a solution is passed through them in a dead-end cell (Figure 1.34a). The solvent permeance values were better than those of other materials used for nanofiltration and the rejection of solutes was high showing good size selectivity[95].

On the other hand, cross-flow nanofiltration (Figure 1.34b) has also been achieved with COFs. To reach this goal, an alumina tube for this type of filtration was functionalised with amino groups that, as has been described several times, allowed the grafting of an imine-based COF to its surface.

The coverage with a 400 nm thick COF layer was complete and uniform (Figure 1.34c-d). As in the previous example, good rejection of dyes dissolved in water was found (Figure 1.34e-f), hinting towards its potential for water purification[127].

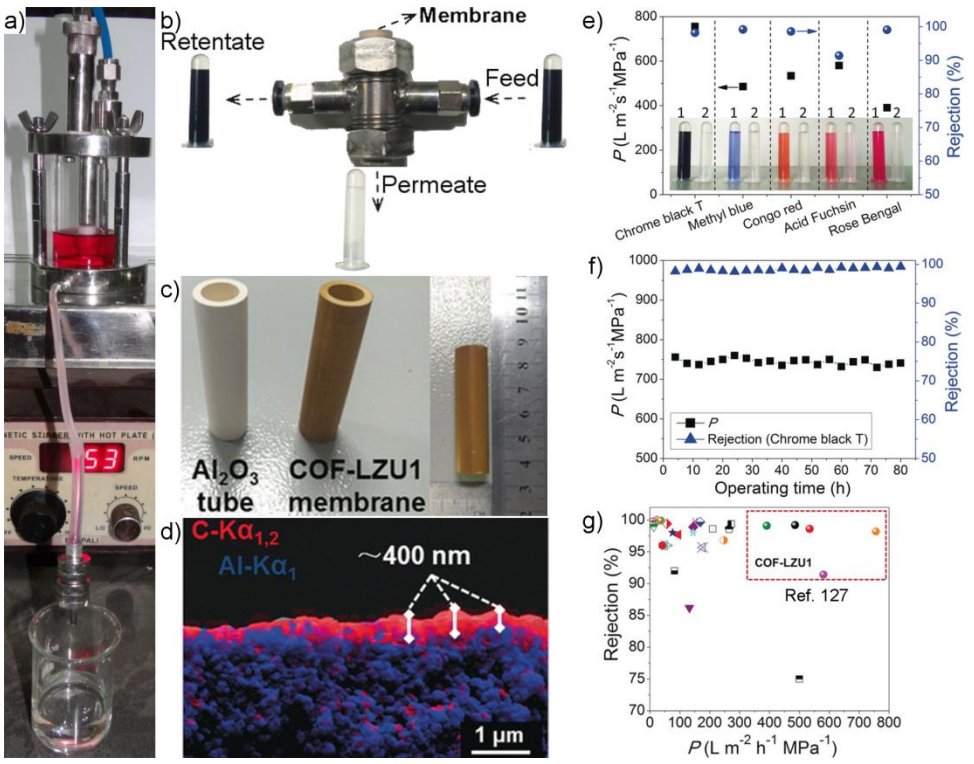

Figure 1.34. a) Setup of nanofiltration with a COF thin film as membrane in a dead-end cell. As can be seen, the filtered solution is colourless. b) Scheme of cross-flow filtration. The mixture is fed from the right and flows around the tubular membrane. Only part of the solvent and small molecules can cross the membrane and are collected at the bottom, while larger molecules and the rest of the solvent exit the system from the left. c) Photographs of an untreated (left) and COF functionalised (right) alumina tube for cross-flow filtration. d) EDX mapping of the cross-section of a COF functionalised tube. C is the tracer for the COF layer and Al for the alumina support. e) Water permeance and rejection rates of different dyes with tubular COF membranes. f) Stability test of the tubular COF membranes. g) Comparison of the performance of COFs in nanofiltration with that of MOFs and other porous materials and composites. Adapted from references 95 and 127.

1.6. Closing remarks

These examples show the importance of processing in bridging the gap between properties and applications. As critical as it has been revealed to be; since the efforts in COF research were first devoted to the creation of new structures with a wide range of topologies, pore sizes, bond types and functional subunits that have allowed an impressive tuning and combination of properties, processing has been overlooked until recently.

In fact, the driving force behind the work presented in this thesis was the lack of and subsequent necessity for processing methodologies at the time the project began. Therefore, the next four chapters will include several new processing procedures for imine-based COFs developed simultaneously to the ones summarised previously, and studies on the effect of said techniques in the properties of the resulting COFs.

1.7. References

(1) Robens, E. Some Intriguing Items in the History of Adsorption. In *Characterization of Porous Solids III*; Rodríguez-Reinoso, F., Rouquerol, J., Unger, K., Sing, K., Eds.; 1994; pp 109–118.

(2) Rouquerol, J.; Rouquerol, F.; Llewellyn, P.; Maurin, G.; Sing, K. S. W. *Adsorption by Powders and Porous Solids: Principles, Methodology and Applications*, 2nd ed.; Elsevier Science, 2014.

(3) Wright, P. A. *Microporous Framework Solids*; Royal Society of Chemistry: Cambridge, 2007.

(4) Kondo, M.; Yoshitomi, T.; Matsuzaka, H.; Kitagawa, S.; Seki, K. Three-Dimensional Framework with Channeling Cavities for Small Molecules:{[M2(4, 4′-Bpy)3(NO3)4]·xH2O}n(M Co, Ni, Zn). *Angew. Chemie Int. Ed. English* **1997**, *36* (16), 1725–1727.

(5) McKeown, N. B.; Makhseed, S.; Budd, P. M. Phthalocyanine-Based Nanoporous Network Polymers. *Chem. Commun.* **2002**, No. 23, 2780–2781.

(6) Côté, A. P.; Benin, A. I.; Ockwig, N. W.; O'Keeffe, M.; Matzger, A. J.; Yaghi, O. M. Porous, Crystalline, Covalent Organic Frameworks. *Science* **2005**, *310* (5751), 1166–1170.

(7) Tozawa, T.; Jones, J. T. a; Swamy, S. I.; Jiang, S.; Adams, D. J.; Shakespeare, S.; Clowes, R.; Bradshaw, D.; Hasell, T.; Chong, S. Y.; et al. Porous Organic Cages. *Nat. Mater.* **2009**, *8* (12), 973–978.

(8) Climate Action, Environment, Resource Efficiency and Raw Materials - European Commission https://ec.europa.eu/programmes/horizon2020/en/h2020-section/climate-action-environment-resource-efficiency-and-raw-materials (accessed May 12, 2018).

(9) Secure, Clean and Efficient Energy - European Commission https://ec.europa.eu/programmes/horizon2020/en/h2020-section/secure-clean-and-efficient-energy (accessed May 12, 2018).

(10) Béguin, F.; Frąckowiak, E. *Supercapacitors: Materials, Systems, and Applications*; Béguin, F., Frąckowiak, E., Eds.; Wiley-VCH Verlag GmbH & Co. KGaA: Weinheim, Germany, 2013.

(11) Dhakshinamoorthy, A.; Asiri, A. M.; García, H. Metal-Organic Framework (MOF) Compounds: Photocatalysts for Redox Reactions and Solar Fuel Production. *Angew. Chemie Int. Ed.* **2016**, *55* (18), 5414–5445.

(12) Wang, C.; DeKrafft, K. E.; Lin, W. Pt Nanoparticles@Photoactive Metal–Organic Frameworks: Efficient Hydrogen Evolution via Synergistic Photoexcitation and Electron Injection. *J. Am. Chem. Soc.* **2012**, *134* (17), 7211–7214.

(13) PRIMA Joint Program https://www.unisi.it/sites/default/files/allegatiparagrafo/PRIMA_0.pdf (accessed May 12, 2018).

(14) United Nations World Water Assessment Programme, W. *The United Nations World Water Development Report 2015: Water for a Sustainable World*; UNESCO: Paris, 2015.

(15) Kim, H.; Yang, S.; Rao, S. R.; Narayanan, S.; Kapustin, E. A.; Furukawa, H.; Umans, A. S.; Yaghi, O. M.; Wang, E. N. Water Harvesting from Air with Metal-Organic Frameworks Powered by Natural Sunlight. *Science* **2017**, *356* (6336), 430–434.

(16) Slater, A. G.; Cooper, A. I. Function-Led Design of New Porous Materials. *Science* **2015**, *348* (6238), aaa8075-aaa8075.

(17) Diercks, C. S.; Yaghi, O. M. The Atom, the Molecule, and the Covalent Organic Framework. *Science* **2017**, *355* (6328).

(18) Biswal, B. P.; Chandra, S.; Kandambeth, S.; Lukose, B.; Heine, T.; Banerjee, R. Mechanochemical Synthesis of Chemically Stable Isoreticular Covalent Organic Frameworks. *J. Am. Chem. Soc.* **2013**, *135* (14), 5328–5331.

(19) Xu, L.; Zhou, X.; Tian, W. Q.; Gao, T.; Zhang, Y. F.; Lei, S.; Liu, Z. F. Surface-Confined Single-Layer Covalent Organic Framework on Single-Layer Graphene Grown on Copper Foil. *Angew. Chemie Int. Ed.* **2014**, *53* (36), 9564–9568.

(20) Banhart, F.; Kotakoski, J.; Krasheninnikov, A. V. Structural Defects in Graphene. *ACS Nano* **2011**, *5* (1), 26–41.

(21) Colson, J. W.; Dichtel, W. R. Rationally Synthesized Two-Dimensional Polymers. *Nat. Chem.* **2013**, *5* (6), 453–465.

(22) Du, Y.; Yang, H.; Whiteley, J. M.; Wan, S.; Jin, Y.; Lee, S.-H.; Zhang, W. Ionic Covalent Organic Frameworks with Spiroborate Linkage. *Angew. Chemie Int. Ed.* **2016**, *55* (5), 1737–1741.

(23) Hunt, J. R.; Doonan, C. J.; LeVangie, J. D.; Côté, A. P.; Yaghi, O. M. Reticular Synthesis of Covalent Organic Borosilicate Frameworks. *J. Am. Chem. Soc.* **2008**, *130* (36), 11872–11873.

(24) Jackson, K. T.; Reich, T. E.; El-Kaderi, H. M. Targeted Synthesis of a Porous Borazine-Linked Covalent Organic Framework. *Chem. Commun.* **2012**, *48* (70), 8823–8825.

(25) Lanni, L. M.; Tilford, R. W.; Bharathy, M.; Lavigne, J. J. Enhanced Hydrolytic Stability of Self-Assembling Alkylated Two-Dimensional Covalent Organic Frameworks. *J. Am. Chem. Soc.* **2011**, *133* (35), 13975–13983.

(26) Kuhn, P.; Antonietti, M.; Thomas, A. Porous, Covalent Triazine-Based Frameworks Prepared by Ionothermal Synthesis. *Angew. Chemie Int. Ed.* **2008**, *47* (18), 3450–3453.

(27) Ren, S.; Bojdys, M. J.; Dawson, R.; Laybourn, A.; Khimyak, Y. Z.; Adams, D. J.; Cooper, A. I. Porous, Fluorescent, Covalent Triazine-Based Frameworks via Room-Temperature and Microwave-Assisted Synthesis. *Adv. Mater.* **2012**, *24* (17), 2357–2361.

(28) Guo, J.; Xu, Y.; Jin, S.; Chen, L.; Kaji, T.; Honsho, Y.; Addicoat, M. a; Kim, J.; Saeki, A.; Ihee, H.; et al. Conjugated Organic Framework with Three-Dimensionally Ordered Stable Structure and Delocalized π Clouds. *Nat. Commun.* **2013**, *4*, 2736.

(29) DeBlase, C. R.; Dichtel, W. R. Moving Beyond Boron: The Emergence of New Linkage Chemistries in Covalent Organic Frameworks. *Macromolecules* **2016**, *49* (15), 5297–5305.

(30) Uribe-Romo, F. J.; Hunt, J. R.; Furukawa, H.; Klöck, C.; O'Keeffe, M.; Yaghi, O. M. A Crystalline Imine-Linked 3-D Porous Covalent Organic Framework. *J. Am. Chem. Soc.* **2009**, *131*, 4570–4571.

(31) Segura, J. L.; Mancheño, M. J.; Zamora, F. Covalent Organic Frameworks Based on Schiff-Base Chemistry: Synthesis, Properties and Potential Applications. *Chem. Soc. Rev.* **2016**, *45* (20), 5635–5671.

(32) Uribe-Romo, F. J.; Doonan, C. J.; Furukawa, H.; Oisaki, K.; Yaghi, O. M. Crystalline Covalent Organic Frameworks with Hydrazone Linkages. *J. Am. Chem. Soc.* **2011**, *133* (30), 11478–11481.

(33) Fang, Q.; Zhuang, Z.; Gu, S.; Kaspar, R. B.; Zheng, J.; Wang, J.; Qiu, S.; Yan, Y. Designed Synthesis of Large-Pore Crystalline Polyimide Covalent Organic Frameworks. *Nat. Commun.* **2014**, *5*, 4503.

(34) Dalapati, S.; Jin, S.; Gao, J.; Xu, Y.; Nagai, A.; Jiang, D. An Azine-Linked Covalent Organic Framework. *J. Am. Chem. Soc.* **2013**, *135*, 17310–17313.

(35) Nagai, A.; Chen, X.; Feng, X.; Ding, X.; Guo, Z.; Jiang, D. A Squaraine-Linked Mesoporous Covalent Organic Framework. *Angew. Chemie Int. Ed.* **2013**, *52* (13), 3770–3774.

(36) Chong, J. H.; Sauer, M.; Patrick, B. O.; MacLachlan, M. J. Highly Stable Keto-Enamine Salicylideneanilines. *Org. Lett.* **2003**, *5* (21), 3823–3826.

(37) Kandambeth, S.; Mallick, A.; Lukose, B.; Mane, M. V; Heine, T.; Banerjee, R. Construction of Crystalline 2D Covalent Organic Frameworks with Remarkable Chemical (Acid/Base) Stability via a Combined Reversible and Irreversible Route. *J. Am. Chem. Soc.* **2012**, *134* (48), 19524–19527.

(38) Waller, P. J.; Lyle, S. J.; Osborn Popp, T. M.; Diercks, C. S.; Reimer, J. A.; Yaghi, O. M. Chemical Conversion of Linkages in Covalent Organic Frameworks. *J. Am. Chem. Soc.* **2016**, *138* (48), 15519–15522.

(39) Stewart, D.; Antypov, D.; Dyer, M. S.; Pitcher, M. J.; Katsoulidis, A. P.; Chater, P. A.; Blanc, F.; Rosseinsky, M. J. Stable and Ordered Amide Frameworks Synthesised under Reversible Conditions Which Facilitate Error Checking. *Nat. Commun.* **2017**, *8* (1), 1102.

(40) Pyles, D. A.; Crowe, J. W.; Baldwin, L. A.; McGrier, P. L. Synthesis of Benzobisoxazole-Linked Two-Dimensional Covalent Organic Frameworks and Their Carbon Dioxide Capture Properties. *ACS Macro Lett.* **2016**, *5* (9), 1055–1058.

(41) Zhuang, X.; Zhao, W.; Zhang, F.; Cao, Y.; Liu, F.; Bi, S.; Feng, X. A Two-Dimensional Conjugated Polymer Framework with Fully Sp 2 -Bonded Carbon Skeleton. *Polym. Chem.* **2016**, *7* (25), 4176–4181.

(42) Wei, P.-F.; Qi, M.-Z.; Wang, Z.-P.; Ding, S.-Y.; Yu, W.; Liu, Q.; Wang, L.-K.; Wang, H.-Z.; An, W.-K.; Wang, W. Benzoxazole-Linked Ultrastable Covalent Organic Frameworks for Photocatalysis. *J. Am. Chem. Soc.* **2018**, jacs.8b00571.

(43) Beaudoin, D.; Maris, T.; Wuest, J. D. Constructing Monocrystalline Covalent Organic Networks by Polymerization. *Nat. Chem.* **2013**, *5* (10), 830–834.

(44) Smith, B. J.; Dichtel, W. R. Mechanistic Studies of Two-Dimensional Covalent Organic Frameworks Rapidly Polymerized from Initially Homogenous Conditions. *J. Am. Chem. Soc.* **2014**, *136* (24), 8783–8789.

(45) Matsumoto, M.; Dasari, R. R.; Ji, W.; Feriante, C. H.; Parker, T. C.; Marder, S. R.; Dichtel, W. R. Rapid, Low Temperature Formation of Imine-Linked Covalent Organic Frameworks Catalyzed by Metal Triflates. *J. Am. Chem. Soc.* **2017**, *139* (14), 4999–5002.

(46) Karak, S.; Kandambeth, S.; Biswal, B. P.; Sasmal, H. S.; Kumar, S.; Pachfule, P.; Banerjee, R. Constructing Ultraporous Covalent Organic Frameworks in Seconds via an Organic Terracotta Process. *J. Am. Chem. Soc.* **2017**, *139* (5), 1856–1862.

(47) Zhao, Y.; Guo, L.; Gándara, F.; Ma, Y.; Liu, Z.; Zhu, C.; Lyu, H.; Trickett, C. A.; Kapustin, E. A.; Terasaki, O.; et al. A Synthetic Route for Crystals of Woven Structures, Uniform Nanocrystals, and Thin Films of Imine Covalent Organic Frameworks. *J. Am. Chem. Soc.* **2017**, *139* (37), 13166–13172.

(48) Vitaku, E.; Dichtel, W. R. Synthesis of 2D Imine-Linked Covalent Organic Frameworks through Formal Transimination Reactions. *J. Am. Chem. Soc.* **2017**, *139* (37), 12911–12914.

(49) Guan, X.; Ma, Y.; Li, H.; Yusran, Y.; Xue, M.; Fang, Q.; Yan, Y.; Valtchev, V.; Qiu, S. Fast, Ambient Temperature and Pressure Ionothermal Synthesis of Three-Dimensional Covalent Organic Frameworks. *J. Am. Chem. Soc.* **2018**, jacs.8b01320.

(50) Jiang, J.; Zhao, Y.; Yaghi, O. M. Covalent Chemistry beyond Molecules. *J. Am. Chem. Soc.* **2016**, *138* (10), 3255–3265.

(51) Tilford, R. W.; Mugavero, S. J.; Pellechia, P. J.; Lavigne, J. J. Tailoring Microporosity in Covalent Organic Frameworks. *Adv. Mater.* **2008**, *20* (14), 2741–2746.

(52) Chandra, S.; Kundu, T.; Kandambeth, S.; Babarao, R.; Marathe, Y.; Kunjir, S. M.; Banerjee, R. Phosphoric Acid Loaded Azo (-N═N-) Based Covalent Organic Framework for Proton Conduction. *J. Am. Chem. Soc.* **2014**, *136* (18), 6570–6573.

(53) Lin, S.; Diercks, C. S.; Zhang, Y.-B.; Kornienko, N.; Nichols, E. M.; Zhao, Y.; Paris, A. R.; Kim, D.; Yang, P.; Yaghi, O. M.; et al. Covalent Organic Frameworks Comprising Cobalt Porphyrins for Catalytic CO2 Reduction in Water. *Science* **2015**, *349* (6253), 1208–1213.

(54) Ding, X.; Guo, J.; Feng, X.; Honsho, Y.; Guo, J.; Seki, S.; Maitarad, P.; Saeki, A.; Nagase, S.; Jiang, D. Synthesis of Metallophthalocyanine Covalent Organic Frameworks That Exhibit High Carrier Mobility and Photoconductivity. *Angew. Chemie Int. Ed.* **2011**, *50* (6), 1289–1293.

(55) Ding, S.-Y.; Gao, J.; Wang, Q.; Zhang, Y.; Song, W.-G.; Su, C.-Y.; Wang, W. Construction of Covalent Organic Framework for Catalysis: Pd/COF-LZU1 in Suzuki–Miyaura Coupling Reaction. *J. Am. Chem. Soc.* **2011**, *133* (49), 19816–19822.

(56) Huang, N.; Krishna, R.; Jiang, D. Tailor-Made Pore Surface Engineering in Covalent Organic Frameworks: Systematic Functionalization for Performance Screening. *J. Am. Chem. Soc.* **2015**, *137* (22), 7079–7082.

(57) Xu, H.; Gao, J.; Jiang, D. Stable, Crystalline, Porous, Covalent Organic Frameworks as a Platform for Chiral Organocatalysts. *Nat. Chem.* **2015**, *7* (11), 905–912.

(58) El-Kaderi, H. M.; Hunt, J. R.; Mendoza-Cortés, J. L.; Côté, A. P.; Taylor, R. E.; O'Keeffe, M.; Yaghi, O. M. Designed Synthesis of 3D Covalent Organic Frameworks. *Science* **2007**, *316* (5822), 268–272.

(59) Lukose, B.; Kuc, A.; Heine, T. The Structure of Layered Covalent-Organic Frameworks. *Chem. - A Eur. J.* **2011**, *17* (8), 2388–2392.

(60) Spitler, E. L.; Koo, B. T.; Novotney, J. L.; Colson, J. W.; Uribe-Romo, F. J.; Gutierrez, G. D.; Clancy, P.; Dichtel, W. R. A 2D Covalent Organic Framework with 4.7-Nm Pores and Insight into Its Interlayer Stacking. *J. Am. Chem. Soc.* **2011**, *133* (48), 19416–19421.

(61) Chen, X.; Addicoat, M.; Irle, S.; Nagai, A.; Jiang, D. Control of Crystallinity and Porosity of Covalent Organic Frameworks by Managing Interlayer Interactions Based on Self-Complementary π-Electronic Force. *J. Am. Chem. Soc.* **2013**, *135* (2), 546–549.

(62) Alahakoon, S. B.; McCandless, G. T.; Karunathilake, A. A. K.; Thompson, C. M.; Smaldone, R. A. Enhanced Structural Organization in Covalent Organic Frameworks Through Fluorination. *Chem. - A Eur. J.* **2017**, *23* (18), 4255–4259.

(63) Vyas, V. S.; Haase, F.; Stegbauer, L.; Savasci, G.; Podjaski, F.; Ochsenfeld, C.; Lotsch, B. V. A Tunable Azine Covalent Organic Framework Platform for Visible Light-Induced Hydrogen Generation. *Nat. Commun.* **2015**, *6*, 8508.

(64) Zhang, Y.; Su, J.; Furukawa, H.; Yun, Y.; Gándara, F.; Duong, A.; Zou, X.; Yaghi, O. M. Single-Crystal Structure of a Covalent Organic Framework. *J. Am. Chem. Soc.* **2013**, *135* (44), 16336–16339.

(65) Kandambeth, S.; Shinde, D. B.; Panda, M. K.; Lukose, B.; Heine, T.; Banerjee, R. Enhancement of Chemical Stability and Crystallinity in Porphyrin-Containing Covalent Organic Frameworks by Intramolecular Hydrogen Bonds. *Angew. Chemie Int. Ed.* **2013**, *52* (49), 13052–13056.

(66) Li, Z.; Feng, X.; Zou, Y.; Zhang, Y.; Xia, H.; Liu, X.; Mu, Y. A 2D Azine-Linked Covalent Organic Framework for Gas Storage Applications. *Chem. Commun.* **2014**, *50* (89), 13825–13828.

(67) Li, Z.; Zhi, Y.; Feng, X.; Ding, X.; Zou, Y.; Liu, X.; Mu, Y. An Azine-Linked Covalent Organic Framework: Synthesis, Characterization and Efficient Gas Storage. *Chem. - A Eur. J.* **2015**, *21* (34), 12079–12084.

(68) Kalidindi, S. B.; Oh, H.; Hirscher, M.; Esken, D.; Wiktor, C.; Turner, S.; Van Tendeloo, G.; Fischer, R. a. Metal@COFs: Covalent Organic Frameworks as Templates for Pd Nanoparticles and Hydrogen Storage Properties of Pd@COF-102 Hybrid Material. *Chem. - A Eur. J.* **2012**, *18* (35), 10848–10856.

(69) Merí-Bofí, L.; Royuela, S.; Zamora, F.; Ruiz-González, M. L.; Segura, J. L.; Muñoz-Olivas, R.; Mancheño, M. J. Thiol Grafted Imine-Based Covalent Organic Frameworks for Water Remediation through Selective Removal of Hg(<scp>ii</Scp>). *J. Mater. Chem. A* **2017**, *5* (34), 17973–17981.

(70) Xu, H.; Tao, S.; Jiang, D. Proton Conduction in Crystalline and Porous Covalent Organic Frameworks. *Nat. Mater.* **2016**, *15* (7), 722–726.

(71) Jin, E.; Asada, M.; Xu, Q.; Dalapati, S.; Addicoat, M. A.; Brady, M. A.; Xu, H.; Nakamura, T.; Heine, T.; Chen, Q.; et al. Two-Dimensional Sp 2 Carbon–conjugated Covalent Organic Frameworks. *Science* **2017**, *357* (6352), 673–676.

(72) Bendikov, M.; Wudl, F.; Perepichka, D. F. Tetrathiafulvalenes, Oligoacenenes, and Their Buckminsterfullerene Derivatives: The Brick and Mortar of Organic Electronics. *Chem. Rev.* **2004**, *104* (11), 4891–4946.

(73) Cai, S.-L.; Zhang, Y.-B.; Pun, A. B.; He, B.; Yang, J.; Toma, F. M.; Sharp, I. D.; Yaghi, O. M.; Fan, J.; Zheng, S.-R.; et al. Tunable Electrical Conductivity in Oriented Thin Films of Tetrathiafulvalene-Based Covalent Organic Framework. *Chem. Sci.* **2014**, *5* (12), 4693–4700.

(74) Shinde, D. B.; Kandambeth, S.; Pachfule, P.; Kumar, R. R.; Banerjee, R. Bifunctional Covalent Organic Frameworks with Two Dimensional Organocatalytic Micropores. *Chem. Commun.* **2015**, *51* (2), 310–313.

(75) Pachfule, P.; Acharjya, A.; Roeser, J.; Langenhahn, T.; Schwarze, M.; Schomäcker, R.; Thomas, A.; Schmidt, J. Diacetylene Functionalized Covalent Organic Framework (COF) for Photocatalytic Hydrogen Generation. *J. Am. Chem. Soc.* **2018**, *140* (4), 1423–1427.

(76) Stegbauer, L.; Schwinghammer, K.; Lotsch, B. V. A Hydrazone-Based Covalent Organic Framework for Photocatalytic Hydrogen Production. *Chem. Sci.* **2014**, *5* (7), 2789–2793.

(77) Lin, G.; Ding, H.; Yuan, D.; Wang, B.; Wang, C. A Pyrene-Based, Fluorescent Three-Dimensional Covalent Organic Framework. *J. Am. Chem. Soc.* **2016**, *138* (10), 3302–3305.

(78) Wan, S.; Guo, J.; Kim, J.; Ihee, H.; Jiang, D. A Belt-Shaped, Blue Luminescent, and Semiconducting Covalent Organic Framework. *Angew. Chemie Int. Ed.* **2008**, *47* (46), 8826–8830.

(79) Crowe, J. W.; Baldwin, L. A.; McGrier, P. L. Luminescent Covalent Organic Frameworks Containing a Homogeneous and Heterogeneous Distribution of Dehydrobenzoannulene Vertex Units. *J. Am. Chem. Soc.* **2016**, *138* (32), 10120–10123.

(80) Dogru, M.; Handloser, M.; Auras, F.; Kunz, T.; Medina, D.; Hartschuh, A.; Knochel, P.; Bein, T. A Photoconductive Thienothiophene-Based Covalent Organic Framework Showing Charge Transfer Towards Included Fullerene. *Angew. Chemie Int. Ed.* **2013**, *52* (10), 2920–2924.

(81) Jin, S.; Supur, M.; Addicoat, M.; Furukawa, K.; Chen, L.; Nakamura, T.; Fukuzumi, S.; Irle, S.; Jiang, D. Creation of Superheterojunction Polymers via Direct Polycondensation: Segregated and Bicontinuous Donor–Acceptor π-Columnar Arrays

in Covalent Organic Frameworks for Long-Lived Charge Separation. *J. Am. Chem. Soc.* **2015**, *137* (24), 7817–7827.

(82) Mei, J.; Diao, Y.; Appleton, A. L.; Fang, L.; Bao, Z. Integrated Materials Design of Organic Semiconductors for Field-Effect Transistors. *J. Am. Chem. Soc.* **2013**, *135* (18), 6724–6746.

(83) Vazquez-Molina, D. A.; Mohammad-Pour, G. S.; Lee, C.; Logan, M. W.; Duan, X.; Harper, J. K.; Uribe-Romo, F. J. Mechanically Shaped Two-Dimensional Covalent Organic Frameworks Reveal Crystallographic Alignment and Fast Li-Ion Conductivity. *J. Am. Chem. Soc.* **2016**, *138* (31), 9767–9770.

(84) Zwaneveld, N. A. A.; Pawlak, R.; Abel, M.; Catalin, D.; Gigmes, D.; Bertin, D.; Porte, L. Organized Formation of 2D Extended Covalent Organic Frameworks at Surfaces. *J. Am. Chem. Soc.* **2008**, *130* (21), 6678–6679.

(85) Liu, X.-H.; Guan, C.-Z.; Ding, S.-Y.; Wang, W.; Yan, H.-J.; Wang, D.; Wan, L.-J. On-Surface Synthesis of Single-Layered Two-Dimensional Covalent Organic Frameworks via Solid-Vapor Interface Reactions. *J. Am. Chem. Soc.* **2013**, *135* (28), 10470–10474.

(86) Colson, J. W.; Woll, A. R.; Mukherjee, A.; Levendorf, M. P.; Spitler, E. L.; Shields, V. B.; Spencer, M. G.; Park, J.; Dichtel, W. R. Oriented 2D Covalent Organic Framework Thin Films on Single-Layer Graphene. *Science* **2011**, *332* (6026), 228–231.

(87) Medina, D. D.; Werner, V.; Auras, F.; Tautz, R.; Dogru, M.; Schuster, J.; Linke, S.; Döblinger, M.; Feldmann, J.; Knochel, P.; et al. Oriented Thin Films of a Benzodithiophene Covalent Organic Framework. *ACS Nano* **2014**, *8* (4), 4042–4052.

(88) Gou, X.; Zhang, Q.; Wu, Y.; Zhao, Y.; Shi, X.; Fan, X.; Huang, L.; Lu, G. Preparation and Engineering of Oriented 2D Covalent Organic Framework Thin Films. *RSC Adv.* **2016**, *6* (45), 39198–39203.

(89) Colson, J. W.; Mann, J. A.; DeBlase, C. R.; Dichtel, W. R. Patterned Growth of Oriented 2D Covalent Organic Framework Thin Films on Single-Layer Graphene. *J. Polym. Sci. Part A Polym. Chem.* **2015**, *53* (2), 378–384.

(90) Bisbey, R. P.; DeBlase, C. R.; Smith, B. J.; Dichtel, W. R. Two-Dimensional Covalent Organic Framework Thin Films Grown in Flow. *J. Am. Chem. Soc.* **2016**, *138* (36), 11433–11436.

(91) Payamyar, P.; Kaja, K.; Ruiz-Vargas, C.; Stemmer, A.; Murray, D. J.; Johnson, C. J.; King, B. T.; Schiffmann, F.; Vandevondele, J.; Renn, A.; et al. Synthesis of a Covalent Monolayer Sheet by Photochemical Anthracene Dimerization at the Air/Water Interface and Its Mechanical Characterization by AFM Indentation. *Adv. Mater.* **2014**, *26* (13), 2052–2058.

(92) Murray, D. J.; Patterson, D. D.; Payamyar, P.; Bhola, R.; Song, W.; Lackinger, M.; Schlüter, A. D.; King, B. T. Large Area Synthesis of a Nanoporous Two-Dimensional Polymer at the Air/Water Interface. *J. Am. Chem. Soc.* **2015**, *137* (10), 3450–3453.

(93) Dai, W.; Shao, F.; Szczerbiński, J.; McCaffrey, R.; Zenobi, R.; Jin, Y.; Schlüter, A. D.; Zhang, W. Synthesis of a Two-Dimensional Covalent Organic Monolayer through Dynamic Imine Chemistry at the Air/Water Interface. *Angew. Chemie Int. Ed.* **2016**, *55* (1), 213–217.

(94) Feldblyum, J. I.; McCreery, C. H.; Andrews, S. C.; Kurosawa, T.; Santos, E. J. G.; Duong, V.; Fang, L.; Ayzner, A. L.; Bao, Z. Few-Layer, Large-Area, 2D Covalent Organic Framework Semiconductor Thin Films. *Chem. Commun.* **2015**, *51* (73), 13894–13897.

(95) Dey, K.; Pal, M.; Rout, K. C.; Kunjattu H, S.; Das, A.; Mukherjee, R.; Kharul, U. K.; Banerjee, R. Selective Molecular Separation by Interfacially Crystallized Covalent Organic Framework Thin Films. *J. Am. Chem. Soc.* **2017**, *139* (37), 13083–13091.

(96) Matsumoto, M.; Valentino, L.; Stiehl, G. M.; Balch, H. B.; Corcos, A. R.; Wang, F.; Ralph, D. C.; Mariñas, B. J.; Dichtel, W. R. Lewis-Acid-Catalyzed Interfacial Polymerization of Covalent Organic Framework Films. *Chem* **2018**, *4* (2), 308–317.

(97) Berlanga, I.; Ruiz-González, M. L.; González-Calbet, J. M.; Fierro, J. L. G.; Mas-Ballesté, R.; Zamora, F. Delamination of Layered Covalent Organic Frameworks. *Small* **2011**, *7* (9), 1207–1211.

(98) Bunck, D. N.; Dichtel, W. R. Bulk Synthesis of Exfoliated Two-Dimensional Polymers Using Hydrazone-Linked Covalent Organic Frameworks. *J. Am. Chem. Soc.* **2013**, *135* (40), 14952–14955.

(99) Backes, C.; Higgins, T. M.; Kelly, A.; Boland, C.; Harvey, A.; Hanlon, D.; Coleman, J. N. Guidelines for Exfoliation, Characterisation and Processing of Layered Materials Produced by Liquid Exfoliation. *Chem. Mater.* **2016**, acs.chemmater.6b03335.

(100) Novoselov, K. S.; Jiang, D.; Schedin, F.; Booth, T. J.; Khotkevich, V. V; Morozov, S. V; Geim, A. K. Two-Dimensional Atomic Crystals. *Proc. Natl. Acad. Sci.* **2005**, *102* (30), 10451–10453.

(101) Chandra, S.; Kandambeth, S.; Biswal, B. P.; Lukose, B.; Kunjir, S. M.; Chaudhary, M.; Babarao, R.; Heine, T.; Banerjee, R. Chemically Stable Multilayered Covalent Organic Nanosheets from Covalent Organic Frameworks via Mechanical Delamination. *J. Am. Chem. Soc.* **2013**, *135* (47), 17853–17861.

(102) Khayum, M. A.; Kandambeth, S.; Mitra, S.; Nair, S. B.; Das, A.; Nagane, S. S.; Mukherjee, R.; Banerjee, R. Chemically Delaminated Free-Standing Ultrathin Covalent Organic Nanosheets. *Angew. Chemie Int. Ed.* **2016**, *55* (50), 15604–15608.

(103) Yang, C.-X.; Liu, C.; Cao, Y.-M.; Yan, X.-P. Facile Room-Temperature Solution-Phase Synthesis of a Spherical Covalent Organic Framework for High-Resolution Chromatographic Separation. *Chem. Commun.* **2015**, *51* (61), 12254–12257.

(104) Kandambeth, S.; Venkatesh, V.; Shinde, D. B.; Kumari, S.; Halder, A.; Verma, S.; Banerjee, R. Self-Templated Chemically Stable Hollow Spherical Covalent Organic Framework. *Nat. Commun.* **2015**, *6* (1), 6786.

(105) Pachfule, P.; Kandmabeth, S.; Mallick, A.; Banerjee, R. Hollow Tubular Porous Covalent Organic Framework (COF) Nanostructures. *Chem. Commun.* **2015**, *1*, 11717–11720.

(106) Gole, B.; Stepanenko, V.; Rager, S.; Grüne, M.; Medina, D. D.; Bein, T.; Würthner, F.; Beuerle, F. Microtubular Self-Assembly of Covalent Organic Frameworks. *Angew. Chemie Int. Ed.* **2018**, *57* (3), 846–850.

(107) Smith, B. J.; Parent, L. R.; Overholts, A. C.; Beaucage, P. A.; Bisbey, R. P.; Chavez, A. D.; Hwang, N.; Park, C.; Evans, A. M.; Gianneschi, N. C.; et al. Colloidal Covalent Organic Frameworks. *ACS Cent. Sci.* **2017**, *3* (1), 58–65.

(108) Zhang, G.; Tsujimoto, M.; Packwood, D.; Duong, N. T.; Nishiyama, Y.; Kadota, K.; Kitagawa, S.; Horike, S. Construction of a Hierarchical Architecture of Covalent Organic Frameworks via a Postsynthetic Approach. *J. Am. Chem. Soc.* **2018**, *140* (7), 2602–2609.

(109) Xu, F.; Jin, S.; Zhong, H.; Wu, D.; Yang, X.; Chen, X.; Wei, H.; Fu, R.; Jiang, D. Electrochemically Active, Crystalline, Mesoporous Covalent Organic Frameworks on Carbon Nanotubes for Synergistic Lithium-Ion Battery Energy Storage. *Sci. Rep.* **2015**, *5*, 8225.

(110) Shi, X.; Yao, Y.; Xu, Y.; Liu, K.; Zhu, G.; Chi, L.; Lu, G. Imparting Catalytic Activity to a Covalent Organic Framework Material by Nanoparticle Encapsulation. *ACS Appl. Mater. Interfaces* **2017**, *9* (8), 7481–7488.

(111) Tan, J.; Namuangruk, S.; Kong, W.; Kungwan, N.; Guo, J.; Wang, C. Manipulation of Amorphous-to-Crystalline Transformation: Towards the Construction of Covalent Organic Framework Hybrid Microspheres with NIR Photothermal Conversion Ability. *Angew. Chemie Int. Ed.* **2016**, *55* (45), 13979–13984.

(112) Li, Y.; Yang, C.-X.; Yan, X.-P. Controllable Preparation of Core–shell Magnetic Covalent-Organic Framework Nanospheres for Efficient Adsorption and

Removal of Bisphenols in Aqueous Solution. *Chem. Commun.* **2017**, *53* (16), 2511–2514.

(113) Wang, L.-L.; Yang, C.-X.; Yan, X.-P. In Situ Growth of Covalent Organic Framework Shells on Silica Microspheres for Application in Liquid Chromatography. *Chempluschem* **2017**, *82* (6), 933–938.

(114) Sun, D.; Jang, S.; Yim, S.-J.; Ye, L.; Kim, D.-P. Metal Doped Core-Shell Metal-Organic Frameworks@Covalent Organic Frameworks (MOFs@COFs) Hybrids as a Novel Photocatalytic Platform. *Adv. Funct. Mater.* **2018**, *28* (13), 1707110.

(115) Sun, J.; Klechikov, A.; Moise, C.; Prodana, M.; Enachescu, M.; Talyzin, A. V. A Molecular Pillar Approach To Grow Vertical Covalent Organic Framework Nanosheets on Graphene: Hybrid Materials for Energy Storage. *Angew. Chemie Int. Ed.* **2018**, *57* (4), 1034–1038.

(116) Biswal, B. P.; Chaudhari, H. D.; Banerjee, R.; Kharul, U. K. Chemically Stable Covalent Organic Framework (COF)-Polybenzimidazole Hybrid Membranes: Enhanced Gas Separation through Pore Modulation. *Chem. - A Eur. J.* **2016**, *22* (14), 4695–4699.

(117) Rodenas, T.; Luz, I.; Prieto, G.; Seoane, B.; Miro, H.; Corma, A.; Kapteijn, F.; Llabrés i Xamena, F. X.; Gascon, J. Metal–organic Framework Nanosheets in Polymer Composite Materials for Gas Separation. *Nat. Mater.* **2015**, *14* (1), 48–55.

(118) Yang, H.; Wu, H.; Yao, Z.; Shi, B.; Xu, Z.; Cheng, X.; Pan, F.; Liu, G.; Jiang, Z.; Cao, X. Functionally Graded Membranes from Nanoporous Covalent Organic Frameworks for Highly Selective Water Permeation. *J. Mater. Chem. A* **2018**, *6* (2), 583–591.

(119) Ying, Y.; Liu, D.; Ma, J.; Tong, M.; Zhang, W.; Huang, H.; Yang, Q.; Zhong, C. A GO-Assisted Method for the Preparation of Ultrathin Covalent Organic Framework Membranes for Gas Separation. *J. Mater. Chem. A* **2016**, *4* (35), 13444–13449.

(120) Valentino, L.; Matsumoto, M.; Dichtel, W. R.; Mariñas, B. J. Development and Performance Characterization of a Polyimine Covalent Organic Framework Thin-Film Composite Nanofiltration Membrane. *Environ. Sci. Technol.* **2017**, *51* (24), 14352–14359.

(121) Lu, H.; Wang, C.; Chen, J.; Ge, R.; Leng, W.; Dong, B.; Huang, J.; Gao, Y. A Novel 3D Covalent Organic Framework Membrane Grown on a Porous α-Al 2 O 3 Substrate under Solvothermal Conditions. *Chem. Commun.* **2015**, *51* (85), 15562–15565.

(122) Fu, J.; Das, S.; Xing, G.; Ben, T.; Valtchev, V.; Qiu, S. Fabrication of COF-MOF Composite Membranes and Their Highly Selective Separation of H 2 /CO 2. *J. Am. Chem. Soc.* **2016**, *138* (24), 7673–7680.

(123) Kandambeth, S.; Biswal, B. P.; Chaudhari, H. D.; Rout, K. C.; Kunjattu H., S.; Mitra, S.; Karak, S.; Das, A.; Mukherjee, R.; Kharul, U. K.; et al. Selective Molecular Sieving in Self-Standing Porous Covalent-Organic-Framework Membranes. *Adv. Mater.* **2017**, *29* (2), 1603945.

(124) Calik, M.; Auras, F.; Salonen, L. M.; Bader, K.; Grill, I.; Handloser, M.; Medina, D. D.; Dogru, M.; Löbermann, F.; Trauner, D.; et al. Extraction of Photogenerated Electrons and Holes from a Covalent Organic Framework Integrated Heterojunction. *J. Am. Chem. Soc.* **2014**, *136* (51), 17802–17807.

(125) Mulzer, C. R.; Shen, L.; Bisbey, R. P.; McKone, J. R.; Zhang, N.; Abruña, H. D.; Dichtel, W. R. Superior Charge Storage and Power Density of a Conducting Polymer-Modified Covalent Organic Framework. *ACS Cent. Sci.* **2016**, *2* (9), 667–673.

(126) Qian, H.-L.; Yang, C.-X.; Yan, X.-P. Bottom-up Synthesis of Chiral Covalent Organic Frameworks and Their Bound Capillaries for Chiral Separation. *Nat. Commun.* **2016**, *7*, 12104.

(127) Fan, H.; Gu, J.; Meng, H.; Knebel, A.; Caro, J. High-Flux Membranes Based on the Covalent Organic Framework COF-LZU1 for Selective Dye Separation by Nanofiltration. *Angew. Chemie Int. Ed.* **2018**, *57* (15), 4083–4087.

Chapter 2: Room temperature synthesis and patterning of COFs

2.1. Introduction

Solvothermal reactions are the most widespread methods to obtain COFs, however, being able to carry out the process at room temperature and ambient pressure conveys numerous benefits, besides a lower energy consumption, it makes scalability easier, allows the study of reaction progress using uncomplicated procedures and opens the door to applying many processing techniques which have proven their effectiveness with other materials.

Some of these techniques are inkjet printing and lithographically-controlled wetting (LCW), which allow positioning of materials on surfaces with micro- o submicrometre resolution. Inkjet printing is widely known for having been the dominant technology for document printing with desktop accessories at offices and homes for many years. Nonetheless, its possibilities are not limited to this mundane application, inks can contain molecules with properties beyond visible light absorption and the support over which the ink is casted does not necessarily have to be paper. Its advantages over other patterning alternatives are that it is a fast and simple technique that can be easily automatised and complex patterns can be effortlessly designed with a computer and directly transferred to virtually any substrate[1]. LCW is a technique that uses a stamp to restrict the regions of a substrate covered by solvent, therefore forcing the material that grows from the solution to replicate the pattern of the stamp. This way it is possible to cover extensive areas at once and use a broad range of solvents, including corrosive ones[2].

In this chapter, the first procedure for room temperature synthesis of imine-linked COFs and its application for creating patterns via inkjet printing and LCW are described.

2.2. Results and Discussion

For this work, an imine-based COF was chosen due to the higher stability they show compared to boron containing linkages and the possibility to modulate the reaction by varying the amount of acid catalyst. Among the vast variety of COFs with imine linkages, the then novel **COF-TAPB-BTCA** (Figure 2.1) was employed to test the feasibility of the approach.

COF-TAPB-BTCA was synthesised from the direct reaction between its two trigonal building blocks: 1,3,5-tris(4'-aminophenyl)benzene (**TAPB**) and 1,3,5-benzenetricarbaldehyde (**BTCA**). When the reaction was conducted by dissolving the precursors in *m*-cresol or dimethylsulfoxide (DMSO) in the presence of acetic acid at room temperature, a yellow gel was formed rapidly. The gel was solvent exchanged several times with tetrahydrofuran (THF) and methanol to yield a yellow solid that was dried in ambient conditions for 2 days prior to being degassed overnight at 150 ºC under vacuum. In order to distinguish the material prepared this

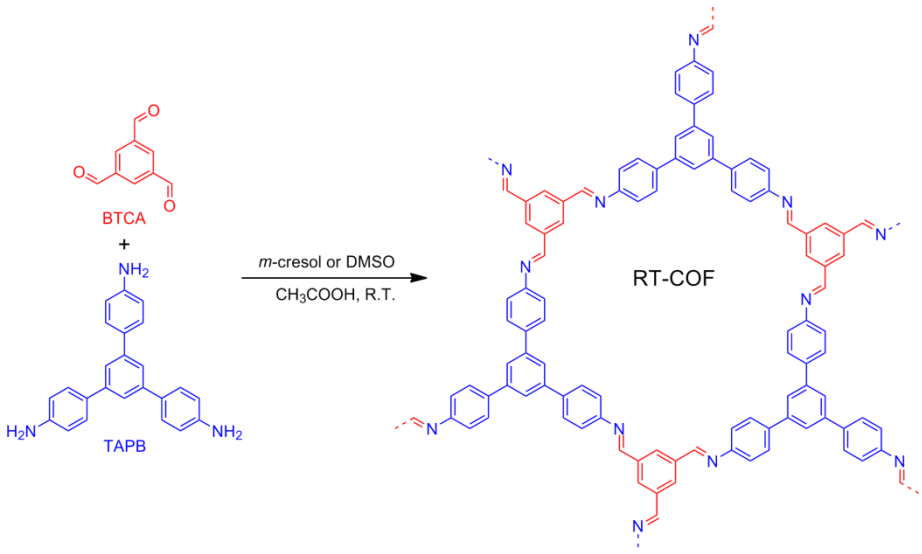

Figure 2.1. Scheme of the synthesis of **RT-COF** (**COF-TAPB-BTCA**).

way from the same structure obtained through a different procedure, it will be referred to as **RT-COF**.

The resulting powder was characterised with the aim of confirming if the intended material had been obtained. The complete insolubility of the solid in all common organic solvents (alkanes, alcohols, acetone, acetonitrile, ethyl acetate, amides, halogenated solvents or toluene, to name some), water, acids and bases made it impossible to use techniques that rely on analysing a solution of the compound, such as standard nuclear magnetic resonance (NMR), on the other hand, this also hinted towards the formation of a polymeric material with an extended network of covalent bonds.

Being therefore limited to solid state characterisation techniques, attenuated total reflectance Fourier transform infrared (ATR-FT-IR) spectroscopy was performed. As can be seen in Figure 2.2, the IR spectrum of **RT-COF** contains the majority of the bands from the building blocks, indicating that the C-C and C-H bonds that form the backbone of the monomers are preserved in the final product. Nevertheless, other features of the spectra are more revealing of the structure of the product. The strong and sharp bands between 3500 and 3200 cm^{-1} in the spectrum of the amine can be attributed to the stretching vibration of the N-H bonds, and its disappearance in the spectra of **RT-COF** indicate that these groups are not present in the product. The great reduction in the intensity of the highly active carbonyl stretching band at 1689 cm^{-1} means that most of the aldehydes have reacted, and the residual signal can be explained due to the presence of the unreacted groups in the borders of the crystallites. Finally, the appearance of the band at 1621 cm^{-1} proves the formation of imine bonds as it is generated by the C-N double bond stretch. These features are consistent with those reported previously for other imine-based COFs[3].

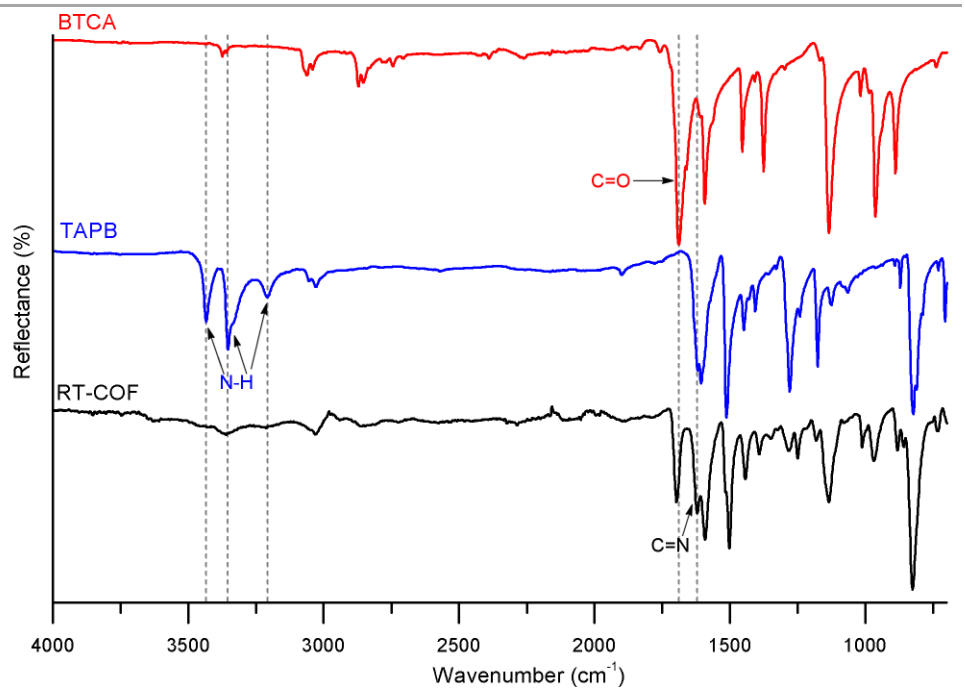

Figure 2.2. ATR-FT-IR spectra of **BTCA** (red), **TAPB** (blue) and **RT-COF** (black).

To further confirm the formation of imine bonds, solid state ^{13}C cross polarization magic angle spinning nuclear magnetic resonance (^{13}C CP-MAS NMR) was performed. The spectra in Figure 2.3 nicely fit with the condensation between the aldehyde and the amine to produce an imine as the resonance at 194.6 ppm present in the spectrum of the aldehyde, which corresponds to the carbon of the carbonyl group, is not in the spectrum of **RT-COF**, while the rest of the peaks from the building blocks are, even if some of them appear as shoulders due to the high degree of overlapping derived from the inherent broadening of signals in solid state NMR. Additionally, the new signal at 156.7 ppm matches with the chemical shift of imine carbons, corroborating that the condensation reaction has happened.

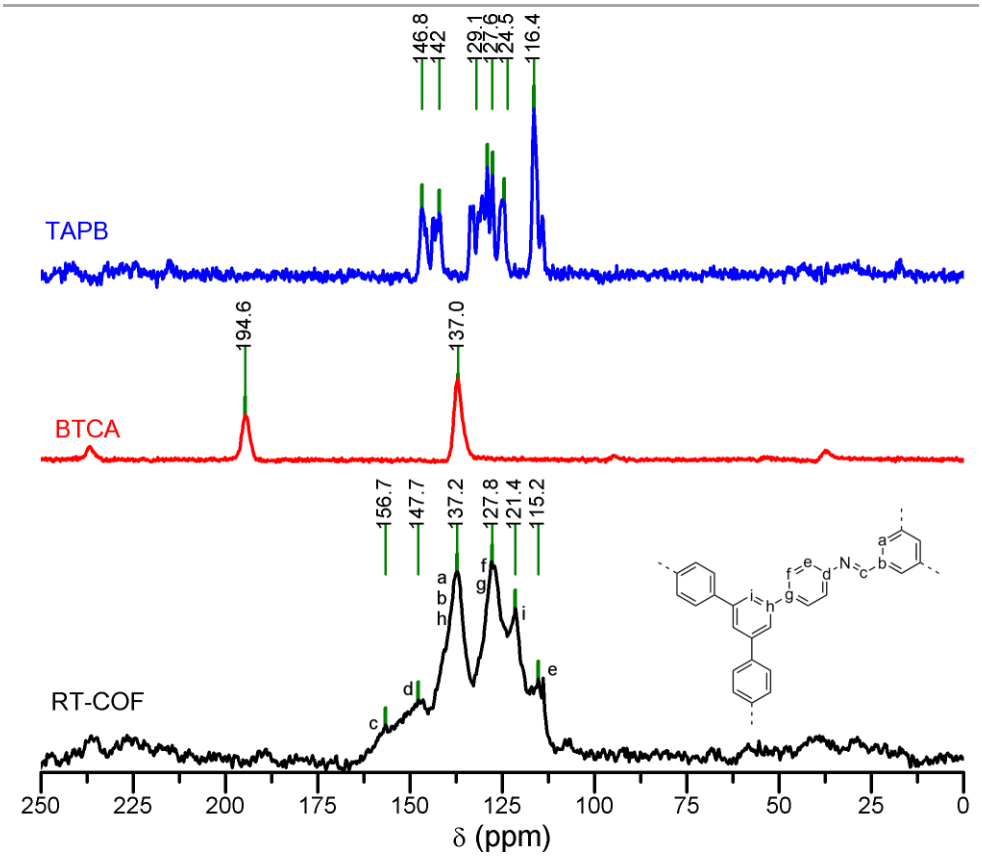

Figure 2.3. Solid state ^{13}C CP-MAS NMR spectra of **TAPB** (blue), **BTCA** (red) and **RT-COF** (black). The signals of RT-COF are assigned in the fragment of the structure at the right.

Even though spectroscopic data confirmed that the product of the room temperature reaction is an imine-linked material which chemical composition fits that of the target **COF-TAPB-BTCA**, it does not provide information about its structure. So, in order to rule out the possibility of the formation of an amorphous polyimine, grazing incidence X-ray diffraction (GIXRD) data of small pieces of **RT-COF** synthesised directly on silicon oxide was obtained (Figure 2.4a). It revealed that the solid obtained was

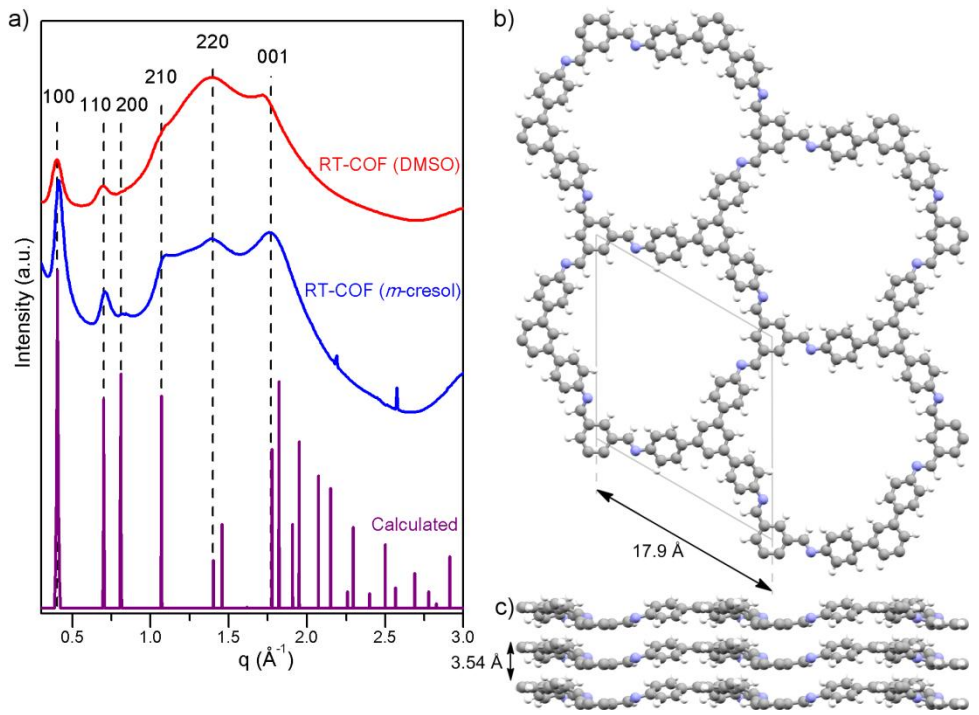

Figure 2.4. a) GIXRD patterns of **RT-COF** prepared in DMSO (red) and *m*-cresol (blue), and calculated from the simulated structure in b) (purple). b-c) Ball-and-stick representation of the simulated structure of **COF-TAPB-BTCA** viewed b) along the *c* axis and c) perpendicular to the *c* axis. The parameters of the unit cell are indicated in the corresponding views. Carbon, nitrogen and hydrogen atoms are represented as grey, blue and white spheres, respectively.

indeed **COF-TAPB-BTCA**, since it was not only crystalline, but also the experimental diffraction patterns matched well with the pattern simulated for the structure obtained by plane-wave density functional theory (DFT) calculations. It should also be noted that, even though both materials exhibited the same structure, the synthesis in *m*-cresol afforded a more crystalline solid; consequently, the following studies were done on samples prepared in *m*-cresol unless otherwise specified.

The proposed structure for **COF-TAPB-BTCA** consists on a trigonal unit cell with $a = b = 17.9$ Å and $c = 3.54$ Å (Figure 2.4b-c). This results in a layered structure following an AA eclipsed stacking sequence with a separation of 3.54 Å between layers. These layers are an extended network made by joining the building blocks with imine bonds forming hexagonal channels with a diameter of 11.9 Å.

Additional proof of the layered hexagonal structure can be obtained from the analysis of **RT-COF** using different microscopy techniques. SEM images (Figure 2.5a) show a morphology of aggregated flakes consistent with the layered structure. More importantly, it was possible to create a suspension of exfoliated flakes by ultrasonication of the gel in methanol. This allowed to study isolated individual flakes by atomic force microscopy (AFM) upon casting of the suspension on silicon oxide substrates. The images obtained (Figure 2.5b-c) show sheets with straight edges and sharp angles of approximately 60º and 120º, the lateral dimensions span over tens of micrometres and the thickness and steps are in a range between 4 and 30 nm, which is not rare since delaminating these materials down to single layers is not common[4].

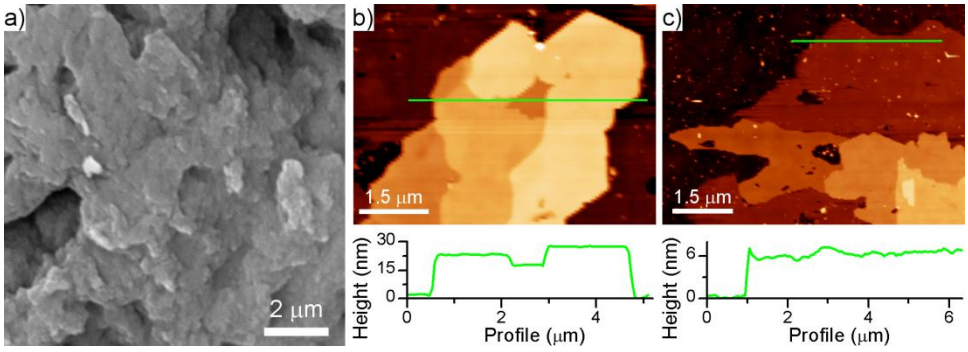

Figure 2.5. a) SEM image of **RT-COF**. b,c) AFM images of **RT-COF** on SiO_2, the height profiles corresponding to the lines drawn on the images are included below them.

TEM studies were also performed by casting on TEM grids the same suspension used for the AFM measurements. Despite the fast degradation of the material under the electron beam some useful information could be gathered. The most striking feature of Figure 2.6a are the Moiré patterns in region A, which can be originated by the overlapping of differently oriented crystallites. Moreover, areas like region B are crystalline nanodomains, that upon closer inspection (Figure 2.6b) reveal periodicities in the range of the pore dimensions and allow to infer the expected hexagonal symmetry, which is more clearly perceived in the fast Fourier transform (FFT) shown in Figure 2.6c. In general, long range order was not detected, which, apart from sample degradation, is expected because of the broad GIXRD peaks.

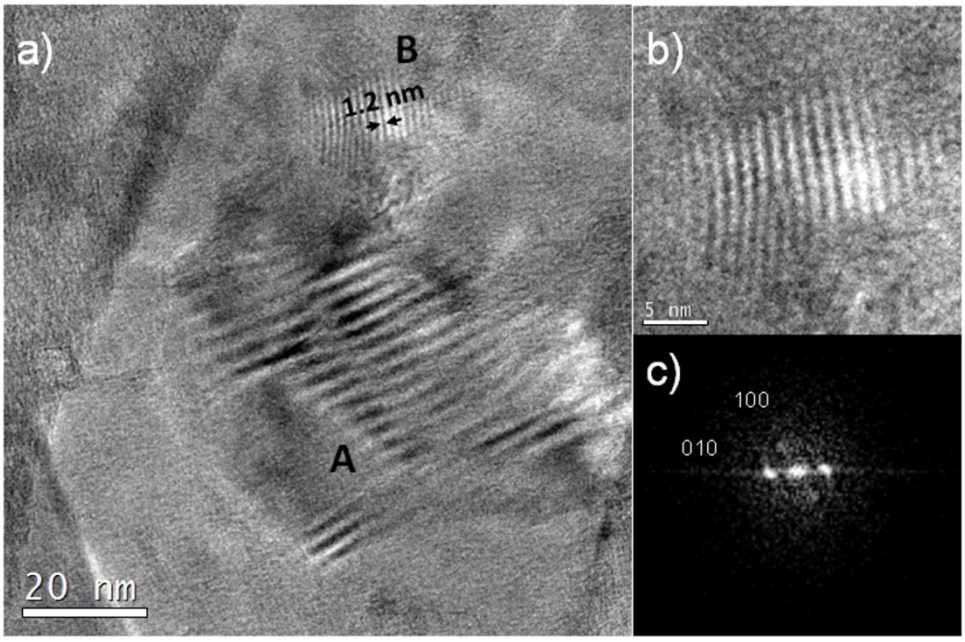

Figure 2.6. a) TEM image of **RT-COF** showing the presence of Moiré patterns (A) and nanodomains (B) of fringes of periodicity in the range of pore size. b) Enlarged image of region B. c) FFT of image b.

Since the presented data unequivocally confirms the formation of the framework, TGA studies were carried to unveil the thermal stability of the material and the presence of guest molecules in the pores with the ultimate goal of optimising an activation procedure for gas adsorption measurements. The TGA trace in Figure 2.7 shows that the COF is stable up to more than 400 ºC and that there is a weight loss of nearly 7.6 % of the initial mass. A first guess is that due to the expected porous nature of the material, ambient water is condensed in the pores. To confirm this hypothesis, elemental analyses of **RT-COF** prepared both in *m*-cresol and DMSO were performed. The results (see section A2.2.1, page 179) do not fit with the expected composition of the evacuated material ($C_{33}H_{21}N_3$), but rather with the formula for **RT-COF** with 2 trapped water molecules per unit cell. This agrees with the TGA, since the expected mass loss of that structure due to water evaporation would be 7.3 %.

Finally, to test the porosity of the room temperature synthesised **RT-COF**, nitrogen adsorption isotherms of the activated material were recorded at

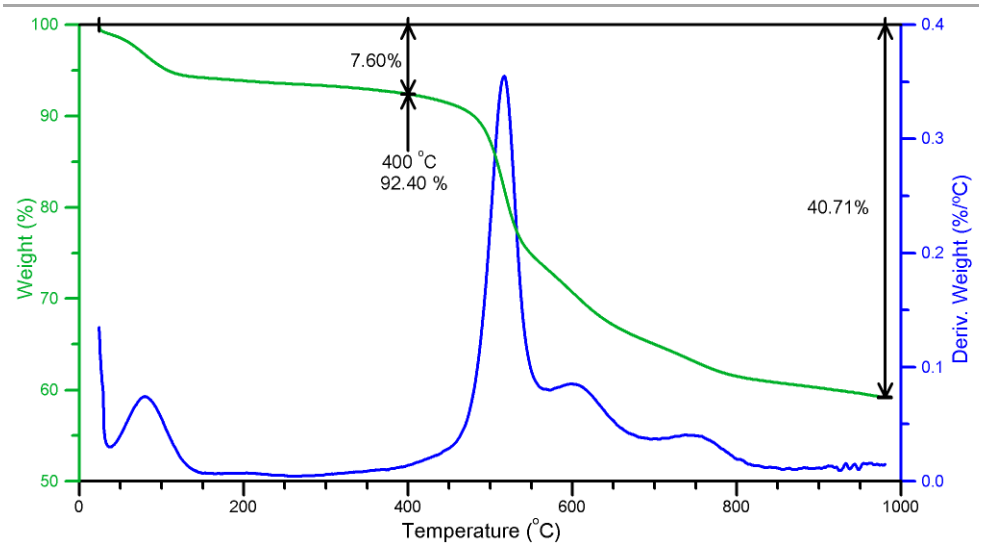

Figure 2.7. TGA trace of **RT-COF** synthesised in *m*-cresol.

77 K (Figure 2.8a). The surface area was calculated by fitting the data to the Brunauer-Emmet-Teller (BET) theory in the range p/p^0 = 0.05-0.3 and a value of 329 m^2 g^{-1} was obtained. This area, although not impressive, was close to other reported values of similar imine-linked COFs prepared using solvothermal methods[5–7]. Additionally, applying the Dubinin-Radushkevich equation to the adsorption branch, a pore volume of 0.224 cm^3 g^{-1} was calculated. To complete the study, CO_2 adsorption isotherms were measured at 195, 273 and 298 K (Figure 2.8b). They showed that the COF is porous to CO_2, and using the Clausius-Clapeyron equation with the data of the isotherms at 273 and 298 K it a the isosteric heat of adsorption of 16.4 kJ mol^{-1} was found at zero coverage, while it is comprised between 15.1 and 18.1 kJ mol^{-1} at high loadings (Figure 2.8c).

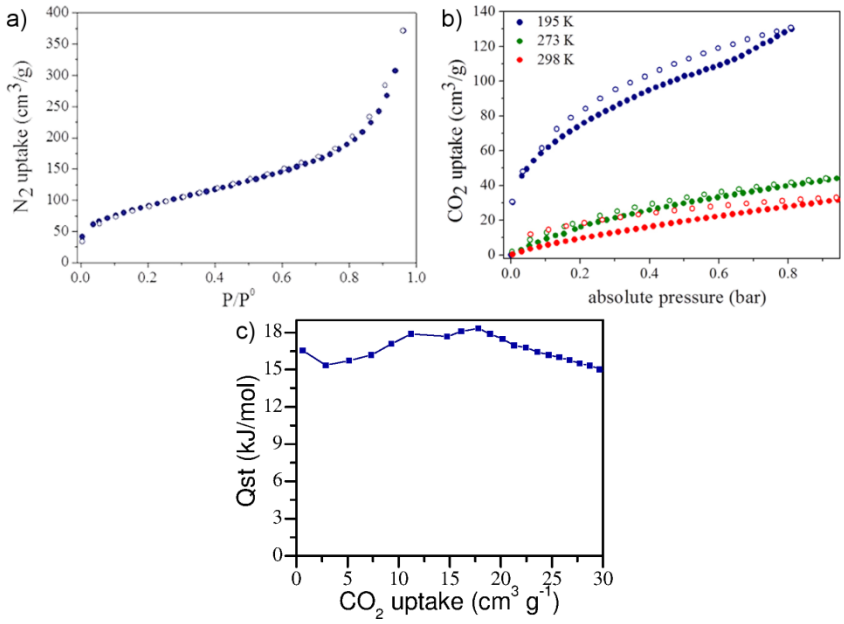

Figure 2.8. a) Nitrogen adsorption isotherm collected at 77 K on **RT-COF**. Filled dots: adsorption, empty dots: desorption. b) CO_2 isotherms collected at 195 (blue), 273 (green) and 298 K (red). c) Isosteric heat of adsorption of CO_2 on RT-COF.

These values are in the range reported for other imine-linked COFs without specific groups to interact with CO_2[8].

With all these data, it could be claimed that the reaction between **TAPB** and **BTCA** in *m*-cresol carried out in ambient conditions with acetic acid as a catalyst produced a porous COF. This was the first procedure to prepare macroscopic quantities of an imine-based COF, since previous reports only described on-surface synthesis of nanometre-thick layers[9].

Thorough studies to elucidate the reason behind these two solvents allowing the obtention of crystalline structures at room temperature in such a short time were not performed. However, it can be hypothesised that the formation of a gel instead of a powdery precipitate plays a significant role since diffusion in the gel should be easier and all the oligomers should be accessible to the solvent and dissolved molecules. This could be important as reversibility would not be confined to the outer surface of the aggregates, making the error correction process more efficient. Finally, the high concentration of acetic acid, the catalyst, lowers the energy barrier of the reaction allowing the reverse (hydrolysis) reaction to occur without the thermal energy available at higher temperatures.

Having developed a method to prepare COFs under mild conditions, many techniques usually not available for processing were at our disposal. Among them, two methodologies that allowed patterning on surfaces relying on the confinement of the reaction in small volumes of building block solutions and the precise and restricted positioning of these volumes on the substrate were chosen: Inkjet printing and LCW[10].

The LCW process is summarised in Figure 2.9. The first step is spreading a solution of the building blocks in *m*-cresol on a silicon oxide wafer (Figure 2.9a). Then, a poly(dimethylsiloxane) (PDMS) stamp is brought in contact with the solution and, due to capillary forces, menisci form and the

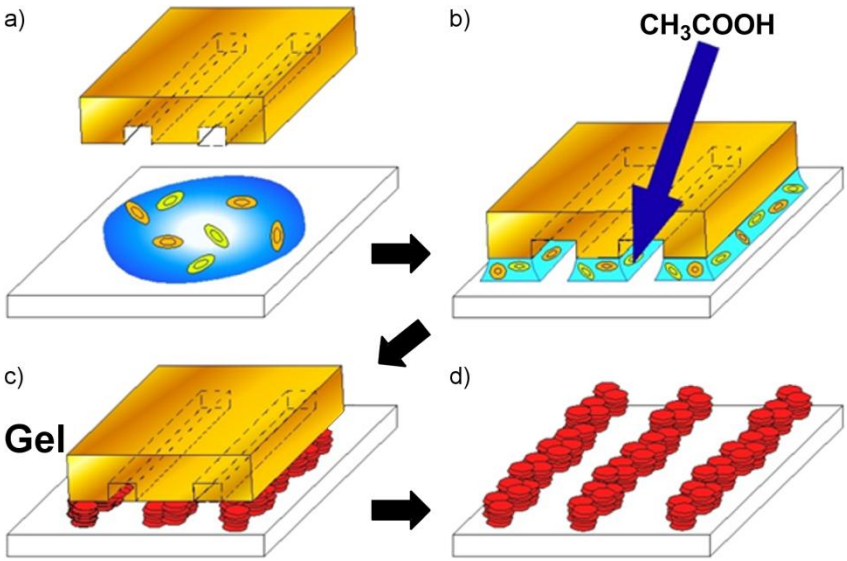

Figure 9. Scheme of the creation of **RT-COF** patterns via LCW.

solution is drawn towards the protrusions of the stamp (Figure 2.9b). Next, acetic acid is added from one of the sides of the stamp, polymerisation begins and the gel is formed in a few seconds (Figure 2.9c). Finally, when the stamp is removed, **RT-COF** has been formed following the shape of the protrusions (Figure 2.9d).

The stamps used to test the approach consisted of parallel stripes with a width of 1 μm. The result is shown in the optical microscopy images in Figure 2.10a-b, where the patterned growth of **RT-COF** according to the design of the stamp is noticeable. Smaller features could also be formed as evidenced by the SEM image in Figure 2.10c, in this case, a stamp with 500 nm wide stripes was used, and the transfer of the design onto the surface is still fairly accurate. Besides confirming the success of the patterning, the samples were analysed by GIXRD (Figure 2.10d), which revealed that the stripes were made of crystalline **RT-COF**. This corroborates that the structure of **RT-COF** is maintained when synthesised

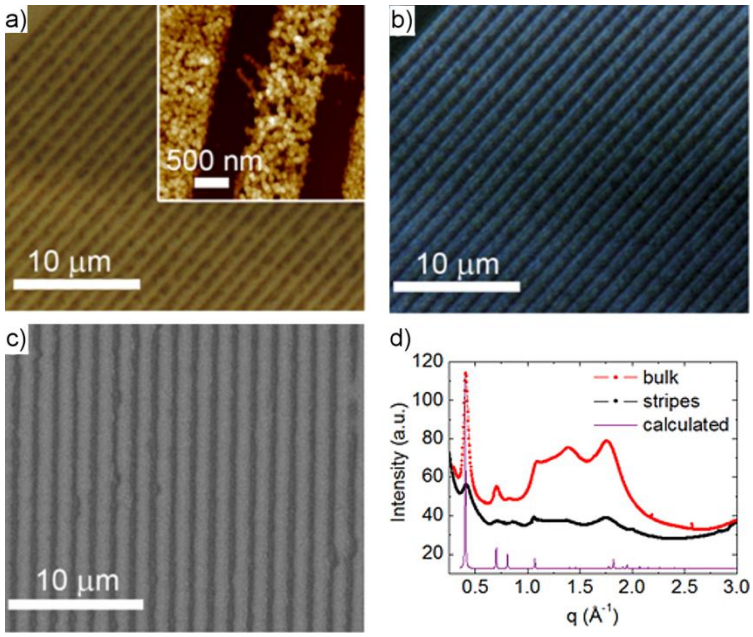

Figure 2.10. a) Bright-field optical image of 1 µm wide **RT-COF** stripes fabricated by LCW. The inset shows a representative AFM image showing the formation of characteristic **RT-COF** flakes. Z scale is 0–50 nm. b) Corresponding POM image. c) Representative SEM image of 500 nm wide RT-COF stripes fabricated by LCW. d) Radial integration of the 2D-GIXRD image collected from the 1 µm wide stripes (black) compared to the one obtained in the synthesis of bulk RT-COF (red) and to the one derived from the theoretical structure (violet).

and structured on surfaces and that the synthetic procedure is not limited to bulk synthesis. To obtain a better insight on the morphology of the material forming the stripes, they were investigated by AFM (inset in Figure 2.10a), showing that they are composed of small platelets with a diameter between 25 and 100 nm and a nearly homogeneous height of 37 nm. It is remarkable that the stripes showed no signs of degradation after several months as well as after treatment with water and alcohols.

The use of inkjet printing allowed the broadening of the scope of supports which could be functionalised with **RT-COF** patterns. Areas of 1 cm^2 could

be covered using an ink consisting in a stoichiometric mixture of **TAPB** and **BTCA** in DMSO which was expelled through the nozzles of the cartridge in the form of 10 pL droplets. Even though very complex or artistic designs can be created easily with this technology, a simple dot array was drawn. The pattern was printed on rigid silicon oxide wafers and flexible acetate sheets, obtaining evenly distributed dots of a uniform size with good resolution (Figure 2.11a-b). A closer inspection of these dots by SEM revealed that they were formed by small disc-shaped flakes (Figure 2.11c-d), as were the stripes obtained by LCW. The analysis by AFM revealed that, even though at first sight both substrates provided the same results, there were some significant differences in the morphology of **RT-COF** grown on silicon dioxide or acetate sheets. The flakes on silicon dioxide had a uniform thickness of 8 nm (Figure 2.11e) while the height of the platelets formed on acetate paper (Figure 2.11f) is in a range of 150-200 nm. This may be a consequence of the higher wettability of silicon dioxide, which causes the droplets to spread more than in the acetate sheets, thus, whereas the area covered by the droplet increases, its height diminishes, and the growth of the COF is confined in a thinner space, not allowing it to grow vertically. This possible explanation is also supported by the fact that the dots printed on silicon dioxide have a diameter of 70 μm while those on acetate sheets are smaller with a 40 μm diameter.

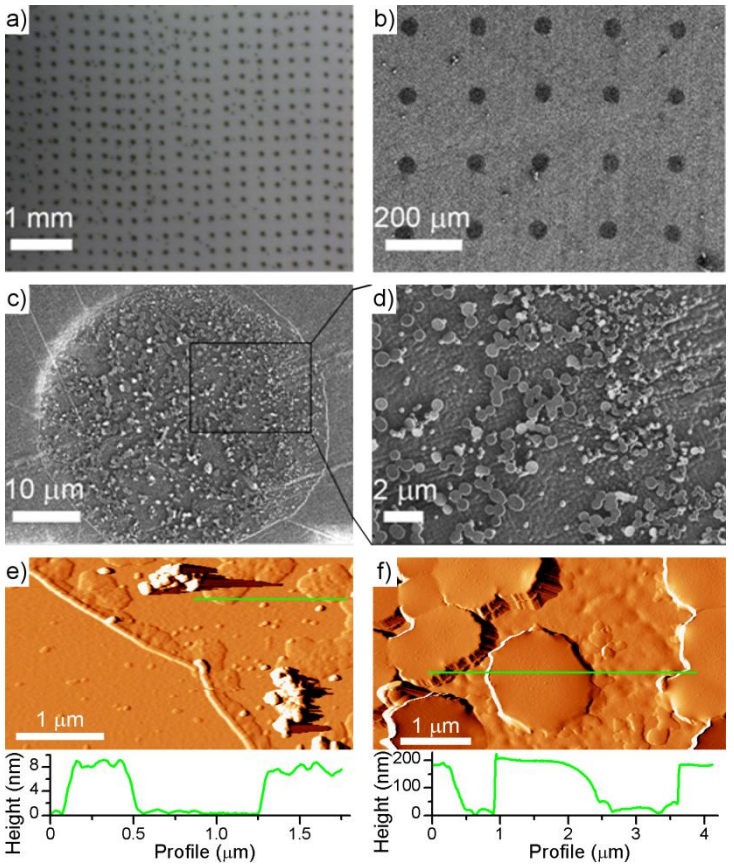

Figure 2.11. a) Representative optical image a 70 µm-in-diameter dot array of **RT-COF** on SiO_2 generated by an ink-jet printer. b) Representative SEM image of a 40 µm-in-diameter dot array of RT-COF on flexible acetate sheet generated by an ink-jet printer. c) SEM image of one of the dots on acetate sheet. d) Magnification of image c), showing the formation of the characteristic RT-COF flakes. e,f) AFM images of RT-COF printed on e) SiO_2 and f) acetate sheet and height profiles corresponding to the lines drawn on the images.

2.3. Conclusions

The work included in this chapter proved that it is possible to synthesise imine-linked COFs at room temperature, using **RT-COF** as an example. The simplicity of the procedure allowed to miniaturise the synthesis and apply inkjet printing and LCW techniques to the preparation of the COF, thus adding new alternatives for the processing of this type of materials. More specifically, these two techniques enable the creation micro- and sub-micrometre patterns on a variety of substrates.

2.3.1. Future prospects

The results presented here have enabled the development of several projects. On the one hand, the formation of the gel and the fast diffusion through it were used to functionalise **COF-TAPB-BTCA** with iron(III) acetylacetonate. The resulting material could be pyrolysed to yield porous nitrogen-doped graphene that can was used to build supercapacitors showing good performance[11]. On the other hand, in a project being currently developed, the inkjet printing technique is being used to cover porous membranes with a continuous COF layer of controlled thickness. These composite membranes are showing promising results in gas separation.

2.4. References

(1) *Inkjet-Based Micromanufacturing*; Korvink, J. G., Smith, P. J., Shin, D.-Y., Eds.; Wiley-VCH Verlag GmbH & Co. KGaA: Weinheim, Germany, 2012.

(2) Cavallini, M.; Gentili, D.; Greco, P.; Valle, F.; Biscarini, F. Micro- and Nanopatterning by Lithographically Controlled Wetting. *Nat. Protoc.* **2012**, *7* (9), 1668–1676.

(3) Uribe-Romo, F. J.; Hunt, J. R.; Furukawa, H.; Klöck, C.; O'Keeffe, M.; Yaghi, O. M. A Crystalline Imine-Linked 3-D Porous Covalent Organic Framework. *J. Am. Chem. Soc.* **2009**, *131*, 4570–4571.

(4) Berlanga, I.; Mas-Ballesté, R.; Zamora, F. Tuning Delamination of Layered Covalent Organic Frameworks through Structural Design. *Chem. Commun.* **2012**, *48* (64), 7976–7978.

(5) Ding, S.-Y.; Gao, J.; Wang, Q.; Zhang, Y.; Song, W.-G.; Su, C.-Y.; Wang, W. Construction of Covalent Organic Framework for Catalysis: Pd/COF-LZU1 in Suzuki–Miyaura Coupling Reaction. *J. Am. Chem. Soc.* **2011**, *133* (49), 19816–19822.

(6) Kandambeth, S.; Mallick, A.; Lukose, B.; Mane, M. V; Heine, T.; Banerjee, R. Construction of Crystalline 2D Covalent Organic Frameworks with Remarkable Chemical (Acid/Base) Stability via a Combined Reversible and Irreversible Route. *J. Am. Chem. Soc.* **2012**, *134* (48), 19524–19527.

(7) Pachfule, P.; Panda, M. K.; Kandambeth, S.; Shivaprasad, S. M.; Díaz, D. D.; Banerjee, R. Multifunctional and Robust Covalent Organic Framework–nanoparticle Hybrids. *J. Mater. Chem. A* **2014**, *2* (21), 7944.

(8) Huang, N.; Krishna, R.; Jiang, D. Tailor-Made Pore Surface Engineering in Covalent Organic Frameworks: Systematic Functionalization for Performance Screening. *J. Am. Chem. Soc.* **2015**, *137* (22), 7079–7082.

(9) Xu, L.; Zhou, X.; Yu, Y.; Tian, W. Q.; Ma, J.; Lei, S. Surface-Confined Crystalline Two-Dimensional Covalent Organic Frameworks via on-Surface Schiff-Base Coupling. *ACS Nano* **2013**, *7* (9), 8066–8073.

(10) Cavallini, M.; Albonetti, C.; Biscarini, F. Nanopatterning Soluble Multifunctional Materials by Unconventional Wet Lithography. *Adv. Mater.* **2009**, *21* (10–11), 1043–1053.

(11) Romero, J.; Rodriguez-San-Miguel, D.; Ribera, A.; Mas-Ballesté, R.; Otero, T. F.; Manet, I.; Licio, F.; Abellán, G.; Zamora, F.; Coronado, E. Metal-Functionalized Covalent Organic Frameworks as Precursors of Supercapacitive Porous N-Doped Graphene. *J. Mater. Chem. A* **2017**, *5* (9), 4343–4351.

Chapter 3: Microfluidic synthesis of COFs

3.1. Introduction

The procedure described in the previous chapter was a substantial advance since it allowed to create patterns of a COF on different surfaces and demonstrated that it was possible to obtain this porous material under mild conditions. However, besides precisely selecting the location of the COF on the substrate and somewhat its thickness, little additional control over the material is achieved. Specifically, although the intermediate formation of the gel could be exploited to some extent[1], the bulk material is still obtained as a powder with a reduced scope of processing alternatives.

With the aim of increasing the processability of the bulk material and considering the apparent flexibility on the synthetic conditions tolerated by COF-TAPB-BTCA and that the confinement of the reaction in small volumes did not hamper its effectiveness, microfluidics appeared as an appealing technique owing to the extraordinary range of possibilities that it offers.

Microfluidic techniques, as their name suggests, consist on the use of micrometre-sized channels through which a liquid flows. The effect of the reduced dimensions of the channels is not limited to diminishing the amount of sample needed, it also generates additional side effects, for instance, most microfluidic devices operate under laminar flow conditions as a consequence of the low Reynolds number. These unconventional effects together with the high degree of fine tuning of the characteristics of the microfluidic chips have rendered this technology highly attractive for

the preparation of materials in uncommon ways[2]. Some of the advantages for the assembly of materials are the precise control of the areas where mass transfer occurs and its rate, this allows to determine spatiotemporally the concentration of reactants and therefore the progress of the reactions and processes taking place in the system, which results for example in the isolation of metastable structures not accessible with bulk procedures. It is also noteworthy the large surface-to-volume ratio of these systems, which, added to the exceptional control of diffusion, enables to modulate nucleation to an extent beyond reach of most techniques.

Having in mind the benefits and countless possibilities microfluidic techniques could contribute to the field of COFs, this chapter describes the adaptation of the synthetic conditions of COFs to meet the requirements of microfluidics. Moreover, the material thus obtained showed an unusual morphology and could be used to create 2D and 3D structures.

3.2. Results and discussion

The proposed approach for the synthesis of imine-based COFs in microfluidic channels was a simple strategy that has also proven its effectiveness for the preparation of coordination polymers[3]. It is schematically presented in Figure 3.1 and consists in injecting a solution of each of the building blocks in separate channels (B and C) that will converge in a bigger channel in which the reaction is expected to occur. Moreover, there are two outer channels in which pure solvent is injected, the function of these sheath flows is to tune the flow focusing conditions, which affects the reaction time along the main channel. In order for this method to succeed, the reaction must proceed extremely fast, so the material is formed before leaving the microfluidic chip.

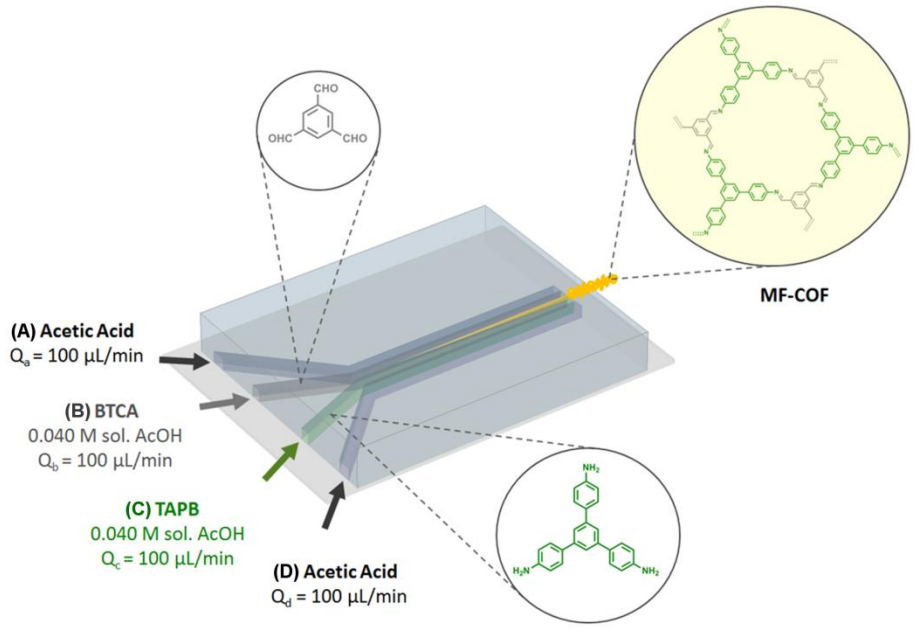

Figure 3.1. Schematic representation of the microfluidic synthesis of COF-TAPB-BTCA.

To explore how to achieve this rapid growth, **COF-TAPB-BTCA** was chosen because, as explained in the previous chapter, its formation at room temperature was possible in a shorter time than that usually needed for solvothermal reactions. However, the reaction rate in *m*-cresol was not high enough for its implementation in the microfluidic device. It was suggested that, as acetic acid is the catalyst of the reaction, an increase of its concentration would accelerate the formation of the COF. Extrapolating this hypothesis to the limit, it was decided to use acetic acid as the solvent of the reaction, thus employing the highest possible concentration of catalyst. In a preliminary test, two solutions of **TAPB** and **BTCA** in acetic acid were mixed in a batch procedure, a highly viscous gel was instantaneously formed as soon as the solutions came in contact. This was deemed quick enough and the project proceeded to optimising the conditions of the microfluidic process using acetic acid solutions.

In order to apply the strategy outlined above, a microfluidic chip made of PDMS was fabricated with four input channels 50 μm wide converging in a main channel 250 μm wide and 1 cm long, all of them having a height of 50 μm (Figure 3.2a). Solutions of **TAPB** and **BTCA** in acetic acid were prepared with a concentration similar to that used in the room temperature synthesis in *m*-cresol. These solutions were injected in the central inlet channels (B and C in Figure 3.1), while acetic acid was injected in channels A and D. All solutions were injected at a flow rate of 100 μL min^{-1} using a syringe pump system. In the main channel, at the interface between the two streams containing the building blocks, the formation of a solid could be seen, and at the outlet, a yellow fibre was continuously produced at a rate of approximately 2 mg min^{-1} (Figure 3.2b).

This promising result prompted for the characterisation of the fibrous material to confirm if a COF had been formed in such a short time with such an astounding morphology. In order to do so, the fibres where

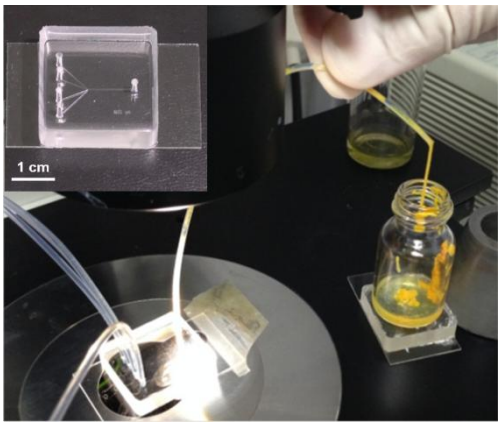

Figure 3.2. Photograph of the microfluidic setup working in continuous flow with a free-standing fibre being produced at the outlet. The inset shows the microfluidic chip.

soaked with THF and methanol to exchange the excess of acetic acid by a more volatile solvent, dried in ambient conditions for 48 hours and finally dried in vacuum at 150 ºC for 12 hours, resulting in a yellow solid that will be named **MF-COF** to distinguish it from the same material prepared with different procedures.

The easiest form to prove if the expected structure was obtained and if the microfluidic technique had an impact on the properties or morphology of the material is to compare the results of the analytical techniques with those obtained for **RT-COF** synthesised in *m*-cresol. However, with the aim of distinguishing between the differences that are due to the change of solvent instead of arising from the peculiar conditions imposed by microfluidics, **COF-TAPB-BTCA** was also synthesised in acetic acid under standard bulk chaotic mixing conditions using concentrations that mimicked those of the microfluidic system. The viscous yellow gel obtained was treated in the same way as were the fibres to yield a yellow powder (**COF-Ac** from this point onwards).

Regarding spectroscopic characterisation, all three materials show the same ATR-FT-IR spectrum (Figure A3.1, page 185), with the characteristic features already discussed in Chapter 1: disappearance of N-H stretch from the amine in the 3500-3300 cm^{-1} region, reduction in the intensity of the C=O stretch of the carbonyl at 1689 and the new C=N stretch at 1623 cm^{-1}. This coincidence extends to the ^{13}C CP-MAS NMR spectra (Figure A3.2, page 186), in which the only difference, if any, is the better resolution of the peak corresponding to the imine carbon (157 ppm) in the materials prepared in acetic acid.

The thermogravimetric analyses (Figure 3.3) also present the same profile that was found for **RT-COF**, with the only difference of the loss of mass at low temperatures. This is easily explained as the profile on that area is characterised by the desorption of volatile guest molecules present in the framework, which is expected to be heavily dependant on the solvents used during the synthesis and the effectiveness of the activation procedure. Nonetheless, the part inherent to the framework, that is, when it decomposes, does not show any change, the material is stable up to 400 ºC and the same decomposition steps can be seen afterwards. Finally, regarding the initial weight losses, they can be fitted with help from the elemental analysis data (see section A3.3, page 183). In **COF-Ac**, the experimental and calculated compositions match well if it is supposed that there are 0.5 molecules of water per unit cell, resulting in an expected weight loss due to water desorption of 1.9 % of the initial weight, matching the 1.9 % value observed in the TGA trace. To fit the analysis of **MF-COF**, it is necessary to consider the inclusion of 1 water molecule and 1 acetic acid molecule per unit cell. In this case, if the acetic acid is assumed to be strongly bound to the imine nitrogen by acid-base interactions and therefore not desorbing before decomposition begins, the water molecules account for 3.4 % of the total weight, while a loss of 3.3 % is detected in TGA.

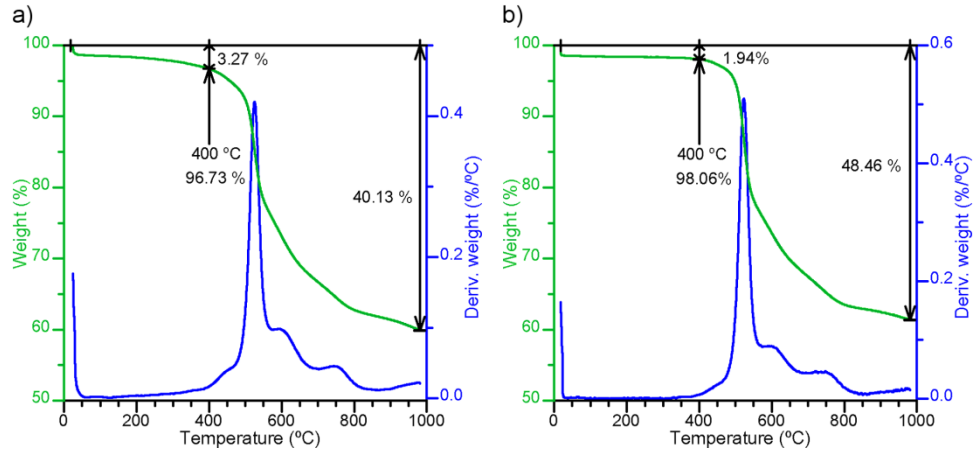

Figure 3.3. a) TGA trace of **MF-COF**. b) TGA trace of **COF-Ac**.

All the spectroscopic techniques and thermogravimetric and elemental analyses, point towards all three synthetic methodologies yielding the same product. However, given the low residence time in the microfluidic chip during which the building blocks were allowed to react (around 11 s), it was still surprising not only that powder X-ray diffraction (PXRD) confirmed that the COF had been formed, but also that the crystallinity of **MF-COF** was significantly higher than that of the product prepared in *m*-cresol and very similar to that of **COF-Ac** (Figure 3.4). This improvement in the order of the material is a result of the high concentration of catalyst. Acetic acid does not only increase the rate of the forward reaction, but also of the reverse one. By performing the reaction in pure acetic acid, a high degree of reversibility is achieved, resulting in dynamic chemical conditions that allow self-repair of defects during COF formation. Finally, the faster formation of an ordered structure in the microfluidic system can be ascribed to the higher control over the mixing of the reactants.

Finally, to complete basic the characterisation of the materials obtained in acetic acid, their porosity was assessed by N_2 adsorption at 77 K after

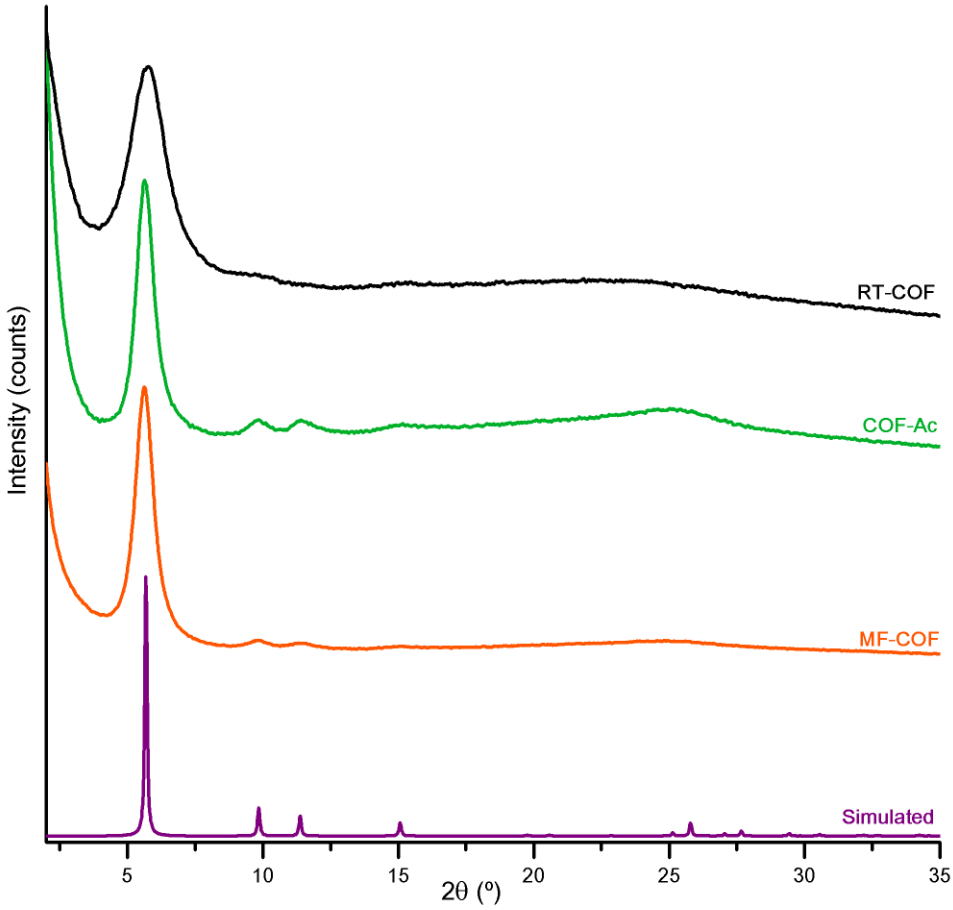

Figure 3.4. PXRD patterns of **RT-COF** (black), **COF-Ac** (green) and **MF-COF** (orange) and simulated PXRD pattern (violet).

activation at 150 ºC under high vacuum. The results showed isotherms typical of microporous materials (Figure 3.5). The BET surface areas of **MF-COF** was found to be 535 m^2 g^{-1}, slightly lower than the value of 705 m^2 g^{-1} calculated for the bulk synthesised **COF-Ac**, but still an improvement over other imine-linked COFs[4–6]. In fact, the lower surface area of the microfluidic prepared material can be blamed on the acetic acid molecules trapped in the pores, which could not be easily desorbed.

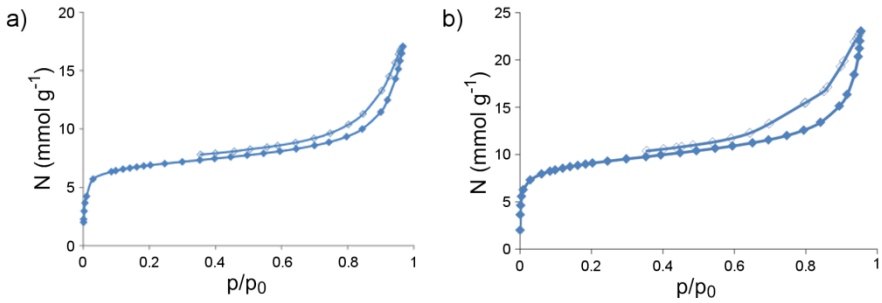

Figure 3.5. N_2 isotherms for a) **MF-COF** and b) **COF-Ac** at 77 K; filled dots: adsorption, empty dots: desorption

Once the chemical and structural identity of the material are proven, it is time to discuss the changes induced by microfluidics in the morphology and organisation of the material at the microscopic scale. With this purpose **MF-COF** and **COF-Ac** were studied with field-emission scanning electron microscopy (FE-SEM). Low magnification images of the fibres of **MF-COF** revealed that the material is composed of a mesh of fibres with a diameter of nearly 70 nm arranged in a macroporous sponge-like 3D branched structure (Figure 3.6a). At higher magnification (Figure 3.6b), it could be observed that the fibres are formed by 40 nm particles anisotropically aggregated in a linear fashion. This alignment of the particles was probably due to the particular limited diffusion imposed under the flow conditions used during the microfluidic synthetic process. It was also possible to obtain TEM images of the fibres by directly dispersing in methanol a small piece as obtained from the outlet of the microfluidic chip. These images (Figure 3.6c-d) confirmed the macroporous sponge-like morphology resulting from the interconnection of fibrous structures. Additionally, the uniform contrast of the particles suggested that the fibres and particles are not hollow, since it has been shown that hollow COF structures present a darker contrast in their outer part in TEM images[7,8]. In contrast with the macroporous structure obtained in microfluidics, batch prepared **COF-Ac** shows a denser morphology in which two different

types of structures can be found. On the one hand, most of the material is formed by aggregated particles around 60 nm in diameter which, instead of being linearly organised, are arranged in rather layered structures (Figure 3.6e). On the other hand, some regions where the particles have complete coalesced resulting in a sheet-like morphology can be found without much difficulty (Figure 3.6f).

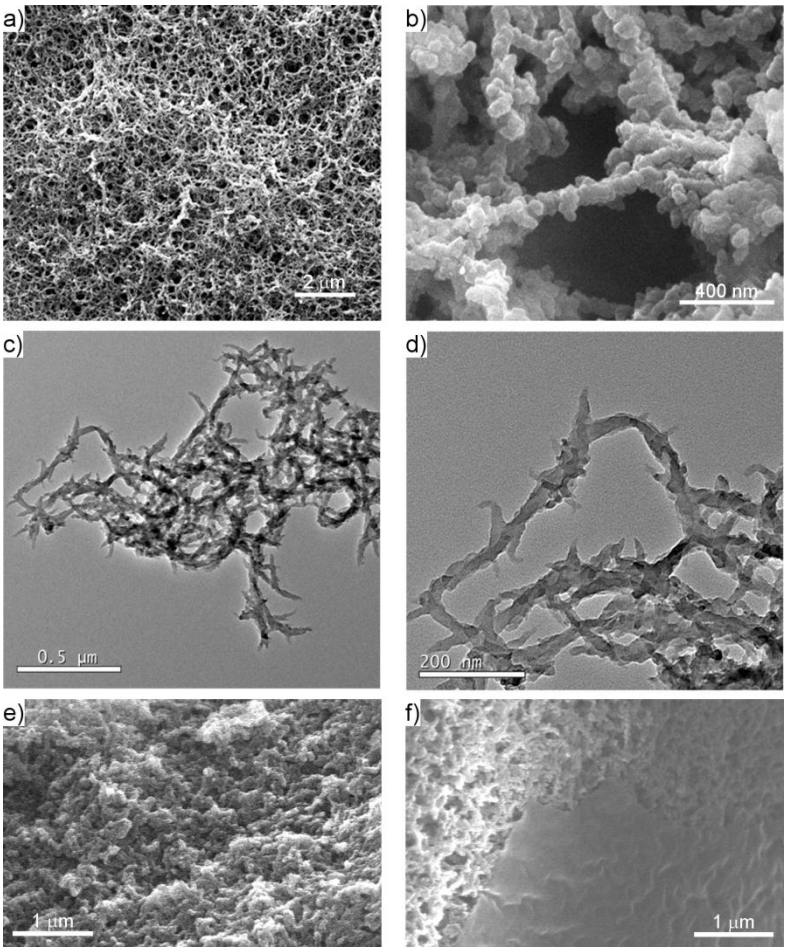

Figure 3.6. a,b) FESEM images and c,d) TEM images of **MF-COF**, showing a fibrous morphology. e,f) FESEM images of **COF-Ac** displaying layered morphology.

Among all the parameters of the microfluidic reaction such as channel dimensions or concentration of the reactants, the easiest one to modify with the smallest risk of clogging of the main channel is the flow rate ratio (FRR). This quantity is defined as the ratio between the flow rates of the sheath flows and the reactant-laden flows. An increase of it therefore means an increase in the amount of pure acetic acid relative to the amount of building block solutions. As has been stated at the beginning of the chapter, a FRR of 1 was used for the synthesis of MF-COF. However, in order to elucidate the effect of increasing it, the results of using a FRR of 4 were investigated. As shown in Figure 3.7, the fibrillar micro-structure is kept intact upon increasing the sheath flows, with the only consequence being the reduction in the amount of **MF-COF** produced.

Finally, an exciting prospect of this synthetic approach derives from the mechanical stability of the fibres. It was thought that their consistency and continuous generation would allow to use the microfluidic setup as a printing device by collecting the fibres coming out from the flexible outlet tube with the desired shape, as depicted in Figure 3.8. First, it was confirmed that both simple and more elaborated flat structures could be created on glass owing to the flexibility of the fibre (Figure 3.9a-b). Next, it was checked that several different substrates that are compatible with

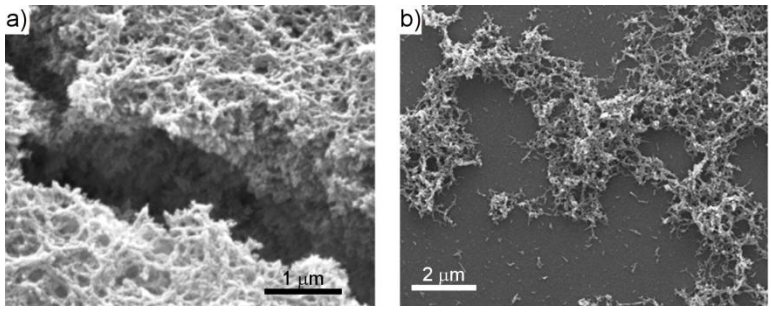

Figure 3.7. FESEM images of **MF-COF** produced at FRR of a) 1 and b) 4.

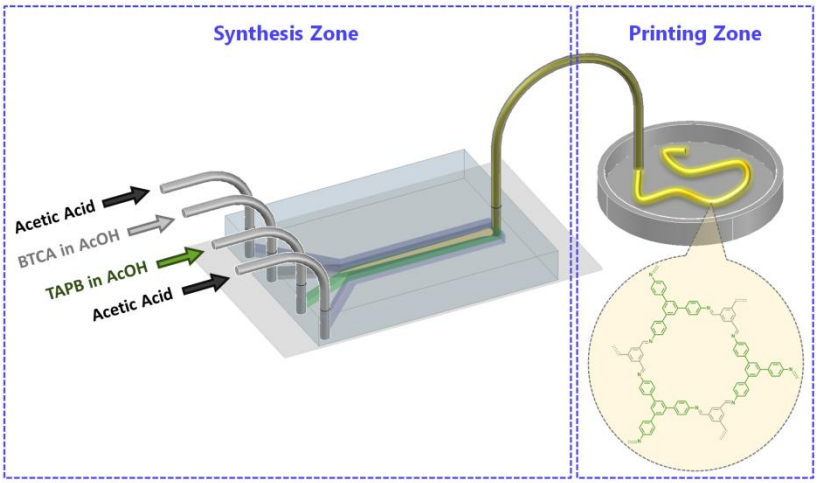

Figure 3.8. Schematic illustration of the microfluidic set-up used for printing **MF-COF** fibres

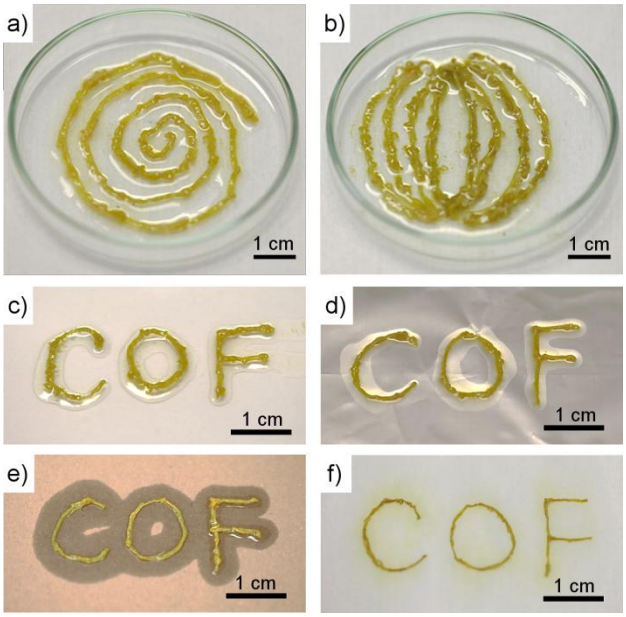

Figure 3.9. Photographs of flat **MF-COF** structures on a,b) glass, c) polystyrene, d) aluminium foil, e) cardboard and f) tissue paper.

acetic acid could be used. As shown in the photographs in Figure 3.9c-f, the desired structure was obtained in several substrates, being remarkable that when it was drawn on porous supports such as paper, it absorbed most of the excess acetic acid, rapidly drying the fibres, which shrink slightly as a result. Last but not least, a significant challenge and advance that was also achieved was the formation of self-standing three-dimensional COF structures. Figure 3.10 shows two networks formed by a set of parallel **MF-COF** fibres supported on a different perpendicular array of fibres.

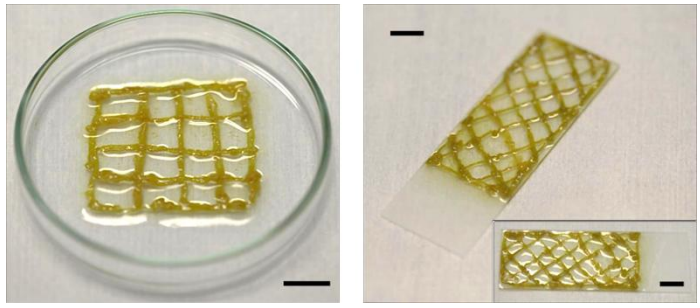

Figure 3.10. Photographs of three-dimensional, mesh-like COF structures. Scale bars = 1 cm.

3.3. Conclusions

Microfluidic conditions were used for the first time to generate **MF-COF**, whose structure and composition were confirmed by suitable characterisation techniques to correspond to the previously reported for **COF-TAPB-BTCA** prepared using bulk conditions. Indeed, a higher quality material is obtained than in previous reports thanks to the higher reversibility of the reaction in pure acetic acid.

Interestingly, the microstructures observed by electron microscopy consist of interconnected fibres leading to a 3D macroporous sponge-like morphology, which is completely different to that obtained conventionally.

Finally, there are two facts that make microfluidic synthesis an attractive production method of COFs. Firstly, it is a continuous process that can be easily scaled up. Lastly, it has been shown that it possesses a great processing potential owing to the mechanical properties of the fibres produced, which allows to create 2D and 3D structures made solely of COF.

3.3.1. Future prospects

Perhaps the most far-reaching result of the work presented in this chapter is the suggested possibility of printing COFs, both on substrates (which had already been achieved at a smaller scale) and, more strikingly, in a process similar to 3D printing. The field of 3D printing has experienced an impressive growth in the last few years[9] and the equipment available cannot be compared with the rudimentary procedure used in this chapter. Consequently, the preparation procedure of **COF-TAPB-BTCA** has been further modified to adapt it to the current 3D printing technology and tests

are being performed to fully ascertain the likelihood of creating COF structures with this methodology.

3.4. References

(1) Romero, J.; Rodriguez-San-Miguel, D.; Ribera, A.; Mas-Ballesté, R.; Otero, T. F.; Manet, I.; Licio, F.; Abellán, G.; Zamora, F.; Coronado, E. Metal-Functionalized Covalent Organic Frameworks as Precursors of Supercapacitive Porous N-Doped Graphene. *J. Mater. Chem. A* **2017**, *5* (9), 4343–4351.

(2) Sevim, S.; Sorrenti, A.; Franco, C.; Furukawa, S.; Pané, S.; DeMello, A. J.; Puigmartí-Luis, J. Self-Assembled Materials and Supramolecular Chemistry within Microfluidic Environments: From Common Thermodynamic States to Non-Equilibrium Structures. *Chem. Soc. Rev.* **2018**.

(3) Rubio-Martinez, M.; Imaz, I.; Domingo, N.; Abrishamkar, A.; Mayor, T. S.; Rossi, R. M.; Carbonell, C.; DeMello, A. J.; Amabilino, D. B.; Maspoch, D.; et al. Freezing the Nonclassical Crystal Growth of a Coordination Polymer Using Controlled Dynamic Gradients. *Adv. Mater.* **2016**, *28* (37), 8150–8155.

(4) Ding, S.-Y.; Gao, J.; Wang, Q.; Zhang, Y.; Song, W.-G.; Su, C.-Y.; Wang, W. Construction of Covalent Organic Framework for Catalysis: Pd/COF-LZU1 in Suzuki–Miyaura Coupling Reaction. *J. Am. Chem. Soc.* **2011**, *133* (49), 19816–19822.

(5) Kandambeth, S.; Mallick, A.; Lukose, B.; Mane, M. V; Heine, T.; Banerjee, R. Construction of Crystalline 2D Covalent Organic Frameworks with Remarkable Chemical (Acid/Base) Stability via a Combined Reversible and Irreversible Route. *J. Am. Chem. Soc.* **2012**, *134* (48), 19524–19527.

(6) Pachfule, P.; Panda, M. K.; Kandambeth, S.; Shivaprasad, S. M.; Díaz, D. D.; Banerjee, R. Multifunctional and Robust Covalent Organic Framework–nanoparticle Hybrids. *J. Mater. Chem. A* **2014**, *2* (21), 7944.

(7) Kandambeth, S.; Venkatesh, V.; Shinde, D. B.; Kumari, S.; Halder, A.; Verma, S.; Banerjee, R. Self-Templated Chemically Stable Hollow Spherical Covalent Organic Framework. *Nat. Commun.* **2015**, *6* (1), 6786.

(8) Pachfule, P.; Kandmabeth, S.; Mallick, A.; Banerjee, R. Hollow Tubular Porous Covalent Organic Framework (COF) Nanostructures. *Chem. Commun.* **2015**, *1*, 11717–11720.

(9) Truby, R. L.; Lewis, J. A. Printing Soft Matter in Three Dimensions. *Nature* **2016**, *540* (7633), 371–378.

Chapter 4: Effect of processing on ionic conductivity and fuel cell application

4.1. Introduction

In the introduction, it was suggested that COFs, and other tailored porous materials, could more easily find a niche in technologies that are not yet consolidated due to some weak points[1]. One of these technologies are proton exchange membrane fuel cells (PEMFC). They have attracted much interest in a context of rising energy consumption under the threat of the exhaustion of fossil fuels. Their advantages over other power sources include a high conversion efficiency, low maintenance, good portability and the use of biofuels or more environmentally friendly fuels such as hydrogen[2,3]. One the main difficulties found when implementing this technology is the choice of a suitable material to act as proton exchange membrane since it has to comply with many requisites: high ionic conductivity but null electronic conductivity, low gas permeability, good chemical and thermal stability, and, of course, the ability of being processed as a thin-film. The most popular material currently used as a solid electrolyte is Nafion, which, despite achieving a proton conductivity of 10^{-1} S cm^{-1}, presents several drawbacks related to production cost, fuel crossover and performance at high temperatures[4]. Consequently, crystalline porous materials have been proposed as proton-conducting materials[5].

A few COFs have been reported to display good ionic conductivities[6–9]. Generally, 2D COFs with aligned pores forming one-dimensional channels

are used, and the two strategies more frequently used to bestow ionic conductivity on the materials in these works are either introducing ionic species in the pores or filling the pores with organic moieties capable of hydrogen bonding that facilitate proton mobility via a Grotthuss mechanism. This seemed a good scenario to exploit the advantages of the synthetic procedures reported on the previous chapters. On the one hand, the gel formed when RT-COF is synthesised in *m*-cresol allows a fast diffusion through it, which is suitable for post-functionalisation[10], in this case, lithium ions. On the other hand, the TGA and elemental analysis of the COFs prepared in acetic acid indicated the presence of tightly bound acetic acid guest molecules. This made these materials susceptible to being studied as ionic conductors.

Therefore, in this chapter, the ionic conductivity of COFs prepared under mild conditions and functionalised with lithium ions and acetic acid will be studied. Additionally, they will be processed to test their performance as fuel cell polymer electrolyte membranes and the impact of synthetic conditions on their behaviour will be discussed.

4.2. Results and Discussion

In order to compare the effect of the functionalisation on the electrical properties, **RT-COF** was prepared in *m*-cresol according to the procedure described in Chapter 1 to be employed as a model of a non-functionalised material. The chosen acetic acid containing material was **COF-Ac** rather than MF-COF due to the higher crystallinity and the easier access in the laboratory of the research group to standard bulk techniques than to microfluidic techniques. Finally, the lithium functionalised COF (named **LiCl-COF** for simplicity) was prepared in a two-step process (Figure 4.1, bottom). First, solutions in *m*-cresol of **TAPB** and **BTCA** were mixed to form the characteristic yellow gel, then, after allowing the framework forming reaction to progress for some time, the gel was immersed in an aqueous solution of lithium chloride and stirred for 24 hours. Next, the gel was filtered and dried in vacuum at 150 ºC to yield **LiCl-COF** as a brown solid.

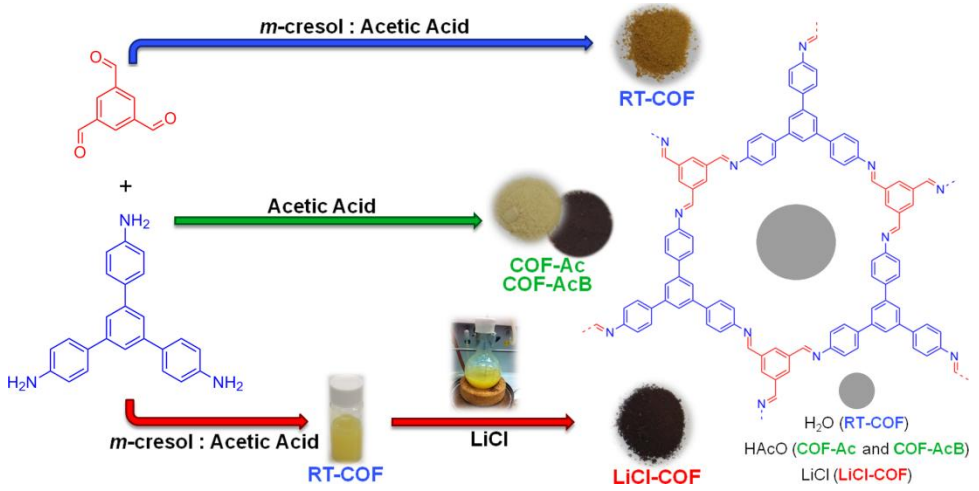

Figure 4.1. Schematic representation of the synthesis and structure of **RT-COF** (top), **COF-Ac** (middle) and **LiCl-COF** (bottom). The grey circle represents the guest molecules accomodated in the channels of the COFs.

Once all the materials were synthesised, they were studied with several techniques prior to performing the conductivity measurements. In general, the aim of this thorough analysis was to know as much as possible about the differences of the differently functionalised COFs so as to allow to explain any differences in the ionic conductivity. Additionally, **LiCl-COF** was characterised to confirm the formation of the ordered structure and

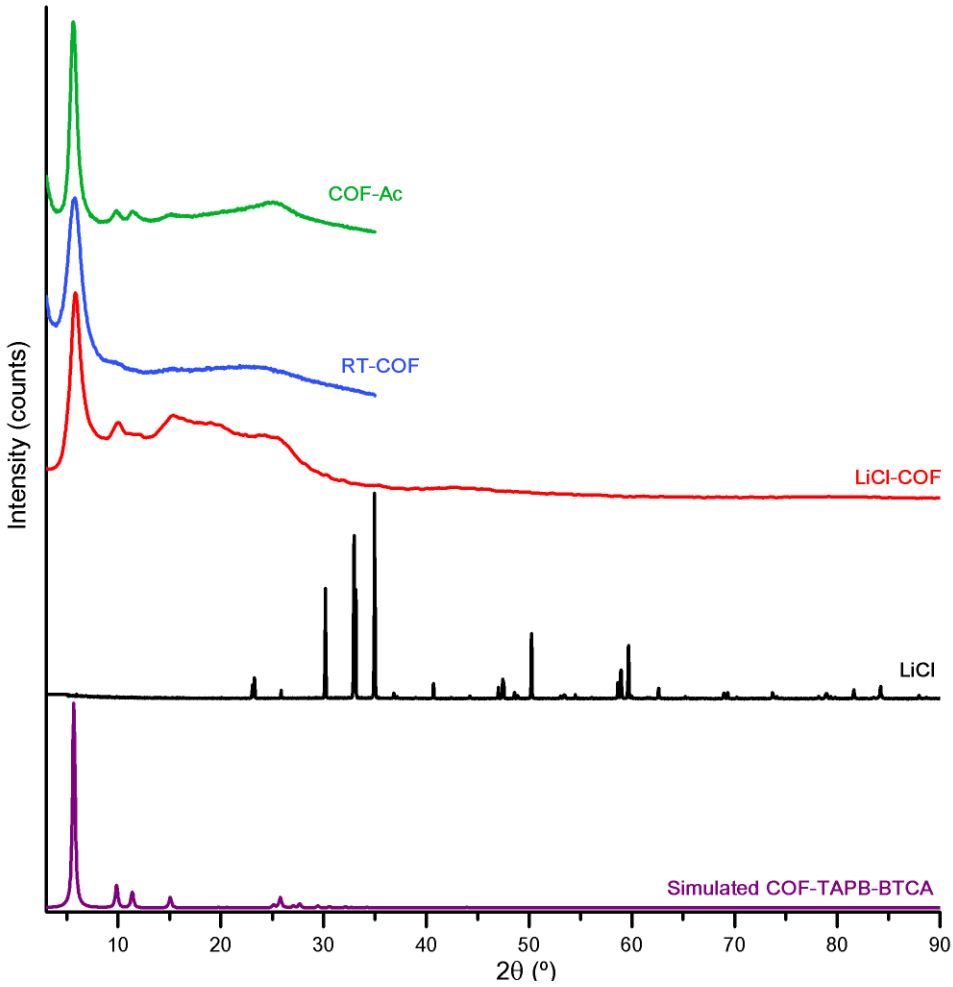

Figure 4.2. PXRD patterns of **COF-Ac** (green), **RT-COF** (blue), **LiCl-COF** (red), LiCl (black) and simulated pattern from the structure of **COF-TAPB-BTCA** (violet).

determine the captured amount of lithium. Some tests of properties such as chemical stability that are inherent to the scaffold of the COF and in principle not heavily influenced by the presence of guest molecules were conducted on **COF-Ac** because it is the most crystalline material.

Firstly, PXRD was performed to corroborate that the impregnation with lithium does not have great negative effect on the order of the material. As shown in Figure 4.2, the PXRD pattern of **LiCl-COF** matched those of the other COFs and the simulated one, confirming the formation of the correct structure even after functionalisation. Moreover, the lack of reflections corresponding to lithium chloride implied that any lithium chloride detected by other techniques is not segregated in the form of crystals of the salt, but rather forming ion pairs in the channels of the framework.

The TGA trace of **LiCl-COF** (Figure 4.3) showed the already familiar decomposition profile starting at 400 ºC that was found for this COF when it was prepared in *m*-cresol and acetic acid (Chapters 2 and 3). However, it was not possible to straightforwardly assign the loss of volatile guests given the complex composition expected. Since standard elemental analysis does not provide information about lithium or chloride, ICP-MS was performed to gain some insight in the uptake of lithium. The suggested Li:Cl:N ratio of 1:2.5:10, together with the information of elemental analysis (see section A4.2.2, page 191) and the 18 % weight loss in the TGA profile, pointed towards a composition of $C_{33}H_{21}N_3 \cdot 0.3$ LiCl·0.5 HCl·5 H_2O. The water content matches well with the amount of volatiles detected by TGA, the presence of such a high amount is not surprising since the ionic species are expected to be solvated. The difference in the ratios of lithium and chloride is explained by the partial protonation the imine groups, which generates positive charges that are balanced with additional chloride anions.

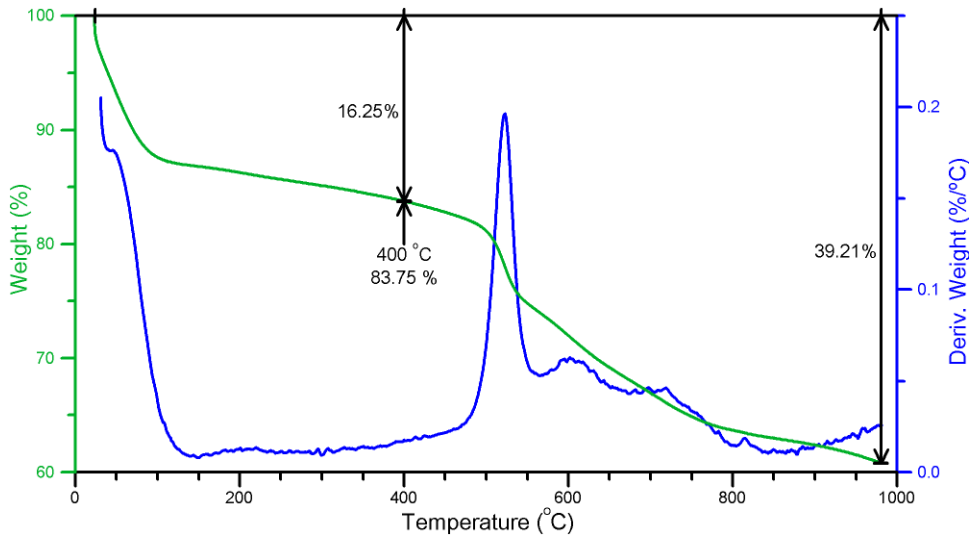

Figure 4.3.TGA trace of **LiCl-COF**.

Infrared spectroscopy (Figure A4.2, page 193) did not add much extra information besides simply confirming the formation of imine bonds, since there are no bands in the 3500-3300 cm^{-1} region corresponding to the N-H stretch of amines and the band at 1621 cm^{-1} is indicative of the C=N stretch of the imine. It also shows a broad band between 3500 and 3000 cm^{-1} which can be attributed to the large amount of water trapped in LiCl-COF.

Given that the lithium and water present in **LiCl-COF** are expected to be central to its ionic conductivity, it was considered important to obtain some information about their environment, although it has to be taken into account that a rigid and precise arrangement of the guests into the pores is not expected. X-ray photoelectron spectroscopy (XPS) was performed with this goal. The N 1s spectrum (Figure 4.4a) showed two components at 397.00 and 398.23 eV which are assigned, respectively, to free imine nitrogen atoms and to imine nitrogen atoms interacting with the solvated lithium cation $[Li(OH_2)_4]^+$ or with protons. The 4:1 ratio between these two

peaks indicates that most of the N atoms are not involved in hydrogen bonding interactions, although taking into account the 1:10 Li:N ratio, this means that nearly all lithium ions are interacting with nitrogen atoms. This environment of lithium ions was also supported by solid state ^{7}Li MAS NMR spectra of **LiCl-COF** at 22 % and 100 % relative humidity (RH) (Figure 4.4b-c). The broad peak at low humidity can be deconvoluted in two components at 0.00 ppm and 0.23 ppm. The less intense peak at 0 ppm is due to free $[Li(OH_2)_4]^+$, while the majority 0.23 ppm component could be due to the solvated ion interacting with the imino group. This is consistent with the presence of a single sharp signal at 0.00 ppm in the spectrum at 100 % RH, in which there is enough water for the ions to be

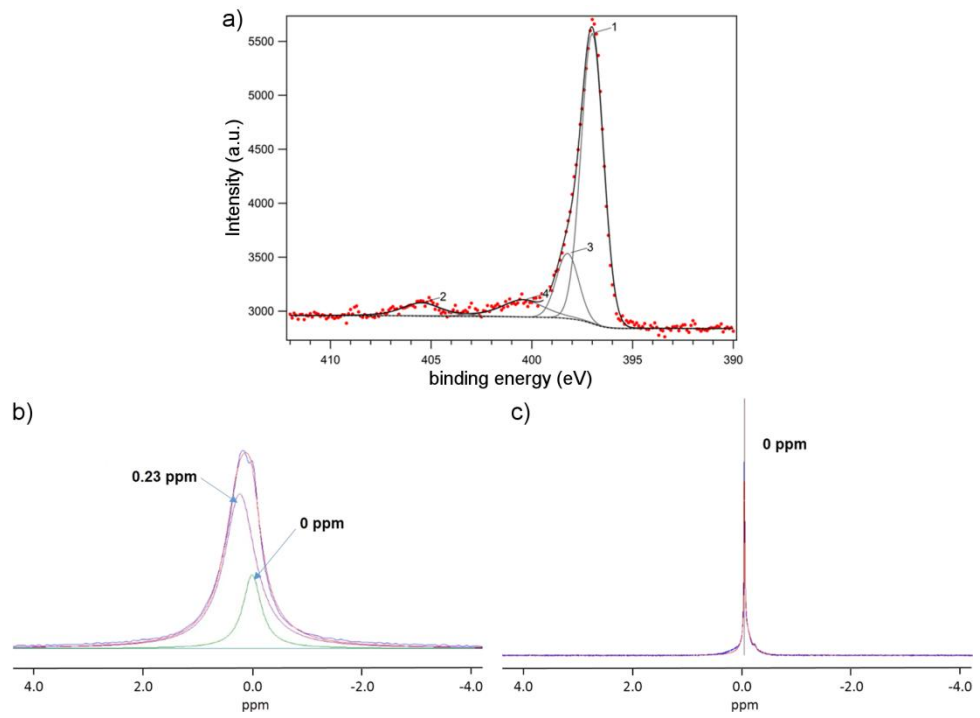

Figure 4.4. a) Experimental XPS data and Gaussian fits to the N 1s spectra of **LiCl-COF**. The line and red points show the fitting curves and experimental data, respectively. b,c) Solid state ^{7}Li MAS NMR spectra of LiCl-COF at 298 K at b) 22 % RH and c) 100 % RH.

free in the pores without much interaction with the groups in the channel walls. This suggests that the environment and mobility of the ions are highly dependent on environmental moisture.

After seeing the huge impact moisture was likely to have on the conductivity of the materials, it was decided to study their porosity and water uptake capabilities. First, nitrogen isotherms (Figure 4.5a) were performed to evaluate the overall porosity of the differently prepared COFs. As reported previously, **RT-COF** showed a BET surface area of 330 m^2 g^{-1} and **COF-Ac** an increased value of 750 m^2 g^{-1} due to the effective acetic acid catalysis. Not surprisingly, the introduction of LiCl in the structure of **LiCl-COF** led to a complete loss of N_2 adsorption capacity, which is indicative of the guest molecules filling the pores of the framework. More interesting were the results of water vapour adsorption. As shown in the isotherms in Figure 4.5b, the material with the highest water uptake was **LiCl-COF**. Even though it may seem counter-intuitive given that it was apparently non-porous due to the presence of lithium and chloride ions, this is perfectly logical as said ions increase the hydrophilic

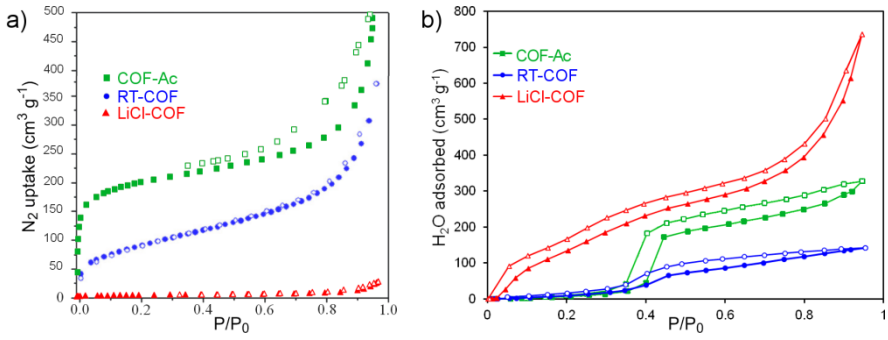

Figure 4.5. a) Nitrogen adsorption isotherms at 77 K for **COF-Ac** (green), **RT-COF** (blue) and **LiCl -COF** (red). b) Water vapor adsorption isotherms at 298 K of **COF-Ac** (green), **RT-COF** (blue) and **LiCl-COF** (red). Filled and open symbols correspond to adsorption and desorption, respectively.

nature of the material. Another noticeable feature of the isotherms is the pronounced step at a relative pressure close to $p/p^0 = 0.4$ that can be seen for **RT-COF** and **COF-Ac**. This type V isotherms are typical for water adsorption in porous materials with hydrophobic walls[11–13]. In contrast, **LiCl-COF** adsorbed water starting from a lower pressure, corroborating its more hydrophilic character.

Aiming to complete the characterisation, TEM studies were carried out to support the structure of the framework proposed from the PXRD data. Since all the materials are formed by the same covalent scaffold, the highest quality **COF-Ac** was dispersed in a 2-propanol:water mixture to obtain a suspension that was casted on TEM grids to allow its analysis in an aberration corrected microscope at a low voltage of 60 kV to keep sample degradation by the electron beam as low as possible. Some representative images are shown in Figure 4.6. The low magnification micrograph in Figure 4.6a evidenced the presence of COF multilayers stacked in two different manners. The regions labelled as (i) followed a random sequence similar to turbostratic carbon leading to an amorphous appearance. Conversely, the zones tagged as (ii) showed an slightly distorted eclipsed stacking resulting in crystalline domains with hexagonal order. This order can be better observed in the higher magnification image in Figure 4.6b, in which the most enlightening areas are marked as A and B. In region A, the hexagonal lattice with apparent periodicities of 0.25 nm that are related to the C-C distance in the COF can be seen. Nevertheless, a more careful inspection allows visualising a diffuse framework of 1.2 nm (Figure 4.6c). This fits well with the pore dimensions of the framework and is supported by the FFT of the image, suggesting that even if the stacking is not perfect, the order in the individual layers is preserved and the orientation of all the layers is nearly parallel. On the other hand, a closer look at region B revealed fringes separated by 0.35

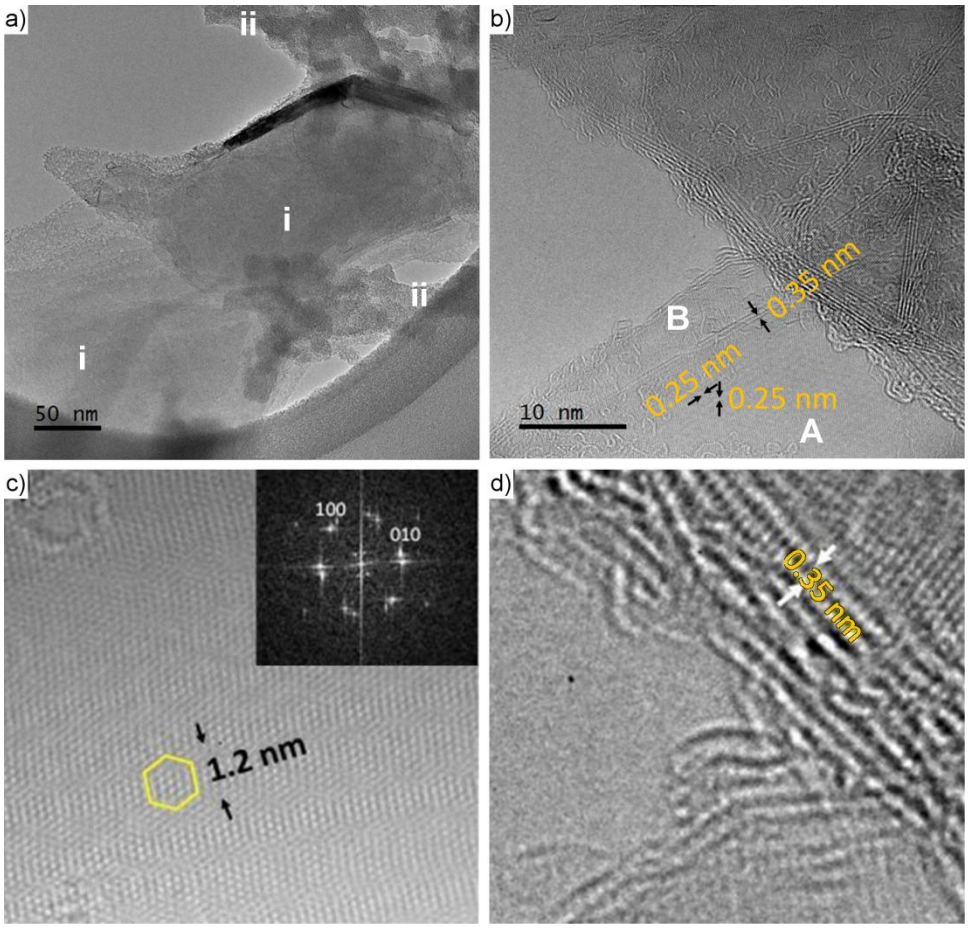

Figure 4.6. a) Characteristic low magnification TEM image of **COF-Ac** showing areas of different type of layer stacking, (i) and (ii), described in the main text. (b) HRTEM image typical of the type (ii) stacking. Two different areas (A and B) are evident. (c) Enhanced detail of zone A and its corresponding FFT. (d) Enhanced detail of zone B.

nm (Figure 4.6d), matching the interlayer distance. All these features were observed in other areas and support the structure proposed from the PXRD data.

Finally, since the working conditions in PEM fuel cells involve a humid environment, the stability of the framework was assessed. For this, **COF-**

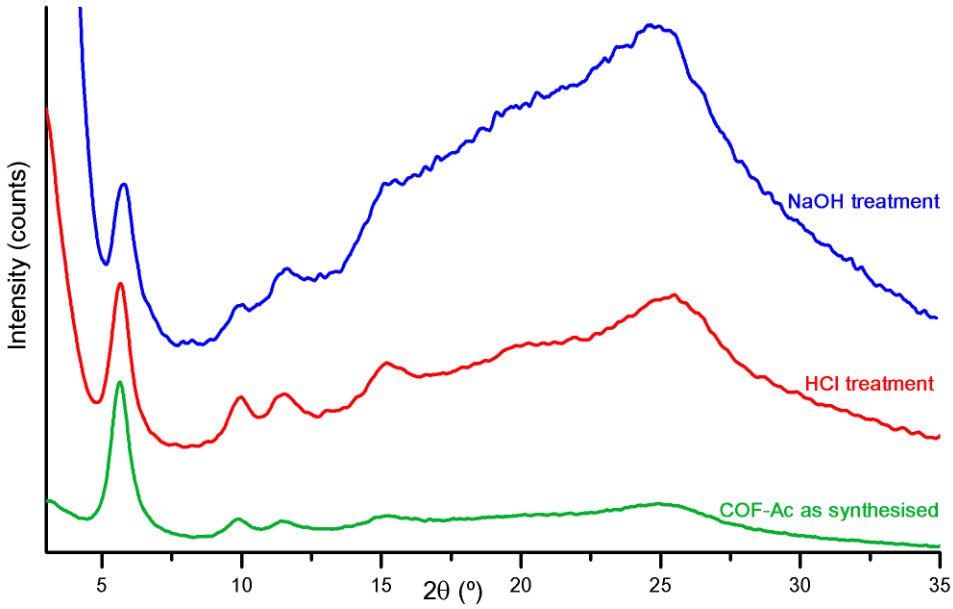

Figure 4.7. PXRD patterns of **COF-Ac** before (green), and after treatment with HCl 12 M (red) and NaOH 14 M (blue).

Ac was immersed in concentrated acidic and basic aqueous solutions at room temperature for 3 days. The amount recovered after washing the samples with water and drying under vacuum at 150 ºC were fairly high, 86 % of the acid treated sample and 90 % when treated with base. These values were similar to those reported for other imine-based COFs[14]. To complete the study, PXRD of the recovered solid was performed, showing no significant loss of crystallinity (Figure 4.7).

Once the structural characterisation was complete, the ionic conductivity of the materials was probed. In order to do so, they were pressed at 300 MPa into pellets with a diameter of 13 mm. Surprisingly, processing **COF-Ac** in this form produced a flexible and quasi-transparent thin film (Figure 4.8a) while the other COFs yielded standard thick pellets. Before jumping into the explanation and consequences of this unexpected result, XRD of

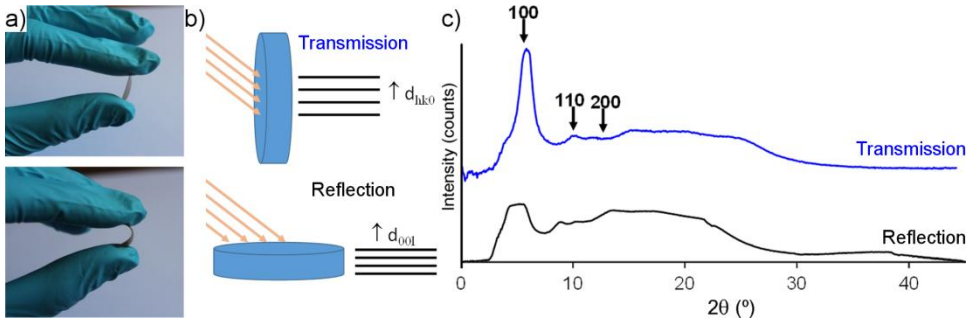

Figure 4.8. a) Pictures of **COF-Ac** film showing its flexibility. b) Scheme of the orientation of the film in reflection and transmission configurations c) XRD patterns of a **COF-Ac** film prepared applying a pressure of 300 MPa measured in transmission and reflection configurations.

the film was carried out to verify if the high pressure applied had damaged the structure of the COF. Aware that lower uniaxial pressures have an effect on the alignment of 2D COFs[6], the film was measured both in reflection and transmission configurations (Figure 4.8b). The results depicted in Figure 4.8c showed that the loss of crystallinity had been moderate and the lower intensity of the 100 peak in reflection mode hinted towards a slight alignment of COF layers in the film.

To improve the understanding of the differences between the **COF-Ac** film and the pellets of **LiCl-COF**, they were analysed by SEM. As shown in Figure 4.9, the pellet was poorly compacted and had a great number of fractures, on the other hand, the surface of the film appeared to be smoother with just some shallow holes decorating it. Being the presence of acetic acid the main difference between the COFs, it was suggested that it might play a role in the better compaction of **COF-Ac**. It was hypothesised that the acid may catalyse the formation of imine bonds at the grain boundaries between the unreacted carbonyl and amino groups that are left in the grain boundaries of the COF crystallites, thus giving rise to the formation of larger aggregates. Alternatively, it could be possible

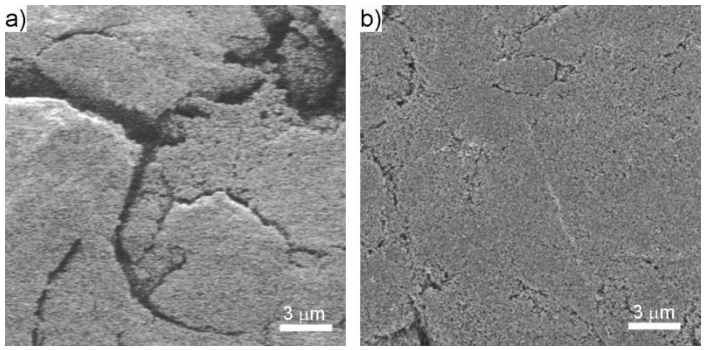

Figure 4.9. a,b) FESEM images of the surface of a) a **LiCl-COF** pellet and b) a **COF-Ac** film.

that the acetic acid molecules mediate in the supramolecular connection of the edges of the COF layers via hydrogen bonding with the amines and aldehydes present at the borders. In order to verify the importance of acetic acid and with the benefits of obtaining tightly packed, uniform thin films in mind, **LiCl-COF** was mixed with a few drops of acetic acid prior to being compressed. The result of the experiment was the formation of a thin-film, confirming that acetic acid was the key factor in the formation of the film and suggesting the potential generalisation of this method to form 100-300 μm thick films of any imine-linked COF.

After unravelling some of the secrets of pellet and film formation, ionic conductivity of pellets of **RT-COF** and **LiCl-COF** and films of **COF-Ac** and **LiCl-COF** was evaluated using electrochemical impedance spectroscopy (EIS) from 298 to 313 K at two difference relative humidities (RH) of 22 % and 100 %. The resistance R of the sample was calculated from the Nyquist plot and was used to calculate the conductivity σ using the expression $\sigma = L/(R \times A)$, where L is the thickness of the sample and A the electrode area. The results summarised in Table 4.1 showed that at low humidities there was no significant ionic transport in any of the different

Table 4.1. Conductivity values at 313 K of **RT-COF** and **LiCl-COF** pellets and **LiCl-COF** and **COF-Ac** films at 22 % and 100 % RH.

	σ, S cm^{-1} at 313 K	
	22 % RH	100 % RH
RT-COF	$<1 \times 10^{-10}$	1.83×10^{-5}
LiCl-COF pellet	$< 1 \times 10^{-10}$	4.83×10^{-3}
LiCl-COF film	$< 1 \times 10^{-9}$	6.45×10^{-3}
COF-Ac	$< 1 \times 10^{-10}$	1.07×10^{-4}

materials, no matter the functionalisation or processing form. However, when the humidity increased, so did the conductivity, reaching values as high as 6.45×10^{-3} S cm^{-1} for the film of **LiCl-COF**. From these values, it was concluded that shaping the **LiCl-COF** as a pellet or a film does not have a significant effect on the conductivity. Moreover, **COF-Ac** showed an intermediate conductivity between the lithium functionalised COFs and the non-functionalised **RT-COF**, following the same trend that was found for water adsorption. This indicated that hydration plays a significant role in proton conduction through these porous materials and therefore, COFs with more hydrophilic channels are expected to be more efficient ionic conductors.

Taking into consideration the combination of good conductivity and processability of the films prepared in the presence of acetic acid, they were chosen to study their ability as solid electrolytes for the construction of proton-exchange membrane fuel cells (PEMFC). The films were used as the solid electrolytes between two electrodes of 40 % wt Pt/C as anode and cathode for the construction of membrane electrode assemblies (MEAs). These assemblies were characterised by SEM, showing the

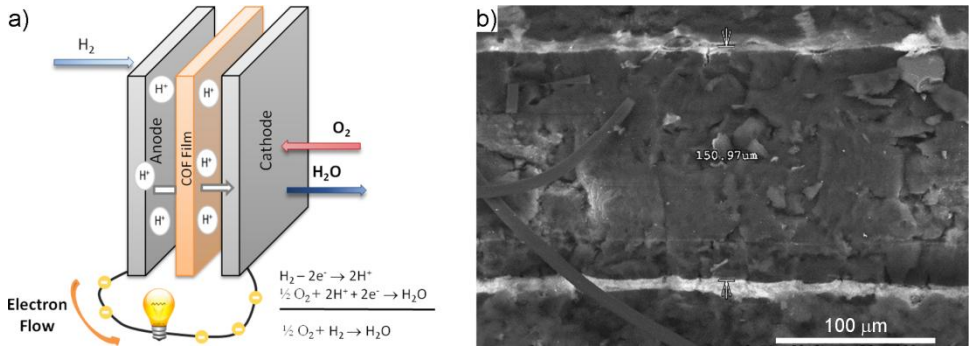

Figure 4.10. a) Scheme of the PEMFCs that uses COF films as membrane electrode assemblies (MEA). b) SEM image of a MEA cross section with **COF-Ac** film as solid electrolyte.

formation of uniform membranes, as the 150 µm thick one resulting from the use of **COF-Ac** that is shown in Figure 4.10b. This compact packing is valuable given the necessity of have a tight barrier for fuel gas separation that prevents hydrogen crossover, which would result in a short circuit of the fuel cell. The measurement of the performance of these MEAs at 323 K provided interesting and unexpected results. More precisely, the maximum power density of 7.64 mA cm^{-2} for the **COF-Ac** film was higher than the value of 4.06 mA cm^{-2} obtained with a film of **LiCl-COF**, despite the latter boasting a better conductivity. This lack of correlation between the values of conductivity and power density was related to the open circuit potential (OCP), which was lower for **LiCl-COF** (0.42 V) than for **COF-Ac** (0.95 V). A low OCP is usually indicative of suboptimal mechanical properties of the MEA, which implied that even though the addition of acetic acid improved the processability of **LiCl-COF** and allowed the formation of films, it was not as effective as in the case of **COF-Ac**.

Such a clear effect of the processing on the device performance motivated the search of a material showing better ionic conductivity than **COF-Ac**

while preserving the good packing behaviour. Considering that after being thoroughly solvent exchanged and dried under vacuum **COF-Ac** contains only a residual amount of acetic acid, the most straightforward idea to improve its conductivity was to increase the quantity of acetic acid remaining after the synthesis. With this goal in mind, the gel that was formed by mixing **TAPB** and **BTCA** dissolved in acetic acid was lightly washed with tetrahydrofuran and dried at room temperature and ambient pressure, avoiding heat and vacuum. The dark red COF so-obtained was expected to retain a bigger amount of acetic acid and will be referred to as **COF-AcB**.

Given the little differences with **COF-Ac**, structural characterisation of **COF-AcB** will be reviewed shortly. First, the PXRD pattern shown in Figure 4.11 matches well with the characteristic pattern of the synthesised framework. Next, the spectroscopic data complied with the expected

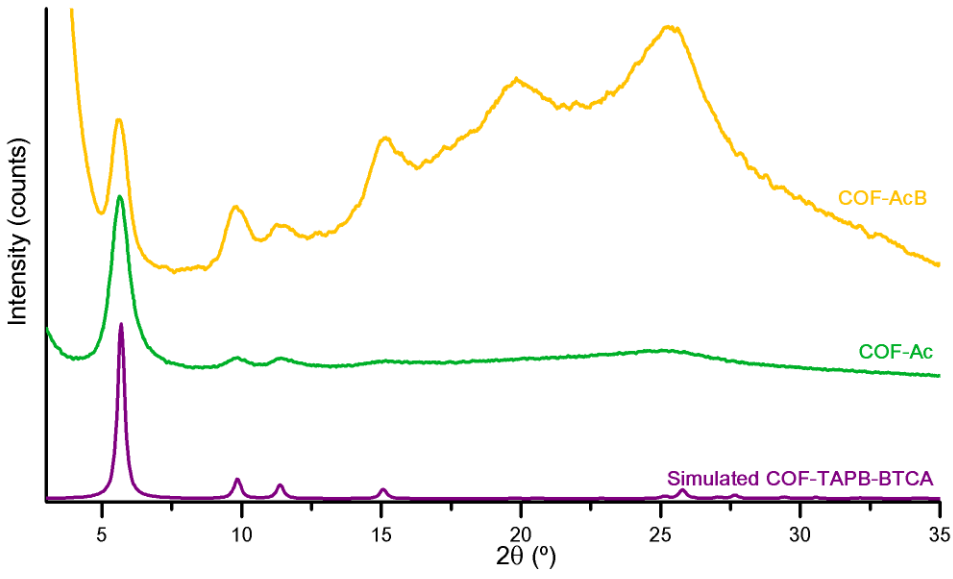

Figure 4.11. PXRD patterns of COF-AcB (orange), COF-Ac (green) and simulated pattern from the structure of COF-TAPB-BTCA (violet).

structure of the COF and additionally it revealed the presence of a higher amount of acetic acid than in **COF-Ac**. In the infrared spectrum (Figure 4.12), bands not pertaining to the COF framework were found at 1250 cm^{-1}, 1705 cm^{-1} and a very broad band over 3000 cm^{-1}, these features match well with the infrared spectra of acetic acid. Similarly, in the ^{13}C NMR spectrum (Figure 4.13), there was an extremely sharp peak at 21 ppm that was assigned to the carbon in the methyl group of acetic acid. Though these techniques detected the presence of acetic acid, they were not able to quantify it, for that purpose, the data obtained from TGA (Figure 4.14) and elemental analysis (see section A4.2.4, page 191) were employed to suggest $C_{33}H_{21}N_3 \cdot 3.5(CH_3COOH)$ as a formula that fits with the element proportions and the 27 % weight loss in the TGA (expected for this formula is 31 %). Finally, a BET surface area of 550 $m^2\ g^{-1}$ was obtained from the N_2 isotherm (Figure 4.15). The value was lower than that of **COF-Ac** despite the use of the same synthetic conditions, this

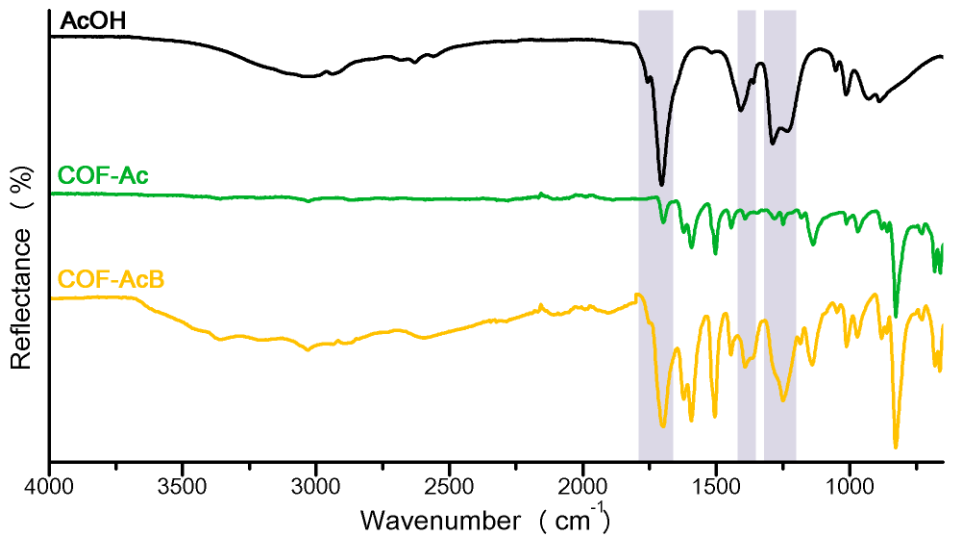

Figure 4.12. ATR-FT-IR spectra of acetic acid (black), COF-Ac (green) and COF-AcB (orange). The grey stripes highlight the bands of acetic acid that can be found also in COF-AcB spectrum.

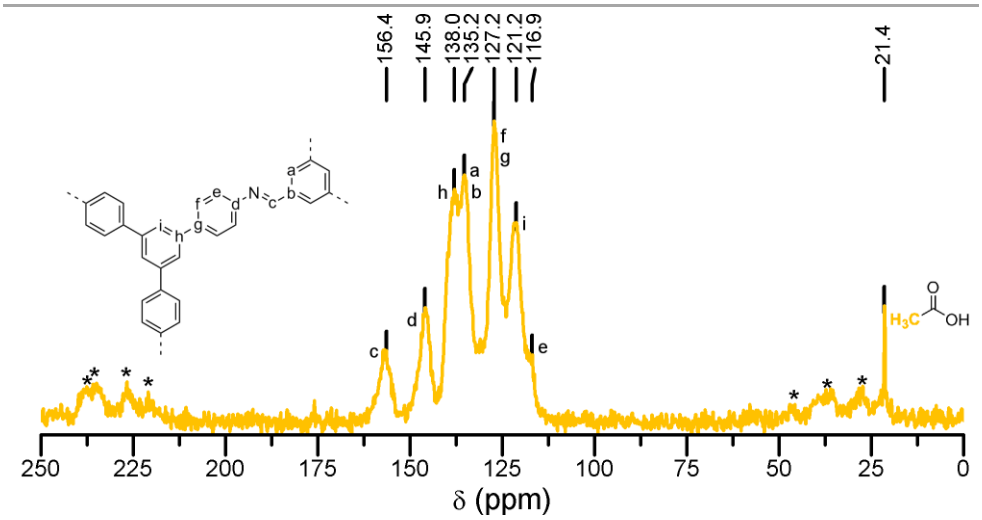

Figure 4.13. Solid state ^{13}C CP-MAS NMR spectrum of COF-AcB. Asterisks denote spinning sidebands.

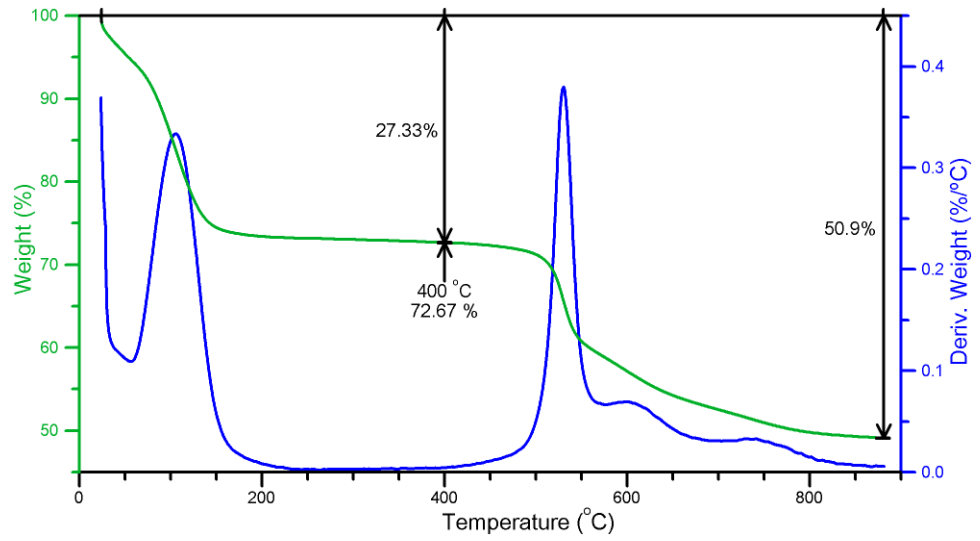

Figure 4.14. TGA trace of COF-AcB.

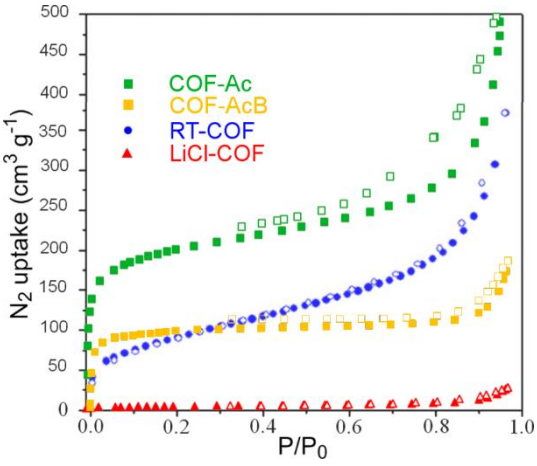

Figure 4.15. Nitrogen adsorption isotherms at 77 K for COF-Ac (green), COF-AcB (orange), RT-COF (blue) and LiCl -COF (red). Filled and open symbols correspond to adsorption and desorption, respectively.

reduction was ascribed to the fill of the channels by the acetic acid molecules. In general, the obtained data supported the formation of the target framework and a higher loading of acetic acid in **COF-AcB**.

After completing the structural characterisation and before carrying out EIS measurements to find the ionic conductivity, the powdery solid had to be shaped. It was gratifying to discover that, after following the same procedure employed for **COF-Ac**, a good quality film was obtained, and even more to confirm by EIS that the increased acetic acid content translated into a 5-fold improvement of the ionic conductivity of **COF-AcB** compared to that of **COF-Ac**. However, before proceeding to test its performance in the fuel cell, it was decided to check the microstructure of the film to try to predict if a mechanical problem like the one presented by **LiCl-COF** was likely to replicate.

Table 2. Conductivity values at 313 K of COF films at 22 % and 100 % RH.

	σ, S cm^{-1} at 313 K	
	22 % RH	100 % RH
LiCl-COF film	$< 1 \times 10^{-9}$	6.45×10^{-3}
COF-Ac	$< 1 \times 10^{-10}$	1.07×10^{-4}
COF-AcB	$< 1 \times 10^{-9}$	5.25×10^{-4}

To study the structure of the films, FESEM and AFM images of the surface of the films were acquired. In order to draw as many conclusions as possible, all the films were studied: **LiCl-COF**, **COF-Ac** and **COF-AcB**.

A FESEM image of the uniform surface of the film of **COF-Ac** was already shown in Figure 4.9; notwithstanding, there were some holes that appeared to be shallow. However, FESEM is not a suitable technique to estimate the depth of these features, so the AFM image and corresponding height profiles in Figure 4.16 were used to more accurately

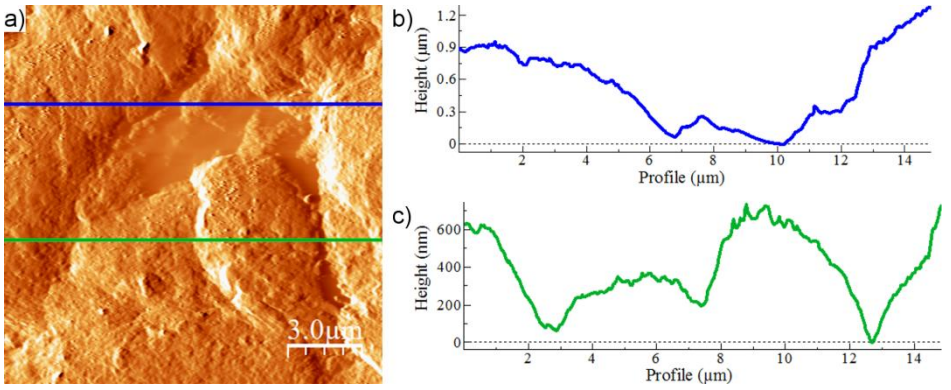

Figure 4.16. a) Representative AFM topographic image of a COF-Ac film. b,c) Height profiles measured along the correspondingly coloured lines drawn in a).

describe the morphology. In general, it can be affirmed that the surface of the film is formed by grains nearly 5 μm wide tightly packed, giving rise to steps 200-400 nm high at the grain boundaries. Nonetheless, it is not flawless and between some of the borders there are gaps smaller than 1 μm and most probably less than 1 μm deep. From the FESEM image it can be estimated that the holes are separated by distances around 3 μm.

The analysis of **LiCl-COF** films rendered very different results, furthermore, due to the massive steps encountered, AFM images were extremely difficult to obtain and therefore scarce. Nonetheless, enough information could be gathered to conclude that the film of **LiCl-COF** was composed of extensive pieces in which the material was more densely and uniformly compacted than in the previous case. However, the boundaries between these fragments were larger, forming long and deep cracks more than 2 μm wide that seem to propagate into the inside of the material.

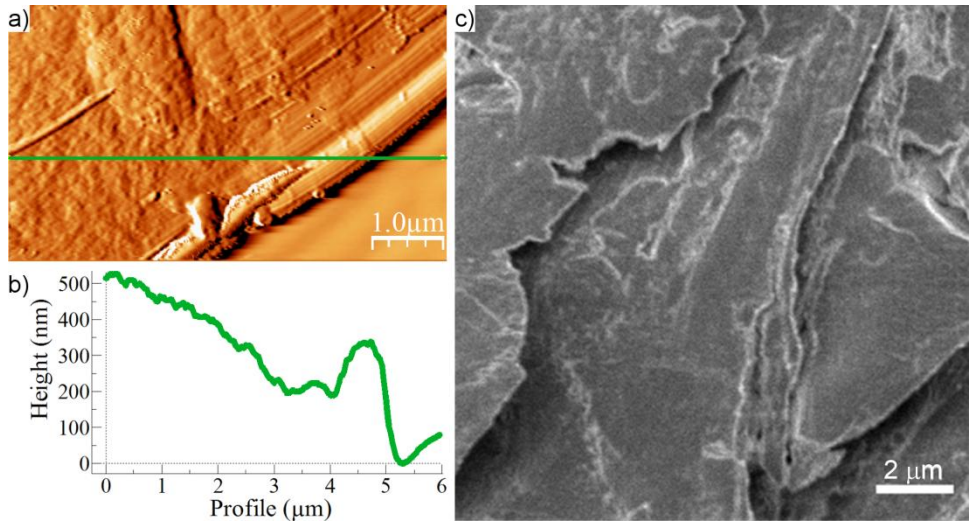

Figure 17. a) Representative AFM topographic image of LiCl-COF. b) Height profile measured along the line drawn in a). c) FESEM image of LiCl-COF.

Finally, the film of **COF-AcB** was more similar to that of **COF-Ac**. As seen in Figure 18, there were grains with a size close to 5 μm forming steps lower than 500 nm at their limits, too. The main difference lies in the size of the hollows, which in this material reach up to 3 μm in diameter, although they remain quite shallow with depths lower than 1 μm, even being the bottom of some of them visible in the SEM micrograph.

This analysis supported the hypothesis that the bad performance of **LiCl-COF** as a fuel cell membrane was due to the poor mechanical stability that led to a high hydrogen crossover rate. Considering the size, depth and amount of cracks present in the surface, it is likely that they formed an interconnected network that provided a path for gases to flow through and reach the opposite end of the cell. On the other hand, the morphology of

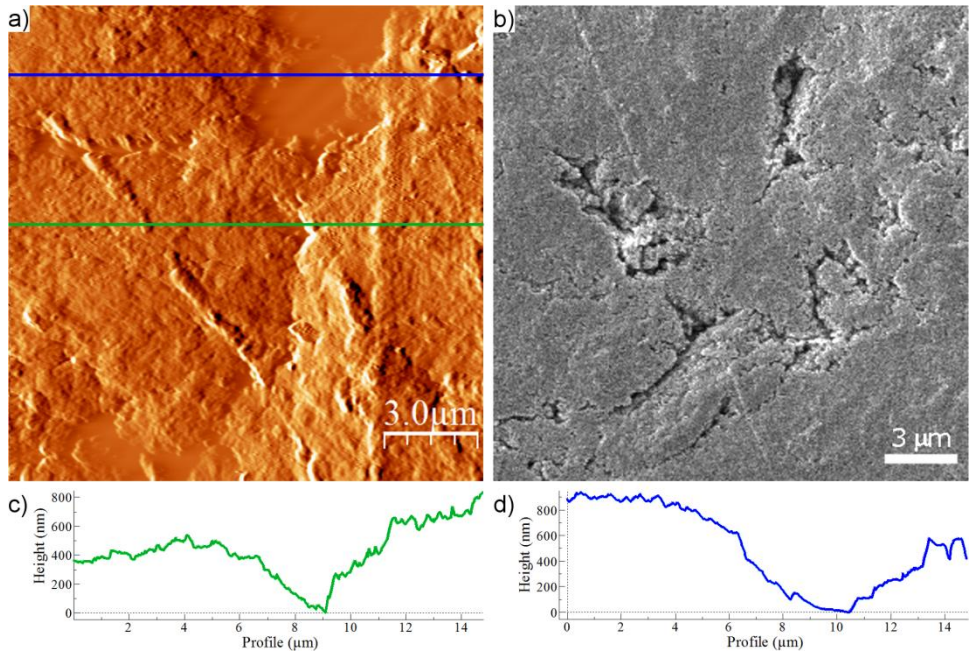

Figure 4.18. a) Representative AFM topographic image of COF-AcB. b) FESEM image of COF-AcB. c,d) Height profiles measured along the correspondingly coloured lines drawn in a).

the film of **COF-Ac** seems to create a more airtight material, which is an advantage for application in fuel cells. Lastly**,** **COF-AcB** showed features similar to **COF-Ac**, so it would be expected to perform reasonably well in the cell.

With this optimistic prospect, a MEA was constructed with a film of **COF-AcB** as solid electrolyte. Measurement of this fuel cell yielded an OCP of 0.88 V, very close to that of **COF-Ac**, and an impressive maximum power density of 12.95 mA cm^{-1}, confirming that it was necessary to achieve a balance between conductivity and mechanical properties to maximise the performance in PEMFC.

Finally, to corroborate that the differences in performance are related to the tightness of the membrane, H_2 crossover was evaluated by linear sweep voltammetry. The values obtained increased in the order **COF-AcB** (2.6×10^{-8} mol cm^{-2} s^{-1}) < **COF-Ac** (3.2×10^{-8}) < **LiCl-COF** (3.7×10^{-8}), which further supported the hypothesis that the higher performance of the acetic acid containing COFs was due to their better processability.

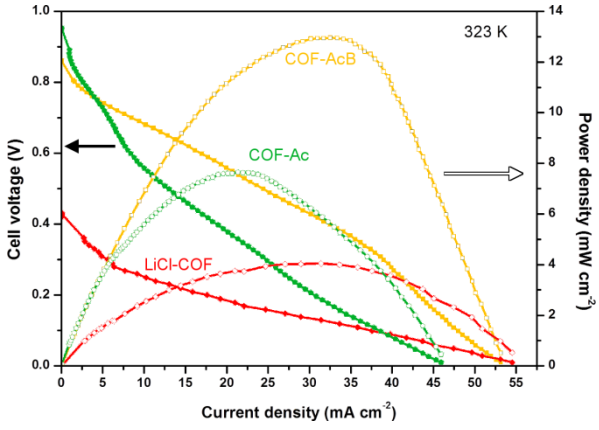

Figure 4.19. Polarisation (filled symbols) and power density (open symbols) curves of COF-AcB (orange), COF-Ac (green) and LiCl-COF (red) films acting as proton exchange membranes of H_2/O_2 fuel cells operating at 323 K.

4.3. Conclusions

In this chapter, COFs impregnated with LiCl and acetic acid were prepared and characterised. These guest molecules were found to increase the hydrophilicity of the materials, which greatly affected their ionic conductivity since all the COFs were found to display negligible conductivity in a dry environment but to increase it several orders of magnitude under high relative humidities.

Moreover, it was found that the presence of acetic acid in the COFs allows to create flexible films thinner than 300 μm by subjecting them to high uniaxial pressure in a process akin to that of pellet formation.

Finally, these COF films were tested as proton-exchange membranes for fuel cells showing promising results, as they outperformed other reported COFs in terms of power density and hydrogen crossover[15], although they were still far from competing with Nafion or COF and MOF composites. However, the most striking result of the measurements of the performances in the fuel cell was that the material with the best conductivity yielded the worst results due to the better formation of a tight membrane in the other, less conductive, acetic acid loaded COFs, highlighting the importance of a proper processing in order to bridge the gap between properties and application.

4.3.1. Future prospects

The work presented in this chapter has been continued with the aim of optimising the preparation of membranes of COFs not only to assess their use in fuel cells, but also in water filtration and gas separation. It has already been demonstrated that films with similar mechanical properties to those of **COF-Ac** can be successfully prepared for a series of different

imine-based COFs and the project is currently in a phase of scaling-up the size of the membranes to allow its implementation in the mentioned applications.

4.4. References

(1) Slater, A. G.; Cooper, A. I. Function-Led Design of New Porous Materials. *Science* **2015**, *348* (6238), aaa8075-aaa8075.

(2) Oliveira Neto, A.; Giz, M. J.; Perez, J.; Ticianelli, E. A.; Gonzalez, E. R. The Electro-Oxidation of Ethanol on Pt-Ru and Pt-Mo Particles Supported on High-Surface-Area Carbon. *J. Electrochem. Soc.* **2002**, *149* (3), A272.

(3) Nataraj, S. K.; Wang, C.-H.; Huang, H.-C.; Du, H.-Y.; Wang, S.-F.; Chen, Y.-C.; Chen, L.-C.; Chen, K.-H. Highly Proton-Selective Biopolymer Layer-Coated Ion-Exchange Membrane for Direct Methanol Fuel Cells. *ChemSusChem* **2012**, *5* (2), 392–395.

(4) Kraytsberg, A.; Ein-Eli, Y. Review of Advanced Materials for Proton Exchange Membrane Fuel Cells. *Energy & Fuels* **2014**, *28* (12), 7303–7330.

(5) Meng, X.; Wang, H.-N.; Song, S.-Y.; Zhang, H.-J. Proton-Conducting Crystalline Porous Materials. *Chem. Soc. Rev.* **2017**, *46* (2), 464–480.

(6) Vazquez-Molina, D. A.; Mohammad-Pour, G. S.; Lee, C.; Logan, M. W.; Duan, X.; Harper, J. K.; Uribe-Romo, F. J. Mechanically Shaped Two-Dimensional Covalent Organic Frameworks Reveal Crystallographic Alignment and Fast Li-Ion Conductivity. *J. Am. Chem. Soc.* **2016**, *138* (31), 9767–9770.

(7) Chandra, S.; Kundu, T.; Kandambeth, S.; Babarao, R.; Marathe, Y.; Kunjir, S. M.; Banerjee, R. Phosphoric Acid Loaded Azo (-N═N-) Based Covalent Organic Framework for Proton Conduction. *J. Am. Chem. Soc.* **2014**, *136* (18), 6570–6573.

(8) Peng, Y.; Xu, G.; Hu, Z.; Cheng, Y.; Chi, C.; Yuan, D.; Cheng, H.; Zhao, D. Mechanoassisted Synthesis of Sulfonated Covalent Organic Frameworks with High Intrinsic Proton Conductivity. *ACS Appl. Mater. Interfaces* **2016**, *8* (28), 18505–18512.

(9) Xu, H.; Tao, S.; Jiang, D. Proton Conduction in Crystalline and Porous Covalent Organic Frameworks. *Nat. Mater.* **2016**, *15* (7), 722–726.

(10) Romero, J.; Rodriguez-San-Miguel, D.; Ribera, A.; Mas-Ballesté, R.; Otero, T. F.; Manet, I.; Licio, F.; Abellán, G.; Zamora, F.; Coronado, E. Metal-Functionalized Covalent Organic Frameworks as Precursors of Supercapacitive Porous N-Doped Graphene. *J. Mater. Chem. A* **2017**, *5* (9), 4343–4351.

(11) Hanzawa, Y.; Kaneko, K. Lack of a Predominant Adsorption of Water Vapor on Carbon Mesopores. *Langmuir* **1997**, *13* (22), 5802–5804.

(12) Paranthaman, S.; Coudert, F.-X.; Fuchs, A. H. Water Adsorption in Hydrophobic MOF Channels. *Phys. Chem. Chem. Phys.* **2010**, *12* (28), 8123.

(13) Canivet, J.; Bonnefoy, J.; Daniel, C.; Legrand, A.; Coasne, B.; Farrusseng, D. Structure–property Relationships of Water Adsorption in Metal–organic Frameworks. *New J. Chem.* **2014**, *38* (7), 3102–3111.

(14) Xu, H.; Gao, J.; Jiang, D. Stable, Crystalline, Porous, Covalent Organic Frameworks as a Platform for Chiral Organocatalysts. *Nat. Chem.* **2015**, *7* (11), 905–912.

(15) Shinde, D. B.; Aiyappa, H. B.; Bhadra, M.; Biswal, B. P.; Wadge, P.; Kandambeth, S.; Garai, B.; Kundu, T.; Kurungot, S.; Banerjee, R. A Mechanochemically Synthesized Covalent Organic Framework as a Proton-Conducting Solid Electrolyte. *J. Mater. Chem. A* **2016**, *4* (7), 2682–2690.

Chapter 5: Encapsulation of nanoparticles in COF spheres

5.1. Introduction

Construction of composites that integrate the singular properties of metal and metal-oxide nanoparticles (NPs) with those of porous materials has been successfully achieved by physical confinement of the NPs in a matrix made of the porous material. This approach sinergistically combines the strengths of the materials and significantly reduces their limitations as the porous matrix acts not only as a sieve, selectively providing access to the NPs, but also as a dispersive and protective medium preventing their aggregation. This combination has proven effective in a number of applications ranging from catalysis[1], gas storage[2] and environmental remediation[3] to batteries[4], magnetic refrigeration[5] and controlled guest release[6].

These types of composites have been prepared with various porous materials such as activated carbon[7], silica[8], zeolites[9] and MOFs[10] using a collection of different strategies. One of the most interesting approaches that has given good results in the preparation of MOF/NP composites is the encapsulation of pre-synthesised NPs into the MOF crystals by forming the MOF in the presence of the NPs[11]. It has the advantage of allowing complete control over the size, shape and composition of the NPs, which are the determining factors of their properties. In some experiments it was possible even to determine the number and localisation of the NPs confined in the MOF crystals[12,13]. However, this method had not been applied to COFs due to the incompatibility of the conditions used to synthesise COFs with NP stability. For this reason, one

of the first examples of NP functionalisation of a COF employed a strategy consisting in infiltrating NP precursors in the already built framework and subsequently growing the NP inside the pores[14].

A further disadvantage of that approach is the lack of dispersibility of the COFs obtained by common methods. That is one of the properties of NPs that depending on the application can either be a boon or turn into a curse. Of course, for solid state applications, an extended matrix that anchors the NPs while preventing aggregation and the ensuing loss of properties is needed. However, especially for use in medical and biological environments, transferring the small size and colloidal nature of the NPs in the final system is essential[15]. Although several works had described procedures to prepare dispersible COF spheres with diameters of a few hundreds of nanometres[16–18] or even smaller[19], none had been used to encapsulate NPs.

In order to overcome this limitation, a two-step strategy was suggested. In a first step, the building blocks of the COF would be mixed in a medium compatible with NPs and that would lead to the formation of a spherical particles of the organic material. If NPs were added to the mixture, it would be possible for them to be embedded in the polymer spheres[20]. Given all the requirements of this first step, it was likely that conditions directly affording a crystalline framework were not found. Therefore, the second step consisted in transforming the probable amorphous network into an ordered COF structure, which shortly before had been demonstrated to be possible[21]. A similar method that had recently been successfully employed to coat 200 nm iron oxide spheres with an imine-based COF[22] served as a positive precedent of the strategy.

Therefore, in this chapter, the formation of spheres of an imine-based COF via a two-step process and its potential to fabricate COF/nanoparticle composites will be described.

5.2. Results and discussion

After screening a range of solvents and conditions, it was found that mixing solutions of **TAPB** and **BTCA** in acetone at room temperature with some acetic acid as catalyst yielded an incredibly stable yellow dispersion (Figure 5.1). Encouraged by the highly homogeneous aspect of the dispersion, dynamic light scattering (DLS) was used to measure the hydrodynamic diameter of the particles (Figure 5.2a), resulting in a fairly monodisperse distribution centered around 800 nm. In order to corroborate this data, the dispersion was centrifuged to isolate the yellow particles, which washed and dried under vacuum to yield a yellow finely powdered solid (named **s-PI** from this point onwards) that was studied by SEM. The micrographs showed particles with a spherical morphology and a diameter close to 600 nm (Figure 5.2b). The statistical analysis of a large number of spheres (Figure 5.2c) confirmed the monodisperse nature of the sample previously indicated by DLS. The higher size measured by DLS was attributed to this technique providing values of hydrodynamic diameter, which includes the solvation shell of the particles and therefore is always larger than the actual size of the particles.

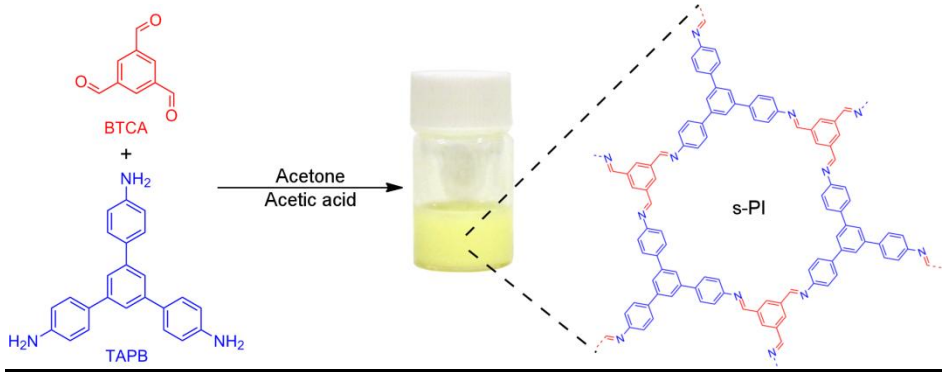

Figure 5.1. Scheme of the synthesis of s-PI as a highly stable dispersion in acetone.

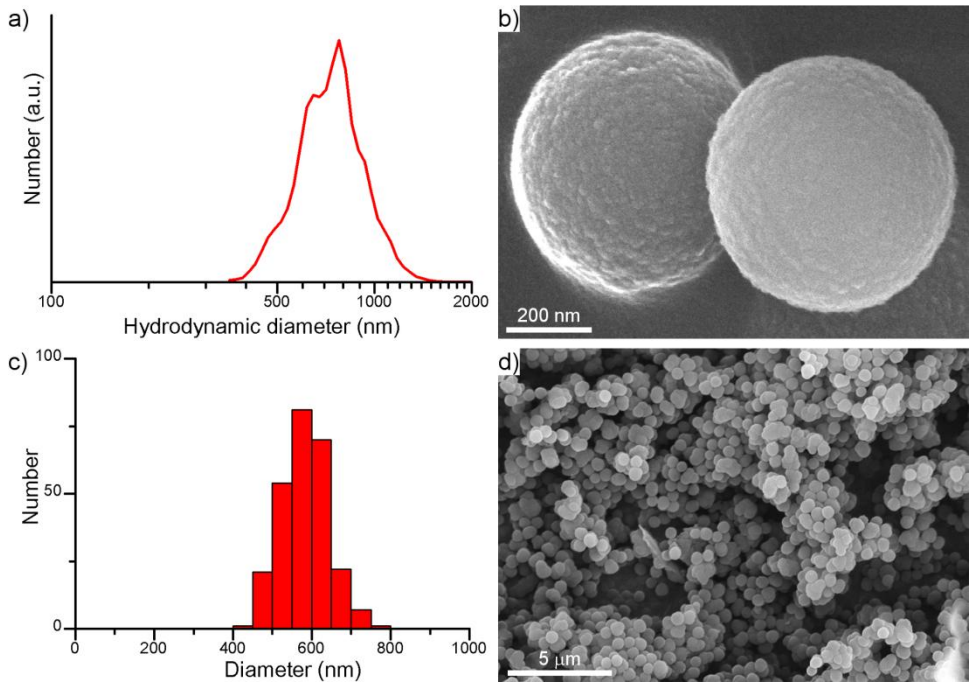

Figure 5.2. a) Hydrodynamic diameter distribution of s-PI as measured by DLS. b) Representative FESEM image of two isolated s-PI spheres. c) Diameter distribution of s-PI spheres using data extracted from the measurement of 250 particles in d). d) Low magnification FESEM image of s-PI.

Intrigued by the high-quality of the morphology, unveiling some details of the formation process of **s-PI** was attempted. Consequently, the evolution of the polymerisation was monitored by DLS and FESEM. Since the reaction proceeds within a few seconds when carried out in the conditions normally used to obtain **s-PI**, these experiments were performed with a lower acetic acid concentration to decrease the reaction rate and allow the characterisation of the intermediate materials involved in the process. From the data in Figure 5.3a, three different stages were differentiated. The first one, at times lower than 28 minutes, was characterised by the presence of small particles around 30-40 nm (Fig 5.3b). Longer reaction times up to 40 minutes led to the slow aggregation of these particles

during stages ii and iii resulting in quasi-spherical particles that growed continuously until forming the final 600 nm spheres (Figure 5.3c-d). It is remarkable that as shown in Figure 5.3e, these newly formed spheres showed significant roughness that decreased over time to yield the smooth particles characteristic of **s-PI** (Figure 5.3f). This roughness

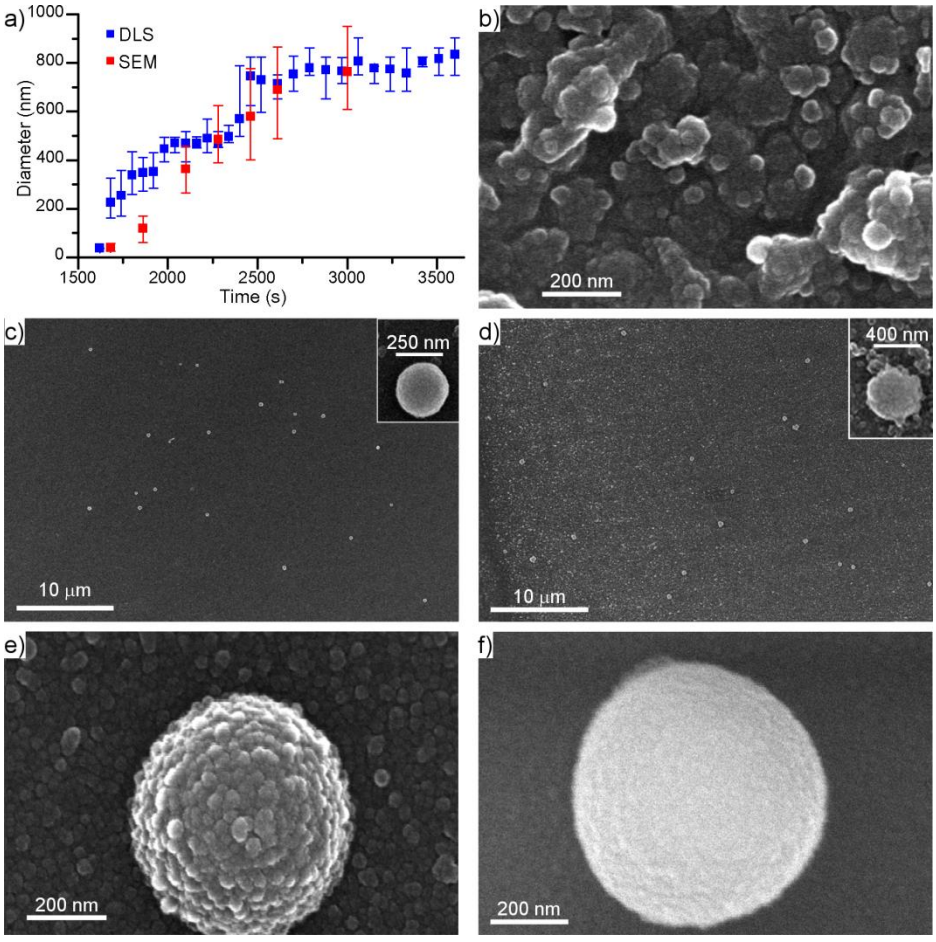

Figure 5.3. a) Evolution of the particle size of s-PI with reaction time. Size estimated by both DLS (blue) and FESEM (red). b-d) Representative FESEM micrograph of spheres isolated at b) stage i, c) stage ii and d) stage iii. Insets show individual particles. e,f) FESEM images of isolated spheres after e) 40 and f) 50 minutes of reaction.

reduction was a consequence of the coalescence of the 30 nm particles facilitated by the presence of reactive groups on their surface and the reversibility of the imine bond.

Having achieved the formation of uniform submicrometric spheres, the PXRD diffraction pattern of **s-PI** was acquired to check if this procedure led to the formation of an ordered material. Disappointingly although not surprisingly, the pattern showed extremely weak reflections at the angles expected for **COF-TAPB-BTCA** (Figure 5.4). This indicated that **s-PI** was a spherical and amorphous polyimine and that the second synthetic step was necessary to obtain a crystalline and porous COF.

The crystallisation of the amorphous **s-PI** was achieved using the conditions reported by Dichtel and co-workers.[21], which enable a high bond reversibility by treating the material with aqueous acetic acid in a dioxane/mesitylene mixture at 70 ºC for 7 days. PXRD (Figure 5.4)

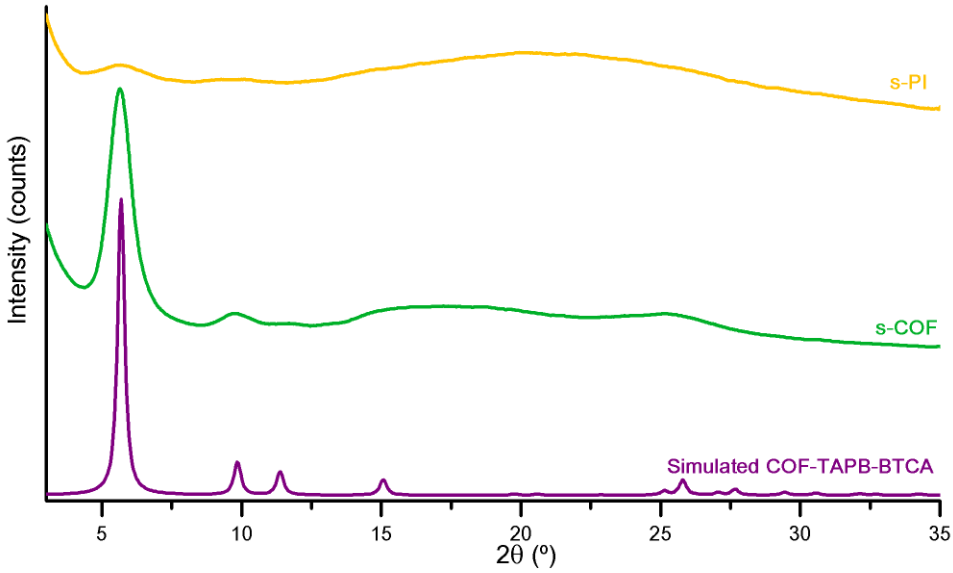

Figure 5.4. PXRD pattern of s-PI (orange), s-COF (green) and simulated pattern from the structure of COF-TAPB-BTCA (violet).

showed a huge increase in crystallinity, moreover, the pattern matched the simulated one for **COF-TAPB-BTCA**, confirming the success of the recrystallisation step. Additionally, the morphology of this crystalline material was studied by FESEM (Figure 5.5), which showed spheres with a diametre close to 600 nm without any significant change in shape and size in comparison to s-PI, apart from a higher roughness. In order to distinguish this ordered spherical COF from the amorphous **s-PI**, it will be referred as s-COF in this chapter.

The structural characterisation of these two materials was completed with infrared and ^{13}C CP-MAS NMR spectroscopies and elemental and thermogravimetric analyses. The ATR-FT-IR shown in Figure 5.6 indicated the formation of imine bonds (C=N stretch at 1623 cm^{-1}) in both materials. However, a slight difference was detected regarding the disappearance of the bands corresponding to unreacted aldehydes and amines, as in s-PI spectrum residual N-H stretchs can be seen and the carbonyl stretch at 1689 cm^{-1} is much more intense than in **s-COF**. This indicated that there was a higher degree of conversion in **s-COF** than in **s-PI**, which is logical since an amorphous network is bound to have unreacted groups not only

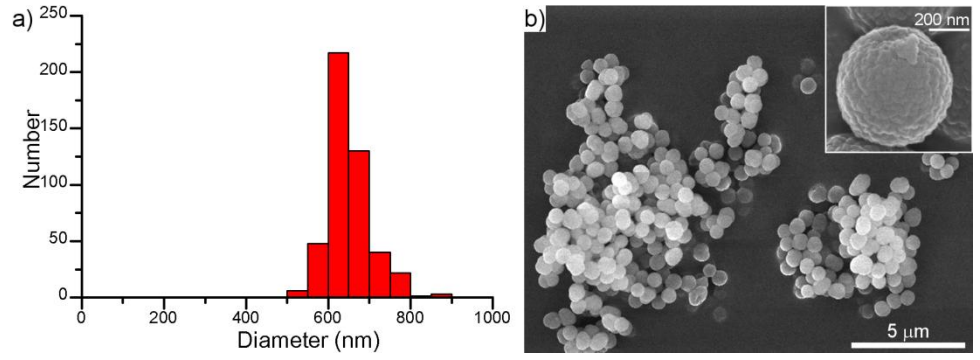

Figure 5.5. a) Diameter distribution of s-COF spheres using data extracted from the measurement of 450 particles imaged by FESEM. b) Representative FESEM image of s-COF spheres. Inset shows an individual particle.

at grain boundaries but throughout the whole material. ^{13}C NMR spectra (Figure A5.1, page 200) were very similar to those shown in other chapters; did not show remarkable differences and complied with the expected structure displaying a new peak at 156.7 ppm corresponding to the imino carbon. The same can be said of the TGAs (Figure A5.2, page 200) and elemental analyses (see section A5.2, page 195), they showed the same decomposition profile as **COF-TAPB-BTCA** prepared with other methods, and the formula $C_{33}H_{21}N_3 \cdot H_2O$ was proposed for both materials, accounting the loss of that water molecule for a 3.8 % weight loss, which is consistent with the TGAs. These data, together with the PXRD diffraction, corroborate the formation of an extended imine-linked network, disordered in the case of **s-PI** and ordered in **s-COF**.

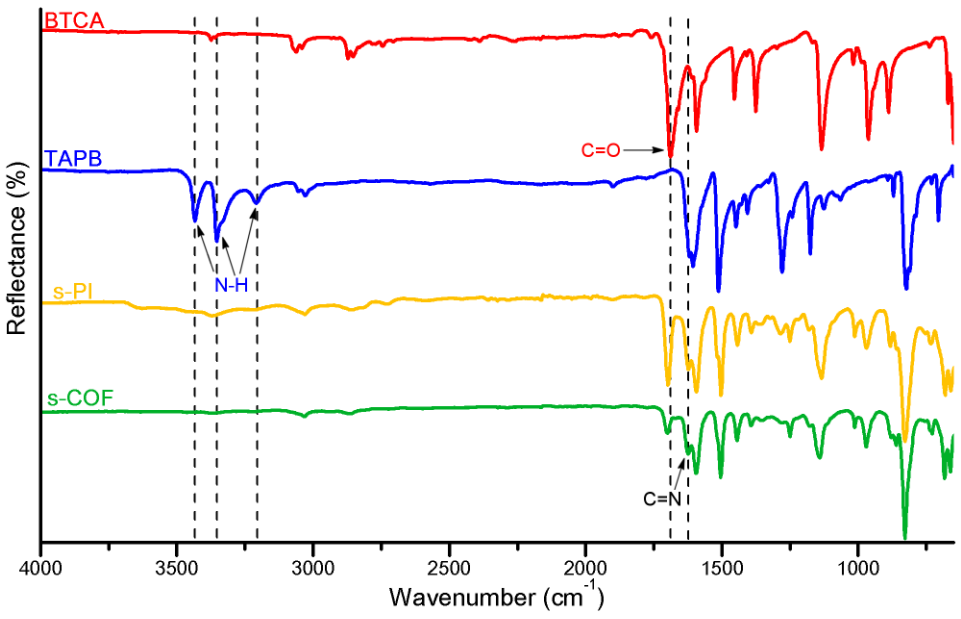

Figure 5.6. ATR-FT-IR spectra of monomers BTCA (red) and TAPB (blue), of s-PI (orange) and of s-COF (green). The most significant changes are highlighted: Disappearance of N-H stretching bands between 3300-3500 cm^{-1}, decrease of the intensity of C=O stretching band at 1689 cm^{-1}, and appearance of C=N stretching band at 1623 cm^{-1}.

The impressive improvement of crystallinity motivated the study of the amorphous to crystalline transformation. To carry out this investigation, samples were collected after subjecting **s-PI** to the recrystallising treatment for 2, 12, 24, 48 and 168 h. They were characterised by PXRD (Figure 5.7), which showed a clear evolution of the crystallinity as a function of time, with all the peaks matching the calculated ones. Furthermore, TEM images of several of the samples were also acquired and both confirm that the morphology of the particles does not undergo any change and reflect the increase in crystallinity. The micrographs in Figure 5.8 corresponding to samples crystallised for different times showed completely round particles of the same size for all the cases. Moreover, the increase in roughness detected by FESEM, was shown to be gradual, and therefore was attributed to the formation of larger crystalline domains of COF that, being an ordered and rigid structure, does not adapt well to the round shape of a sphere.

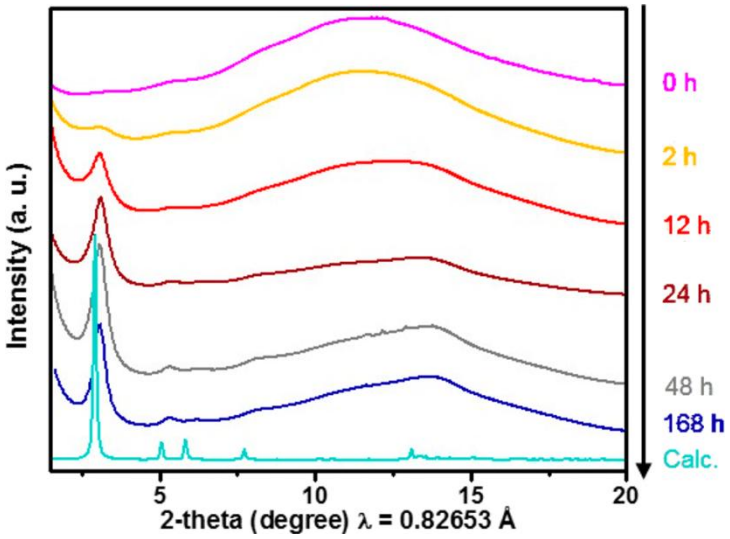

Figure 5.7. PXRD patterns from s-PI and s-COF recrystallised for 2, 12, 24, 48 and 168 h and simulated pattern from the structure of COF-TAPB-BTCA, showing the evolution of crystallinity during the amorphous-to-crystalline transformation.

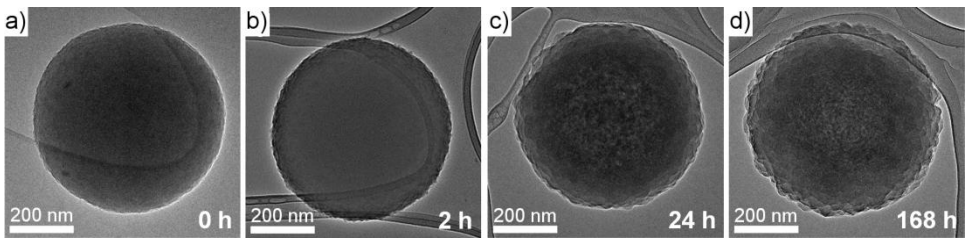

Figure 5.8. TEM images showing the evolution of the roughness of the spheres after being recrystallised for a) 0, b) 2, c) 24, and d) 168 h.

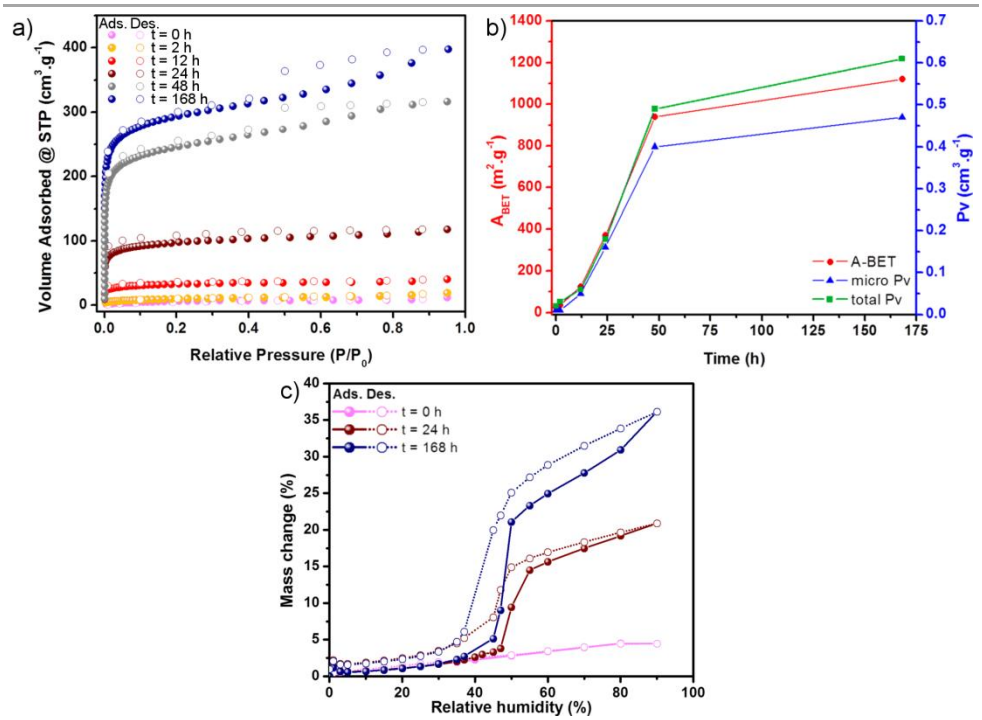

Figure 5.9. Evolution of porosity with crystallisation time as evidenced by a) nitrogen isotherms of s-COF recrystallised for 0 (pink), 2 (orange), 12 (red), 24 (brown), 48 (grey) and 168 h (blue). b) BET surface area (red) and micropore (blue) and total pore (green) volume as a function of recrystallisation time. c) water sorption uptake of s-COF recrystallised for 0 (pink), 24 (brown) and 168 h (blue).

The increase in the quality of the material was further confirmed by the N_2 adsorption isotherms obtained at 77 K (Figure 5.9a). The calculated BET surface areas showed a dramatic and gradual increase from non-porous s-PI with an area of 25 m^2 g^{-1} and a pore volume of 0.02 cm^3 g^{-1} to the highly porous **s-COF** treated for 7 days that displayed an area of 1120 m^2 g^{-1} and a pore volume of 0.61 cm^3 g^{-1} (Figure 5.9b). In light of the high porosity found, CO_2 and water vapour sorption were also investigated. The water vapour isotherms of **s-PI**, **s-COF** and the material crystallised for 24 h showed a gradual transition from hydrophobic to hydrophilic behaviour (Figure 5.9c). While the water uptake of **s-PI** is limited to 0.04 g_{water} g_{COF}^{-1}, the more porous s-COF showed a capacity of 0.37 g_{water} g_{COF}^{-1} and the type V isotherm typical of water sorption in porous materials with hydrophobic walls[23,24]. Finally, the CO_2 sorption isotherms of **s-PI** shown in Figure 5.10a proved that it was slightly porous to CO_2 despite its non-accessibility to N_2. Also, as expected, **s-COF** exhibited a much higher uptake. The heats of adsorption derived from the isotherms collected at temperatures between 258 and 298 K fell in the usual range for materials without a special design to interact with CO_2[25]. The slightly higher values of **s-PI** were attributed to its smaller pore, which is suggested by the fact that it is non-porous to N_2.

It was clear that most of the properties improve along crystallinity and that the morphology of the particles was maintained. However, there was an essential property of **s-PI** that had not been tested, it had been described previously that it was possible to prepare stable dispersions of **s-PI** in water, a solvent irreplaceable in many applications[26]. Satisfyingly, as can be seen in Figure 5.11, the DLS measurements did not show a significant change in the size of the particles, implying that the degree of aggregation is similar for both materials and that the water dispersibilty of **s-PI** is preserved in **s-COF** after the crystallisation treatment.

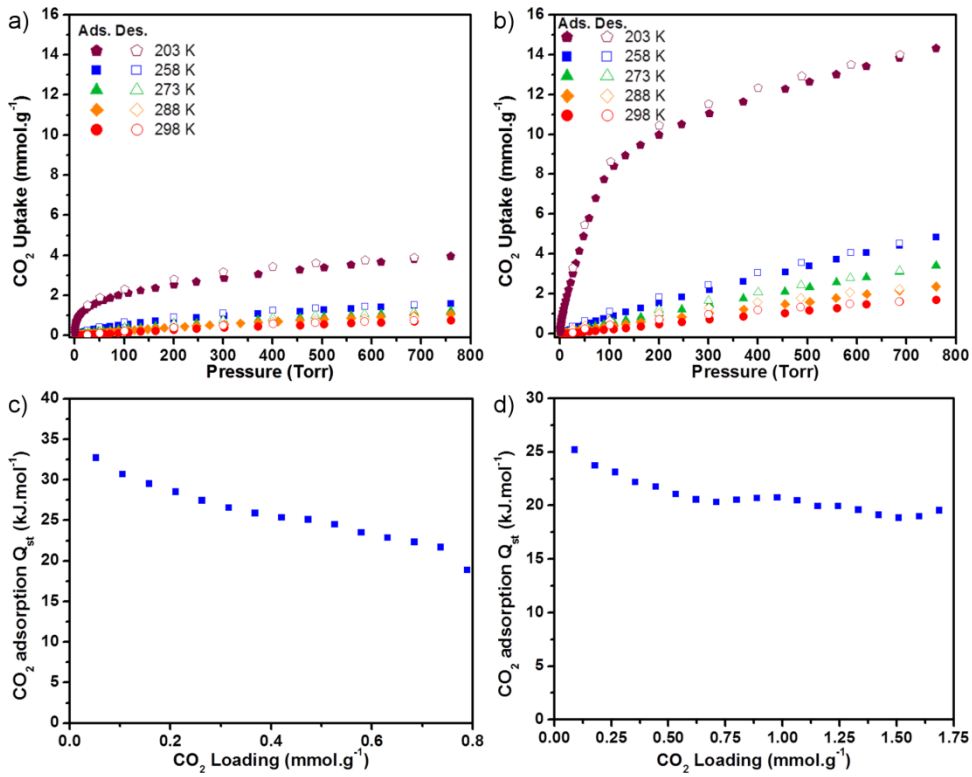

Figure 5.10. a,b) CO_2 sorption isotherms collected at 203 K, 258 K, 273 K, 288 K and 298 K for a) s-PI and b) s-COF. c,d) Heat of adsorption of CO_2 for c) s-PI and d) s-COF.

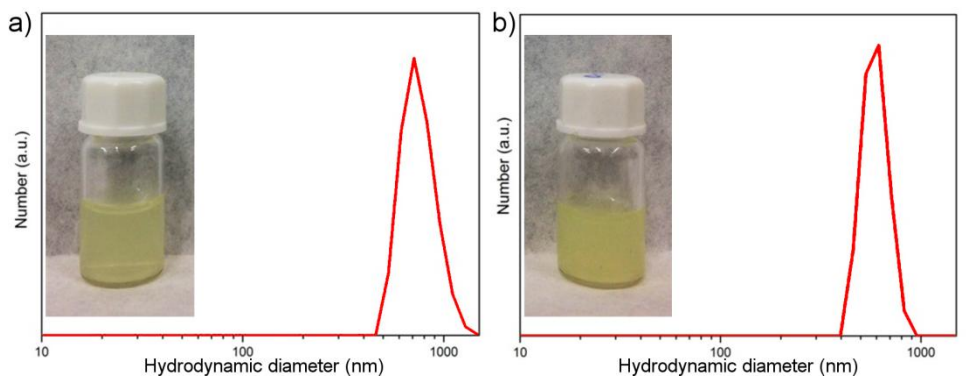

Figure 5.11. DLS measurements of aqueous colloidal suspensions of a) s-PI and b) s-COF. The insets show photographs of the corresponding dispersions.

Having proven the validity of the methodology to transform an amorphous imine-linked polymer into a crystalline and porous COF without affecting its shape and size, the fabrication of the composites of metal and metal oxide NPs confined inside dispersible COF spheres was taken over. The strategy is summarised in Figure 5.12 and begins by forming the spherical **s-PI** in the presence of NPs, which was anticipated to lead to non-porous spheres with trapped NPs. Finally, these spheres are subjected to the recrystallisation process, yielding COF spheres with NPs in the inside. Since the NPs are immobilised in the polymer sphere, they are expected to not be affected by the conditions used in the second step.

First, the strategy was tested with Fe_3O_4 NPs with a diameter around 10 nm. To allow dispersion of the NPs in acetone, which is the solvent for the first step, they were functionalised with polyvinylpyrrolidone (PVP). The building blocks (**TAPB** and **BTCA**) were dissolved in the NP suspension in acetone and subsequently mixed under ultrasonication to reduce the aggregation of the polyimine particles driven by the magnetism of the NPs. This led to the formation of a brownish yellow powder that was recrystallised as explained above. The final material could be dispersed in water and showed was attracted to magnets (Figure 5.13a), which hinted

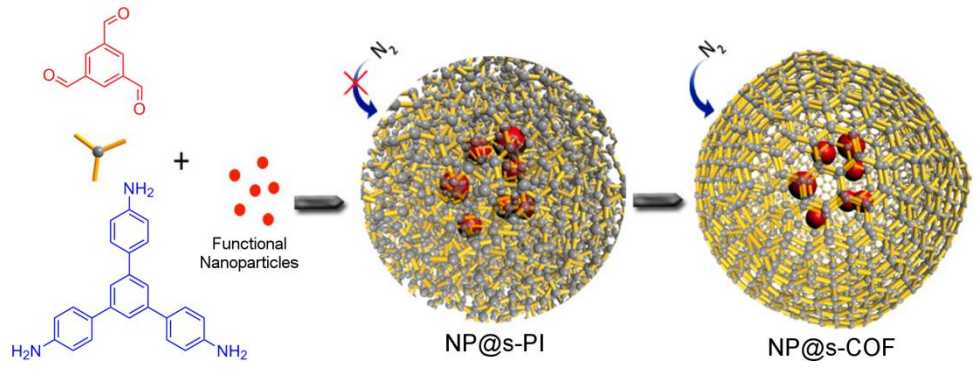

Figure 5.12. Scheme for the encapsulation of NPs in COF spheres following a two-step process.

towards the success of the encapsulation of Fe_3O_4 NPs. To fully assess the effectiveness of the strategy, high-angle annular dark-field scanning transmission electron microscopy images of both the amorphous material (**Fe_3O_4@s-PI**) and the crystallised one (**Fe_3O_4@s-COF**) were acquired (Figure 5.13b-c). The images showed sub-micrometre spheres correlating well with those of non-functionalised s-COF. Additionally, dispersed close

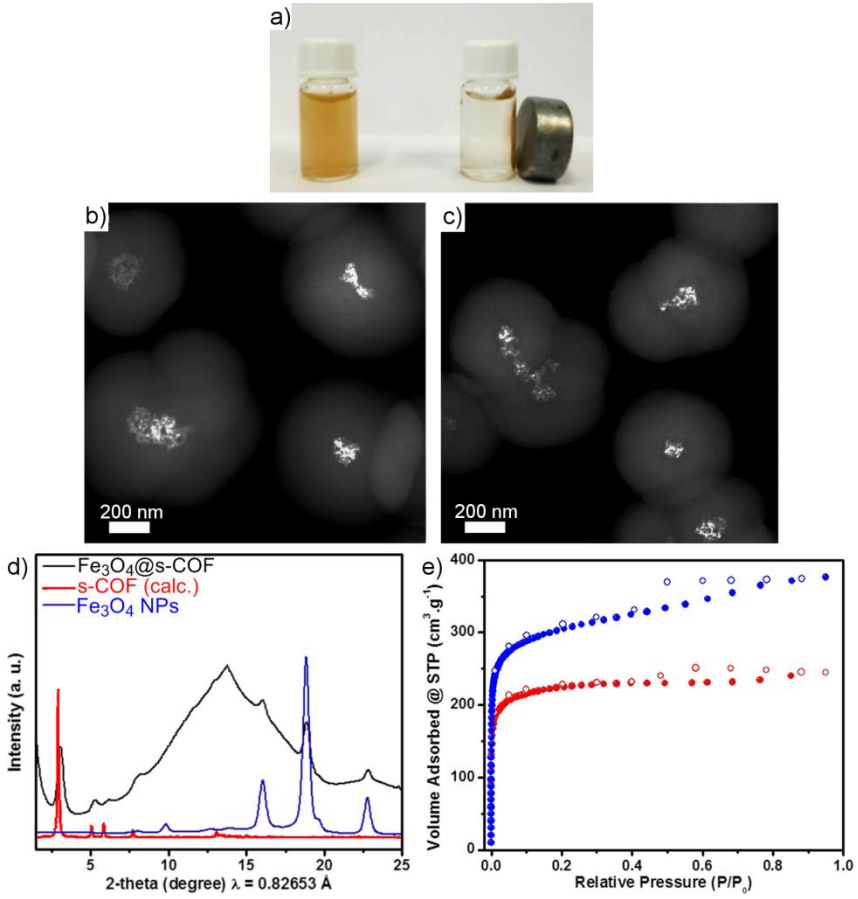

Figure 5.13. a) Photograph of Fe_3O_4@s-COF dispersed in water being attracted to a magnet. b,c) HAADF-STEM images of b) Fe_3O_4@s-PI and c) Fe_3O_4@s-COF. d) PXRD pattern of Fe_3O_4@s-COF (black) and Fe_3O_4 NPs (blue) and calculated PXRD pattern of s-COF (red). e) N_2 sorption isotherms of s-COF (blue) and Fe_3O_4@s-COF (red).

to the center of these spheres, small bright dots were found, these light features were believed to be the Fe_3O_4 NPs. This suggestion was confirmed by energy-dispersive X-ray (EDX) microanalysis, which revealed that every sphere contained iron, oxygen, nitrogen and carbon. The presence of Fe_3O_4 NPs was corroborated by PXRD (Figure 5.13d), which showed both the signature peaks of the COF matrix and of the iron oxide particles. In order to quantify the iron content in the composite, it was analysed by ICP-MS, which afforded a result of 7.6 % w/w of Fe_3O_4 content. Last, N_2 sorption at 77 K was used to evaluate the permanent porosity of **Fe_3O_4@s-COF** (Figure 5.13e). As expected, the sample was porous but its BET area of 880 $m^2\ g^{-1}$ and pore volume of 0.38 $cm^3\ g^{-1}$ were lower than those of **s-COF**, which is reasonable given that the iron oxide NPs are not porous.

The functionalisation with Fe_3O_4 NPs imparts the COF with magnetic properties, allowing for example its fast and easy recovery from solution as shown in Figure 5.13a. With the aim of broadening the scope of properties that COFs can be provided with, gold and palladium NPs of 9 and 3 nm, respectively, were used to prepare catalytically active dispersible composites. The same procedure described above was followed, in this case dissolving the building blocks in suspensions of either Au or Pd NPs. Figure 5.14 shows the PXRD patterns of **Au@s-COF** and **Pd@s-COF**, which exhibited the characteristic peaks of s-COF as well as the diffractions associated with the corresponding metal NPs, confirming the presence of both materials in the composite. Moreover, HAADF-STEM images of the amorphous and crystalline materials both showed spheres with a few metal NPs close to their center (Figure 5.15), which indicated the success and generality of this approach to encapsulate NPs in polyimine spheres that can be transformed to highly crystalline and porous COFs without modifying neither the size and shape of the matrix nor the size of the metal NPs.

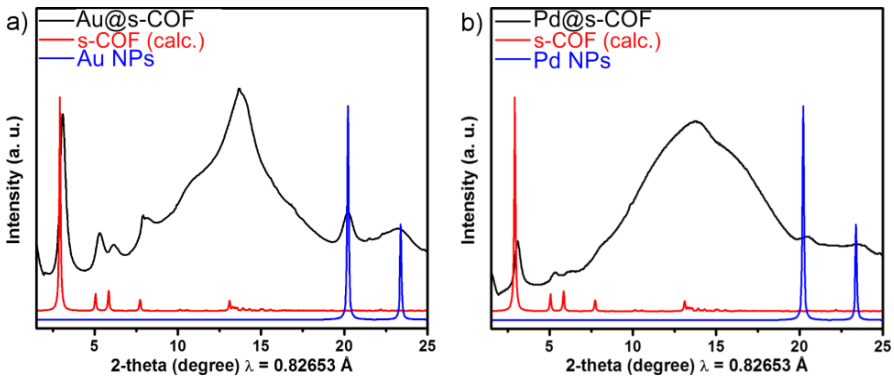

Figure 5.14. a) PXRD patterns of s-COF (red), Au NPs (blue) and Au@s-COF (black). b) PXRD patterns of s-COF (red), Pd NPs (blue) and Pd@s-COF (black).

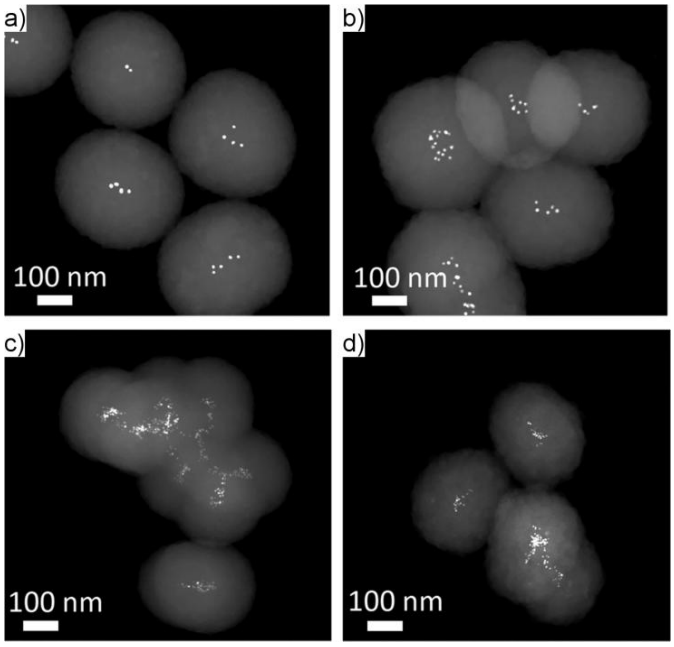

Figure 5.15. HAADF-STEM images of a) Au@s-PI, b) Au@s-COF, c) Pd@-sPI and d) Pd@s-COF. All of them showing several metal NPs encapsulated in the center of the organic spherical matrix.

Finally, it was left to verify that the catalytic properties of the metal NPs had not been lost in the process. In fact, this type of composite should prove very attractive for heterogenous catalysis. However, for this to happen, besides the metal retaining its properties, the COF matrix should allow accessibility of the molecules to the embedded NPs. As a proof-of-concept, the reduction of 4-nitrophenol into 4-aminophenol by sodium borohydride ($NaBH_4$), a typical model reaction for nanoparticle catalysis[27], was carried out with these gold and palladium composites as catalysts (Figure 5.16a).

To perform this test, five different experiments were run, using **Au@s-COF** (Au content: 3.5 % w/w) and **Pd@s-COF** (Pd content: 1.1 % w/w), their amorphous counterparts **Au@s-PI** and **Pd@s-PI** and non-functionalised s-COF. Aqueous dispersions of each of the solids were prepared and mixed with solutions of $NaBH_4$ and 4-nitrophenol. The progress of the reaction was followed by ultraviolet-visible (UV-Vis) spectroscopy as the band at 400 nm corresponding to the nitroarene is expected to decrease, accompanied by the appearance of a new band at 305 nm generated by the reduced 4-aminophenol. While the control experiment with s-COF showed no change, and therefore no sign of catalytic activity, over 16 minutes and the same happened with the amorphous **Au@s-PI** and **Pd@s-PI**; the porous **Au@s-COF** and **Pd@s-COF** allowed the reaction to be complete after 10 and 14 minutes, respectively (Figure 5.16b-f). Moreover, as shown in Figure 5.16g, the morphology of the composite is retained after the catalysis test and the NPs are still encapsulated in the **s-COF** matrix. Several conclusion were derived from these results. The lack of activity of **s-COF** demonstrated that the imine-linked framework was not able to catalyse this reaction, proving that the catalytically active part are the metal NPs. Moreover, the fact that the amorphous **Au@s-PI** and **Pd@s-PI** were not able to catalyse

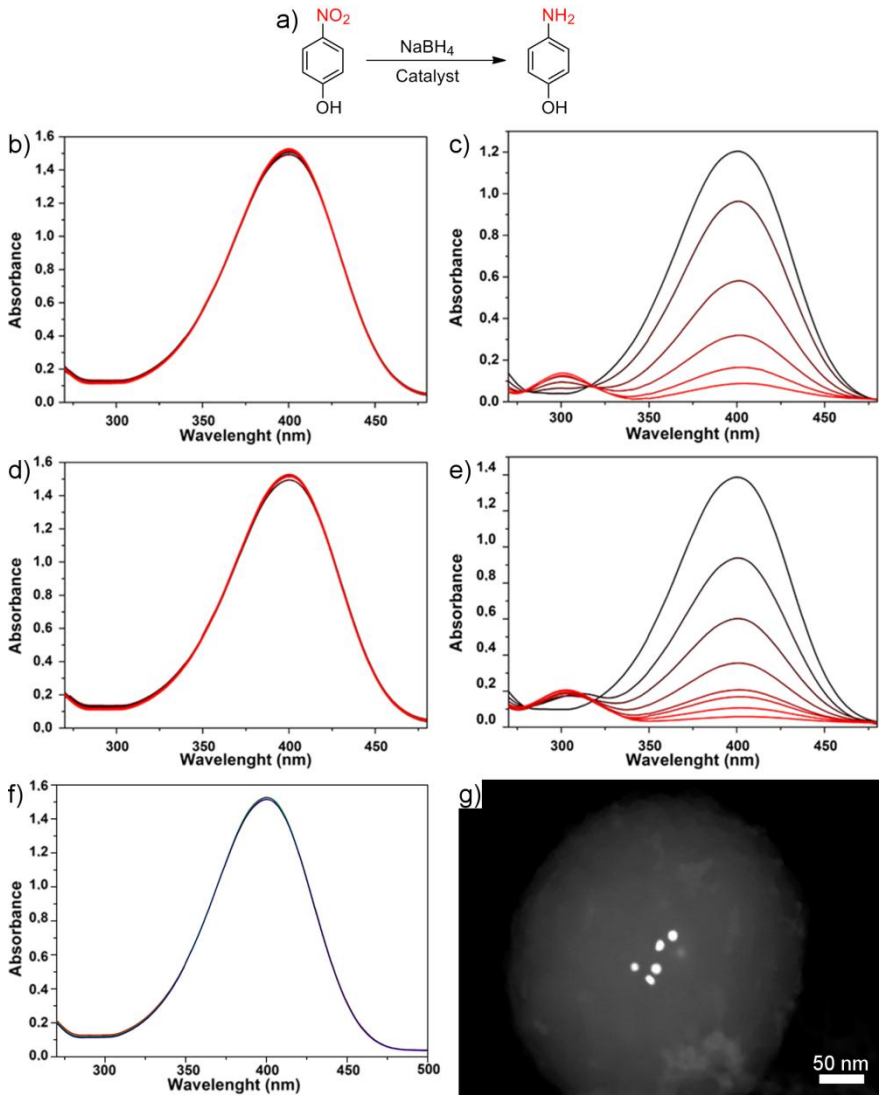

Figure 5.16. a) Scheme of the model reaction used to assess the catalytic properties of the composites. b-f) Evolution of 4-nitrophenol reduction followed by UV-Vis spectroscopy when b) Au@s-PI, c) Au@s-COF, d) Pd@s-PI, e) Pd@s-COF and f) s-COF are used as catalyst. The spectra were collected at intervals of 2 min. g) HAADF-STEM image of Au@s-COF after catalysis.

either highlights the importance of a porous matrix that allows access to the functional NPs. Additionally, since the only way for these non-porous composites to catalyse the reaction would have been if some non-confined particles were present, either because of lixiviation or because they were not encapsulated during the synthesis, these experiments allowed to rule out these two possibilities. As a result, it was claimed that the metal NPs confined in s-COF are not damaged by the recrystallisation procedure and maintain their catalytic properties, which can be employed thanks to the porosity of the COF matrix, that allows the reactants to diffuse through it and reach the NPs.

5.3. Conclusions

In this chapter, the formation of crystalline COF submicrometric spheres in a two-step process was described. This strategy proved extremely successful as the initially formed amorphous spheres were transformed in highly crystalline and porous ones while maintaining size, shape and some important properties such as water dispersibility.

Additionally, the developed methodology allowed the fabrication of composites with metal and metal oxide nanoparticles. These composites consist in COF spheres with several nanoparticles around the center of the sphere that due to the porous nature of the COF can be easily reached by external molecular species. During the synthetic process, the properties of the nanoparticles are preserved, which allows to obtain materials with magnetic or catalytic properties.

5.3.1. Future prospects

Regarding hypothetical extensions of this work, the broad scope of NPs that can be incorporated into the COF spheres could be used to co-encapsulate different types of NPs, thus generating a material that would benefit, for example, from the catalytic properties of gold NPs, the magnetic properties of iron oxide NPs and the porosity of COFs and could be employed for size selective, easily recoverable, water dispersible catalysts. Moreover, as well as NP encapsulation, it can also be suggested the possibility of encapsulating molecular species, which could be useful in remediation or molecular delivery.

Moreover, there are already tangible examples of the use of this two-step strategy. In a recent work, spray-drying was used to prepare COFs. This is an easily scalable technique that also provides some control on

morphology, and hollow capsules were obtained. Despite these advantages, the short reaction times did not allow the formation of crystalline COFs directly in the spray-dryer. Therefore, the recrystallisation procedure was employed to transform the amorphous material into porous and crystalline without affecting the capsule morphology[28].

5.4. References

(1) Mei, Y.; Lu, Y.; Polzer, F.; Ballauff, M.; Drechsler, M. Catalytic Activity of Palladium Nanoparticles Encapsulated in Spherical Polyelectrolyte Brushes and Core−Shell Microgels. *Chem. Mater.* **2007**, *19* (5), 1062–1069.

(2) Zlotea, C.; Campesi, R.; Cuevas, F.; Leroy, E.; Dibandjo, P.; Volkringer, C.; Loiseau, T.; Férey, G.; Latroche, M. Pd Nanoparticles Embedded into a Metal-Organic Framework: Synthesis, Structural Characteristics, and Hydrogen Sorption Properties. *J. Am. Chem. Soc.* **2010**, *132* (9), 2991–2997.

(3) Yang, J.; Zhang, H.; Yu, M.; Emmanuelawati, I.; Zou, J.; Yuan, Z.; Yu, C. High-Content, Well-Dispersed γ-Fe 2 O 3 Nanoparticles Encapsulated in Macroporous Silica with Superior Arsenic Removal Performance. *Adv. Funct. Mater.* **2014**, *24* (10), 1354–1363.

(4) Zou, R.; Liu, Q.; He, G.; Yuen, M. F.; Xu, K.; Hu, J.; Parkin, I. P.; Lee, C.-S.; Zhang, W. Nanoparticles Encapsulated in Porous Carbon Matrix Coated on Carbon Fibers: An Ultrastable Cathode for Li-Ion Batteries. *Adv. Energy Mater.* **2017**, *7* (2), 1601363.

(5) Zeleňáková, A.; Hrubovčák, P.; Kapusta, O.; Zeleňák, V.; Franco, V. Large Magnetocaloric Effect in Fine Gd 2 O 3 Nanoparticles Embedded in Porous Silica Matrix. *Appl. Phys. Lett.* **2016**, *109* (12), 122412.

(6) Lai, C.-Y.; Trewyn, B. G.; Jeftinija, D. M.; Jeftinija, K.; Xu, S.; Jeftinija, S.; Lin, V. S.-Y. A Mesoporous Silica Nanosphere-Based Carrier System with Chemically Removable CdS Nanoparticle Caps for Stimuli-Responsive Controlled Release of Neurotransmitters and Drug Molecules. *J. Am. Chem. Soc.* **2003**, *125* (15), 4451–4459.

(7) He, C.; Wu, S.; Zhao, N.; Shi, C.; Liu, E.; Li, J. Carbon-Encapsulated Fe 3 O 4 Nanoparticles as a High-Rate Lithium Ion Battery Anode Material. *ACS Nano* **2013**, *7* (5), 4459–4469.

(8) Caruso, F.; Spasova, M.; Salgueiriño-Maceira, V.; Liz-Marzán, L. M. Multilayer Assemblies of Silica-Encapsulated Gold Nanoparticles on Decomposable Colloid Templates. *Adv. Mater.* **2001**, *13* (14), 1090–1094.

(9) Chen, J.; Feng, Z.; Ying, P.; Li, C. ZnO Clusters Encapsulated inside Micropores of Zeolites Studied by UV Raman and Laser-Induced Luminescence Spectroscopies. *J. Phys. Chem. B* **2004**, *108* (34), 12669–12676.

(10) Hu, P.; Zhuang, J.; Chou, L.-Y.; Lee, H. K.; Ling, X. Y.; Chuang, Y.-C.; Tsung, C.-K. Surfactant-Directed Atomic to Mesoscale Alignment: Metal Nanocrystals

Encased Individually in Single-Crystalline Porous Nanostructures. *J. Am. Chem. Soc.* **2014**, *136* (30), 10561–10564.

(11) Lu, G.; Li, S.; Guo, Z.; Farha, O. K.; Hauser, B. G.; Qi, X.; Wang, Y.; Wang, X.; Han, S.; Liu, X.; et al. Imparting Functionality to a Metal–organic Framework Material by Controlled Nanoparticle Encapsulation. *Nat. Chem.* **2012**, *4* (4), 310–316.

(12) Chen, L.; Peng, Y.; Wang, H.; Gu, Z.; Duan, C. Synthesis of Au@ZIF-8 Single- or Multi-Core–shell Structures for Photocatalysis. *Chem. Commun.* **2014**, *50* (63), 8651.

(13) Li, S.; Huo, F. Hybrid Crystals Comprising Metal-Organic Frameworks and Functional Particles: Synthesis and Applications. *Small* **2014**, *10* (21), 4371–4378.

(14) Kalidindi, S. B.; Oh, H.; Hirscher, M.; Esken, D.; Wiktor, C.; Turner, S.; Van Tendeloo, G.; Fischer, R. a. Metal@COFs: Covalent Organic Frameworks as Templates for Pd Nanoparticles and Hydrogen Storage Properties of Pd@COF-102 Hybrid Material. *Chem. - A Eur. J.* **2012**, *18* (35), 10848–10856.

(15) Horcajada, P.; Chalati, T.; Serre, C.; Gillet, B.; Sebrie, C.; Baati, T.; Eubank, J. F.; Heurtaux, D.; Clayette, P.; Kreuz, C.; et al. Porous Metal–organic-Framework Nanoscale Carriers as a Potential Platform for Drug Delivery and Imaging. *Nat. Mater.* **2010**, *9* (2), 172–178.

(16) Zhou, T.-Y.; Lin, F.; Li, Z.-T.; Zhao, X. Single-Step Solution-Phase Synthesis of Free-Standing Two-Dimensional Polymers and Their Evolution into Hollow Spheres. *Macromolecules* **2013**, *46* (19), 7745–7752.

(17) Kandambeth, S.; Venkatesh, V.; Shinde, D. B.; Kumari, S.; Halder, A.; Verma, S.; Banerjee, R. Self-Templated Chemically Stable Hollow Spherical Covalent Organic Framework. *Nat. Commun.* **2015**, *6* (1), 6786.

(18) Yang, C.-X.; Liu, C.; Cao, Y.-M.; Yan, X.-P. Facile Room-Temperature Solution-Phase Synthesis of a Spherical Covalent Organic Framework for High-Resolution Chromatographic Separation. *Chem. Commun.* **2015**, *51* (61), 12254–12257.

(19) Smith, B. J.; Parent, L. R.; Overholts, A. C.; Beaucage, P. A.; Bisbey, R. P.; Chavez, A. D.; Hwang, N.; Park, C.; Evans, A. M.; Gianneschi, N. C.; et al. Colloidal Covalent Organic Frameworks. *ACS Cent. Sci.* **2017**, *3* (1), 58–65.

(20) Imaz, I.; Hernando, J.; Ruiz-Molina, D.; Maspoch, D. Metal-Organic Spheres as Functional Systems for Guest Encapsulation. *Angew. Chemie Int. Ed.* **2009**, *48* (13), 2325–2329.

(21) Smith, B. J.; Overholts, A. C.; Hwang, N.; Dichtel, W. R. Insight into the Crystallization of Amorphous Imine-Linked Polymer Networks to 2D Covalent Organic Frameworks. *Chem. Commun.* **2016**, *52* (18), 3690–3693.

(22) Tan, J.; Namuangruk, S.; Kong, W.; Kungwan, N.; Guo, J.; Wang, C. Manipulation of Amorphous-to-Crystalline Transformation: Towards the Construction of Covalent Organic Framework Hybrid Microspheres with NIR Photothermal Conversion Ability. *Angew. Chemie Int. Ed.* **2016**, *55* (45), 13979–13984.

(23) Hanzawa, Y.; Kaneko, K. Lack of a Predominant Adsorption of Water Vapor on Carbon Mesopores. *Langmuir* **1997**, *13* (22), 5802–5804.

(24) Paranthaman, S.; Coudert, F.-X.; Fuchs, A. H. Water Adsorption in Hydrophobic MOF Channels. *Phys. Chem. Chem. Phys.* **2010**, *12* (28), 8123.

(25) Huang, N.; Krishna, R.; Jiang, D. Tailor-Made Pore Surface Engineering in Covalent Organic Frameworks: Systematic Functionalization for Performance Screening. *J. Am. Chem. Soc.* **2015**, *137* (22), 7079–7082.

(26) Rodríguez-San-Miguel, D.; Corral-Pérez, J. J.; Gil-González, E.; Cuellas, D.; Arauzo, J.; Monsalvo, V. M.; Carcelén, V.; Zamora, F. Sub-Micron Spheres of an Imine-Based Covalent Organic Framework: Supramolecular Functionalization and Water-Dispersibility. *CrystEngComm* **2017**, *19* (33), 4872–4876.

(27) Aditya, T.; Pal, A.; Pal, T. Nitroarene Reduction: A Trusted Model Reaction to Test Nanoparticle Catalysts. *Chem. Commun.* **2015**, *51* (46), 9410–9431.

(28) Garzón-Tovar, L.; Avci-Camur, C.; Rodríguez-San-Miguel, D.; Imaz, I.; Zamora, F.; Maspoch, D. Spray Drying for Making Covalent Chemistry II: Synthesis of Covalent–organic Framework Superstructures and Related Composites. *Chem. Commun.* **2017**, *53* (82), 11372–11375.

Conclusions

The work presented previously was focused on the processability of covalent organic frameworks, which is on a par with properties regarding their performance in potential applications.

One of the first advances derived from this work was the realisation of room temperature synthesis of imine-linked COFs[1], which until then had only been reported in solvothermal conditions.

The demonstration of this possibility had game changing outcomes for COF processability. In a first work, it allowed the patterning on a variety of substrates using conventional and fully developed techniques such as inkjet printing, or also lithographically controlled wetting. Moreover, knowing that it did not necessarily have to be a futile effort, other conditions that allowed a mild synthesis were found and adapted to microfluidic systems[2], which offer a great number of novel possibilities and uncoventional effects.

It was also demonstrated that, when conditions directly yielding an ordered material cannot be used because there are other more stringent requirements, it is a feasible approach to first prepare an amorphous network with the desired morphological and functional characteristics and later recrystallise it to obtain the target crystalline and porous COF[3].

Finally, the synthesis of a series of COFs impregnated with different species to promote their ionic conductivity exposed the massive effect processing has on the potential of a material in carrying out a task. In this case, a COF with worse electrical properties but better processing, outperformed a more conductive one in their application as proton exchange membranes in fuel cells[4].

In summary, methodologies to process in COFs were developped, providing procedures to prepare them with two-dimensional (surface patterning), one-dimensional (microfluidic fibres) or zero-dimensional (spheres) morphologies, and the application to fuel cells evidenced the critical role of processing on the performance of the materials.

References

(1) de la Peña Ruigómez, A.; Rodríguez-San-Miguel, D.; Stylianou, K. C.; Cavallini, M.; Gentili, D.; Liscio, F.; Milita, S.; Roscioni, O. M.; Ruiz-González, M. L.; Carbonell, C.; et al. Direct On-Surface Patterning of a Crystalline Laminar Covalent Organic Framework Synthesized at Room Temperature. *Chem. - A Eur. J.* **2015**, *21* (30), 10666–10670.

(2) Rodríguez-San-Miguel, D.; Abrishamkar, A.; Navarro, J. A. R.; Rodriguez-Trujillo, R.; Amabilino, D. B.; Mas-Ballesté, R.; Zamora, F.; Puigmartí-Luis, J. Crystalline Fibres of a Covalent Organic Framework through Bottom-up Microfluidic Synthesis. *Chem. Commun.* **2016**, *52* (59), 9212–9215.

(3) Rodríguez-San-Miguel, D.; Yazdi, A.; Guillerm, V.; Pérez-Carvajal, J.; Puntes, V.; Maspoch, D.; Zamora, F. Confining Functional Nanoparticles into Colloidal Imine-Based COF Spheres by a Sequential Encapsulation-Crystallization Method. *Chem. - A Eur. J.* **2017**, *23* (36), 8623–8627.

(4) Montoro, C.; Rodríguez-San-Miguel, D.; Polo, E.; Escudero-Cid, R.; Ruiz-González, M. L.; Navarro, J. A. R.; Ocón, P.; Zamora, F. Ionic Conductivity and Potential Application for Fuel Cell of a Modified Imine-Based Covalent Organic Framework. *J. Am. Chem. Soc.* **2017**, *139* (29), 10079–10086.

Conclusiones

El trabajo presentado anteriormente se centra en la procesabilidad de COFs basados en enlace imina, que tiene una importancia comparable a las propiedades del material en relación a su rendimiento en potenciales aplicaciones.

Uno de los primeros avances derivados de este trabajo fue la demostración de que es posible sintetizar COFs basados en enlace imina a temperatura ambiente[1], ya hasta entonces solo estaba descrita la síntesis de estos materiales en condiciones solvotermales.

Este descubrimiento ha propiciado numerosos resultados y avances en el procesado de COFs. En un primer trabajo, se consiguió la creación de diseños con estos materiales en una variedad de sustratos usando técnicas establecidas como impresión por inyección de tinta o "lithographically controlled wetting". Por otra parte, sabiendo que no era necesariamente un esfuerzo en vano, se exploraron otras condiciones de síntesis suaves que permitieron adaptar la producción de estos materiales a sistemas de microfluídica[2], que ofrecen un gran número de posiblidades novedosas y poco convencionales.

También se ha demostrado que, si no se pueden usar directamente condiciones que proporcionen materiales cristalinos debido a la existencia de otros requisitos más severos, es factible enfocar la síntesis a través de la preparación de una red amorfa con la morfología y propiedades deseadas para a continuación obtener el COF cristalino y poroso mediante recristalización[3].

Por último, la síntesis de una serie de COFs impregnados con diferentes moléculas que incrementan su conductividad reveló la crucial importancia que el procesado tiene en el potencial de un material en una determinada

aplicación. En este caso, un COF con peor conductividad pero mejor procesado, dio mejores resultados como membrana de intercambio de protones en un pila de combustible que otro material con mejores propiedades eléctricas.

En resumen, se han desarrollado varias metodologías para procesar COFs, proporcionando procedimientos para prepararlos con morfologías bidimensionales (deposición en superficie), unidimensionales (fibras mediante microfluídica) o cero-dimensionales (esferas), y la aplicación en pilas de combustible ha hecho patente el papel fundamental que juega el procesado en el rendimiento de los materiales.

Appendix

A1. General materials and methods

A1.1. Materials

All the general chemicals and solvents were obtained from commercial sources and used without further purification unless otherwise specified. 1,3,5-tris(4'-aminophenyl)benzene was prepared according to the procedure detailed below.

A1.1.1. Synthesis of 1,3,5-tris(4'-aminophenyl)benzene

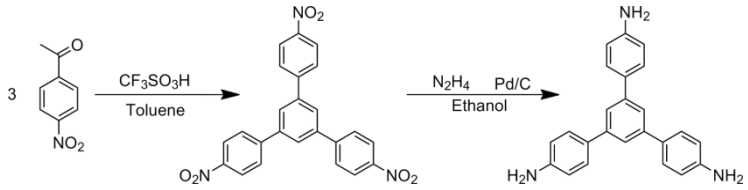

Figure A1.1. Scheme of the synthesis of 1,3,5-tris(4'-aminophenyl)benzene.

Add trifluoromethanesulfonic acid (0.5 mL, 5.7 mmol) to a suspension of 4'-nitroacetophenone (25 g, 152 mmol) in 100 mL of toluene. Stir the solution under reflux in a Dean-Stark apparatus for 7 days. Cool the black reaction mixture and filter off to obtain a black solid. Wash the solid with boiling DMF until it turns white-pale yellow. 1,3,5-tris(4'-nitrophenyl)benzene was obtained as an off-white solid in 75 % yield (16.7 g).

Suspend 3 g of 1,3,5-tris(4'-nitrophenyl)benzene and 0.3 g of Pd on carbon (10 % wt) in 80 mL of ethanol. Heat until reflux and then add

dropwise 10 mL of hydrazine hydrate. After refluxing for 4 h add 5 mL of hydrazine hydrate. Keep refluxing for a total of 16 h and filter the hot solution through celite, wash the celite with hot THF to extract the precipitated product and evaporate the solvent. White crystals of 1,3,5-tris(4'-aminophenyl)benzene are formed. The crystals are filtered and washed with cold water and ethanol. Finally, the white solid is dried in vacuum at 60 ºC for 12 h to yield 2.25 g of 1,3,5-tris(4'-aminophenyl)benzene in 94 % yield. ^{1}H-NMR (300 MHz , THF-d_8): δ (ppm) 7.56 (s, 3H), 7.46 (d, J = 8.6 Hz, 6H), 6.68 (d, J = 8.6 Hz, 6H), 4.55 (s, 6H), agrees with previously reported spectra[1].

A1.2. Methods

Attenuated Total Reflectance Fourier-Transform Infrared Spectroscopy. ATR-FT-IR spectra were recorded in a Perkin Elmer Spectrum 100 with a PIKE Technologies MIRacle Single Reflection Horizontal ATR Accesory with a spectral range of 4000-650 cm^{-1}.

Solid-State ^{13}C CP-MAS Nuclear Magnetic Resonance Spectroscopy. High resolution solid-state nuclear magnetic resonance (NMR) spectra were recorded at ambient pressure on a Bruker AV 400 WB spectrometer using a triple channel (BL4 X/Y/^{1}H) and Bruker magic angle-spinning (MAS) probe with 4 mm (outside diameter) zirconia rotors and Kel-F stoppers. Cross-polarization with MAS (CP-MAS) was used to acquire ^{13}C data at 100.61 MHz. The ^{1}H ninety degree pulse widths were both 3.1 µs. The CP contact time was 3.5 ms. High power two-pulse phase modulation (TPPM) 1H decoupling was applied during data acquisition. The decoupling frequency corresponded to 80 kHz. The MAS sample spinning rate was 10 kHz. Recycle delays between scans were 4 s. The ^{13}C chemical shifts are given relative to tetramethylsilane as zero ppm.

Thermogravimetry. Thermogravimetric analyses were run on a Thermobalance TGA Q-500 thermal gravimetric analyzer. The sample was deposited in a platinum pan. N_2 was used as a purge gas at a flow of 90 mL min^{-1}. The samples were heated at 10 K min^{-1}

Elemental Analysis: Elemental analyses were obtained using LECO CHNS-932 elemental analyzer.

Powder X-Ray Diffraction: PXRD patterns were collected with a Bruker D8 Advance X-ray diffractometer (Cu-Kα radiation; λ = 1.5418 Å) equipped with a Lynxeye detector. Samples were mounted on a flat glass plate. Patterns were collected in the 3.5°<2θ<35° range with a step size of 0.016° and exposure time of 0.8 s/step.

Field-Emission Scanning Electron Microscopy: FESEM images were acquired on a Philips XL 30 S-FEG microscope operating at an accelerating voltage of 10 kV. Samples were previously coated with chromium in a sputter Quorum Q150T-S.

Scanning Electron Microscopy: SEM images were acquired on a Hitachi S-3000N microscope operating at an accelerating voltage of 20 kV. Samples were previously coated with gold in a sputter Caoter SC502.

Atomic Force Microscopy: AFM images were acquired in dynamic mode using a Nanotec Electronica System operating at room temperature in ambient air conditions. The images were processed using WSxM (freely downloadable scanning probe microscopy software from www.nanotec.es). For AFM measurements, commercial Olympus Si/N cantilevers were used with a nominal force constant of 0.75 N/m.

Dynamic Light Scattering: DLS studies were carried out using a Vasco 1 particle size analyser of Cordouan Technologies.

A2. Chapter 2 methods and experimental procedures

A2.1. Methods

Transmission Electron Microscopy: TEM images were acquired on a FEI Tecnai G2 F20 microscope equipped with a 200 kV microprobe.

Adsorption studies: N_2 (77 K) and CO_2 (195, 273 and 298 K) isotherms were collected using an AutosorbIQ. **RT-COF** was activated at 150 ºC under vacuum overnight. The pore volume calculations were performed using the Dubinin-Radushkevich equation and the isosteric heat of adsorption (Qst) was calculated using the Clausius-Clapeyron equation.

Inkjet Printing: The printer used was a Fujifilm Dimatrix (DMP-2831) with piezoelectric inkjet technology. This printer can create and define patterns over an area of about 200 x 300 mm and handle substrates up to 25 mm thick with an adjustable Z height. The printer offers a variety of patterns using the pattern editor program. This system enables easy printing of structures and samples for process verification and prototype creation. The cartridge reservoir has a capacity of 1.5 mL. Each single-use cartridge has 16 nozzles linearly spaced at 254 µm, however only one nozzle was used for printing experiments with typical drop sizes of 10 pL.

2D-Grazing Incidence X-Ray Diffraction: The 2D-GIXRD images were recorded at the ELETTRA-XRD1 beamline at Trieste's synchrotron facility (Italy) using a monochromatic beam with a wavelength of 1 Å. The incident angle of the X-ray beam, α_i, was chosen close to the critical angle for total reflection of the organic film (i.e. 0.12°). The diffraction patterns were recorded using a 2D camera (Pilatus detector) placed normal to the incident beam direction.

DFT Calculations: Periodic models of COF-TAPB-BTCA were optimised with the CASTEP plane-wave DFT code, version 6.1[2]. A cutoff-energy of 280 eV was used to construct the plane-wave basis, with Vanderbilt ultra-soft pseudopotentials[3] and the Perdew-Burke-Ernzerhof (PBE) generalized gradient-corrected functional[4] was used to compute the ground-state wavefunction. A dispersion-interaction correction[5] was used to compensate for the known underestimation of van deer Waals interactions in DFT calculations. The reciprocal space was sampled with a k-point mesh of 0.05 $Å^{-1}$ in order to have the same sampling regardless of the unit cell size. A grid scale of 2.1 was used for numerical integration in real space.

A2.2. Experimental procedures

A2.2.1. Synthesis of RT-COF

100 mg (0.285 mmol) of 1,3,5-tris(4'-aminophenyl)benzene (TAPB) were dissolved in 6 mL of *m*-cresol or DMSO. 46.1 mg (0.285 mmol) of 1,3,5-benzenetricarboxaldehyde (BTCA) were dissolved in 4 mL of *m*-cresol or DMSO and 1 mL of glacial acetic acid. Both solutions were subsequently mixed at room temperature. It was observed, almost immediately, the formation of a yellow gel. After 30 minutes, the gel was washed with tetrahydrofuran (4x100 mL) and methanol (4x100 mL) and isolated by filtration. The resulting solid was dried under ambient conditions for 2 days. The solid obtained was dried under vacuum (50 mbar) at 150 ºC for 24 h to yield 126 mg (0.275 mmol; 96 % yield) of RT-COF as a yellow solid. Elemental analysis calculated for $C_{33}H_{21}N_3 \cdot 2H_2O$: C: 79.98 %, H: 5.08 %, N: 8.48 %. Found in *m*-cresol: C: 78.59 %, H: 4.91 %, N: 8.57 %. Found in DMSO: C: 77.40 %, H: 4.78 %, N: 8.39 %.

A2.2.2. AFM sample preparation

SiO_2 (300 nm thick)/Si substrates were used. Prior to sample preparation, they were cleaned by ultrasonication at 380 W in acetone for 15 min and in 2-propanol for another 15 min, and then dried under an argon flow.

Samples were prepared by first dispersing 0.26 mg of RT-COF in 5 mL of methanol, and then sonicating the resulting suspension with an ultrasonication bath (Elma, 37 kHz, 380 W) for 15 min. Thereafter, the suspension was ultra-centrifuged (MPW-350R centrifuge) at 9000 rpm for 10 min. The resulting solution was diluted with methanol to a concentration close to 10^{-4} mg/mL. The diluted solutions were adsorbed on the SiO_2/Si substrates by dropcasting deposition for 10 min at 20 ^{o}C, and then dried under argon flow.

A2.2.3. TEM sample preparation

Samples were prepared by first dispersing 0.26 mg of RT-COF in 5 mL of methanol, and then sonicating the resulting suspension with an ultrasonication bath (Elma, 37 kHz, 380 W) for 15 min. Thereafter, the suspension was ultra-centrifuged (MPW-350R centrifuge) at 9000 rpm for 10 min. The resulting solution was diluted with methanol to a concentration close to 10^{-4} mg/mL. The diluted solution was casted on copper TEM grids coated with lacey carbon film (200 mesh, EMS).

A2.2.4. LCW patterning

Spread on a SiO_2 surface 20 µL of a TAPB and BTCA solution in *m*-cresol with a 2.8×10^{-3} M concentration of both molecules. Place in contact with the solution a PDMS stamp (formed by protrusions shaped as parallel lines 220 nm high, 1 µm or 500 nm width and 1.5 µm pitch). A meniscus is

formed. Pour 2 µL of acetic acid at one of the open ends of the stamp. RT-COF is formed in the microchannels in a few seconds.

A2.2.5. Inkjet printing patterning

The ink consists on 10 mL of a DMSO solution with 10 mg (0.028 mmol) of TAPB and 4.3 mg (0.028 mmol) of BTCA. This solution is poured into a cartridge and dot arrays are printed using only one nozzle to cast 10 pL drops onto the SiO_2/Si or acetate sheet substrates.

A3. Chapter 3 methods, experimental procedures and additional data

A3.1. Materials

The PDMS base and curing agent were purchased from Dow Corning (Sylgard 184 Silicone elastomer kit).

A3.2. Methods

Microfluidic device fabrication: The silicon master mold used for the fabrication of the microfluidic chips was produced using standard photolithography techniques as described in detail elsewhere.[2] The microfluidic chips employed in this work were fabricated through a conventional polydimethylsiloxane (PDMS) replica molding process. In brief, a mixture of PDMS base and curing agent 10:0.9 ratio by weight was casted against the silicon master mold, previously passivated with chlorotrimethylsilane under vacuum for 30 min, and was then cured at 70 ºC for 3 hours. Next, the cured PDMS was peeled off from the master mold and cut with a razor blade resulting in a PDMS slab with channel features and dimensions of 24 × 24 mm^6. The four inlets and the outlet channel of the PDMS slab were punched with a biopsy punch (1.5 mm, Miltex GmBH, Germany) and subsequently bonded against a glass coverslip (24 × 40 mm^2, #5, Menzel-Glaser, Germany) using a laboratory corona discharge (BD-20ACV, Electro-Technic Products, USA). Finally, the bonding was further facilitated by heating the assembled structure at 70 ºC for 4 hours.

The microfluidic device used in this work was comprised of four converging input channels and one main reactor channel. The height of all

channels was 50 µm and the main channel length was set at 1 cm. The width of the four input channels and main channel were 50 µm and 250 µm, respectively.

Transmission Electron Microscopy: TEM studies were performed on a JEOL JEM-2100 microscope operating at 200 kV. Samples were prepared by sonicating in methanol at 35 kHz for 10 minutes a small piece of MF-COF as obtained directly from the outlet of the microfluidic device. Then, a drop of the suspension was poured over a TEM grid (200 mesh, gold-based holey carbon film, Quantifoil®)

Gas Adsorption: Conventional adsorption isotherms were measured using a Micromeritics Tristar 3000 volumetric instrument under continuous adsorption conditions. Brunauer-Emmet-Teller (BET) and Langmuir analyses were carried out to determine the total specific surface areas for the N_2 isotherms at 77 K. Prior to measurement, powdered samples were heated at 423 K for 12 h and outgassed to 10^{-6} Torr.

A3.3. Experimental procedures

A3.3.1. Synthesis of COF-Ac

100 mg (0.285 mmol) of TAPB were dissolved in 14.2 mL of glacial acetic acid. 46 mg (0.285 mmol) of BTCA were dissolved in 14.2 mL of glacial acetic acid. Both solutions were mixed at room temperature and an orange gel formed immediately. After 30 minutes, the gel was washed with tetrahydrofuran (4x100 mL) and methanol (4x100 mL) and isolated by filtration. The resulting solid was dried under ambient conditions for 2 days. The solid obtained was dried under vacuum (50 mbar) at 150 ºC for 24 h to yield 116 mg (89 % yield) of COF-Ac as a yellow solid. Elemental

analysis calculated for $C_{33}H_{21}N_3 \cdot 0.5H_2O$: C: 84.43 %, H: 4.69 %, N: 8.96 %. Found: C: 83.07 %, H: 4.81 %, N: 8.72 %.

A3.3.2. Synthesis of MF-COF

Solutions in acetic acid of 1,3,5-benzenetricarboxaldehyde (0.040 M) and 1,3,5-tris-(4'-aminophenyl)benzene (0.040 M) were prepared and filtered using syringe filters with a pore size of 0.45 µm (Titan Syringe Filter, Fisher Scientific). In a typical experiment, the solutions of 141 mg of TAPB in 10 mL acetic acid and 65 mg of BTCA in 10 mL acetic acid were injected into the two middle input channels of the microfluidic device (B and C in Figure 3.1 in Chapter 3) at a flow rate of 100 µL/min. In order to control the reaction time in the main channel, we supplied two sheath flows of pure acetic acid that allow the tuning of the flow focusing conditions, and thereby, the reaction time of the reagents along the main channel. For the synthesis of MF-COF fibres, the flow rates of the sheath flows were optimized and maintained at 100 µL/min. All solutions were injected into the microfluidic device using a syringe pump system (neMESYS module, Cetoni GmbH Korbußen) that facilitated an accurate control of all the input flow rates, individually. Following the synthesis, the yellowish MF-COF fibres were collected from the outlet of the microfluidic device and immersed in a petri dish filled with acetic acid. The fibers were washed with tetrahydrofuran (4×100 mL) and methanol (4×100 mL) and isolated by filtration. The resulting solid was dried under ambient conditions for 2 days. The solid obtained was dried under vacuum (50 mbar) at 150 ºC for 24 h to yield MF-COF as an orange solid with 92 % yield. Elemental analysis calculated for $C_{33}H_{21}N_3 \cdot 1H_2O \cdot 1CH_3COOH$: C: 78.19 %, H: 5.06 %, N: 7.82 %. Found: C: 77.44 %, H: 4.90 %, N: 8.08 %.

A3.4. Additional data

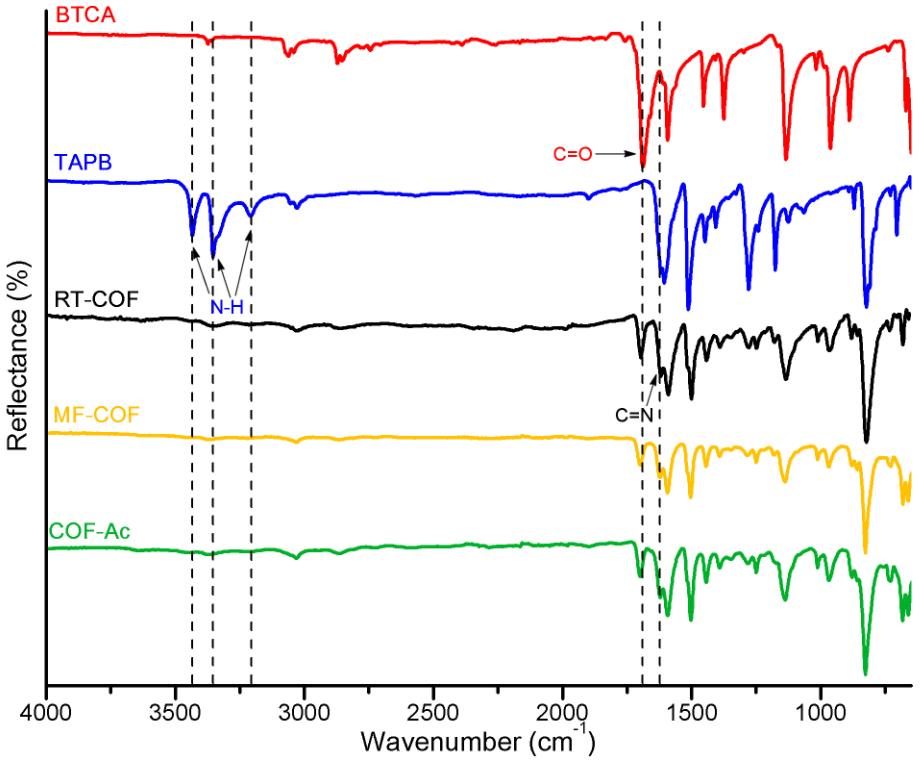

Figure A3.1. ATR-FT-IR spectra of monomers BTCA (red) and TAPB (blue), of RT-COF (black), of MF-COF (orange) and of COF-Ac (green). The most significant changes are highlighted: Disappearance of N-H stretching bands between 3300-3500 cm^{-1}, decrease of the intensity of C=O stretching band at 1689 cm^{-1}, and appearance of C=N stretching band at 1623 cm^{-1}.

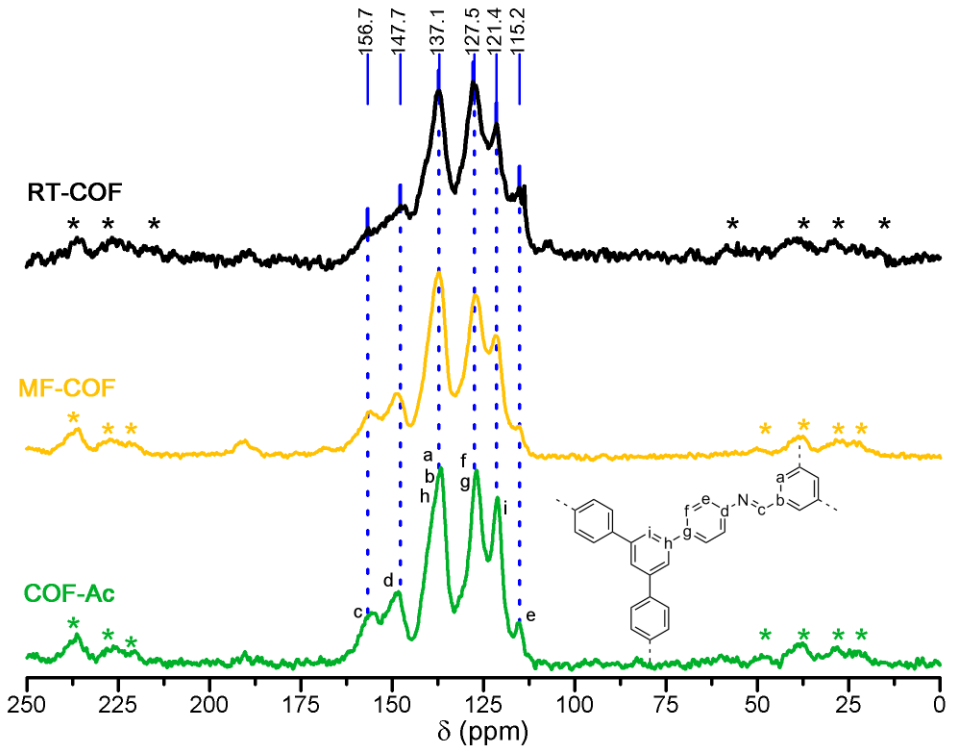

Figure A3.2. Solid state ^{13}C CP-MAS NMR spectra of RT-COF (black), MF-COF (orange) and COF-Ac (green). The signals of RT-COF are assigned in the fragment of the structure at the right. Asterisks denote spinning sidebands.

A4. Chapter 4 methods, experimental procedures and additional data

A4.1. Methods

X-ray diffraction patterns of presed films were acquired on a single crystal Bruker D8 Venture diffractometer using CuKα radiation (λ = 1.5406 Å) under transmission and reflection modes using a single crystal Bruker D8 Venture instrument.

^{7}Li MAS NMR spectroscopy: ^{7}Li MAS NMR spectra were recorded using a external magnetic field of 9.4 T and a resonance frequency of 155.50 MHz. The experiments were performed at room temperature by rotating the sample around the magic angle (54º44 ', with respect to the external magnetic field) with a speed of 10 kHz. For the acquisition of the spectra single pulse sequences were used, with the following parameters: irradiation pulse duration of 3.5 μs; Time interval between successive accumulations of 5s. To determine the chemical shift values in the spectra, a 1M LiCl solution was used as a reference.

Nitrogen and water adsorption: N_2 adsorption isotherms were measured at 77 K on a Micromeritics Tristar 3000 volumetric instrument, and H_2O vapour adsorption isotherms were measured at 298 K on a volumetric apparatus Quantachrome Hydrosorb 1000 HT where temperature was controlled by a Julabo thermostatic bath. Prior to measurements, powder samples were heated for 7 h at 423 K and outgassed to 10^{-6} Torr.

X-ray photoelectron spectroscopy. XPS spectra were recorded on a Kratos AXIS Ultra DLD spectrometer using a monochromatic Al Kα irradiation source (1486.6 eV) operated at 600 W.

High Resolution Transmission Electron Microscopy: HRTEM images were obtained in a *JEOL-JEM GRAND ARM 300cF* microscope equipped with a Cs Corrector (ETA-JEOL). A precise measurement of the aberrations and an optimized correction has been done using the corrector control software JEOL COSMO. The accelerating voltage was set to 60 kV in order to minimize the sample damage. The HRTEM images were acquired by a slow-scan CCD camera (4096 x 4096 pixels, Gatan OneView Camera). *Sample preparation*: 1 mg of **COF-Ac** was sonicated in 3 mL of isopropanol: water 8:2 at 320 W and 37 kHz in a sonication bath (Elma Sonic P300H) for 30 minutes. The resulting suspension centrifuged at 1500 rpm (211 rcf) for 5 minutes. Several drops of the suspension were casted on the TEM grids (200 mesh, copper-based holey carbon film, EMS).

Electrochemical impedance spectroscopy: EIS data were collected using an Autolab electrochemical system II PGSTAT30 (Ecochemie, The Netherlands) impedance analyzer over the frequency range from 1 Hz to 1 MHz with an AC signal amplitude of 10 mV (rms) around the open circuit potential. All measurements were collected using a two-probe method. AC measurements through path were performed to determine the conductivity parameters at different relative humidity conditions (22 and 100 % RH). The temperature range studied spanned from 298 to 373 K at 22 % RH and 313 K at 100 % RH. The 100 % RH value was obtained by bubbling a N_2 flow through ultra-pure water heated at 313 K. The temperature was monitored by using thermocouples placed inside the camera and close to the sample. The electrical contact between the sample and the symmetric stainless steel disk electrodes, for the through plane measurements, was made by applying a pressure of 350 N cm torque with a conductivity cell configuration SS/COF/SS, where SS refers to stainless steel and COF refers to the pellet of the studied material. Each impedance measurement was repeated three times with different films in order to corroborate the

consistency of the conductivity measurements. The conductivity values at different temperatures, σ (S cm^{-1}), and constant humidity (22% RH) were determined from the Nyquist plot by arc extrapolation to the Z´ axis on the high frequency side using the ZView 3.1 (Scribner Association) Software. XRPD analyses of the COF materials were carried out before and after the impedance analyses in order to confirm the integrity of the compound during impedance analysis.

Fuel cell measurements: Membrane-electrode assembly (MEA) fabrication was performed using a standard polymer electrolyte membrane fuel cell (PEMFC) protocol (Figure A4.1). **COF-Ac**, **COF-AcB** and **LiCl-COF** films were used as solid electrolyte. Commercial Pt/C catalyst (40 wt.%, Johnson Matthey) was sprayed onto a carbon cloth gas diffusion layer (ELAT GDL-LT 1200W) and used as electrode. The inks were prepared by mixing the catalyst powder with an isopropanol/deionized water solution (2:1 vol.) and a 4 wt.% amount of Nafion® ionomer solution (5 wt. %) on the dry electrode. Pt loading on the electrodes was set to 0.4 mg cm^{-2}. The membrane was then sandwiched between electrodes into the single-cell (Electrochem Inc.) with a final active area of 0.78 cm^2.

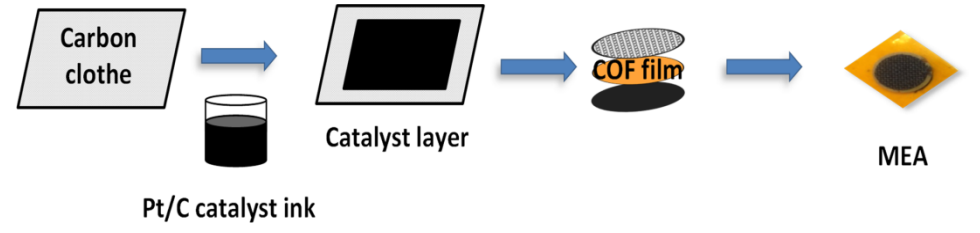

Figure A4.1. Schematic representation of the MEA preparation using COF films as solid electrolyte.

To study this MEA, a test station (FCTS series, Arbin Instruments) controlled with an electrical load system (MITS PRO-FCTS series, Arbin Instruments) was used. The anode and cathode was fed with a flow of 40

ml min^{-1} at atmospheric pressure and 100% of relative humidity (RH) of pure H_2 and O_2 (Air Liquide), respectively. The operating temperature was maintained at 303 or 323 K. The low flow of gas was used in order to prevent the mechanical breakdown of the film.

Linear sweep voltammetry (LSV) was also measured in the constituted single-cell. The cathode was evaluated as working electrode and the anode as reference and counter electrode. Measurements were performed with and Autolab potentiostat between 0.1 and 0.7 V vs. OCP at 2 mV s^{-1} scan rate.

A4.2. Experimental procedures

A4.2.1. Synthesis of RT-COF

100 mg (0.285 mmol) of 1,3,5-tris(4'-aminophenyl)benzene (TAPB) were dissolved in 6 mL of *m*-cresol. 46.1 mg (0.285 mmol) of 1,3,5-benzenetricarboxaldehyde (BTCA) were dissolved in 4 mL of *m*-cresol and 1 mL of glacial acetic acid. Both solutions were subsequently mixed at room temperature. It was observed, almost immediately, the formation of a yellow gel. After 30 minutes, the gel was washed with tetrahydrofuran (4x100 mL) and methanol (4x100 mL) and isolated by filtration. The resulting solid was dried under ambient conditions for 2 days. The solid obtained was dried under vacuum (50 mbar) at 150 ºC for 24 h to yield 126 mg (0.275 mmol; 96 % yield) of RT-COF as a yellow solid. Elemental analysis calculated for $C_{33}H_{21}N_3 \cdot 2H_2O$: C: 79.98 %, H: 5.08 %, N: 8.48 %. Found in *m*-cresol: C: 78.59 %, H: 4.91 %, N: 8.57 %.

A4.2.2. Synthesis of LiCl-COF

100 mg (0.285 mmol) of 1,3,5-tris(4-aminophenyl)benzene (TAPB) were dissolved in 5 mL of m-cresol and 46.1 mg (0.285 mmol) of 1,3,5-benzenetricarbaldehyde (BTCA) were dissolved in another 5 mL of the same solvent and 1 mL glacial acetic acid. Both solutions were mixed at room temperature and a yellow gel formed immediately. After 30 minutes of reaction, the gel was suspended in 100 mL of 30 g/L LiCl aqueous solution and the mixture was stirred during 24 h. Then, it was filtered and dried at 373 K under vacuum (50 mbar) overnight to yield 155 mg (88 % yield) of LiC-COF as a brown solid. Elemental analysis calculated for $C_{33}H_{21}N_3 \cdot 0.3LiCl \cdot 0.5HCl \cdot 5H_2O$: C, 68.27 %; H, 5.47 %; N, 7.24 %; Found: C, 66.95 %; H, 5.65 %; N, 6.80 %.

A4.2.3. Synthesis of COF-Ac

100 mg (0.285 mmol) of TAPB were dissolved in 14.2 mL of glacial acetic acid. 46 mg (0.285 mmol) of BTCA were dissolved in 14.2 mL of glacial acetic acid. Both solutions were mixed at room temperature and an orange gel formed immediately. After 30 minutes, the gel was washed with tetrahydrofuran (4x100 mL) and methanol (4x100 mL) and isolated by filtration. The resulting solid was dried under ambient conditions for 2 days. The solid obtained was dried under vacuum (50 mbar) at 150 ºC for 24 h to yield 116 mg (89 % yield) of COF-Ac as a yellow solid. Elemental analysis calculated for $C_{33}H_{21}N_3 \cdot 0.5H_2O$: C: 84.43 %, H: 4.69 %, N: 8.96 %. Found: C: 83.07 %, H: 4.81 %, N: 8.72 %.

A4.2.4. Synthesis of COF-AcB

100 mg (0.285 mmol) of 1,3,5-tris(4-aminophenyl)benzene (TAPB) were dissolved in 14.2 mL of glacial acetic acid. 46 mg (0.285 mmol) of 1,3,5-

benzenetricarbaldehyde (BTCA) were dissolved in 14.2 mL of glacial acetic acid. Both solutions were mixed at room temperature and an orange gel formed immediately. After 72 h, the gel was washed with tetrahydrofuran (100 mL) and isolated by filtration. The resulting solid was dried under ambient conditions for 2 days to yield 163 mg (86 % yield) of COF-AcB as a red solid. Elemental analysis calculated for $C_{33}H_{21}N_3 \cdot 3.5(CH_3COOH)$: C: 71.74 %, H: 5.26 %, N: 6.27 %; Found: C 68.78 %, H: 5.50 %, N: 6.44 %.

A4.2.5. RT-COF and LiCl-COF pellet fabrication

Pellets of RT-COF and LiCl-COF were prepared by submitting 50 mg of powder of the material to a pressure of 400 MPa for 5 minutes using an uniaxial hydraulic press.

A4.2.6. LiCl-COF film fabrication

Films of LiCl-COF were prepared by adding 20 µL of acetic acid to 40 mg of LiCl-COF and mixing them by grinding in an agate mortar. After approximately 2 minutes the powder is dry. Then, it is submitted to a pressure of 400 MPa for 5 minutes using an uniaxial hydraulic press.

A4.2.7. COF-Ac and COF-AcB film fabrication

Films of COF-Ac and COF-AcB were prepared by submitting 30 mg of powder of the material to a pressure of 400 MPa for 5 minutes using an uniaxial hydraulic press.

A4.2.8. Stability tests

Stability tests were carried out by immersing 10 mg of COF-Ac in 1 mL of aqueous solutions of HCl (12 M) or NaOH (14 M) and stirring the

suspension for 72 hours. Then, the samples were washed with water and dried under vacuum at 150 ºC for 24 hours.

A4.3. Additional data

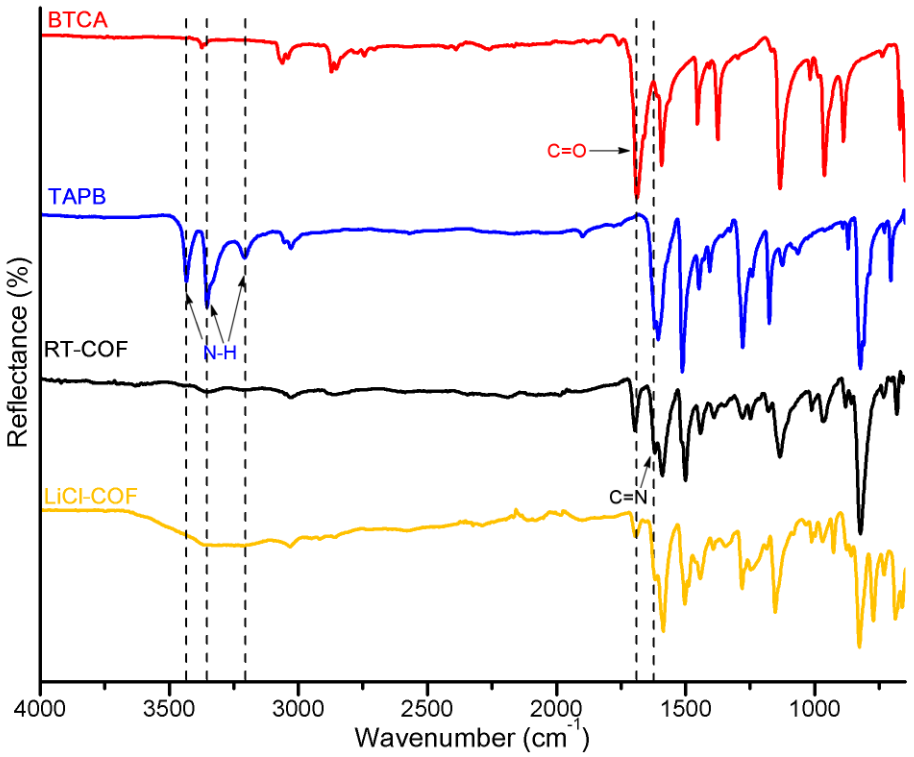

Figure A4.2. ATR-FT-IR spectra of monomers BTCA (red) and TAPB (blue), of RT-COF (black) and of LiCl-COF (orange). The most significant changes are highlighted: Disappearance of N-H stretching bands between 3300-3500 cm^{-1}, decrease of the intensity of C=O stretching band at 1689 cm^{-1}, and appearance of C=N stretching band at 1623 cm^{-1}.

A5. Chapter 5 methods, experimental procedures and additional data

A5.1. Methods

Transmission Electron Microscopy: High-Angle Annular Dark-Field Scanning Transmission Electron Microscopy (HAADF-STEM) were collected on a Transmission Electron Microscope FEI Tecnai G2 F20 at 200 kV.

Powder X-Ray Diffraction: PXRD data were collected at 100 K at XALOC beamLine at ALBA synchrotron[7] (λ = 0.82653 Å). Data were integrated and scaled using the Fit2D program[8].

Inductively Coupled Plasma - Mass Spectrometry: -MS measurements were performed using an ICP-MS Agilent Series 7500.

Gas adsorption: Volumetric N_2 and CO_2 sorption isotherms were collected at 77 K (N_2) and 203 K, 258 K, 273 K, 288 K, 298 K (CO_2) using an ASAP 2020 HD (Micromeritics). Temperature was controlled by a liquid nitrogen bath (77 K) or Lauda Proline RP 890 chiller (203 K – 298 K). As recommended by Rouquerol (COPS X conference, Characterization of Porous Solids, Granada, 2014), Brunner Emmet Teller (BET) area and total pore volumes are selected preferentially to Langmuir model for the evaluation and comparison of the porosity of MOFs. BET areas (A_{BET}) were calculated using MicroActive software within an appropriate pressure range in order to keep the C constant positive, using the criteria recommended by Rouquerol *et al*.[9] The micropore volumes (V_μ) were calculated at P/P0 = 0.3, whereas the total pore volumes (V_t) were calculated at P/P0 = 0.95. Samples were outgassed for 12 h under secondary vacuum at 150 ^oC.

UV−Visible Spectroscopy: UV−visible spectra were acquired with a Shimadzu UV- 2400 spectrophotometer. Samples were placed in a cell, and spectral analysis was performed at room temperature.

A5.2. Experimental procedures

A5.2.1. Synthesis of s-PI

BTCA (46 mg, 0. 28 mmol) was dissolved in 15 mL of acetone and 3 mL of acetic acid. Separately, TAPB (100 mg, 0.28 mmol) was also dissolved in 15 mL of acetone. The resulting solutions were mixed and stirred for 1 h. A turbid yellow suspension was formed. The reaction mixture was centrifuged at 18407 rcf for 2 min. The supernatant was removed and the yellow solid was washed twice with 20 mL of acetone and twice with 20 mL of tetrahydrofuran (THF), isolating it by means of centrifugation at 18407 rcf for 2 min. Finally, the solid was allowed to dry in ambient conditions for 48 h and under vacuum at 150 ºC for 24 h to produce 116 mg (85 % yield) of s-PI as a yellow powder. Elemental analysis calculated for $C_{33}H_{21}N_3 \cdot H_2O$: C: 83.02 %; H: 4.82 %; N: 8.81 %. Found: C: 82.97 %; H: 4.88 %; N: 8.56 %.

A5.2.2. Synthesis of s-COF

s-PI (116 mg) was dispersed in a mixture of 10.5 mL of 1,4-dioxane, 2.1 mL of mesitylene, 2.1 mL of water and 3.1 mL of acetic acid and heated at 70 ºC for 7 days. After cooling, the mixture was centrifuged at 2348 rcf for 3 min. The supernatant was removed and the yellow solid was washed with toluene (20 + 12 mL), isolating it by means of centrifugation at 2348 rcf for 3 min. Finally, the solid was allowed to dry in ambient conditions for 48 h and under vacuum at 150 ºC for 24 h to produce 112 mg (97 % yield) of s-COF as a yellow powder. Elemental analysis calculated for

$C_{33}H_{21}N_3 \cdot H_2O$: C: 83.02 %; H: 4.82 %; N: 8.81 %. Found: C: 83.20 %; H: 4.91 %; N: 8.22 %.

A5.2.3. PVP Stabilized Gold Nanoparticles

A solution of 2.2 mM sodium citrate in Milli-Q water (150 mL) was heated with a heating mantle in a 250 mL three-necked round-bottomed flask for 15 min under vigorous stirring. A condenser was utilized to prevent the evaporation of the solvent. After boiling had commenced, 1 mL of $HAuCl_4$ (25 mM) was injected. The colour of the solution changed from yellow to bluish gray and then, to soft pink in 10 min. Under these conditions, the resulting particles (9 ± 2.4 nm, $\sim 3 \times 10^{12}$ NPs/mL) were coated with negatively charged citrate ions and hence, they were well suspended in H_2O. After the gold nanoparticle solution was cooled to room temperature, a solution of 0.5 g poly (vinylpyrrolidone) (PVP, MW = 40,000) in water (20 mL) was added dropwise to the gold nanoparticle solution under continuous stirring, and the mixture was further stirred at room temperature for 24 h. Then, 600 mL of acetone were added to this mixture and left overnight. The supernatant was removed, and the resulting nanoparticles were washed one time with methanol and twice with acetone, and finally dispersed in 10 mL of acetone at a concentration of 0.6 $mg.mL^{-1}$.[10]

A5.2.4. PVP Stabilized Palladium Nanoparticles

Na_2PdCl_4 (44 mg) was dissolved in 20 mL of ethylene glycol in the presence of 222 mg of poly (vinylpyrrolidone) (PVP, MW = 55,000) in a three-neck round- bottomed flask. This solution was heated up to 180 °C for 10 min and, after cooling down to room temperature, 150 mL of acetone was added to the as-synthesized PVP stabilized palladium nanoparticles. Then, the precipitated nanoparticles were dispersed in

ethanol, washed twice with ethanol and once with acetone, and finally redispersed in acetone to give a colloidal solution of palladium nanoparticles at a concentration of 0.5 mg mL^{-1}. The average size of the palladium nanoparticles was 3.3 ± 1.1 nm.

A5.2.5. PVP Stabilized Iron Oxide Nanoparticles

Iron oxide magnetic nanoparticles were prepared by the conventional co-precipitation method. 4 g of $FeCl_3 \cdot 6H2O$, 1.25 g of $FeCl_2 \cdot 4H_2O$ and 300 mg of poly (vinylpyrrolidone) (PVP, MW = 55,000) were dissolved in 50 mL of Milli-Q water under nitrogen under vigorous stirring at 80˚ C. Then, 0.5 mL of NH_4OH (15 M) was added and the solution was heated for another 1.5 h. After cooling, the nanoparticles were sequentially washed with Milli-Q water and ethanol several times. Finally, nanoparticles were washed twice with acetone and the cleaned nanoparticles were dispersed in acetone at a concentration of 1 mg mL^{-1}. The average size of the iron oxide nanoparticles was 9.8 ± 3.9 nm.[11]

A5.2.6. Synthesis of Au@s-COF

BTCA (20 mg, 0.12 mmol) was dissolved in 1.33 mL of gold nanoparticle suspension, 5.33 mL of acetone and 1.33 mL of acetic acid. Separately, TAPB (43 mg, 0.12 mmol) was also dissolved in 1.33 mL of gold nanoparticle suspension and 5.33 mL of acetone. The resulting solutions were mixed and stirred for 1 h. A pink precipitate was formed in a turbid salmon suspension. The reaction mixture was centrifuged at 24 rcf for 5 min. The turbid salmon supernatant was removed and the pink solid was washed twice with 9 mL of acetone and twice with 9 mL of THF, isolating it by means of centrifugation for 5 min at 94 rcf. The solid (Au@s-PI) was dispersed in a mixture of 5.25 mL of 1,4-dioxane, 1.05 mL of mesitylene, 1.05 mL of water and 1.56 mL of acetic acid and heated at 70 ºC for 7

days. After cooling, the mixture was centrifuged at 2348 rcf for 3 min. The supernatant was removed and the solid was washed with thrice with 6 mL of toluene, isolating it by means of centrifugation at 2348 rcf for 3 min. Finally, the solid was allowed to dry in ambient conditions for 48 h and under vacuum at 80 ºC for 24 h to produce 8.5 mg of Au@s-COF as a brownish-pink powder.

A5.2.7. Synthesis of Pd@s-COF

BTCA (20 mg, 0.12 mmol) was dissolved in 1.33 mL of palladium nanoparticle suspension, 5.33 mL of acetone and 1.33 mL of acetic acid. Separately, TAPB (43 mg, 0.12 mmol) was also dissolved in 1.33 mL of palladium nanoparticle suspension and 5.33 mL of acetone. The resulting solutions were mixed and stirred for 1 h. A black precipitate was formed in a turbid yellow suspension. The reaction mixture was centrifuged at 24 rcf for 5 min. The turbid yellow supernatant was removed and the black solid was washed twice with 9 mL of acetone and twice with 9 mL of THF, isolating it by means of centrifugation for 5 min at 94 rcf. The solid (Pd@s-PI) was dispersed in a mixture of 5.25 mL of 1,4-dioxane, 1.05 mL of mesitylene, 1.05 mL of water and 1.56 mL of acetic acid and heated at 70 ºC for 7 days. After cooling, the mixture was centrifuged at 2348 rcf for 3 min. The supernatant was removed and the yellow solid was washed with thrice with 6 mL of toluene, isolating it by means of centrifugation at 2348 rcf for 3 min. Finally, the solid was allowed to dry in ambient conditions for 48 h and under vacuum at 80 ºC for 24 h to produce 10 mg of Pd@s-COF as a yellow powder.

A5.2.8. Synthesis of Fe_3O_4@s-COF

BTCA (150 mg, 0.93 mmol) was dissolved in 25 mL of iron oxide nanoparticle suspension, 25 mL of acetone and 10 mL of acetic acid.

Separately, TAPB (325 mg, 0.93 mmol) was also dissolved in 25 mL of iron oxide nanoparticle suspension and 25 mL of acetone. The resulting solutions were mixed and ultrasonicated for 1 h. A brown precipitate was formed in a turbid yellow suspension. The turbid yellow supernatant was removed by means of magnetic decantation. The brown solid was washed thrice with 30 mL of acetone and twice with 30 mL of THF. The solid (Fe_3O_4@s-PI) was dispersed in a mixture of 34.25 mL of 1,4-dioxane, 6.85 mL of mesitylene, 6.85 mL of water and 10.2 mL of acetic acid and heated at 70 ºC for 7 days. After cooling, the supernatant was removed by means of magnetic decantation and the solid was washed once with 25 mL of ethanol and twice with 20 mL of toluene. Finally, the solid was allowed to dry in ambient conditions for 48 h and afterwards was dried under vacuum at 80 ºC for 24 h to produce 142 mg of Fe_3O_4@s-COF as a yellow powder.

A5.2.9. 4-nitrophenol reduction

The catalytic reactions were conducted by mixing 0.5 mL of an aqueous solution of $NaBH_4$ (1.3 M) with 3.0 mL of an aqueous solution of 4-nitrophenol (0.125 mM). After 2 min, 0.2 mL of an aqueous solution of 0.15 mg mL^{-1} of Pd@s-PI/Pd@s-COF or 0.4 mL of an aqueous solution of 0.15 mg mL^{-1} of Au@s-PI/Au@s-COF were injected into the reaction mixture. The catalytic reaction was then followed every 2 min by UV−Vis spectroscopy in the range of 280−460 nm.

A5.3. Additional data

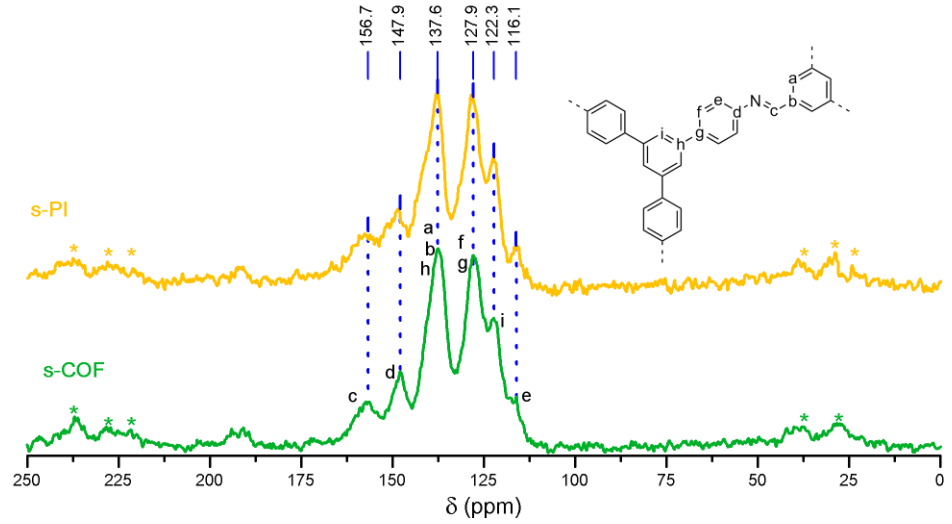

Figure A5.1. Solid state ^{13}C CP-MAS NMR spectra of s-PI (orange) and s-COF (green). The signals of RT-COF are assigned in the fragment of the structure at the right. Asterisks denote spinning sidebands.

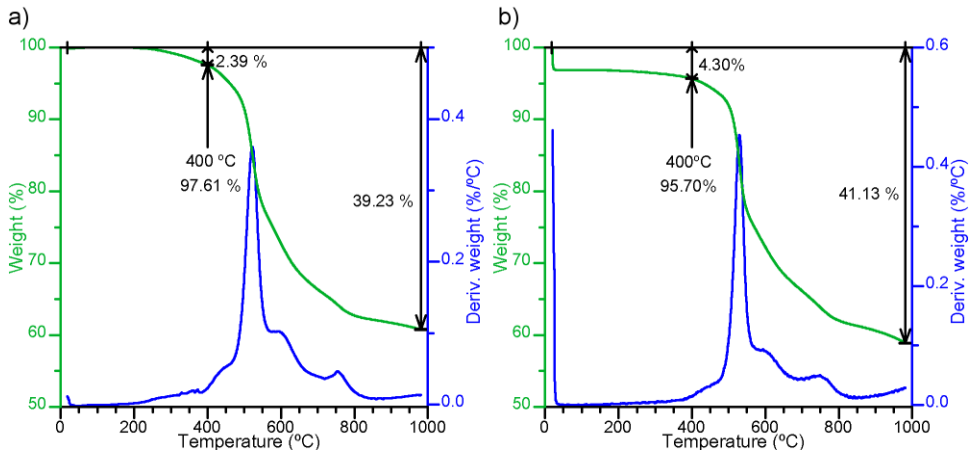

Figure A5.2. a) TGA trace of s-PI. b) TGA trace of s-COF.

A6. References

(1) Bao, C.; Lu, R.; Jin, M.; Xue, P.; Tan, C.; Xu, T.; Liu, G.; Zhao, Y. Triphenyl Benzene-Bridged Fluorescent Silsesquioxane: Shape-Controlled Hybrid Silicas by Hydrolytic Conditions. *J. Nanosci. Nanotechnol.* **2006**, *6* (8), 2560–2565.

(2) Clark, S. J.; Segall, M. D.; Pickard, C. J.; Hasnip, P. J.; Probert, M. I. J.; Refson, K.; Payne, M. C. First Principles Methods Using CASTEP. *Zeitschrift für Krist. - Cryst. Mater.* **2005**, *220* (5/6).

(3) Vanderbilt, D. Soft Self-Consistent Pseudopotentials in a Generalized Eigenvalue Formalism. *Phys. Rev. B* **1990**, *41* (11), 7892–7895.

(4) McNellis, E. R.; Meyer, J.; Reuter, K. Azobenzene at Coinage Metal Surfaces: Role of Dispersive van Der Waals Interactions. *Phys. Rev. B* **2009**, *80* (20), 205414.

(5) Perdew, J. P.; Burke, K.; Ernzerhof, M. Generalized Gradient Approximation Made Simple. *Phys. Rev. Lett.* **1996**, *77* (18), 3865–3868.

(6) Abrishamkar, A.; Paradinas, M.; Bailo, E.; Rodriguez-Trujillo, R.; Pfattner, R.; Rossi, R. M.; Ocal, C.; DeMello, A. J.; Amabilino, D. B.; Puigmartí-Luis, J. Microfluidic Pneumatic Cages: A Novel Approach for In-Chip Crystal Trapping, Manipulation and Controlled Chemical Treatment. *J. Vis. Exp.* **2016**, No. 113.

(7) Juanhuix, J.; Gil-Ortiz, F.; Cuní, G.; Colldelram, C.; Nicolás, J.; Lidón, J.; Boter, E.; Ruget, C.; Ferrer, S.; Benach, J. Developments in Optics and Performance at BL13-XALOC, the Macromolecular Crystallography Beamline at the Alba Synchrotron. *J. Synchrotron Radiat.* **2014**, *21* (4), 679–689.

(8) Hammersley, A. FIT2D: An Introduction and Overview. In *European Synchrotron Radiation Facility Internal Report ESRF97HA02T*; 1997; pp 1–33.

(9) Rouquerol, J.; Rouquerol, F.; Llewellyn, P.; Maurin, G.; Sing, K. S. W. *Adsorption by Powders and Porous Solids: Principles, Methodology and Applications*, 2nd ed.; Elsevier Science, 2014.

(10) Bastús, N. G.; Comenge, J.; Puntes, V. Kinetically Controlled Seeded Growth Synthesis of Citrate-Stabilized Gold Nanoparticles of up to 200 Nm: Size Focusing versus Ostwald Ripening. *Langmuir* **2011**, *27* (17), 11098–11105.

(11) Liu, X.; Ma, Z.; Xing, J.; Liu, H. Preparation and Characterization of Amino–silane Modified Superparamagnetic Silica Nanospheres. *J. Magn. Magn. Mater.* **2004**, *270* (1–2), 1–6.